Crystal Engineering of Dynamic Metal-Organic Frameworks for Applications in Chromic Sensing and Capturing of Small Molecules

GIFT MEHLANA

Thesis presented for the degree of

DOCTOR OF PHILOSOPHY

In the Department of Chemistry

University of Cape Town

August 2014

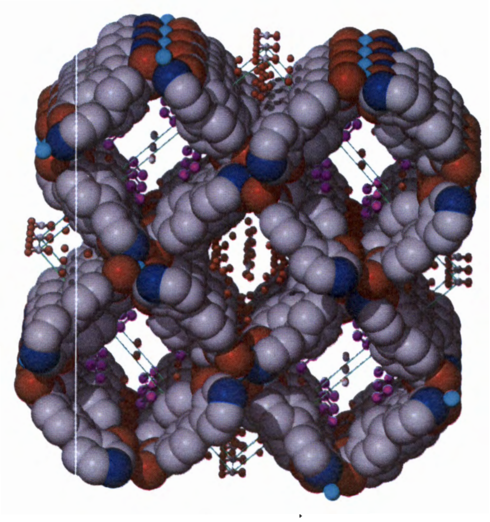

Sports and the arts have the power to move people emotionally. Even in the natural sciences, similar effects can be seen in reactions to revelations from mathematics or astronomy. It is in our power as chemists to unlock mysteries that likewise inspire feelings of wonder and passion. We must strive to uncover facts that turn conventional wisdom on its head and create a new chemistry.

(S. Kitagawa)

Acknowledgments

Special thanks go to:

- Professor Susan A. Bourne and Dr Gaëlle Ramon for their priceless supervision and support during the course of my doctoral studies.

- Professor Lars Öhrström at the Department of Chemical and Biological Engineering at Chalmers University of Technology in Göteborg, Sweden for his supervision with all the work related to network analysis and for hosting me.

- Dr Hong Su for her assistance on single crystal X-ray diffraction data collection.

- Dr Dyanne Cruinkshank for training me to use different instruments as well as computer programs. Your efforts did not go unnoticed.

- Professor Dave Billing of University of Witwatersrand in Johannesburg for your help and supervision in Rietveld refinement in TOPAS.

- The Equity Development Program (UCT Chemistry Department), the National Research Foundation (NRF), International Centre for Diffraction Data (ICDD) and the University of Cape Town for financial support.

- The past and present members of the Supramolecular Chemistry research group for their friendship and support.

- Finally to my family. I dedicate this thesis to you.

Publications and Conferences

Parts of this thesis have been published:

1. G. Mehlana, G. Ramon, S. A. Bourne, *CrystEngComm*, 2014, **DOI 10.1039/C4CE00496E**

   Title: The role of CH-pi interactions in modulating the breathing amplitude of a square lattice 2D net: Alcohol sorption studies.

2. G. Mehlana, G. Ramon, S. A. Bourne, *CrystEngComm*, 2013, **45**, 9521

   Title: Methanol mediated crystal transformations in a solvatochromic metal organic framework constructed from Co(II) and 4-(4-pyridyl) benzoate.

3. G. Mehlana, G. Ramon, S. A. Bourne, *Zeitschrift für Kristallographie*, Crystalline Materials, 2013, **228**, 318.

   Title: Alcohol responsive 2D coordination network of 3-(4-pyridyl)benzoate and Zinc(II).

4. G. Mehlana, S. A. Bourne, G. Ramon and L. Öhrström, *Cryst. Growth Des.*, 2013, **13**, 633.

   Title: Concomitant metal organic frameworks of cobalt(II) and 3(4-Pyridyl)benzoate: Optimized synthetic conditions of solvatochromic and thermochromic systems.

5. G. Mehlana. Susan A Bourne and Gaëlle Ramon, *Dalton Trans.*, 2012, **41**, 4224.

   Title: A new class of thermo- and solvatochromic metal organic frameworks based on 4-(4-pyridyl) benzoic acid.

Parts of this thesis have been presented at the following conferences:

6. XXIV International Conference of Coordination and Bioinorganic Chemistry, 2nd to the 7th of June **2013**, Smolenice Slovakia.
   Title: Water and methanol mediated structural transformations in a solvatochromic metal organic framework constructed from 4-(4-pyridyl)benzoate and Co(II) (oral presentation).

7. Indaba 7. Insights from Structure. 2nd to the 7th of September **2012**, Skukuza South Africa.
   Title: Rare polymorphism in metal organic frameworks (poster presentation). Won the best poster prize award.

8. Division conference, 24th to the 25th of May **2012**, Vann Sweden.
   Title: Chemo-sensing and thermochromic metal organic frameworks based on 3-(4-pyridyl)benzoic acid (poster presentation).

9. Trends in Inorganic Chemistry Symposium, 23th of May **2012**, University of Stockholm, Sweden.
   Title: Chemo-sensing and thermochromic metal organic frameworks based on 3-(4-pyridyl)benzoic acid (poster presentation).

10. Young Scientist Symposium Conference, 24th of November **2011**, University of Western Cape, South Africa .
    Title: A new Class of Thermo- and Solvatochromic Metal Organic Frameworks based on 4-(4-pyridyl)benzoic acid (oral presentation).

Abstract

Gift Mehlana August 2014

Crystal Engineering of Dynamic Metal-Organic Frameworks for Applications in Chromic Sensing and Capturing of Small Molecules

Crystal engineering of metal organic frameworks (MOFs) has developed rapidly over the years. This has been fuelled by useful properties endowed by these materials. MOFs present a unique platform to control chemical and physical properties through manipulation of the components that construct these materials. In this thesis a series of MOFs prepared from 3-(4-pyridyl)benzoate or 4-(4-pyridyl)benzoate with Co(II), Zn(II) and Ni(II) are presented. Most materials were synthesised under solvothermal conditions. The link between the phenyl and pyridyl ring in the ligand allows for conformational change through varying the dihedral angles between these two parts. The carboxylate moiety can also rotate relative to the phenyl ring and its ability to assume different coordination modes under different environments is of utmost importance in achieving flexibility for the design. Structural elucidation of compounds was performed by single crystal X-ray diffraction. Topological analysis was performed on the networks formed by the compounds to have a better understanding of the network connectivity. Bulk material was characterised by thermal methods such as thermogravimetric analysis (TGA), differential scanning calorimetry (DSC), variable temperature powder X-ray diffraction (PXRD) studies and by hot stage microscopy (HSM). Thermochromic and solvatochromic properties of the activated phases were investigated by spectroscopic techniques. Dynamic motion of the networks upon guest loss and absorption by activated phases were evaluated by single crystal X-ray diffraction studies using Pawley fitting methods. Standard kinetic models were used to analyse the kinetics of guest uptake from isothermal experiments. Non-isothermal experiments were conducted using the TGA and the activation energies were determined for guest desolvation using the Ozawa and Flynn method.

This study demonstrates the application of MOFs as sensing devices thanks to changes in the coordination geometry around the metal centre, solvent interactions with host framework or changes in the ligand conformation upon guest loss or absorption, all of which can trigger d-d and π to π^* transitions to occur resulting in a visible colour change.

Abbreviations and compound codes

34pba	3-(4-pyridyl)benzoate
44pba	4-(4-pyridyl)benzoate
HSM	Hot stage microscopy
TGA	Thermogravimetric analysis
DSC	Differential scanning Calorimetry
IR	Infrared
UV-Vis	Ultraviolet visible
MLCT	Metal to ligand charge transfer
MOF	Metal organic framework
SBU	Secondary building unit
MeOH	Methanol
EtOH	Ethanol
DMF	N,N-dimethylformamide
2D	Two dimensional
3D	Three dimensional
1	$\{[Co(34pba)_2]\cdot DMF\}_n$
2	$\{[Co(34pba)_2]\cdot DMF\}_n$
3	$\{[Zn(34pba)_2]\cdot DMF\}_n$
4	$\{[Zn(34pba)_2]\cdot DMF\}_n$
5	4-(4-pyridyl)benzoic acid
6	$\{[Co_4(44pba)_8]\cdot 4DMF\cdot 0.5EtOH\cdot 4H_2O\}_n$
7	$\{[Ni_4(44pba)_8]\cdot 4DMF\cdot 0.5EtOH\cdot 3H_2O\}_n$
8	$\{[Co(44pba)_2]\cdot 2.5CH_3OH\cdot H_2O\}_n$
9	$\{[Co(44pba)_2(CH_3OH)_2]\cdot 2CH_3OH\cdot 0.5H_2O\}_n$
10	$\{[Co_{0.5}(44pba)(CH_3OH)]\cdot 0.5CH_3OH\cdot 0.25H_2O\}_n$
11	$\{[Ni(44pba)_2]\cdot 0.5CH_3OH\cdot 2.5H_2O\cdot 0.1I_2\}_n$

Table of contents

Chapter 1: Introduction

Chapter 2: Experimental

Chapter 3: Topological analysis of network structures

Chapter 4: 3-(4-pyrdidyl)benzoate compounds of Co(II)

Chapter 5: 3-(4-pyrdidyl)benzoate compounds of and Zn(II)

Chapter 6: 4-(4-pyridyl)benzoate compounds of Co(II) or Ni(II)

Chapter 7: Guest exchange studies in MOFs of Co(II) and Ni(II) assembled from 4-(4-pyridyl)benzoate

Chapter 8: Conclusions

Chapter 1

Introduction

This chapter discusses general aspects such as nomenclature and topology associated with metal-organic frameworks and coordination polymers. Different types of interpenetration associated with networks and the impact of such phenomenon on the physical and chemical properties are presented. Solvatochromic properties in metal-organic frameworks and solid state reactions of dynamic materials are also discussed. The motivation, justification and objectives of the study presented in this thesis are given towards the end of the chapter.

1.1 Crystal Engineering

R. Pepinsky was the first person to introduce the term crystal engineering in 1955.[1] However this term is normally associated with G.M.J. Schmidt who applied the topochemical principle to correlate the solid state reactivity of photodimerizable compounds, notably *trans*-cinnamic acids with their crystal structures.[2] Schmidt's article resulted in an evolution on the perception of crystal engineering. It became unambiguous that crystal engineering in the context of organic solids is closely linked to the ideas derived from supramolecular chemistry. Desiraju defined crystal engineering as the understanding of intermolecular interactions in the context of crystal packing and the utilization of such understanding in the design of new solids with desired physical and chemical properties.[3] To make crystals by design one has to have an understanding of the supramolecular interactions that can be used to assemble molecular components into a desired architecture. Several supramolecular interactions between atoms such as coordination bonds, van der Waals forces and hydrogen bonds are involved in assembling molecular components into a target network. The energy associated with these bonding interactions spans a wide range with van der Waals having the lowest energy. Based on the bonding types at stake, it becomes easier to select the right target materials and the appropriate synthetic strategies. These take into account energy associated with bond breaking and bond formation and can ultimately lead to the desired target network from a building block.

Coordination chemistry which at first mainly focused on molecular complexes has evolved rapidly to a periodical coordination chemistry focussing on networks of complexes. This has been achieved by the use of polydentate ligands which can link metal centres in extended networks as illustrated in Figure 1.1.[4] Metal organic frameworks (MOFs) or coordination polymers constitute the largest number of 'engineered' crystals. This is attributed to several useful properties endowed by these materials such as sensing, capturing of gases, storage, drug delivery and catalysis.[5-9] The challenges associated with the crystal engineering of MOFs with void space is self-entanglement of the network,[10,11] as well as designing frameworks which can withstand guest release and uptake. While there is much interest in this class of compounds, it is currently difficult to design or predict the outcome product between the metal ions and the organic ligands.[6] However, In the early 1990s Robson[12,13] expanded the ideas of Wells on inorganic network structures into the realm of MOFs. The concept of "node" and "spacer" has been successful on several occasions in producing the desired network structures.[14]

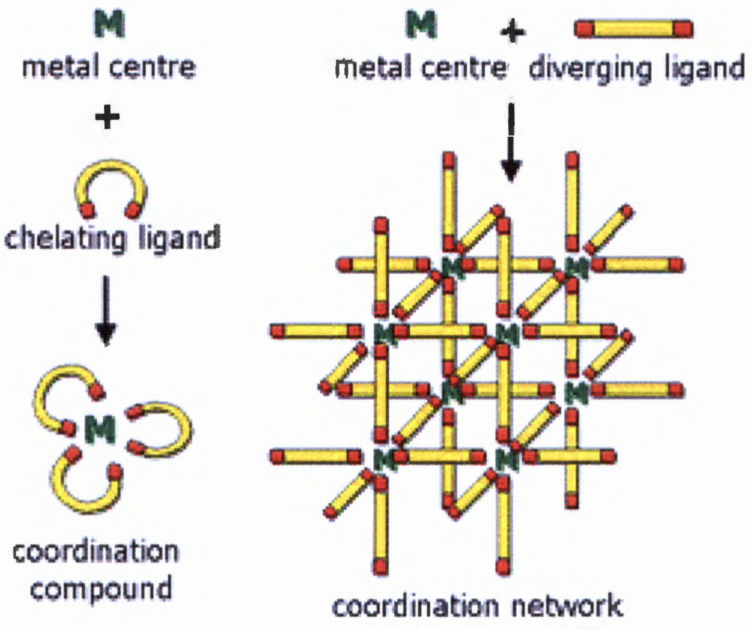

Figure 1.1: A schematic illustration of the transition from molecular to periodical coordination chemistry by Braga. From coordination complexes (left) to coordination complexes (right).[4]

The major drawback of this concept is supramolecular isomerism as several structures with different topologies can be obtained from the same building blocks. Factors such as metal to ligand ratio, solvents, and the reaction conditions can profoundly influence the outcome of the products. One typical example is Davies' work in which two MOFs were prepared from zinc(II) sulphate and 1,3,5-benzenetricarboxylic acid by varying the reaction conditions.[15] One major aim of crystal engineering is to control the factors that lead to supramolecular isomerism by assembling molecular building blocks into the desired network through control of the supramolecular interactions.

Crystal engineering has developed rapidly over the years from its "organic" cradle and now spans across all areas of chemistry, with relevant interdisciplinary interactions with biology, physics and informatics. In biology, crystal engineering involves the understanding of the interactions between biological matrices and the crystalline phase.[16,17] In solid state reactivity chemistry, it is perceived as a tool that enables topochemical control of reactivity and stereochemistry. Those working in supramolecular chemistry view crystal engineering as a way of exploiting the non-covalent interactions to assemble molecular components into the desired architectures. All this shows that the subject of crystal engineering is global and is practiced by scientists with different interests but all sharing the idea of making a crystal with a purpose.

1.2 Supramolecular isomerism

The occurrence of different solid state packing arrangements of compounds that yield the same vapour or liquid phase is referred to as polymorphism.[18] This definition suits very well for organic molecular systems. For MOFs, the existence of different crystal structures assembled from the same building blocks is more appropriately termed supramolecular isomerism[14] and is related to structural isomerism at molecular level. Supramolecular isomerism could be a result of the same molecular components generating different supramolecular synthons and could be synonymous with polymorphism. In the presence of guest molecules in the framework, the term isomerism is very controversial as it is mostly used to refer to the framework only.[19-21] Pseudo-polymorphism has been used to refer to supramolecular isomers which have different solvent molecules in their cavities.[22] However the use of the term Pseudo-polymorphism has fallen out of favour. An illustration of the structural diversity that may arise from the same starting molecular components is given in Figure 1.2.

Supramolecular isomerism in MOFs may be grouped based on analogues drawn at molecular level. The following classes of isomerism exist in the field of MOFs:

Structural supramolecular isomerism: Different superstructures exist for the same metal ions and ligands used for synthesis.[23] The networks are completely different even though their chemical formula and chemical components are the same.

Conformational supramolecular isomerism: this arises from the change of conformation of a flexible ligand in the network which generates a different but often related architecture. Conformational polymorphism is closely related to this subject.[24]

Interpenetration supramolecular isomerism: These are isomers which arise as a result of the difference in the degree of interpenetration of the nets.[25] The non-interpenetrated structure and interpenetrated structure exhibit different properties, hence they can be considered as different compounds.

Optical supramolecular isomerism; these are possible as achiral starting materials may form crystals that are chiral [26,27].

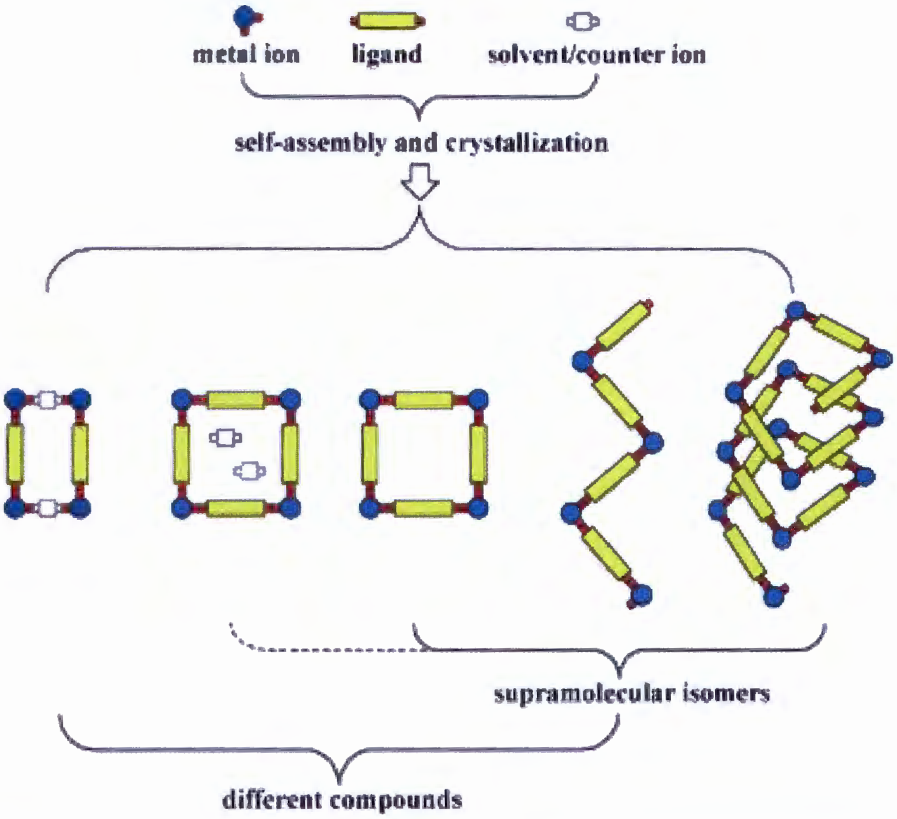

Figure 1.2: A Figure taken from a review paper by Zhang *et al* [19] illustrating different levels of structural diversity in the synthesis of MOFs

1.3 Nomenclature of metal organic frameworks and coordination polymers

Terminology and nomenclature create added value. These are regarded as tools which incorporate new findings into greater weave of science and allow us to move from specific to general.[28] MOFs and coordination polymers[29] constitute an interdisciplinary field with origins in inorganic and coordination chemistry. Due to the diversity in both focus and scientific base of those working within this field, this has led to numerous terminologies for this class of compounds, thus creating unnecessary confusion and additional misunderstanding. There has been much debate on the difference between a metal organic framework and a coordination polymer. In a paper published in Dalton in 2008,[30] Richard Robson wrote:

> *"The MOF terminology is unnecessarily restrictive: why should we set aside as a special category called MOFs, those coordination polymers that happen to make use of organic bridging ligands (or some even more narrowly defined sub-group thereof) and relegate networks formed from perfectly respectable "inorganic" bridging species to some limbo?"*

From Robson's argument it is clear that one can easily draw a conclusion that metal organic frameworks are coordination polymers and that there is no need to give a special category to this group of compounds. Because of the different terminologies which were used to describe this class of compounds, the International Union of Applied Chemistry (IUPAC) task group on Coordination Polymers and MOFs was started in 2009 and was chaired by Lars Öhrström since its inception in 2009. This group has documented, analysed and evaluated the existing practices in a continuous dialogue with researchers in this field. The IUPAC recommendations on terminology were published in 2013 in the Journal of Pure Applied Chemistry.[31]

A *coordination polymer* as defined in 2013 IUPAC recommendations is a coordination compound with repeating coordination entities which extend in 1, 2, or 3 dimensions.[31] It should be noted that these compounds do not necessarily need to be crystalline. A typical example of a coordination polymer is illustrated in Figure 1.3 in which the cobalt (II) ions are bridged by 4,4'-bipyridine ligands.

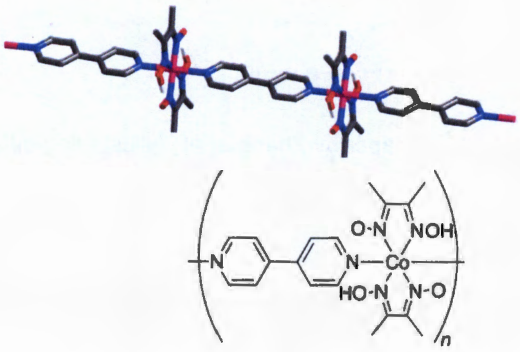

Figure 1.3: A classical example of a 1D coordination polymer. The hydrogen atoms were omitted for clarity. Colours: Co (mauve), N (blue), O (red), C(grey).[32]

The term *coordination network* has also appeared in literature to describe this class of compounds. This is defined as a compound which extends through repeating coordination entities, but cross links between two or more individual chains. The term coordination polymer and coordination network are synonymous. A coordination network is a subset of a coordination polymer. A typical example is given in Figure 1.4 constructed from dihydroxybenoquinone (dhbq) and Y, La, Ce, Gd, Yb or Lu to give a 2D hexagonal grid structure.

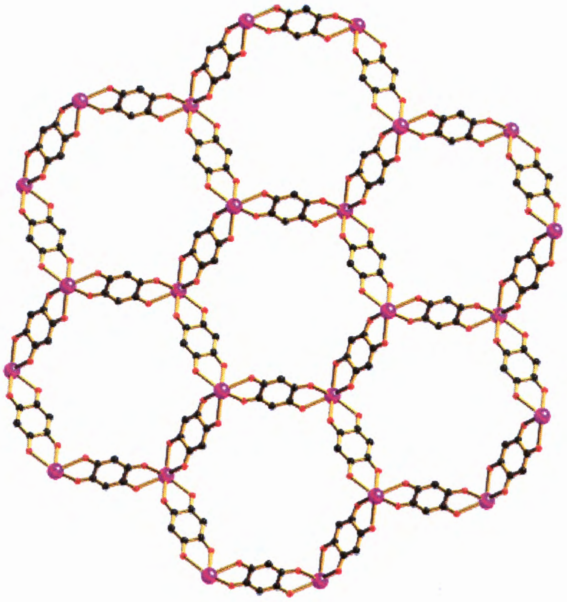

Figure 1.4: A 2D coordination network formulated as $M_2(dhbq)_3{\cdot}24H_2O$ (M = Y, La, Ce, Gd, Yb and Lu). Note that this compound is referred to as a coordination polymer in the paper by Robson et al.[30]

According to the IUPAC recommendations, a coordination network with organic ligands containing potential voids is referred to as a *metal organic framework*, abbreviated MOF.[31] The IUPAC definition is not restrictive contrary to previous definitions which require that a MOF should be made up of secondary building units, and be exclusively applied to ligands with carboxylates[33] as put forward by Yaghi's and O'Keeffe. Compounds which contain both the carboxylate groups and nitrogen atoms binding to the metal ions would have to be excluded in O'Keeffe and Yaghi's definition although Yaghi's earlier definitions of a MOF encompassed compounds based on M-N linkages.[34] Table 1.1 gives the difference between a MOF and a coordination polymer as suggested by Tranchemontagne *et al.* It seems the definition given by the IUPAC is more encompassing and comes at a time when many 3D compounds with both the carboxylate and the pyridyl moieties are being developed.

Table 1.1. The difference between a MOF and a coordination polymer as put forward by Tranchemontagne *et al* in a paper published in Chemistry Society Reviews[33]

Property	***MOF 5***	***$Zn(L)_2(ClO_4)_2$****
Joint (Secondary Building Unit (SBU))	Polyatomic (OZn_4)	Monoatomic
Framework pores	Neutral, Can be empty	Must contain counter Ions
Formal bond valence (Zn-O or Zn-N)	1/2	0
Estimated Link energy (2Zn-O or Zn-N)kJ/mol	363	100-150
Zn-X bond to break to excise SBU	12	4
Estimated energy to excise SBU/kJ/mol	2200	400-600

*L = N,N' -Bis(4-pyridyl) urea.

Figure 1.5 shows a compound which was referred to as a coordination polymer but not a metal organic framework. Based on the IUPAC defination, this compound can be regarded as both a coordination polymer and a metal organic framework.

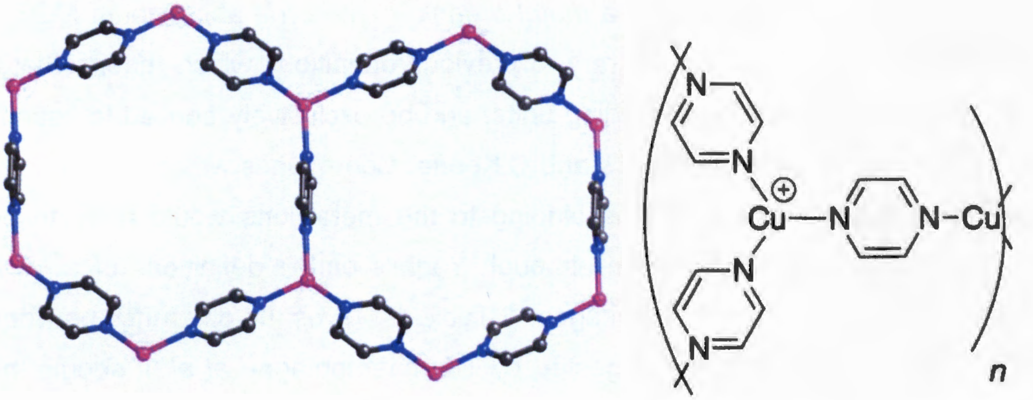

Figure 1.5: A Figure taken from a paper by Öhrström *et al*[31] illustrating a coordination network from Kitagawa's group[35] that can be viewed both as a 2D- coordination polymer and a metal organic framework following IUPAC recommendations.

A structure which was referred to as MOF is depicted in Figure 1.6. This compound meets the definition of a MOF given in table 1.1. Analysis of the definitions given by IUPAC shows that MOFs are coordination networks and that coordination networks are a subset of coordination polymers. In this thesis, the term MOF will be used to describe our compounds.

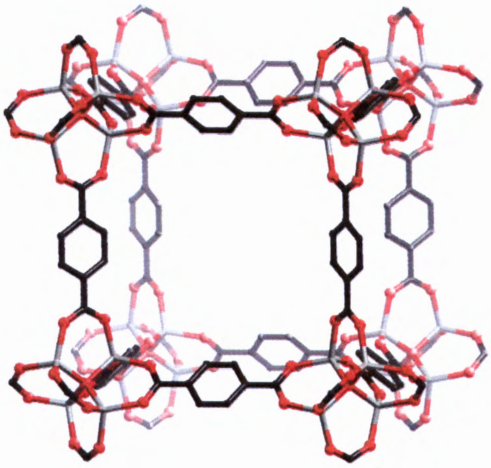

Figure 1.6: MOF -5 [36] made in Yaghi's group assembled from Zn_4O secondary building units bridged by six benzene-1,4-dicarboxylates. Colours: Zn (Light grey), C (grey), O (red).

1.4 Interpenetration

Interpenetration is the most investigated type of entanglement and is very common with metal organic frameworks.[37] Interpenetration is a phenomenon whereby the voids of a network are filled by other independent frameworks and these networks can only be disentangled through bond breaking.[38] The interpenetration of identical networks is referred to as homocatenation, while heterocatenation is the interpenetration of different networks.[14] As for MOFs and coordination polymers, the terms polycatenation and interpenetration are sometimes used interchangeably in the literature. However, the classification of entanglements shows that polycatenation is significantly different from interpenetration.[37] For polycatenation, the motifs could be different or the same types in 0D,1D or 2D nets with closed loops that can be interlocked. On the other hand, for interpenetration the individual nets should be identical and have the same topology. In polycatenation the number of entangled motifs can be finite or infinite; this is not the case with interpenetration because the number of interpenetrated networks is finite. The resultant dimensionality for polycatenation is higher than all the individual motifs, whereas interpenetrated networks have the same dimensionality as the single networks.[39] In this thesis the words interpenetration and polycatenation are used interchangeably, preferring the term interpenetration.

Interpenetration is the most common form of entanglement.[40,41] There are a significant number of reported cases of interpenetration in MOFs. This is because interpenetrated networks minimise the empty space due to nature's abhorrence of vacuum thus enhancing framework stability through formation of repulsive forces that prevent single nets from collapsing on themselves.[37] Interpenetration normally arises when long linkers are used for the construction of porous materials. Thus, the construction of highly porous MOFs from elongated organic linkers poses a great challenge, as interpenetration is highly favoured to increase framework stability and also close the void space.

1.4.1 Interpenetration in 2D networks

Parallel and inclined interpenetration are the two main forms of interpenetration found in 2D MOFs. The majority of these are primarily based on (4,4) or (6,3) topological nets. The topology descriptors will be discussed in chapter 3.

In parallel interpenetration a new 2D layered or a 3D structure is obtained. A typical example of parallel interpenetration is a MOF formulated as $\{[Co_2(pcp)_2(bpp)]\cdot 2CH_3OH]\}_n$ where pcp is 1,3-bis(4-carboxy-phenoxy)propane and bpp is 1,3-bis(4-pyridyl)propane which was prepared under hydrothermal conditions. The network of the compound comprises of 2D sheets with an **sql** (4,4) topology.[42] These sheets interpenetrate in such a way that a loop is catenated with a single loop from each of the 2 neighbouring sheets. The interpenetrating sheets have parallel mean planes which are offset giving rise to 2D to 3D parallel interpenetration. This form of entanglement is achieved by rotation of 90° of each sheet relative to its two adjacent neighbours as shown in Figure 1.7.

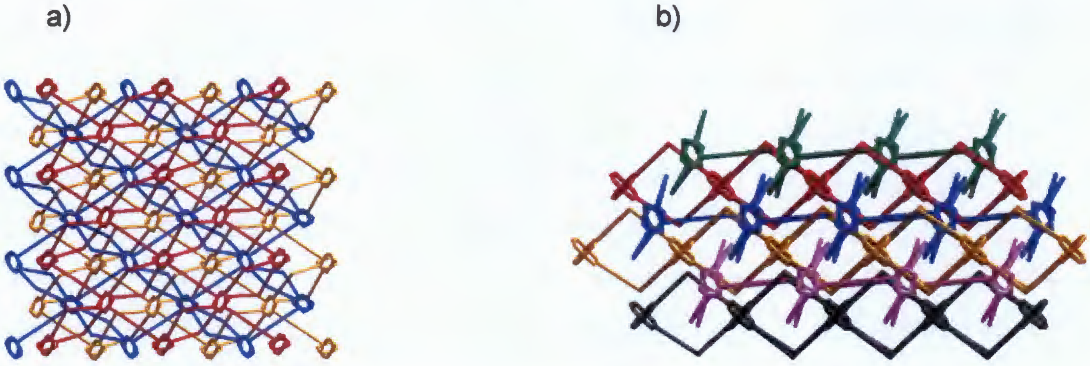

Figure 1.7: A Figure taken from a paper by Liu *et al* [42] illustrating a 3-fold parallel interpenetration from 2D to 3D a) The central network in blue interpenetrates with both the red net (above) and the orange net (below). b). Side view of the interpenetrated network.

In case of inclined interpenetration, dimensionality increases from 2D to 3D in the final structure. Inclined interpenetration leads only to 3D networks. These can be grouped into parallel/parallel, diagonal/diagonal and parallel/diagonal inclined interpenetration. A typical example of inclined interpenetration is found in a coordination compound $[Ni(C_{10}H_6O_4)(C_{10}H_8N_2)(H_2O)_2]_n$ assembled from 4-carboxylatocinnamate and 4,4'-bipyridine which act as bidentate bridging ligands, connecting the Ni^{II} centres in an octahedral coordination geometry into a 2D (4,4) layer.[43] Each 2D layer interpenetrates two identical layers to give an overall 3D structure as illustrated in Figure 1.8.

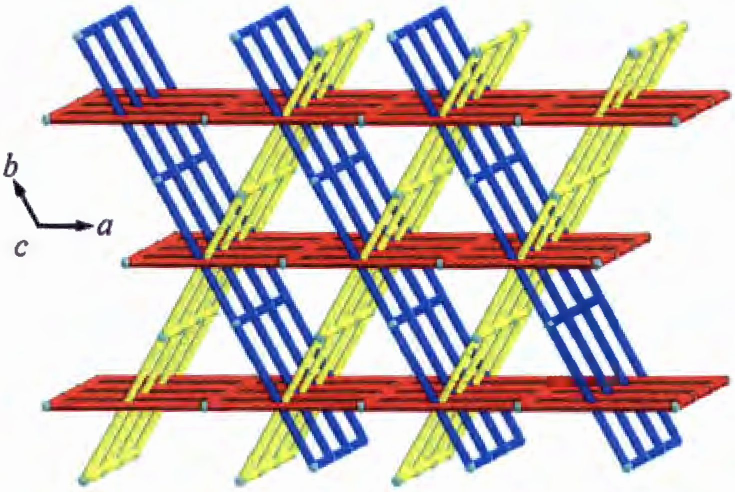

Figure 1.8: A schematic illustration of the 2D to 3D inclined interpenetration of the **sql** nets.[43]

1.4.2 Interpenetration in 3D networks

Interpenetration in 3D networks is very common. Different degrees of interpenetration have been observed, with the highest being a 54-fold **srs** interpenetrated MOF[44] $\{[Ag_3(OH)(H_2O)_2(Tipa)_{2.5}][Mo_2O_7]34.5H_2O\}_n$ (Tipa = tri(4- imidazolylphenyl)amine), which contains 3-connecting ligands and 2-connecting metal ions. MOFs with a **dia** topology have very high propensity for the formation of networks which are highly interpenetrated .[45,46]

1.4.3 Functional effects of interpenetration in 3D networks

Creation of MOFs with high surface areas is a huge challenge owing to interpenetration of individual networks. Engineering of MOFs with large pores for storage of large substrates is also hampered by this phenomenon. It is mainly because of these reasons that interpenetration was labelled as a nuisance for scientists whose aims are to make porous materials with high surface area. On the other hand, for those interested in studying the topology of MOFs, interpenetration is an interesting phenomenon.[44]

Despite all the negative effects of interpenetration, Zhou found that interpenetration can enhance uptake of hydrogen gas.[47,48] This was done by comparing a 2-fold interpenetrated network (PCN-6) and its non-interpenetrated (PCN-6`) MOF counterpart. It was also noted that the surface area of the PCN-6` (2700 m^2/g) structure was lower than that of PCN-6 (3800 m^2/g) indicating a 41% enhancement in Langmuir surface area upon interpenetration. This was attributed to the generation of new absorption sites and some small pores upon interpenetration. The presence of small pores increases the interactions between the guest molecules and the host framework; this explains the enhancement of hydrogen uptake in PCN-6. Computational studies with Grand Canonical Monte Carlo (GCMC) simulations have shown that interpenetrated frameworks, with more metal-corner sites per unit volume exhibit higher hydrogen uptake at low temperatures and low pressure regime.[49] The opposite is true for non-interpenetrated MOFs with larger free volumes for adsorbed molecules, which generally present high absorption capacities at higher temperatures and pressures.

Having observed the positive effects of interpenetration, it can be concluded that this phenomenon can be used for practical advantage if one desires MOFs with small pore sizes which could be of paramount importance to hydrogen and carbon dioxide absorption.[48,50] Furthermore, the interaction of interpenetrated nets can result in dynamic breathing behaviour which could be beneficial to storage and separation of gases.[10,51] This implies that interpenetration and non-interpenetration have their own advantages, and the occurrence of interpenetration should never be viewed negatively.

1.4.4 Interpenetration control

The desire to engineer crystals which are highly porous has resulted in several strategies being used to control the degree of interpenetration. Solvent templating has been used in many studies with great success.[10,52] This is because the MOF crystals will grow around the surface of the template thereby hindering the entanglement of multiple nets. Secondary building units (SBU) have also been used to address this issue.[53] The length of the linker influences the degree of interpenetration, while the size of the SBU determines the free volume. This implies that the MOFs constructed from small SBU units are likely to have small free volumes as a result of linkers occupying the void space.[54] Reaction conditions such as temperature and concentration have also been found to have a great influence on interpenetration of MOFs. Dilute solutions are likely to give non-interpenetrating MOFs with large pores if long linkers are used. This idea was demonstrated by synthesing of IRMOF

(Isoreticular MOF) 10, -12, -14 and -16 in which each pair consisting of one non-interpenetrated and the other 2-fold interpenetrated network were obtained depending on the concentration of the initial mixture.[55] It has also been demonstrated that lower temperatures usually favour non-interpenetrated structures. Recently nonporous to mesoporous MOFs have been prepared by decreasing the reaction temperature.[56]

1.4.5 Interpenetration transformations

Researchers often encounter smaller surface area of a material upon activation than would be expected from single crystal diffraction analysis of the original empty network.[57-59] This phenomenon has been attributable to possible framework collapse or the material irreversibly transforming into an unknown non-porous material upon desolvation. A recent study by Aggarwal *et al* on a known doubly interpenetrated MOF with the formula $Zn_2(ndc)_2(bpy)$ (where ndc is naphthalene dicarboxylate and bpy = 4,4'-bipyridine) found that the compound switches to a three-fold interpenetrated net upon loss of *N,N*-dimethyl formamide (DMF) molecules.[60] This is contrary to previous reports which suggested collapse in framework upon desolvation of the guest.[59] The mechanism for the conversion was supported by computational models. Figure 1.9 shows the proposed mechanism. In the scheme shown stage 1 is the double interpenetrated network which undergoes transformations through stages 2, 3, 4, 5, 6, 7 to give the triply fold network in stage 8. The study led by Barbour's group reveals that the change in the degree of interpenetration should be considered as a plausible possibility when explaining the loss of porosity in MOFs upon desolvation. Such findings may fuel questions regarding the control of interpenetration. Is it necessary to control the degree of interpenetration if a material converts to a closed form upon desolvation as a result of generation of additional nets? Therefore, it is important to understand structure-function relationships at molecular level and manipulate interpenetration for beneficial use.

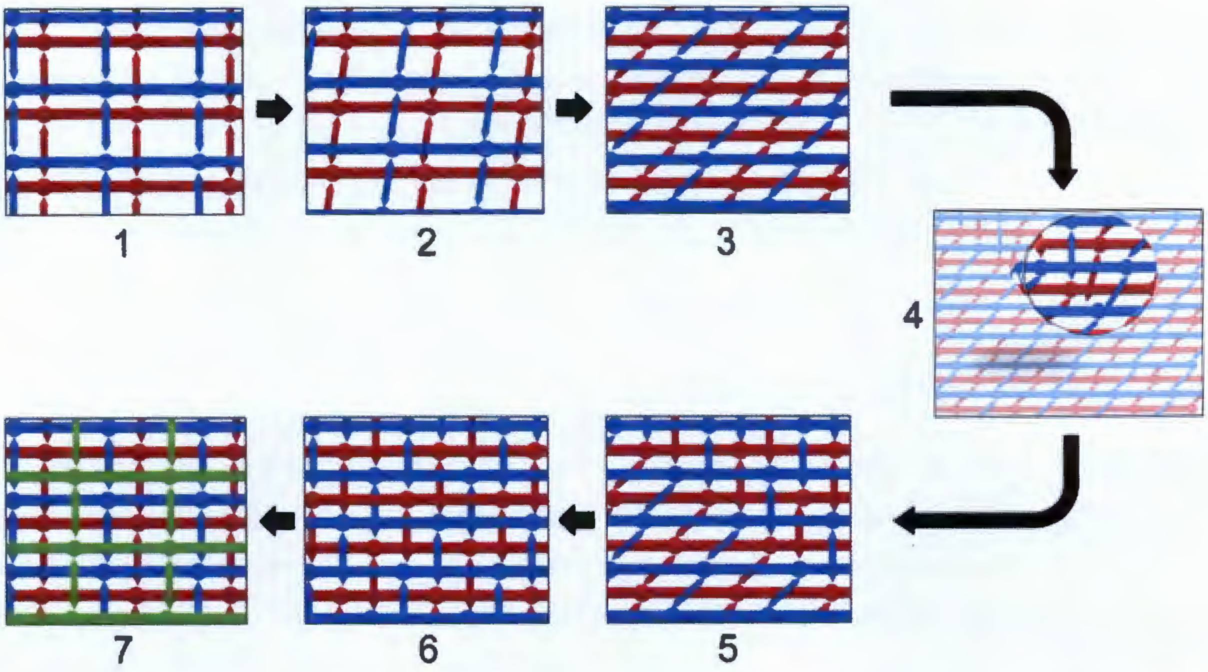

Figure 1.9: Proposed mechanism for the conversion of the doubly interpenetrated to a triply interpenetrated form of $Zn_2(ndc)_2(bpy)$. Independent nets are depicted in red, blue and green. The Zn_2 clusters are presented as circles, the ndc ligands by solid lines, and the bpy ligands by double-ended arrows. The projection given shows the ndc-linked layers forming horizontal planes. These are pillared in the vertical direction by the bpy ligands. Picture taken from a paper by Aggarwal *et al*[60]

1.5 Solvatochromic properties in MOFs

Some of the MOFs synthesised during the course of this project exhibited some solvatochromic behaviour. This section discusses MOFs found in literature which showed solvatochromic response under different solvent systems. Understanding the origins of these effects is important for the design and application of sensors.

One of the most powerful means of transducing a sensing signal is a visible colour change that can be exhibited by a material. Solvatochromism may be defined as the ability of a chemical species to change colour upon inclusion of different solvents as a result of the shift in the absorption spectrum of the material.[61] This arises from the change in the energy gap between the ground state and the excited state, which is triggered by the interactions between the chromospheres and the solvent molecules.[62] MOFs exhibit solvatochromic behaviour which stem from different mechanisms, these include solvent polarity and specific solvent-chromospheres interactions, changes in the coordination geometry of the centre which leads to changes in the visible d-d energy transitions[63, 64,] as well as metal to ligand charge transfer (MLCT) and π to π* transitions.[65] Solvatochromic MOFs are rare owing to the difficulty associated in achieving stable pores and solvatochromism in the materials.[65]

In an effort to prepare a solvatochromic MOF, Zhong Lu *et al*[65] used a solvatochromic ligand 3,6-di(pyridine-4-nyl)-1,2,4,5-tetrazine (dptz) and Cu (I) was chosen as the metal centre since it has a d^{10} configuration and therefore allows one to observe low lying electronic transitions.[66] The reaction of the chosen components gave a nanotubular MOF $\{[(WS_4Cu_4)I_2(dptz)_3]\cdot DMF\}_n$. The nanotubular compound exhibited reversible solvatochromic response upon inclusion of different solvent guests (acetonitrile, water, methanol, DMF, acetone, ethanol and dichloromethane) in its channels which was easily noticed by visual colour change as highlighted in Figure 1.10. The Figure also shows the ultraviolet visible (UV-Vis) spectra which is consistent with the observed colours. The solvent polarity parameters[67] (E_T^N) and band gaps show good positive correlation as depicted on the right of Figure 1.10. The best fits were obtained by grouping the solvents into non hydroxylic solvents and hydroxylic solvents. Plots of the band gaps against the E_T^N values for the hydroxylic solvents gave a correlation coefficient of 0.977 while a value of 0.996 was obtained for non hydroxylic solvents.

The solvatochromic behaviour of the nanotubular MOF was attributed to MLCT. It was also reported that the ligand used for synthesis played a major role in the solvatochromic response of the MOF, which was ascribed to the strong π- acceptor property as well as the labile electronic structure to the solvent polarity.[68]

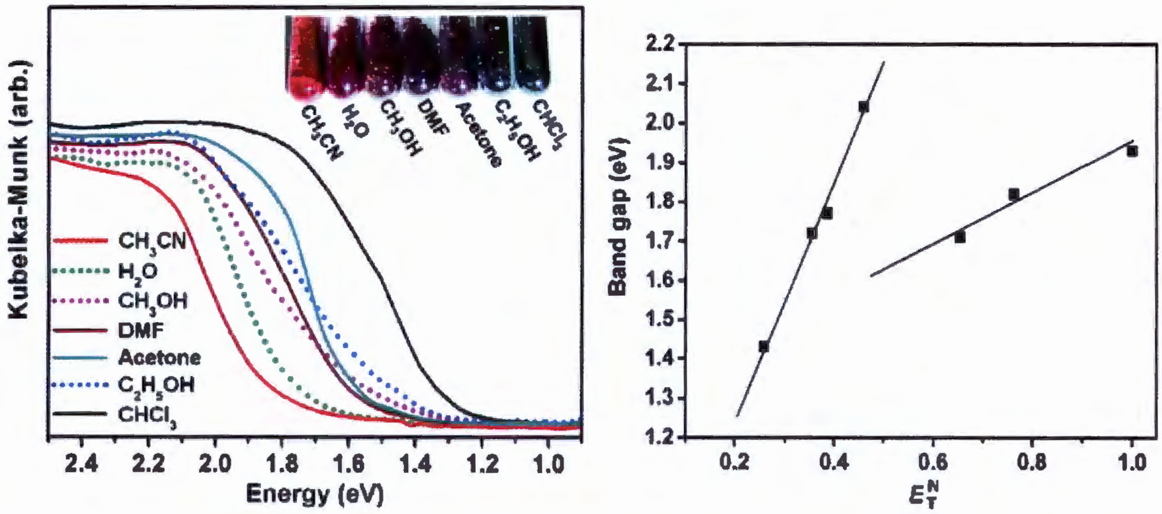

Figure 1.10: Left: The UV-vis spectra and photograph of the inclusion compounds. Right: Band gaps of the inclusion compounds against E_T^N values as reported in a paper by Zhong Lu *et al* [65]

Encouraged by the findings of Zhong Lu *et al* , Sun *et al* [69] evaluated the solvatochromic effects of a mesoporous chiral MOF assembled from a predesigned hexatopic ligand 5, 5’, “-(1,3,5,-triazine-2,4,6-triyl) tris-(azanediyl) triisophthalate (TATAT) and zinc (II) ions.

The solvothermal reaction product obtained was a 3D anionic MOF which has a channel volume of 69.8 % of the unit cell volume. Channels found in the structure run in three crystallographic directions with dimensions of 17 x 23 Å. Figure 1.11 shows the 3D structure of the reported compound.

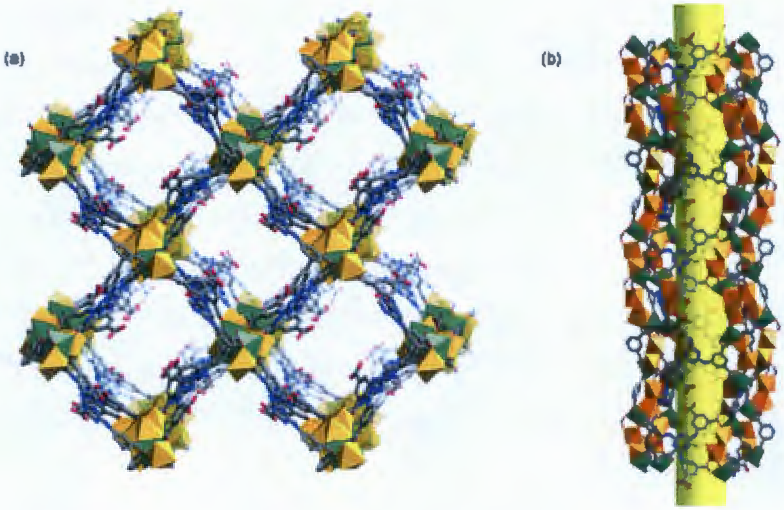

Figure 1.11: A Figure from a paper by Chun-Yi Sun *et al* [69]. a) 3D structure of the chiral framework as viewed along the c-axis. b) 1D mesoporous nanotubes that exists in the chiral network.

Fresh samples of the 3D chiral network were immersed in acetone and ethanol, a visible colour change was observed from colourless to light yellow after thirty minutes and five hours respectively and the intensity of the colour increased over time. Figure 1.12 shows the photographs of the sample in the two different solvents acetone and ethanol.

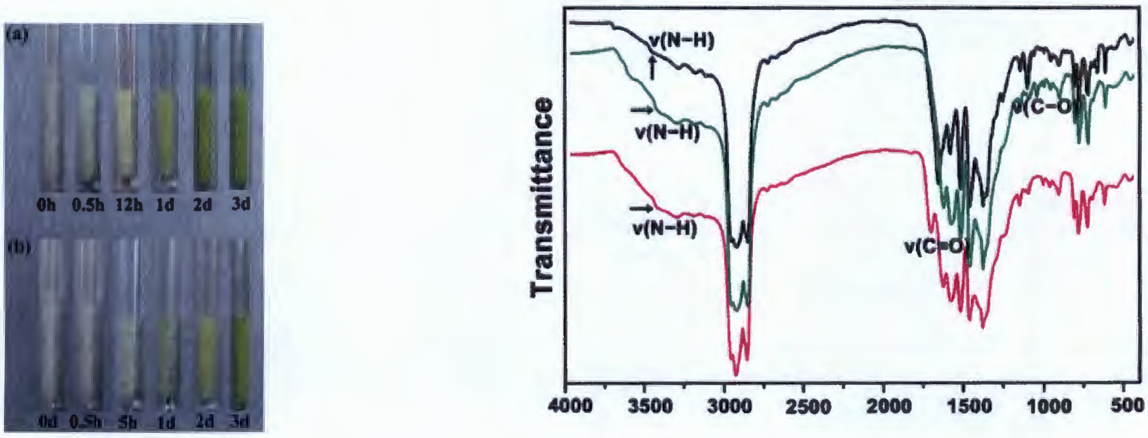

Figure1.12: left (a) acetone loaded compound. b) ethanol loaded compound. right, infrared of solvent loaded compounds, black as made compound, green ethanol loaded, pink acetone loaded compound. The pictures were taken from a paper by Sun *et al.*[69] Note that the pictures have been cropped to extract the required information only.

The solvatochromic effect of this compound was investigated using infrared spectroscopy (IR) and particular attention was paid to the C=O and NH bands. The bands were found to shift to lower wavenumbers due to hydrogen bonding interactions between the solvent molecules with the host framework.[7] The authors concluded that the observed solvatochromic effects are most likely to be due to host-guest interactions although MLCT and π to π* transitions of the ligand may not be ruled out.

A 2-fold interpenetrated MOF with the formula $\{[Cu_2(4\text{-pmpmd})_2(CH_3OH)_4(opd)_2]\cdot 2H_2O\}_n$ [4-pmpmd = N,N′-bis(4-pyridylmethyl)phenyldiimide; opd = *o*-phthalate] was prepared by Li *et al.*[70] Removal of the coordinated solvent molecules and water molecules in the structure by heating resulted in a colour change from blue to purple. Interestingly the blue colour could be regained on immersion of the activated phase in water or methanol solvents. It was noted that the other solvents such as ethanol, chloroform, acetone, benzene, tetrahydrofuran (THF) and dimethyl sulfoxide (DMSO) failed to induce a colour change in the material which could be easily seen by the naked eye.

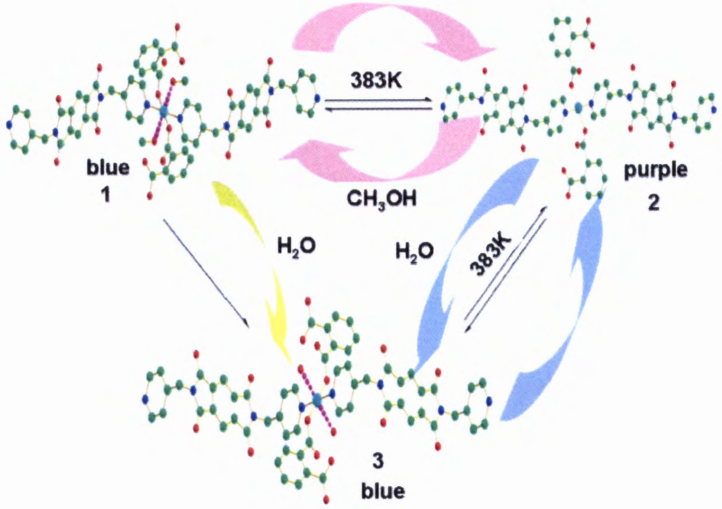

Figure 1.13: A summary of the colour changes observed under different conditions. **1** represents the as-made material, **2** material formed after removal of coordinated solvents, **3** upon exposure of **1** to air or immersing **2** in water. This scheme was extracted from a paper by Li *et al* [70]

When the UV-Vis spectrum of the activated phase (purple in colour) was compared to the UV-Vis of the complex formed after immersing it in water (blue in colour) there was a 140 nm red shift of the absorption band which was induced by binding of the water molecules to the copper metal sites. The authors concluded that the activated phase of the synthesised material represents a simple copper (II)- based optical sensor for small hydroxylic molecules whose response is driven by a change of the metal-based d-d transitions on coordinating of the methanol or water to the metal centre.[71,72]

From the MOFs presented so far which have some solvatochromic properties, it can be concluded that hydrogen bonding interactions between the guest and the host framework, changes in coordination geometry of the metal centre induced by coordinating solvents, as well as MLCT are the main factors responsible for this phenomenon.

1.6 Solid state transformations

Understanding the mechanisms of solid state transformations is of great importance in the field of crystal engineering. Such an understanding makes it possible to design reactive solids and conduct reactions in the solid state easily. The use of single crystal x-ray diffraction to track single crystal to single crystal transformations opens avenues for the systematic study of solid state transformations. This allows for the visualisation of the structure changes during the transformation process. However, following such reactions is not easy as crystallinity is not always retained due to movement of atoms.[73,74]

Structural transformations in MOFs are usually triggered by external stimuli, such as heat, pressure, and guest molecules. Flexible MOFs can undergo several types of dynamic structural rearrangements which may give rise to high selectivity for guest inclusion, step wise sorption, as well as guest–opening absorption behaviours. Dynamic processes which result in pore expansion are driven by either of the following three mechanical factors (i) movement of interpenetrated motifs[75] (ii) reorientation or cleavage of coordination bonds[76,77] and (iii) ability of the bridging ligand to undergo free rotation.[78,79] The latter involves the rotation of a restricted part of the bridging ligand, which may result in subtle changes in the conformation of the ligand, and trigger drastic changes in the characteristics of the pore volume and geometry thus enhancing guest inclusion.

1.6.1 Dynamic motion in 3D networks

A great deal of attention has been recently focussed on studying the dynamic transformation which is brought about by changes in the ligand conformations.[80-82] An example of a MOF with a ligand which change conformation due to rotation was presented by Horike *et al.*[78] The MOF $[Zn_2(1,4\text{-ndc})_2(dabco)]_n$ coded **2** in their paper; where 1,4-ndc=1,4-naphthalenedicarboxylate and dabco=1,4-diazabicyclo[2,2,2]octane) comprises of paddle-wheel Zn^{2+} dimers which are linked by 1,4-ndc ions. This results in regular square-grid-type layers parallel to the *ab* plane, and these layers are pillared by dabco molecules. The authors illustrated the rotation of the 1,4-ndc ligand induced by benzene guest molecules as displayed in Figure 1.14.

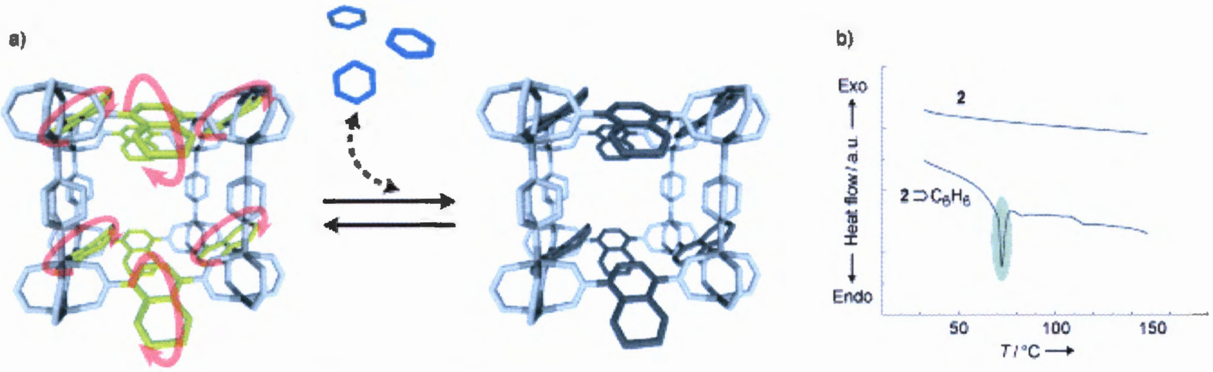

Figure 1.14: Figure by Horike *et al* [78] a) an illustration of the dynamic motion of the ligands induced by benzene molecules. Rotationally free naphthalene rings are yellow, b) the DSC of **2** and the benzene inclusion compounds. The highlighted area corresponds to the static and dynamic states of the benzene inclusion compound.

A study by Zhou *et al* [83]on a MOF formulated as $[Mn(34pba)_2]\cdot DMF$ where 34bpa is the 3-(4-pyridyl) benzoate shows that the ligand undergoes conformational revision upon relocation of the guest DMF molecules at different temperatures. Figure 1.15 depicts these conformational changes and guest relocation which results in crystal lattice deformation

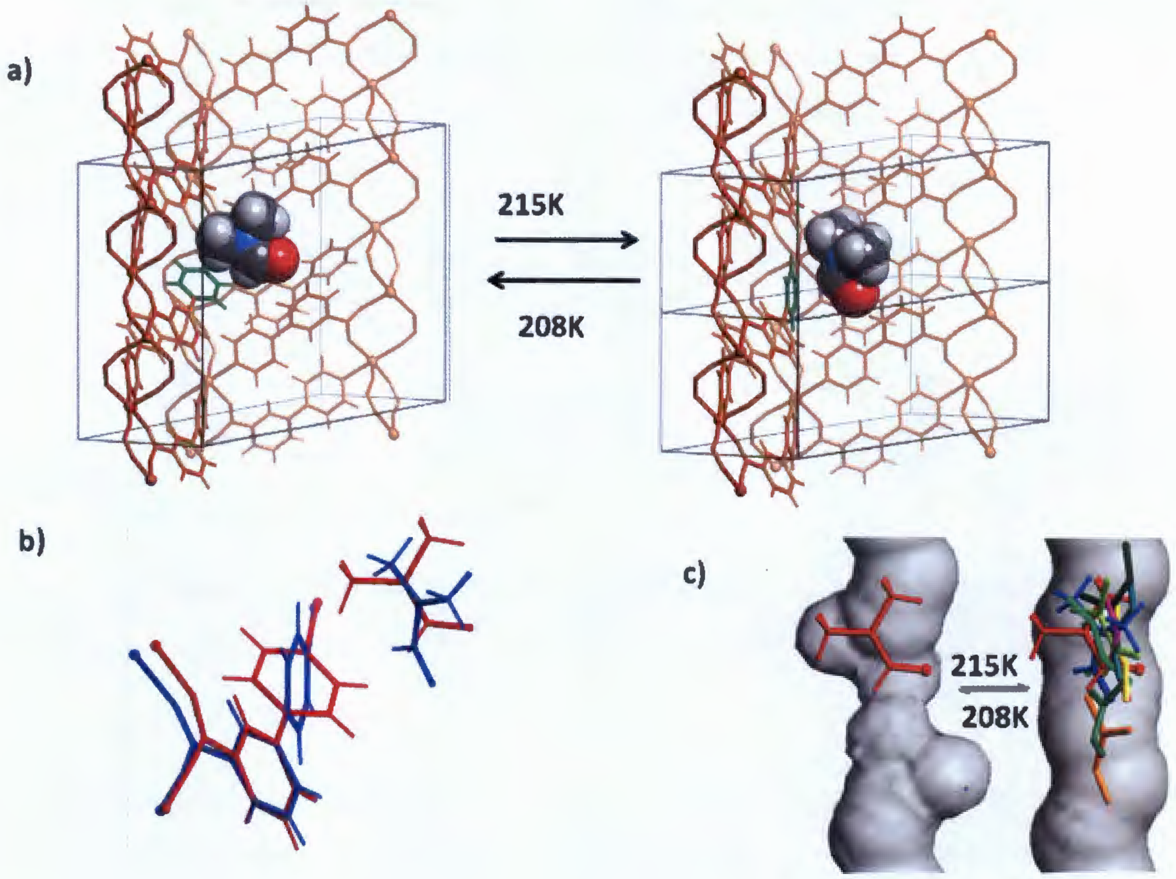

Figure 1.15: Images extracted from a paper by Zhou *et al.*[83] a) Reversible structural transformations between two temperatures (215K and 208K). The pyridyl ring of the ligand which undergoes conformational change is highlighted in green, the orientation of the DMF molecule at the two temperatures is highlighted in space filling model (the other DMF molecules in the asymmetric unit were omitted for clarity). (b) Structural changes of the key local fragments (red: 208 K, blue: 215K). (c) Change of pore geometry around the conformation-revering ligand. Host-guest compatibility was evaluated by overlapping several DMF molecules above the pore surfaces (red 208K, blue: 215K, other colours without hydrogen are possible locations of DMF molecules which were derived from molecular dynamic simulations)

The authors reported that an increase in the solvent –accessible void volume was observed when the temperature was decreased from 215K (18.3%) to 208 K (20.2%) which was attributed to generation of additional cavities as a result of change in the ligand conformation.

1.6.2 Dynamic motion of 2D layers

The advancement of microporous MOFs has gained much consideration owing to their potential applications, for example, gas storage, sensing, separation and catalysis.[6,84] One major drawback of MOFs is that the combination of inorganic parts and organic spacers in the crystalline state brings about robust materials. Interestingly, applications, for example, guest selectivity and separation are better served by guest responsive MOFs which can experience reversible structural conversions between large and small cavities.[85] Several kinds of guest-induced structural flexibility have been reported, including "gate-opening" or "breathing" behaviour. Recently a great number of studies have been devoted towards understanding the breathing phenomenon in MOFs and some studies have highlighted the thermodynamic basis for such behaviour.[86-90] Dynamic breathing movement in MOFs may happen through a displacive phase transition, DPT (without bond breaking) or a reconstructive phase transition RPT (including bond breaking).[91] The latter is uncommon and includes creation of open metal sites which can enhance the sorption of guest molecules. A recent review by Ferey *et al* outlined some of the empirical requirements of breathing in 3D compounds assembled from organic linkers and secondary building units (SBU).[91] In his paper he stated that SBU which permit breathing are those which possess a mirror plane with the carboxylates in symmetrical position with respect to the mirror plane. He further points out that only ditopic carboxylate ligands can allow breathing. This is because between two SBU metal clusters the kneecaps provided by the O...O axes of the different carboxylate ought to be parallel for possible phase rotations. This condition inhibits the use of tri- or tetratopic ligands for expecting swelling which is the case of MOF-77,[92] MIL-103,[93] which contain tritopic 1,3,5-benzene trisbenzoate and MIL-102[94] formed with the naphthalene 1,4,5,8-tetracarboxylate.

MOFs composed of 2D interdigitated layers which are of interest as the ability of the 2D layers to glide past each other allows for the accommodation of large guest molecules with diameters larger than the initial pores of framework.[95,96] Such motion of the 2D layers is normally triggered by the $\pi \cdots \pi$ and $C\text{-}H \cdots \pi$ interactions of the incoming guest molecules with the host framework. This implies that the surface area of the guest molecule plays a major role in modulating the dynamic motion of the framework. It follows that 2D MOFs should be highly selective to guest molecules with a larger surface area compared to the ones with a smaller surface area.

1.7 Kinetic models for solid state reactions

Reactions in the solid state have been discussed comprehensively by Brown *et al.*[97] The rate of a reaction in the solid state can be described by equation 1.1

$$d\alpha/dt = Ae^{-(Ea/RT)}\, f(\alpha) \qquad 1.1$$

Where, A is the frequency factor, E_a is the activation energy, T is the absolute temperature, R is the gas constant, $f(\alpha)$ is the reaction model, and α is the conversion level defined by equation 1.2 for a gravimetric measurement

$$\alpha =(m_o - m_t)/(m - m_\infty) \qquad 1.2$$

Solid state reactions are often studied by thermogravimetry, other analytical methods such as differential scanning calorimetry (DSC),[98] powder X-ray diffraction (PXRD) and nuclear magnetic resonance (NMR) can also be used.

Analysis of reactions can be performed by either fitting models or model free. The former is applied to isothermal reactions while the latter is applied to non-isothermal reactions. The disadvantage of model free is that one cannot determine the model of the reaction and the description of the reaction is not complete without knowing the mechanism.

A model is defined as a theoretical mathematical description of the events that occur during the experiment. In the context of solid state reactions, a model describes a particular reaction type and translates that mathematically into a rate law. Many mathematical models for solid state reactions have been developed based on certain mechanistic assumptions. Reaction models are generally grouped based on the graphical shape of their isothermal curves (α *vs* t) or their mechanistic assumptions. Based on the shape of their kinetic curves, kinetic models can be group into acceleratory, deceleratory or sigmoidal models. For non-isothermal reactions, α-temperature plots are not distinctive in their shapes. Mechanistic assumptions can be classified into nucleation, geometrical contraction, and diffusion or reaction order. These mathematical models are given in Table 1.1

Table 1.1: Classification of kinetic models and their integral form

		Kinetic Model	***f(α)***
	Sigmoidal Curves	B1: Prout-Tompkins	$\ln[\alpha/(1-\alpha)]$
		A2: Avrami-Evrami-Erofeev	$[-\ln(1-\alpha)]^{1/2}$
		A3 :Avrami-Evrami-Erofeev	$[-\ln(1-\alpha)]^{1/3}$
		A4 :Avrami-Evrami-Erofeev	$[-\ln(1-\alpha)]^{1/4}$
	Acceleratory curves	P1: power law	$\alpha^{1/n}$
		E1: exponential law	$\ln\alpha$
Deceleratory α-time curves	Geometrical models	R2: contracting area	$1-(1-\alpha)^{1/2}$
		R3: contacting volume	$1-(1-\alpha)^{1/3}$
	Diffusion models	D1: one-dimensional	α^2
		D2: two-dimensional	$(1-\alpha)\ln(1-\alpha)+\alpha$
		D3: three-dimensional	$[1-(1-\alpha)^{1/3}]^2$
		D4: Ginstling-Brounshtein	$(1-2\alpha/3)-(1-\alpha)^{2/3}$
	Order of reaction	F1: first order	$-\ln(1-\alpha)$
		F2: second order	$1/(1-\alpha)$
		F3 : third order	$[1/(1-\alpha)]^2$

The derivation of the kinetic models in Table 1.1 have been described in detail by Khawam and Flanagan.[99] The physical meaning of some of the kinetic models presented in Table 1.1 will be discussed in Chapter 5.6 and Chapter 6.8 dealing with sorption of guest molecules in porous MOFs.

1.8 Organic linkers

Two pyridyl carboxylate organic linkers were used for the synthesis of MOFs in this project. These are 3-(4-pyridyl)benzoate and 4-(4-pyridyl)benzoate whose corresponding acids are shown in Figure 1.16. The MOFs made from these linkers inherit early aspects of Robson's coordination polymers based on 4,4-bipyridine and of the carboxylate MOFs, such as Yaghi's MOF-5. It is one reason why the terminology in this field of study needs to be inclusive rather than restrictive.[31] The usefulness of these compounds in the design of porous materials is discussed in this section.

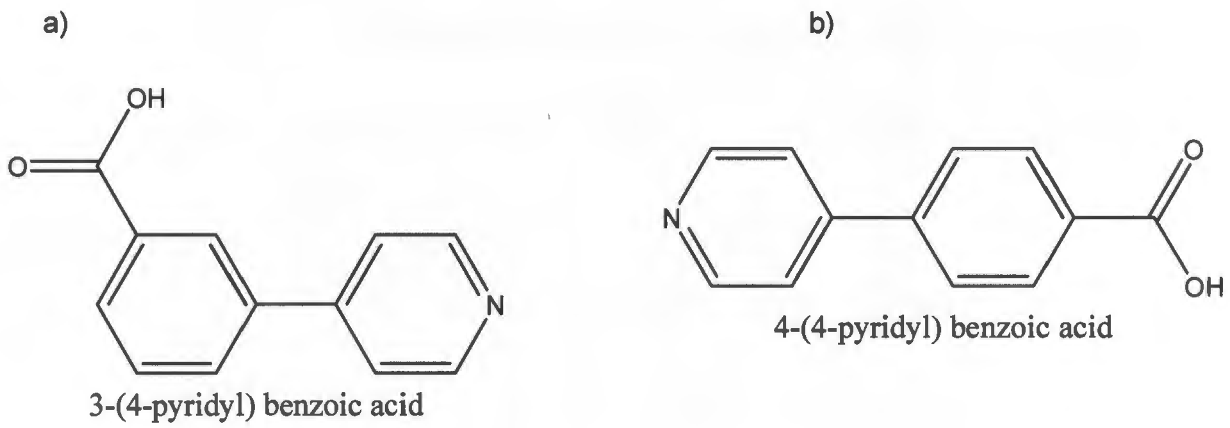

3-(4-pyridyl) benzoic acid

4-(4-pyridyl) benzoic acid

Figure 1.16: a) 3-(4-pyridyl)benzoic acid, b) 4-(4-pyridyl)benzoic acid

1.8.1 4-(4-pyridyl)benzoate

This is an asymmetrical ditopic organic linker comprising of the pyridyl and carboxylate moieties which are both capable of binding to the metal centre to afford extended networks. The different binding modes that can be assumed by the carboxylate moiety make it easy to obtain diverse structures with different physical and chemical properties. Furthermore, carboxylate groups form strong coordination bonds with metal ions which may be suitable to create robust frameworks. In addition to that, aromatic carboxylates are able to aggregate metal ions into M-O-C clusters, thereby generating secondary building units (SBU) in *situ*. SBU also provide some degree of robustness in the structure. The ability of the ligand to change its conformation between the aryl ring and the pyridyl ring may give rise to dynamic structures. The combination of all these factors should result in a MOF which is robust upon guest loss as well as flexible under different conditions

Several crystal structures with different topologies and interesting properties have been prepared using this ligand.[100-105]

1.8.2 3-(4-pyridyl)benzoate

Just like the 4-(4-pyridyl)benzoate, the labile conformations and coordination modes of 3-(4-pyridyl)benzoate play a key role in the construction of various structures which can be achieved by varying the synthetic conditions. Furthermore, different network connectivity and porosities can be realised depending on the shape and the bridging angles of the ligand.[106] The ligand has been used in the synthesis of MOFs with magnetic,[107] luminescence,[108,109] fluorescent[110] and large thermal expansion properties.[106,111] Asymmetrical ligands have gained considerable attention because they are prototypes for supramolecular self-assembly processes including metal-organic helices. [112,113]

1.9 Metal ions

The metal salts used in this project for the assembly of MOFs with pydridyl carboxylate ligands were, cobalt(II) nitrate hexahydrated, nickel(II) nitrate hexahydrated and zinc(II) nitrate hexahydrated. Metal ions play a significant role in the behaviour of the assembled MOFs; these include storage, transport, molecular recognition as well as structural transformations. The versatile coordination chemistry of these metals can result in different structures to be engineered from simple molecular components.

1.9.1 Cobalt and nickel transition metals

Cobalt is a 3d transition metal which exhibits diverse coordination modes and oxidation states. Cobalt(II) complexes are known to undergo relatively facile inter-conversion between octahedral and tetrahedral geometries. This inter-conversion is accompanied by a drastic colour change which makes cobalt a good candidate for synthesis of thermochromic and solvatochromic MOFs. To date, many MOFs based on cobalt metal centres have been synthesised and characterised.[114,115] Cobalt based MOFs exhibiting interesting magnetic properties have been observed.[116-116] A helical cobalt MOF **LAF-1**,[107] [$Co_2(OH)(3,4\text{-}PBC)_3$] (where 3,4-PBC is 3-(4-pyridyl) benzoate) has been reported to show significant overall antiferromagnetic properties.

In another related study a MOF $[Co_3(pybz)_2(pico)_2]_n$ (pybz = 4-(pyridin-4-yl)benzoate, pico = 3-hydroxypicolinate),exhibiting a ferromagnetic long range order was assembled from cobalt(II) and a mixed ligand system.[119] The magnetic property was attributed to the cooperative magnetic effect of the intra-and inter-trimer arrangements in the 2D magnetic system which was brought about by the changes in the bridging modes of the carboxylate moieties. In a fairly recent study, Zeng *et al* [103] constructed a chiral **dia** network $[Co(pybz)_2]$. 2DMF using 4-(4-pyridyl) benzoate and Co(II). The compound exhibited some paramagnetic properties due to the long distance between the Co(II) in the chiral network. Carbon dioxide sorption studies conducted at 195 K showed an absorptive capacity of 133 cm^3/g at low pressure. The activated phase of the compound was also able to absorb 212 cm^3/g of hydrogen at 77 K and 95 cm^3/g of methane at 35 bar and 298 K. The compound showed no uptake of nitrogen.

In cases where nickel is used as metal centres, electronic transitions from $3A_2g$ ground state to $3T_2g$, $3T_1g$ (3F) and $3T_1g$ (3P) excited states are responsible for colour changes observed in nickel complexes. The colour changes observed in nickel complexes coupled with porosity of MOFs also make this metal ion a good candidate to detect inclusion of guest molecules through visible colour change. The incorporation of porosity and unsaturated Ni^{2+} sites afford MOFs with catalytic properties[120,121] and strong hydrogen binding affinity.[122,123] Zhang *et al*[124,125] constructed a series of isoreticular MOFs with an **ncb** topology using nickel and 4-(4-pyridyl)benzoate with different combinations of a dicarboxylate ligands. The compounds showed some interesting gas sorption behaviours.

1.9.2 Zinc

Zinc has been widely used in the synthesis of metal organic frameworks for various useful applications.[126-129] The metal ion can readily form SBUs in *situ* with carboxylate moiety, thus providing some form of rigidity to the overall structure.[130-132] Another important property of zinc is that it exhibits rich coordination chemistry, this allows for the fabrication of various structures with beautiful topologies by careful control of the reaction conditions. One particular example of a MOF assembled from zinc(II) and 4-(4-pyridyl) benzoate is a double walled MOF displayed in Figure 1.17. The compound showed some interesting iodine uptake and cooperative anisotropic electrical conductivity behaviour attributable to I_2- π-electron interactions.[100]

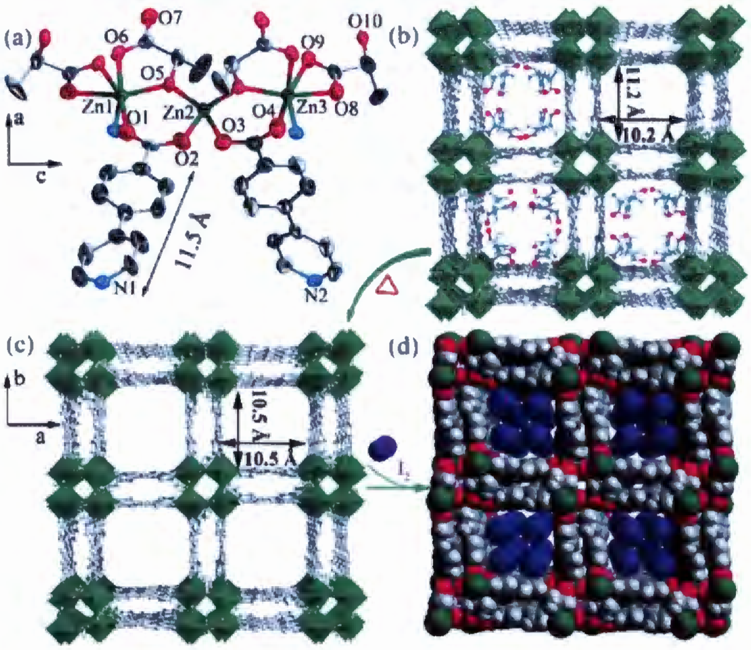

Figure 1.17: A schematic illustration of the double walled MOF by Zeng *et al* [100] (a) coordination environment of the zinc (II) ions, (b) the crystal structure of the MOF with guest molecules in the channels, (c) the empty framework highlighting the sizes of the channels (d) the expected structure of the iodine loaded compound.

1.10 Motivation and objectives of this study

1.10.1 Motivation

There is a growing interest in MOFs constructed from ligands containing mixed donor atoms owing to their particular topologies and some potential applications such as gas storage, molecular recognition and photochemistry. Pyridyl carboxylates, containing N- and O-donors have been widely explored in the design and construction of 1D, 2D and 3D porous coordination polymers. Pyridyl carboxylate ligands have been used as organic ligands for the design and construction of MOFs which have polymeric structural motifs due to the presence of N and O donor atoms. However, very little has been reported yet using the specific ligands discussed in section 1.7.1 and 1.7.2. The use of long ligands in the construction of MOFs usually results in the formation of interpenetrated structures. However, if interpenetration is avoided by the use of suitable spacers and template solvents, MOFs with large channels can be obtained and be used in gas storage and in guest exchange processes.

In this project, pyridyl carboxylate ligands in particular 3-(4-pyridyl)benzoate (34pba) and 4-(4-pyridyl)benzoate (44pba) were used to connect metal ions to give 2D and 3D extended structures. Prior to this study a few compounds based on 34pba and 44pba had been synthesised and were found to exhibit interesting properties.[107,109,110] The connection between the pyridyl ring and the phenyl ring may give rise to some degree of flexibility, and if this component is incorporated into a MOF we reasoned that we might be able to realise dynamic materials. The flexibility of the materials would arise from the ability of the ligands to rotate about their connecting points as well as the different binding modes that can be assumed by the carboxylate moiety under various conditions.

1.10.2 Objectives

The objectives of the project presented in this thesis were:

- Synthesis of MOFs based on 3-(4-pyridyl)benzoate and 4-(4-pyridyl)benzoate ligands using Zn(II), Co(II) and Ni(II) metal ions.
- Structural elucidation by single crystal X-ray diffraction
- Characterisation of the MOFs by thermal techniques, X-ray diffraction and spectroscopic methods.
- Topological analysis of the MOF networks.
- Property evaluation of the prepared materials:
    - Guest exchange studies
    - Vapour sorption studies
    - Adsorption and desorption kinetic studies
    - Thermochromic and solvatochromic studies

1.11 References

1. R. Pepinsky, *Phys.Rev.*, 1955, **100**, 971.

2. (a) G. M. J. Schmidt, *Pure Appl. Chem.*, 1971, **27**, 647. (b) B. M. D. Cohen, G. M. J. Schmidt and F. I. Sonntag. *J. Chem. Soc.*, 1964, 2000.

3. G. R. Desiraju, Crystal Engineering: *The design of Organic Solids, Elsevier*, Amsterdam, 1989.

4. D. Braga, *Chem. Commun.*, 2003, 2751.

5. T. K. Maji and S. Kitagawa, *Pure Appl. Chem.*, 2007, **79**, 2155.

6. M. Dincă and J. R. Long, *Angew. Chem. Int. Ed. Engl.*, 2008, **47**, 6766.

7. P. Horcajada, C. Serre, G. Maurin, N. A Ramsahye, F. Balas, M. Vallet-Regí, M. Sebban, F. Taulelle, and G. Férey, *J. Am. Chem. Soc.*, 2008, **130**, 6774.

8. J. Cui, Y. Li, Z. Guo, and H. Zheng, *Chem. Commun.*, 2013, **49**, 555.

9. S. Yang, X. Lin, W. Lewis, M. Suyetin, E. Bichoutskaia, J. E. Parker, C. C. Tang, D. R. Allan, P. J. Rizkallah, P. Hubberstey, N. R. Champness, K. M. Thomas, A. J. Blake, and M. Schröder, *Nat. Mater.*, 2012, **11**, 710.

10. S. Bureekaew, H. Sato, R. Matsuda, Y. Kubota, R. Hirose, J. Kim, K. Kato, M. Takata, and S. Kitagawa, *Angew. Chem. Int. Ed. Engl.*, 2010, **49**, 7660.

11. O. Shekhah, H. Wang, M. Paradinas, C. Ocal, B. Schüpbach, A. Terfort, D. Zacher, R. A. Fischer, and C. Wöll, *Nat. Mater.*, 2009, **8**, 481.

12. B. F. Abrahams, B. F. Hoskins, and R. Robson,*J.Am.Chem.Soc.,* 1991,**113**, 3606.

13. B. F. Abraham, B. F. Hoskins, J. Liu, and R. Robson, *J.Am.Chem.Soc.,* 1991, **113**, 3045.

14. B. Moulton and M. J. Zaworotko, *Chem.Rev.*, 2001.**101**,1629.

15. K. Davies, S. A. Bourne, L. Öhrström, and C. L. Oliver, *Dalt. Trans.*, 2010, **39**, 2869.

16. L. Addadi and M. Geva, *CrystEngComm*, 2003, **5**, 140.

17. J. Aizenberg, G. Lambert, S. Weiner, and L. Addadi, *J. Am. Chem. Soc.*, 2002, **124**, 32.

18. J. Bernstein, *Polymophism in Molecular Crystals*, Clarendon Press, Oxford, 2002.

19. J.-P. Zhang, X.-C. Huang, and X.-M. Chen, *Chem. Soc. Rev.*, 2009, **38**, 2385.

20. J. Liang, B. Wu, C. Jia, and X.-J. Yang, *CrystEngComm*, 2009, **11**, 975.

21. S. A. Bourne. In Supramolecular Chemistry: From Molecules to Nanomaterials. Editors P.A. Gale, J.W. Steed. John Wiley & Sons Ltd. UK. 2012.

22. M. du Plessis and L. J. Barbour, *Dalton Trans.*, 2012, **41**, 3895.

23. T. Panda, P. Pachfule, and R. Banerjee, *Chem. Commun.*, 2011, **47**, 7674.

24. J. Bernstein, J. A. R. P. Sarma, and A. Gavezzotti, *Chem. Phys. Lett.*, 1990, **174**, 361.

25. J. Lee, C. Chen, H. M. Lee, E. Passaglia, F. Vizza, and W. Oberhauser, *Cryst. Growth Des.,* 2011, **11**, 1230.

26. A. J. Blake, N. R. Champness, P. Hubberstey, W. Li, M. A. Withersby, and M. Schro. *Coord. Chem. Rev.*, 1999, **183**, 117.

27. I. D. Cunningham, S. J. Coles, and M. B. Hursthouse, *Chem. Commun.*, 2000, 61.

28. S. R. Batten, N. R. Champness, X.-M. Chen, J. Garcia-Martinez, S. Kitagawa, L. Öhrström, M. O'Keeffe, M. P. Suh, and J. Reedijk, *CrystEngComm*, 2012, **14**, 3001.

29. K. M. Fromm, *Angew. Chemie Int. Ed.*, 2009, **48**, 4890.

30. R. Robson, *Dalton Trans.*, 2008, 5113.

31. S. R. Batten, N. R. Champness, X. Chen, J. Garcia-martinez, S. Kitagawa, L. Öhrström, M. O. Keeffe, M. P. Suh, and J. Reedijk, *Pure Appl. Chem.*, 2013, **85**, 1715.

32. F.Kubel and J.Strahle.,*Z.Naturforsh., B:Chem.Sci.*, 1982, **37**, 272.

33. D. J. Tranchemontagne, J. L. Mendoza-Cortés, M. O'Keeffe, and O. M. Yaghi, *Chem. Soc. Rev.*, 2009, **38**, 1257.

34. O. M. Yaghi, M. O'Keeffe, N. W. Ockwig, H. K. Chae, M. Eddaoudi, and J. Kim, *Nature*, 2003, **423**, 705.

35. S.Kitagawa, M. Munakata and T. Tanimura, *Inorg. Chem.*,1992, **31**, 1714.

36. H. Li, M. Eddaoudi, M. O'Keeffe and O. M. Yaghi, *Nature.*, 1999, **402**, 276.

37. H. Jiang, T. A. Makal, and H. Zhou, *Coord. Chem. Rev.*, 2013, **257**, 2232.

38. S. R. Batten and R. Robson, *Angew. Chemie Int. Ed.*, 1998, **37**, 1460.

39. H.-L. Jiang, T. A. Makal, and H.-C. Zhou, *Coord. Chem. Rev.*, 2013, **257**, 2232.

40. I. A. Baburin, V. A. Blatov, L. Carlucci, G. Ciani, and D. M. Proserpio, *J. Solid State Chem.*, 2005, **178**, 2452.

41. L. Carlucci, G. Ciani, and D. M. Proserpio, *Coord. Chem. Rev.*, 2003, **246**, 247.

42. J.-Q. Liu, Y.-Y. Wang, P. Liu, Z. Dong, Q.-Z. Shi, and S. R. Batten, *CrystEngComm*, 2009, **11**, 1207.

43. S. Wang, D. Wang, J. Dou, and D. Li, *Acta Crystallogr. Sect. C Cryst. Struct. Commun.*, 2010, **66**, 141.

44. H. Wu, J. Yang, Z.-M. Su, S. R. Batten, and J.-F. Ma, *J. Am. Chem. Soc.*, 2011, **133**, 11406.

45. J.-J. Cheng, Y.-T. Chang, C.-J. Wu, Y.-F. Hsu, C.-H. Lin, D. M. Proserpio, and J.-D. Chen, *CrystEngComm*, 2012, **14**, 537.

46. Y. Hsu, C. Lin, J. Chen, and J. Wang, *Cryst. Growth Des.*, 2008, **8**, 1094.

47. D. Sun, S. Ma, Y. Ke, D. J. Collins, and H.-C. Zhou, *J. Am. Chem. Soc.*, 2006, **128**, 3896.

48. S. Ma, D. Sun, M. Ambrogio, J. a Fillinger, S. Parkin, and H.-C. Zhou, *J. Am. Chem. Soc.*, 2007, **129**, 1858.

49. P. Ryan, L. J. Broadbelt, and R. Q. Snurr, *Chem. Commun.*, 2008, 4132.

50. J. Kim, S.-T. Yang, S. B. Choi, J. Sim, J. Kim, and W.-S. Ahn, *J. Mater. Chem.*, 2011, **21**, 3070.

51. K. L. Mulfort and J. T. Hupp, *J. Am. Chem. Soc.*, 2007, **129**, 9604.

52. D. Tanaka and S. Kitagawa, *Chem. Mater.*, 2008, **20**, 922.

53. N. L. Rosi, M. Eddaoudi, J. Kim, M. O'Keeffe, and O. M. Yaghi, *Angew. Chem. Int. Ed. Engl.*, 2002, **41**, 284.

54. M. Eddaoudi, D. B. Moler, H. Li, B. Chen, T. M. Reineke, M. O'Keeffe, and O. M. Yaghi, *Acc. Chem. Res.*, 2001, **34**, 319.

55. M. Eddaoudi, J. Kim, N. Rosi, D. Vodak, J. Wachter, M. O'Keeffe, and O. M. Yaghi, *Science*, 2002, **295**, 469.

56. J. Zhang, L. Wojtas, R. W. Larsen, M. Eddaoudi, and M. J. Zaworotko, *J. Am. Chem. Soc.*, 2009, **131**, 17040.

57. B. Chen, S. Ma, F. Zapata, E. B. Lobkovsky, and J. Yang, *Inorg. Chem.*, 2006, **45**, 5718.

58. B. Chen, S. Ma, E. J. Hurtado, E. B. Lobkovsky, C. Liang, H. Zhu, and S. Dai, *Inorg. Chem.*, 2007, **46**, 8705.

59. B.-Q. Ma, K. L. Mulfort, and J. T. Hupp, *Inorg. Chem.*, 2005, **44**, 4912.

60. H. Aggarwal, P. M. Bhatt, C. X. Bezuidenhout, and L. J. Barbour, *J. Am. Chem. Soc.*, 2014, **136**, 3776.

61. L. E. Kreno, K. Leong, O. K. Farha, M. Allendorf, R. P. Van Duyne, and J. T. Hupp, *Chem. Rev.*, 2012, **112**, 1105.

62. G. Mehlana, S. A. Bourne, and G. Ramon., *Dalton Trans*, 2012, **41**, 4224

63. K. Uemura, S. Kitagawa, M. Kondo, K. Fukui, R. Kitaura, H.-C. Chang, and T. Mizutani, *Chemistry*, 2002, **8**, 3586.

64. M. Du, X.-G. Wang, Z.-H. Zhang, L.-F. Tang, and X.-J. Zhao, *CrystEngComm*, 2006, **8**, 788.

65. Z.-Z. Lu, R. Zhang, Y.-Z. Li, Z.-J. Guo, and H.-G. Zheng, *J. Am. Chem. Soc.*, 2011, **133**, 4172.

66. H. V. R. Dias, H. V. K. Diyabalanage, M. A Rawashdeh-Omary, M. a Franzman, and M. a Omary, *J. Am. Chem. Soc.*, 2003, **125**, 12072.

67. C. Reichardt, *Chem. Rev.*, 1994, **94**, 2319.

68. T. Kern, U. Monkowius, M. Zabel, and G. Knör, *Eur. J. Inorg. Chem.*, 2010, **2010**, 4148.

69. C.-Y. Sun, X.-L. Wang, C. Qin, J.-L. Jin, Z.-M. Su, P. Huang, and K.-Z. Shao, *Chemistry*, 2013, **19**, 3639.

70. G. Li, L. Li, J. Liu, T. Yang, and C. Su,*Cryst. Growth Des.*, 2013, **13**, 1518.

71. F. Llabresixamena, O. Casanova, R. Galiassotailleur, H. Garcia, and a Corma, *J. Catal.*, 2008, **255**, 220.

72. M. A Rawashdeh-Omary, M. D. Rashdan, S. Dharanipathi, O. Elbjeirami, P. Ramesh, and H. V. R. Dias, *Chem. Commun.*, 2011, **47**, 1160.

73. L. R. MacGillivray, G. S. Papaefstathiou, T. Friscić, T. D. Hamilton, D.-K. Bucar, Q. Chu, D. B. Varshney, and I. G. Georgiev, *Acc. Chem. Res.*, 2008, **41**, 280.

74. J. J. Vittal, *Coord. Chem. Rev.*, 2007, **251**, 1781.

75. G. J. Halder, C. J. Kepert, B. Moubaraki, K. S. Murray, and J. D. Cashion, *Science*, 2002, **298**, 1762.

76. D. Bradshaw, J. E. Warren, and M. J. Rosseinsky, *Science*, 2007, **315**, 977.

77. R. Matsuda, R. Kitaura, S. Kitagawa, Y. Kubota, T. C. Kobayashi, S. Horike, and M. Takata, *J. Am. Chem. Soc.*, 2004, **126**, 14063.

78. S. Horike, R. Matsuda, D. Tanaka, S. Matsubara, M. Mizuno, K. Endo, and S. Kitagawa, *Angew. Chem. Int. Ed. Engl.*, 2006, **45**, 7226.

79. E. Y. Lee, S. Y. Jang, and M. P. Suh, *J. Am. Chem. Soc.*, 2005, **127**, 6374.

80. J. Seo, R. Matsuda, H. Sakamoto, C. Bonneau, and S. Kitagawa, *J. Am. Chem. Soc.*, 2009, **131**, 12792.

81. Y.-S. Wei, K.-J. Chen, P.-Q. Liao, B.-Y. Zhu, R.-B. Lin, H.-L. Zhou, B.-Y. Wang, W. Xue, J.-P. Zhang, and X.-M. Chen, *Chem. Sci.*, 2013, **4**, 1539.

82. P. G. Yot, Q. Ma, J. Haines, Q. Yang, A. Ghoufi, T. Devic, C. Serre, V. Dmitriev, G. Férey, C. Zhong, and G. Maurin, *Chem. Sci.*, 2012, **3**, 1100.

83. H.-L. Zhou, R.-B. Lin, C.-T. He, Y.-B. Zhang, N. Feng, Q. Wang, F. Deng, J.-P. Zhang, and X.-M. Chen, *Nat. Commun.*, 2013, **4**, 2534.

84. B. Liu, Y. Li, L. Hou, G. Yang, Y.-Y. Wang, and Q.-Z. Shi, *J. Mater. Chem. A*, 2013, **1**, 6535.

85. Z. Wang and S. M. Cohen, *J. Am. Chem. Soc.*, 2009, **131**, 16675.

86. I. Imaz, G. Mouchaham, N. Roques, S. Brandès, and J.-P. Sutter, *Inorg. Chem.*, 2013, **52**, 11237.

87. F. Millange, N. Guillou, R. I. Walton, J.-M. Grenèche, I. Margiolaki, and G. Férey, *Chem. Commun.*, 2008, 4732.

88. F. Millange, C. Serre, N. Guillou, G. Férey, and R. I. Walton, *Angew. Chem. Int. Ed. Engl.*, 2008, **47**, 4100.

89. S. Henke, A. Schneemann, A. Wütscher, and R. A Fischer, *J. Am. Chem. Soc.*, 2012, **134**, 9464.

90. C. Mellot-draznieks, A. H. Fuchs, A. Boutin, D. Chimie, D. P. Chimie, and U. V Pierre, 2009, 3442.

91. G. Férey and C. Serre, *Chem. Soc. Rev.*, 2009, **38**, 1380.

92. R. F. Bruinsma, P. G. De Gennes, J. B. Freund, and D. Levine, 2004, **427**, 523.

93. T. Devic, C. Serre, N. Audebrand, J. Marrot, and G. Férey, *J. Am. Chem. Soc.*, 2005, **127**, 12788.

94. S. Surblé, F. Millange, C. Serre, T. Düren, M. Latroche, S. Bourrelly, P. L. Llewellyn, and G. Férey, *J. Am. Chem. Soc.*, 2006, **128**, 14889.

95. S. Sanda, S. Parshamoni, and S. Konar, *Inorg. Chem.*, 2013, **52**, 12866.

96. X.-H. Jin, J.-K. Sun, L.-X. Cai, and J. Zhang, *Chem. Commun.*, 2011, **47**, 2667.

97. M.E . Brown, 'Introduction to Thermal Analysis - Techniques and applications', Chapter 13, Chapman and Hall, London, 1988.

98. S. Vyazovkin and I. Dranca, *J. Phys. Chem. B*, 2005, **109**, 18637.

99. A. Khawam and D. R. Flanagan, *J. Phys. Chem. B*, 2006, **110**, 17315.

100. M.-H. Zeng, Q.-X. Wang, Y.-X. Tan, S. Hu, H.-X. Zhao, L.-S. Long, and M. Kurmoo, *J. Am. Chem. Soc.*, 2010, **132**, 2561.

101. M. C. Das, H. Xu, S. Xiang, Z. Zhang, and H. D. Arman, *Chem. Eur. J.*, 2011, **17**, 7817.

102. O. R. Evans and W. Lin, *Acc. Chem. Res.*, 2002, **35**, 511.

103. M.-H. Zeng, Y.-X. Tan, Y.-P. He, Z. Yin, Q. Chen, and M. Kurmoo, *Inorg. Chem.*, 2013, **52**, 2353.

104. W. Zhi-long, *Chinese J.Struct.Chem*, 2009, **28**, 1453.

105. Z. Yin, Q.-X. Wang, and M.-H. Zeng, *J. Am. Chem. Soc.*, 2012, **134**, 4857.

106. H. Zhou, M. Li, D. Li, J. Zhang, and X. Chen, *Sci. China Chem.*, 2014, **57**, 1.

107. J. Luo, Y. Zhao, H. Xu, T. L. Kinnibrugh, D. Yang, T. V Timofeeva, L. L. Daemen, J. Zhang, W. Bao, J. D. Thompson, and R. P. Currier, *Inorg. Chem.*, 2007, **46**, 9021.

108. F. Guo, *J. Inorg. Organomet. Polym. Mater.*, 2009, **19**, 406.

109. B.-L. Wu, R.-Y. Wang, H.-Y. Zhang, and H.-W. Hou, *Inorganica Chim. Acta*, 2011, **375**, 2.

110. C.-Y. Niu, X.-F. Zheng, Y. He, Z.-Q. Feng, and C.-H. Kou, *CrystEngComm*, 2010, **12**, 2847.

111. H. Zhou, R. Lin, C. He, Y. Zhang, N. Feng, Q. Wang, F. Deng, J. Zhang, and X. Chen, *Nat. Commun.*, 2013, **4**, 1.

112. J. Zhou, G. Bian, J. Dai, Y. Zhang, Q. Zhu, and W. Lu, 2006, **45**, 8486.

113. A.-M. Stadler, N. Kyritsakas, G. Vaughan, and J.-M. Lehn, *Chemistry*, 2007, **13**, 59.

114. Z. R. Herm, J. a Swisher, B. Smit, R. Krishna, and J. R. Long, *J. Am. Chem. Soc.*, 2011, **133**, 5664.

115. Y. Gong, Y.-C. Zhou, T.-F. Liu, J. Lü, D. M. Proserpio, and R. Cao, *Chem. Commun.*, 2011, **47**, 5982.

116. S. Vilminot, G. André, F. Bourée-Vigneron, P. J. Baker, S. J. Blundell, and M. Kurmoo, *J. Am. Chem. Soc.*, 2008, **130**, 13490.

117. M. Murrie, S. J. Teat, H. Stoeckli-Evans, and H. U. Güdel, *Angew. Chem. Int. Ed. Engl.*, 2003, **42**, 4653.

118. N. Snejko, E. Gutie, J. L. Martı, and M. A. Monge, *Chem. Matter.*, 2002, 14, 1879.

119. M.-H. Zeng, Y.-L. Zhou, M.-C. Wu, H.-L. Sun, and M. Du, *Inorg. Chem.*, 2010, **49**, 6436.

120. N. Guillou, Q. Gao, P. M. Forster, S. Park, J. Chang, M. Nogue, S. Park,*G. Fearey,* and A. K. Cheetham, *Angew. Chem. Int. Ed* 2001, 40, 2831.

121. R.-Q. Zou, H. Sakurai, and Q. Xu, *Angew. Chem. Int. Ed. Engl.*, 2006, **45**, 2542.

122. P. M. Forster, J. Eckert, B. D. Heiken, J. B. Parise, J. W. Yoon, S. H. Jhung, J.-S. Chang, and A. K. Cheetham, *J. Am. Chem. Soc.*, 2006, **128**, 16846.

123. C. Lamberti, A. Zecchina, E. Groppo, and S. Bordiga, *Chem. Soc. Rev.*, 2010, **39**, 4951.

124. Y.-B. Zhang, H.-L. Zhou, R.-B. Lin, C. Zhang, J.-B. Lin, J.-P. Zhang, and X.-M. Chen, *Nat. Commun.*, 2012, **3**, 642.

125. Y.-B. Zhang, W.-X. Zhang, F.-Y. Feng, J.-P. Zhang, and X.-M. Chen, *Angew. Chem. Int. Ed. Engl.*, 2009, **48**, 5287.

126. G. Mehlana, G. Ramon, and S. A. Bourne, *Zeitschrift für Krist. - Cryst. Mater.*, 2013, **228**, 318.

127. A. D. Burrows, D. M. Hodgson, M. F. Mahon, and N. Cessford, *CrystEngComm*, 2012, **14**, 188.

128. Z. Behaviors, X. Lin, A. J. Blake, C. Wilson, X. Z. Sun, N. R. Champness, M. W. George, P. Hubberstey, R. Mokaya, and M. Schro, *J. Am. Chem. Soc,* 2006,**128**, 10745.

129. B. A Blight, R. Guillet-Nicolas, F. Kleitz, R.-Y. Wang, and S. Wang, *Inorg. Chem.*, 2013, **52**, 1673.

130. J. Kim, B. Chen, T. M. Reineke, H. Li, M. Eddaoudi, D. B. Moler, M. O'Keeffe, and O. M. Yaghi, *J. Am. Chem. Soc.*, 2001, **123**, 8239.

131. Q.-R. Fang, G.-S. Zhu, M. Xue, Q.-L. Zhang, J.-Y. Sun, X.-D. Guo, S.-L. Qiu, S.-T. Xu, P. Wang, D.-J. Wang, and Y. Wei, *Chemistry*, 2006, **12**, 3754.

132. H. Li, B. Zhao, R. Ding, Y. Jia, H. Hou, and Y. Fan, *Cryst. Growth Des.,* 2012, **12**, 4170.

Chapter 2

Experimental

The general synthetic procedures used to prepare MOFs are outlined in this chapter. Techniques used for structural elucidation and full characterisation of the synthesised materials are also presented.

2.1 Materials for synthesis

Compounds used for synthesis of the MOFs were purchased from CGene Tech, Inc in USA. 4-(4-pyridyl)benzoic acid and 3-(4-pyridyl)benzoic acid having a 97% purity were used as received.

The metal salts cobalt nitrate hexahydrate ($Co(NO_3)_2{\cdot}6H_2O$), zinc nitrate hexahydrate ($(ZnNO_3)_2{\cdot}6H_2O$) nickel nitrate hexahydrate ($Ni(NO_3)_2{\cdot}6H_2O$) all having a purity greater than 98% were purchased from Sigma Aldrich.

The solvents used for synthesis were N,N-dimethylformamide (DMF) 99.8% purity, ethanol (99% purity) and methanol (99% purity) and were also purchased from Sigma Aldrich.

2.2 General synthetic procedures

Single crystals of MOFs were obtained by solvothermal, hydrothermal or solvent evaporation techniques. Detailed synthetic procedures for different metal organic frameworks made will be given in the relevant chapters. The majority of the synthetic methods involved dissolving the ligand in DMF and dissolving the metal salt in methanol or ethanol before mixing the solutions. For the solvothermal reaction, the mixed solutions were placed in an autoclave and sealed tightly and heated in an oven at a particular temperature. Crystals were obtained after slow cooling of the solutions. For the slow evaporation method, the mixed solutions were left to evaporate at room temperature which resulted in the formation of single crystals.

2.3 Thermal analysis

Thermogravimetric analysis (TGA), differential scanning calorimetry (DSC) and hot stage microscopy (HSM) were used to evaluate the physical properties of the compounds. These techniques determine the change in physical properties of the sample as a function of temperature.

2.3.1 Thermogravimetric analysis (TGA)

TGA experiments were performed using a TA Instrument TA-Q500 with the Universal Analysis 2000 software and a 50 $cm^3{\cdot}min^{-1}$ dry nitrogen gas flow rate.

Thermogravimetric analysis was used to model the number of guest molecules in the crystal structure and to determine the thermal stability of the host framework. Before performing TGA, samples were surface dried on a filter paper. Samples in the range of 1-5 mg were placed in open aluminium pans. To get the best resolution different heating rates were used depending on the nature of the sample under analysis. The most commonly used heating rate was 10 K·min^{-1}.

2.3.2 Differential scanning calorimetry (DSC)

This technique measures the difference in the heat flow between the sample and a reference as a function of temperature under controlled heating and atmosphere. This allows for the determination of the enthalpy of various thermal events as well as the melting point of the sample. Crystals were thoroughly surface dried on a filter paper before performing DSC experiments. Samples weighing between 0.5 and 1.5 mg were transferred to a closed vented aluminium pans. Different heating rates which ranged from 1 to 20 K·min^{-1} were used to obtain the best resolution. However the most commonly used heating rate was 10 K·min^{-1}. The upward and downward peaks on the DSC traces correspond to exothermic and endothermic reactions respectively.

DSC runs were performed on a TA instruments DSC-Q200 machine. The instrument was calibrated using standard materials. A nitrogen purge gas flowing at a rate of 50 cm·min^{-1} was used for this machine. The data was analysed using the Universal Analysis 2000 program and plotted using Microsoft Excel.

2.3.4 Hot stage microscopy (HSM)

Using the hot stage microscopy, the physical processes occurring on a crystal under controlled heating were correlated with the thermal events recorded on the TGA and DSC. HSM experiments may also be used to observe visual changes (thermochromic effects) which may not be detected by DSC or TGA. The instrument allows one to observe recrystallisation, polymorphic transitions, solvent desorption and melting points amongst others. The events recorded with the HSM occur at slightly higher temperatures than those of events recorded with DSC and TGA temperatures recorded for the same events. This is attributed to the differences in the crystal size and the conditions under which the HSM, TGA and DSC experiments were performed.

In a typical experiment crystals were placed on a cover slip under silicone oil and viewed under a Nikon SMZ-10 stereoscopic microscope fitted with a Linkam THMS600 hot stage and a Linkam TP92 temperature control unit. A real-time Sony Digital Hyper HAD colour video was used to capture the images at different temperatures. Images were viewed with the Soft Imaging System program analysis.[1] A heating rate of 10 K·min^{-1} was used to study the thermal behaviour of the crystals over a temperature range of 25 °C to 400 °C.

2.4 Elemental analysis

Elemental analysis experiments were performed on a Fisons EA1108 CHNS-O Elemental Analyser to determine the percentage of carbon, hydrogen and nitrogen present in a sample. The results were then compared to the percentages calculated from compound compositions determined from single crystal X-ray diffraction.

2.5 Fourier transform infrared analysis (FT-IR)

IR studies were carried out on a Perkin-Elmer Spectrum 100FT-IR using KBr pellets or a Bruker Alpha spectrometer equipped with an ATR platinum Diamond reflectance for solid samples. Samples were scanned over a range of 4000 cm^{-1} to 450 cm^{-1}. These instruments were used to study the changes in the coordination mode of the carboxylate moiety to the metal centre and change in the absorption characteristic bands in the ligands and guests.

2.6 Solid state (Diffuse reflectance) electronic spectra

Diffuse reflectance electronic spectra were measured on polycrystalline samples using an Analtikjena Specord 210-plus UV-Vis spectrophotometer over a range of 300-800 nm, at a scanning rate of 5 nm s^{-1}.

2.7 X-Ray Diffraction

2.7.1 Single crystal X-ray diffraction

Good quality single crystals were selected from the mother liquor to perform single crystal X-ray diffraction. To prevent loss of solvent molecules or decomposition crystals were immediately covered in paratone oil. A suitable single crystal was selected under a microscope and attached on a nylon loop connected to a rigid mounting. Where the single crystals were large, they were cut to obtain an appropriate size. This was followed by mounting the nylon loop on the goniometer head under a cold stream of nitrogen gas. Single crystal data collections were performed on a Bruker KAPPA APEX II Duo diffractometer using MoKα ($\lambda = 0.71069$ Å). X-rays were generated by a Bruker K780 generator powered at 50 kV and 30 mA.

Data collections were carried out at low temperature (173(2)K) using a Cryostream cooler (Oxford Cryostems, UK) at a flow rate of 20 $cm^3 \cdot min^{-1}$. Unit cell refinement and data reduction were carried out using the program SAINT.[2] The program SADABS[3] was used to correct for Lorentz-polarisation and absorption effects on all intensity data.

For each structure, the space group was determined from systematic absences in the X-ray intensity data. The XPREP[4] program was used to confirm the space group. This program prepares input files which are then used for structure solution by direct methods using the SHELXS[5] programme. All non-hydrogen atoms were located using SHELXS-97 and refined by full matrix least square on F^2 with anisotropic thermal parameters using SHELXL[5] within X-SEED[6] interface. The non-hydrogen atoms were refined anisotropically. In cases of severe disorder of guest molecules some non-hydrogen atoms were refined with isotropic temperature factors and specific details will be given in the data chapters. Hydrogen atoms were placed with geometric constraints and were refined with isotropic temperature factors. Ideal bond lengths (± 0.005 Å) and angles were achieved by applying the DFIX restraints in situations of disorder.

2.7.2 Powder X-ray diffraction (PXRD)

The experiments were performed using two diffractometers, the D8 Advance diffractometer or the Huber Imaging Plate Guinier Camera 670.

Some powder diffraction measurements were performed on a Huber Imaging Plate Guinier Camera 670 with a Ni-filtered CuKα radiation ($\lambda = 1.5406$ Å). The X-rays were generated by a Philips X-ray generator at 20 mA and 40 kV. The generator is fitted with a Philips fine – focus tube PW2273/20 and a Huber Guinier Monochromator Series 611/15 Huber D-83253 imaging plate. Samples were applied to a MYLAR polyester film with a thin layer of paratone oil and suspended on flat sample holder. For variable temperature studies, a Huber high–temperature controller HTC 9634 was used, with samples placed in a capillary rotation device. Samples were scanned over the 2θ range of 4°- 100° with a step size of 0.005°.

The data obtained from PXRD studies was plotted using Excel and the appropriate 2θ was plotted.

Some powder diffraction measurements were performed on a Bruker D8 Advance diffractometer equipped with a Lynxeye detector using CuKα-radiation (λ = 1.5406 Å) at 298 K (25 °C). Samples were crushed into a fine powder and placed on a zero background sample holder and scanned over the 2θ range of 4° to 40° with a step size of 0.01°. X-rays were generated by a current flow of 40 mA and an accelerating voltage of 30 kV. A receiving slit of 0.6 mm and primary and secondary slits of 2.5 mm were used. Variable temperature PXRD studies were conducted within a temperature range of 30 – 320 °C, the X-rays were generated by a voltage of 40 kV and a current flow of 40 mA. Samples were scanned within a 2θ range of 4 - 40° with a step size of 0.02° to give a total of 1758 steps. The total time of exposure of the sample to radiation at a given temperature was 7 minutes 52 seconds. A 0.5 $K{\cdot}min^{-1}$ heating rate was used to increase the temperature. The generated powder data were saved as text files and the PXRD traces plotted using Excel.

To perform Pawley fitting[7] in TOPAS[8], the crystallographic data from single crystal data of the compound under study was inserted in the phase details section and allowed to refine. The PV-TCHZ pseudo-Voigt function included in the peak picking routine in TOPAS was used for profile fitting and was allowed to refine. The unit cell parameters were validated by profile matching using the hkl-phase refinement in TOPAS over a two theta range of 4-40°. The 5th order Chebychev function was used to model the background. To account for sample displacement caused by the zero background sample holder a parameter was included and allowed to refine.

To perform quantitative Rietveld refinement, two crystallographic information files for compounds **3** and **4** (presented in this thesis) were loaded into the TOPAS program. The 4th order Chebychev function was used to model the background. The 1/X Bkg function was also used to allow use of the Chebychev polynomial function with fewer constraints. This function also accounts for increasing background due to air scattering. The Lorentz polarisation factor was set to 26.4° to account for polarisation effects coming from the secondary graphite monochromator. Preferred orientation was modelled using the spherical harmonics of 4th order for the two compounds. Profile fitting was done using the The PV-TCHZ pseudo-Voigt function. All the lattice parameters were set to refine.

Calculated Powder X-ray diffraction patterns were generated by the LAZY PULVERIX program from single crystal X-ray data. The program calculates PXRD patterns using the same X-ray source (λ = 1.5406 Å) as that used experimentally. These patterns are used to determine the phase purity of the bulk material by comparing them to the experimental PXRD patterns. Experimental PXRD patterns were also used to check that the desired product has been made.

2.8 Solvent vapour sorption studies

Compounds were activated at elevated temperatures (see relevant Chapters for details) under vacuum. When activated the samples do not take up water rapidly from the air. Samples were then placed in small vials which were not capped. The small vials containing the activated samples were then placed in large vials containing the respective dry solvents. The large vials were capped and sealed tightly and left at room temperature for 24 hours. An example of this setup is displayed in Figure 2.1. The resultant inclusion compounds were analysed by thermal techniques, PXRD, and spectroscopic techniques. Detailed information will be given in the data chapters.

Figure 2.1: A typical solvent vapour sorption setup experiment. The large outer vial contains the dry solvent and is capped and sealed tightly. The inner small vial contains the activated material under study. From left to right: the solvents are n-propanol, methanol and ethanol:

2.9 Solvent sorption kinetics

The rate of uptake of solvents (the solvents used for the compounds studied are discussed in the relevant chapters) by the activated phases of MOFs was determined using an in-house built equipment within a temperature range of 20 – 33 °C. This sorption balance is shown in Figure 2.2. A balance, placed in an oven in which the temperature is regulated by a thermostat, was connected to a computer which tracks the progress of the sorption kinetics.

The sample holder is contained within the brass cylinder which has eight solvent chambers that are evenly distributed around the sample. The brass cylinder fits over the sample and can be sealed. The solvent is placed in the solvent chambers before sealing the cylinder and allowing the vapour pressure to equilibrate for at least 30 minutes. The scale is zeroed and the sample exposed to the vapour by removing the seal between the sample and the solvent vapour and the monitoring computer program (PB303S31) started.[9] The increase in mass with respect to time is recorded. When the reaction reaches completion, the program alphatime.exe[9] is used to analyse the extent of reaction α which is defined as:

$$\alpha = (m_o - m_t)/(m - m_\infty) \qquad (2.1)$$

where, m_o is the initial weight, m_t is the weight at t, and m_∞ is the final weight. From this, the rate constant and the rate law that governs the sorption process can be determined

Figure 2.2: Right: In-house built balance for monitoring the uptake of solvent vapours. The thermostat regulates the temperature by switching on/off the light bulbs and Left: the solvent chambers where the solvent under study is placed. A thermometer is also inserted which monitors the temperature.

2.10 Non-isothermal desorption kinetics

To ensure consistent and reproducible results, the sample size used for each non-isothermal run was kept small and relatively constant (1.5-2.5 mg) for each experiment. The material was evenly spread at the bottom of the pan before being placed in the TG instrument. The temperature range and heating rates used for the desorption of the guest molecules are given in the relevant sections dealing with desorption kinetics. The activation energy for guest desorption was determined using the Ozawa, Flynn and Wall method.[10] The method relies on the use of several heating rates and temperatures being recorded at specific conversion levels for each heating rate. The conversion levels are defined in terms of percentages based on the extent of reaction (α). Using equation 2.2, the activation energy at each conversion level can be determined, where β_α is the heating rate, A_α is the frequency factor, $E_{a\alpha}$ is the activation energy, T_α is the temperature at each conversion level, and g(α) refers to the kinetic model. The thermogravimetric traces were converted to extent of reaction (α) versus temperature curves. Plots of log β_α versus $1/T_\alpha$ were then used to calculate the activation energy at each conversion level.

$$\log \beta\alpha = \log(A_\alpha E_{a\alpha} / g(\alpha)R) - 2.315 - 0.457(E_{a\alpha}/RT_\alpha) \qquad (2.2)$$

2.11 References

1. Soft Imaging GmbH: Digital Solutions for Imaging and Microscopy, Version 3.2 for Windows, © 1987-2000.
2. *SAINT, version 7.60a*, Bruker AXS Inc, Madison, WI, USA, 2006.
3. G. M. Sheldrick, *SADABS*, *version 2.05*, 2007.
4. XPREP, Data Preparation and Reciprocal Space Exploration, Version 5.1© Bruker Analytical X-ray Systems, 1997.
5. (a) G. M. Sheldrick, SHELXS-97, Program for Crystal Structure Solution, University of Göttingen, Germany, 1997, (b) G. M. Sheldrick, SHELXL-97, Program for Crystal Structure Solution, University of Göttingen, Germany, 1997
6. L. J. Barbour, *J. Supramol. Chem.*, 2001,**1**, 189.
7. G. S. Pawley, *J. Appl. Crystallogr.*, 1981, **14**, 357.
8. A. A. Coelho, *TOPAS-Academic, version 4.1 (Computer software)*, Coelho Software, Brisbane, 2007.
9. L.J Barbour, *Private Communication.*
10. T. Ozawa, *Bull. Chem. Soc. Jpn.* 1965, **38**, 1881.

Chapter 3

Topological analysis of network structures

In this chapter, the importance of reducing complicated structures using the node and spacer approach is given. The choice of node placement which ultimately results in the underlying topology is discussed. The nomenclature and symbols used to describe the topology of crystal structures and the computer software used for topological analysis are presented. Finally the importance of topology in reticular synthesis of MOFs is briefly discussed.

3.1 Network topology

Topological analysis allows one to understand the structure of the products obtained from a given reaction, compare these materials with what other scientists have made, efficiently communicate results to colleagues, and more importantly make new materials by design.[1]

Topology deals with properties that are invariant for an object when subjected to bending, compression or stretching. Thus two nets are topologically the same if they can be transformed into each other without breaking the network bonds.

3.2 Node or vertex assignment

Topological studies allow one to define crystal structures using vertices (or nodes – the terms are interchangeable) that have specific geometry and are linked to other nodes via linkers[2]. The knowledge of topologies can facilitate the synthesis of targeted network architectures and allow the judicious selection of simple node and spacer.[3] The simplest topologies are uninodal comprising of one kind of node and kind of edge (or spacer/linker/ligand). In determining the topology of a given network, one has to decide where to place the node(s). For MOFs, nodes can be placed on metal atoms or at the centre of a metal cluster. For organic ligands, nodes can be placed at the centre of all branching points of the molecular fragment. In placing the nodes, it is very important to avoid over-simplification by skipping potential node points as this will result in loss of structural information.

To generate networks that are useful in interpreting, understanding and comparing structures, Öhrström suggested the following basic ideas:[1]

- The links between nodes should follow molecules and not go through solvent filled voids in the structure
- Nodes should be simplified to avoid complicated multinodal nets

Figure 3.1 depicts the topology obtained for a structure when nodes are placed at different points. In the picture in Figure 3.1.a the nodes are placed at the centre of the metal cluster (dark red) and at the centre of each phenyl ring (green). Connecting neighbouring nodes will give detailed structural information (in other words the information of the structure is stored in the underlying topology of the net) as the green node is 3-connected. Figure 3.1.b shows the nodes being placed at the centre of the metal clusters (dark red) and between the phenyl rings (green). Node assignment between the phenyl rings is an oversimplification and results in loss of structural information as the green node becomes 4-connected and does not have any resemblance to the original structure.

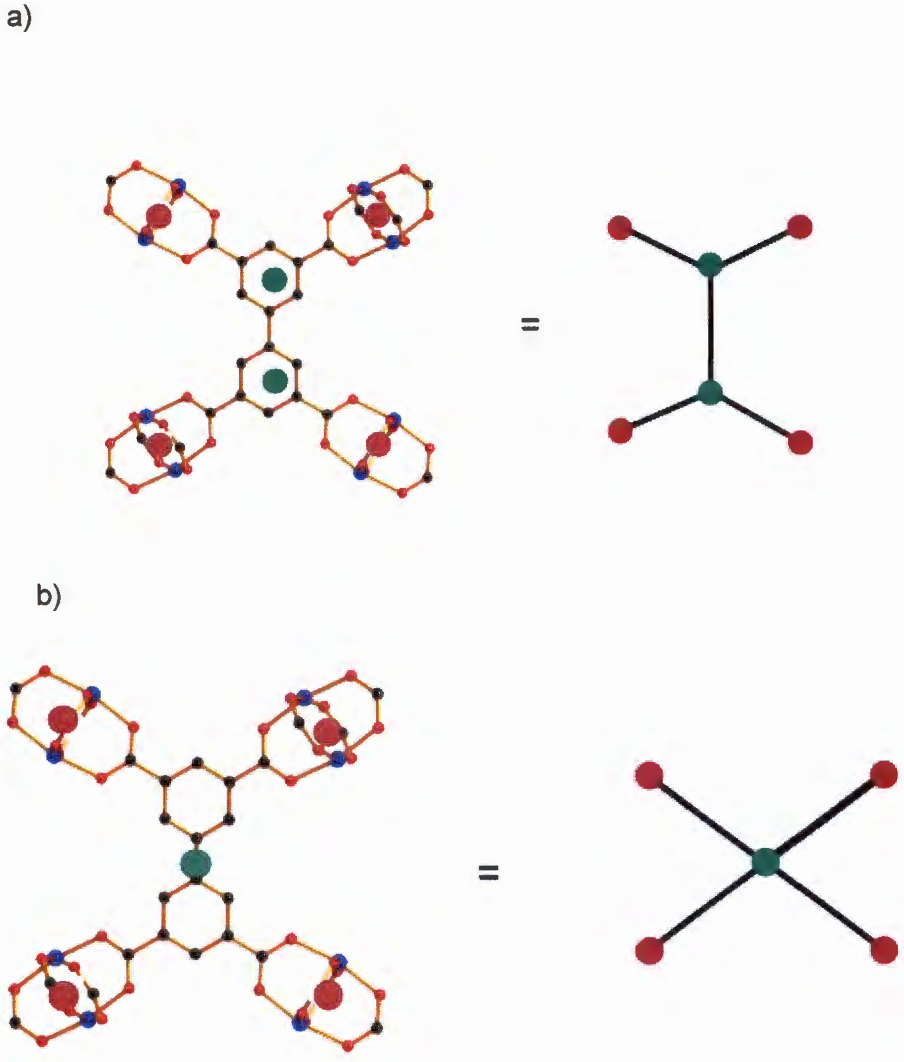

Figure 3.1: a) Node assignment which results in storage of structural information in the underlying net. b) node assignment which results in loss of structural information

Figure 3.2 gives detailed information on the underlying nets that would be produced should the node assignment in Figure 3.1 be followed. With MOF-505 assembled from a tetratopic linker linked by Cu_2 paddle wheels,[4] placing a node at the centre of each phenyl ring and at the centre of the paddle wheel generates a binodal 3,4 –connected net (Figure 3.2.b). If one considers merging the two phenyl rings together, and make it a single node as well as placing another node at the centre of the paddle wheel, then a binodal 4,4- connected net is formed (Figure 3.2.c). This latter net does not resemble the original structure. Such simplification is not useful for other applications where the knowledge of topology is applied. This is especially the case in reticular synthesis (section 3.5) as suggested by O'Keeffe and Yaghi.[5]

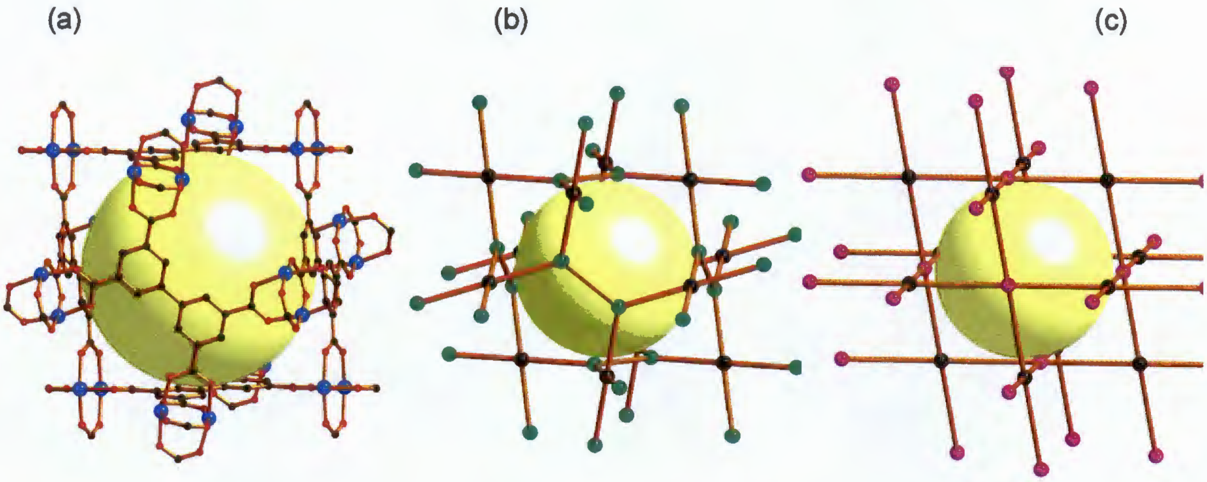

Structure 3,4-connected net 4,4-connected net

Figure 3.2: a) Structure of MOF-505, b) 3-4-connected binodal net, c) 4,4-connected binodal net.[4]

If one looks at the 3,4 connected net, it may be easy to tell what sort of building blocks can be used to assemble a structure similar to MOF-505, but a totally different structure will be obtained if one looks at the 4-4-connected net.

3.3 Net symbols and nomenclature

Wells[6] developed the notation (n, p) to describe the arrangement of atoms or molecules in two and three dimensions. This was based on the number of topologically unique nodes in a network and the connectivity of the shortest ring. In this notation "n" is the size of the smallest ring and "p" denotes the number of links at each node to the neighbouring nodes. The nets based on this notation are called uniform nets. The graphite structure given in Figure 3.3 has a (6,3) net. The number 6 represents the size of the smallest ring in the net and 3 corresponds to the connectivity at each node.

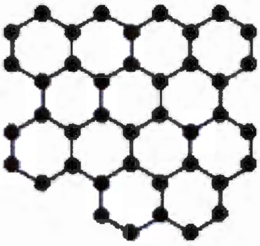

Figure 3.3: Network connectivity of the graphite structure, using Wells' notation the structure has a (6,3) net.

One major limitation of this notation is that there exist nets that have the same "n" and "p" values. For more complex nets, the Wells POINT SYMBOL is used to describe them. Nodes are connected together by edges. A ring is defined as the shortest circuit that takes one back to the starting node. The point symbol is given in the form of $A^{a}.B.^{b}.C^{C}$...the capital letters *A, B, C,....* represent the sizes of the rings emanating from a node, where A < B < C....etc. The numbers of circuits at that node are denoted by the superscripts *a, b, c....* The net given in Figure 3.4 is a (4,4) net based on the (n,p) notation. For any given node, A, B, C and D there are four links. The fundamental rings which are defined by the link pairs AB, BC, CD and AD comprise of four nodes each. However, the shortest path that connects the AC or BD link pairs has six nodes. Note that this is not the fundamental ring and is referred to as a circuit. Thus, the point symbol for the square grid net would be $4^4.6^2$.

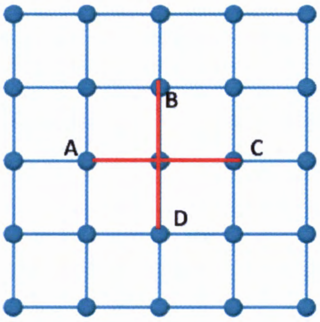

Figure 3.4: Square grid net showing the link pairs AB, BC, AC and AD.

The VERTEX SYMBOL is a set of numbers which lists how many of the shortest rings join each pair of links emerging from a node. It is presented in the form $A_a.B_b.C_C$ ...... A, B, C.... indicates the sizes of the smallest ring at an angle and a, b, c.... are the number of the rings. The '*' indicates that there is no ring contained in an angle. The vertex symbol is usually enough to distinguish between two nets, however in situations where nets have the same vertex symbols, these are distinguished by the topological density value (TD_{10}). The TD_{10}

value is determined from the sum of the first ten shells of topological neighbouring nodes with a weighted average given where more than one type of nodes is present including the original node.

There is a misconception in literature where the Schläfli symbol is used to describe the topology of nets. Blatov *et al* discourage the use of this notation as it refers to a symbol of tiling rather than topology.[7] It is unfortunate that the point symbol has also been called the Schläfli symbol.[8] Yaghi and O'Keeffe have written many papers which are dedicated to topological studies of periodic nets.[9-13] In one of their recent papers,[5] they discourage authors referring to a point symbol and vertex symbol as 'topology'. They argue that nets with different topologies may exhibit the same point symbol. This is because there are 14 distinct uninodal nets in the Reticular Chemistry Structure Resource (RCSR) with a point symbol of 6^6 and if one includes polytypes of the diamond/lonsdaleite type, then there are an infinite number of nets in which all vertices have the point symbol 6^6. These authors explicitly state that the best way to describe a net found in the RCSR is to use RCSR symbol which will be discussed in the next paragraph.

Codes which comprise of three letters such as **abc** or symbols with extensions as in **abc-d** are used to designate the topology found in networks of MOFs. These are very similar to the codes used for zeolites. Nets found in MOFs are coded using small letters while capital letters are used for those found in zeolites. This is done to avoid confusion. For example a code **sod** is used for topology in a coordination polymer while **SOD** is used for the same topology symbol found in a zeolite. The RCSR (www.rcsr.anu.edu.au) is a database which contains these codes with their corresponding point and vertex symbols.[14] This database contains about 2000 entries and a much larger database is being developed in the Euclidean Patterns in Non-Euclidean Tiling (EPINET: www.epinet.anu.edu.au) project which began in 2005 and has about 15000 three-periodic nets to date.[15]

The majority of 3D nets found in MOFs are named after common inorganic structures; such as **dia** (diamond), **qtz** (quarzt), **cds** ($CdSO_4$), **bbn** (boron nitride) **pts** (platinum sulphide).

3.4 Computer programs for topological analysis

The two programmes used for topological studies in this project are Systre[16] (Symmetry, Structure, Recognition and Refinement) and TOPOS.[17] When the nodes are identified, the coordinates of each unique crystallographic node and those of the nearest neighbour together with the space group are presented to Systre. The Systre software finds the net embedding with maximum symmetry and low density and gives a topological classification using a built-in archive taken mostly from the RCSR database. In situations where new nets are found, TOPOS can be consulted for vertex and point symbols. The RCSR contains maximum symmetry embedding of two and three-periodic nets considered important for crystal chemistry and crystal design.

TOPOS is integrated with two databases on topological types, which are TOPOS Topological Database (TTD) and Topological Types Observed (TTO). The TTD part consists of information on topological indices of nets found in the RCSR and EPINET.[15,18] The TTO collects the links between the topological types and the crystal structure data found in the crystallographic database. Using the TTD and TTO, the TOPOS software is able to classify, rationalise, and predict (i) the topological type of the underlying net including the degree and type of interpenetration, (ii) the maximum symmetry embedding of new nets, (iii) as well as automatic search for net representations and automatic simplification of the net.

3.5 Reticular synthesis

The knowledge of topology is very useful in reticular synthesis which has become an integral part of crystal engineering. Reticular synthesis is a process of assembling judiciously designed rigid molecular building blocks into a predetermined architecture held together by strong bonds.[19] The challenge associated with reticular synthesis is that there are multiple possible structures when starting from one node and one linker. For example, linking tetrahedral building blocks together into structures with one kind of vertex may lead to more than 100 topologically different networks, and the challenge lies on selecting the appropriate one. Yaghi argues that, if one is able to identify reaction conditions that reproducibly lead to a particular secondary building unit (SBU: geometry of units defined by points of extension such as carbon atoms of the carboxylate), then the control of the vertex geometry in the resulting structure is possible. Hence, one should be able to predict the underlying topology because the linkers remain intact and their geometry is preserved during the assembly process.[15] The process of preparing MOFs with the same topology by increasing the size of the linker is termed isoreticular synthesis. This strategy has been employed in the synthesis of isoreticular MOFs with different pore geometries by extending the length of the linkers as well as functionalising them.[20-22] Figure 3.5 illustrates an SBU and ligands used in isoreticular synthesis of SURMOF-2 analogues.[22]

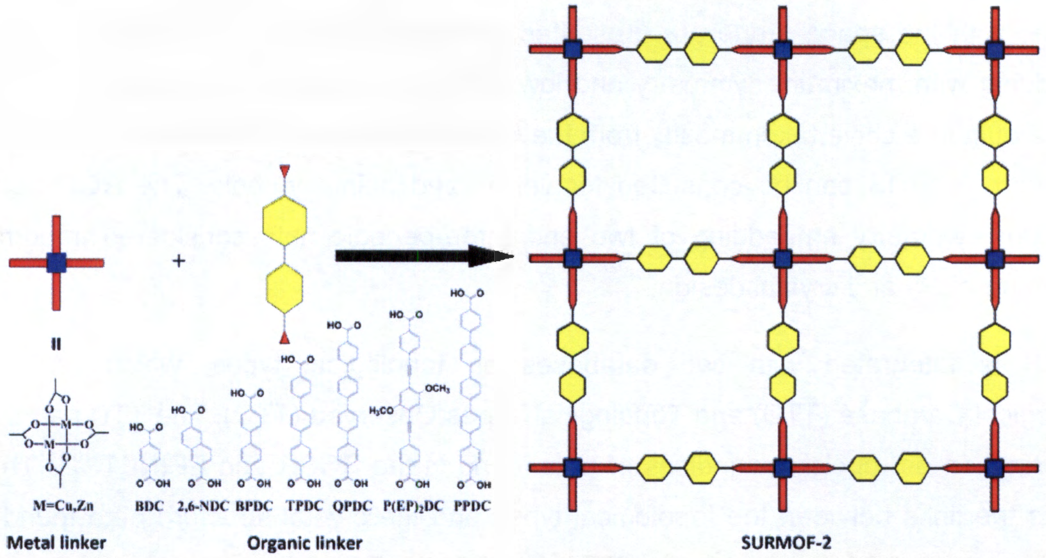

Figure 3.5: Lui *et al* demonstrated isoreticular synthesis of SURMOF-2 analogues.[22]

3.6 Summary

A complex crystal structure can be reduced to a simple net by identifying the nodes, followed by linking the neighbouring nodes to form the underlying net. This process is like reverse engineering. The reason for studying the topology of crystal structures is to find out how they are constituted and then apply this knowledge to design better materials (reticular chemistry).

3.7 References

1. L. R. Öhrström, in *Supramolecular Chemistry: From Molecules to Nanomaterials,* Volume 6, DOI 10.1002/9780470661345.smc120 Ed: P.A. Gale, J.W. Steed. 2012, John Wiley & Sons Ltd, Chichester, UK.

2. B. Moulton and M. J. Zaworotko, *Chem. Rev*, 2001, **101**, 1629.

3. Y.-B. Zhang and J.-P. Zhang, *Pure Appl. Chem*, 2013, **85**, 405.

4. B. Chen, N. W. Ockwig, A. R. Millward, D. S. Contreras, and O. M. Yaghi, *Angew. Chem. Int. Ed*, 2005, **44**, 4745.

5. M. O'Keeffe and O. M. Yaghi, *Chem. Rev*, 2012, **112**, 675.

6. A. F. Wells, *Structural Inorganic Chemistry.*, Oxford University Press, London, 1975.

7. V. a. Blatov, M. O'Keeffe, and D. M. Proserpio, *CrystEngComm*, 2010, **12**, 44.

8. S. Natarajan and P. Mahata, *Chem. Soc. Rev*, 2009, **38**, 2304.

9. V. A. Blatov, O. Delgado-friedrichs, M. O. Keeffe, M. Davide, and O. Keeffe, *Acta. Crystallogr. Sect A*, 2007, 63, 418.

10. O. Delgado-Friedrichs, M. O'Keeffe, and O. M. Yaghi, *Phys. Chem. Chem. Phys*, 2007, **9**, 1035.

11. C. Bonneau, O. Delgado-Friedrichs, M. O'Keeffe, and O. M. Yaghi, *Acta Crystallogr. Sect A,* 2004, **60**, 517.

12. O. D. Friedrichs, O. Keeffe, and O. M. Yaghi, *Acta Crystallogr. Sect A*, 2003, 22.

13. O. Delgado-Friedrichs, M. O'Keeffe, and O. M. Yaghi, *Acta. Crystallogr. Sect A,* 2006, **62**, 350.

14. M. O. Keeffe, M. A. Peskov, S. J. Ramsden, and O. M. Yaghi, *Acc. Chem. Res* 2008, **41**, 1782.

15. S. J. Ramsden, V. Robins, and S. T. Hyde, *Acta Crystallogr. Sect A,* 2009, **65**, 81.

16. O. Delgado-Friedrichs and M. O'Keeffe, *Acta. Crystallogr. Sect A*, 2003, **59**, 351.

17. TOPOS 4.0, http://www.topos.ssu.samara.ru/, accesed May 2012.

18. S. T. Hyde, O. Delgado Friedrichs, S. J. Ramsden, and V. Robins, *Solid State Sci*, 2006, **8**, 740.

19. O. M. Yaghi, M. O'Keeffe, N. W. Ockwig, H. K. Chae, M. Eddaoudi, and J. Kim, *Nature*, 2003, **423**, 705.

20. S. J. Garibay and S. M. Cohen, *Chem. Commun*, 2010, **46**, 7700

21. J. Liu, B. Lukose, O. Shekhah, H. K. Arslan, P. Weidler, H. Gliemann, S. Bräse, S. Grosjean, A. Godt, X. Feng, K. Müllen, I.-B. Magdau, T. Heine, and C. Wöll, *Sci. Rep*, 2012, **2**, 921.

22. Z. Min, M. a. Singh-Wilmot, C. L. Cahill, M. Andrews, and R. Taylor, *Eur. Jour. Inorg. Chem*, 2012, **201**, 4419.

Chapter 4

3-(4-Pyridyl)benzoate compounds of and Co(II)

In this chapter, two concomitantly synthesised structural isomers with useful properties assembled from 3-(4-pyridyl)benzoate and Co(II) ions are presented. The synthetic methods used to prepare these materials are described. The thermochromic properties of each compound were investigated by infrared spectroscopy and powder X-ray diffraction and were attributed to a change in the coordination geometry around the Co(II) ions. In parallel, the solvatochromic properties and solvent loading behaviour were investigated for one isomer since there was not enough material for the other.

Two novel compounds were prepared using 3-(4-pyridyl) benzoate (34pba) as a linker. The compounds are **1** and **2** with molecular formula: $\{[Co(34pba)_2]\cdot DMF\}_n$. Although these compounds have the same molecular formula they exhibit different solid state arrangements. Figure 4.1 shows the powder X-ray diffraction (PXRD) patterns of these compounds simulated from their single crystal structures.

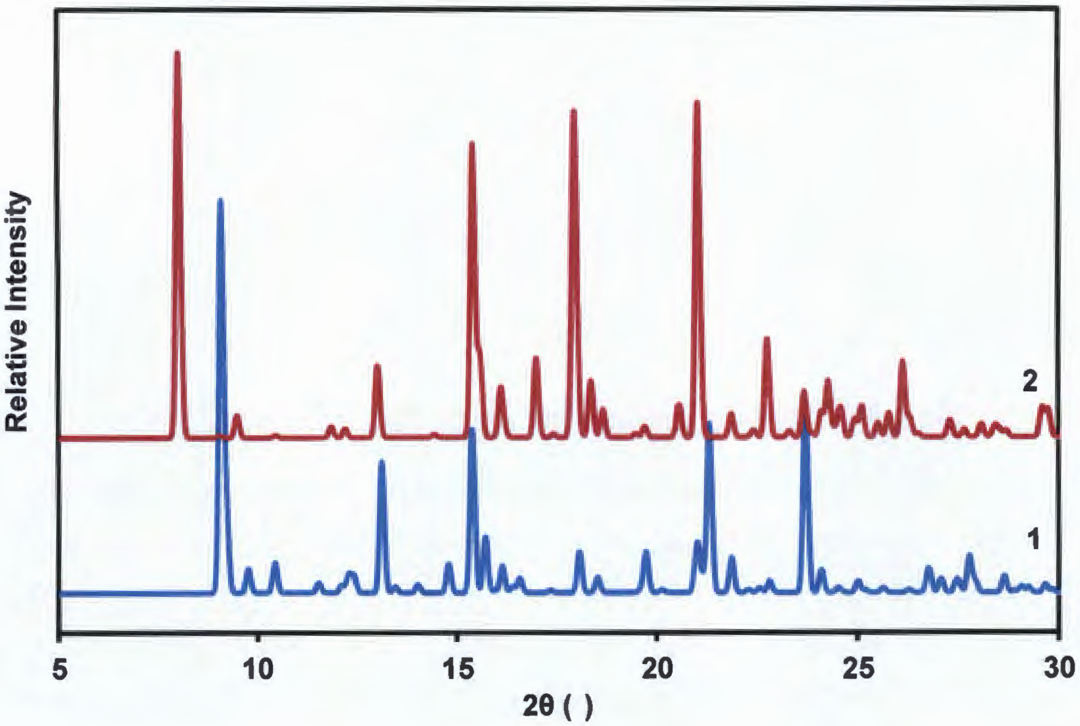

Figure 4.1: PXRD traces of compound **1** and **2** illustrating structural diversity despite the same molecular formula exhibited by the MOFs.

4.1 Synthesis of compounds 1 and 2

Compound **1** and **2** were synthesised under solvothermal conditions and crystallised concomitantly in one reaction pot. The crystals of **1** and **2** were identified based on their colour and shape as displayed in Figure 4.2.

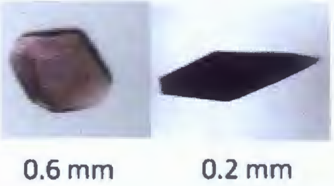

Figure 4.2: Left: crystal image of compound **1**, right: crystal image of compound **2**:

Reaction conditions were optimised and compound **1** was obtained exclusively as a pure phase. However, **2** could not be isolated as a pure phase by optimising the reaction conditions. Table 4.1 shows different reaction conditions that lead to the formation of a reported hydrogen bonded complex,[1] **1**, **2** and the **unknown phase**. Structural information for the **unknown phase** was not obtained due to poor diffraction of the crystals.

In experiments ***a*** and ***b***, 20 mg (0.1 mmol) and 40 mg (0.2 mmol) of the ligand was used respectively, while for experiment ***c*** - ***e*** the amount of ligand used was 80 mg (0.4 mmol). The amount of the cobalt nitrate hexahydrate used in all experiments was kept constant (29 mg, 0.1 mmol). In a typical experiment, cobalt (II) nitrate hexahydrate was dissolved in 2 cm^3 of methanol and 3-(4-pyridyl) benzoic acid dissolved in 5 cm^3 of N,N-dimethyl formamide (DMF) with heating and stirring. The two solutions were combined in a 15 cm^3 autoclave which was sealed tightly and heated at *ca* 2 °C min^{-1} to a particular temperature (see Table 4.1). Crystals were obtained upon cooling the reactants to room temperature at *ca* 0.5 °C min^{-1}.

Table 4.1: Reaction conditions leading to the formation of **1** and **2**

Experiment number	*Temperature/°C*	*metal: ligand*	*Time/ hours*	*Product*	*Predominant phase*
a	105	1:1	24	Discrete complex[1]	
b	105	1:2	24	Discrete complex[1]	
c	105	1:4	24	**1** and **2**	**1**
d	120	1:4	24	**1**	**1**
e	75	1:4	24	**2** and **unknown phase**	**unknown phase**

At 105 °C (experiment **c**), **1** and **2** are formed concomitantly with **1** being the major phase as confirmed by visual inspection under the microscope. Increasing the temperature of the reaction to 120 °C leads to the isolation of **1** as a pure phase. Elemental analysis was not carried out because compounds **1** and **2** have the same elemental composition, hence it cannot be used to assess the compositional purity. Compound **2** could not be obtained as a pure phase since decreasing the temperature from 105 to 75 °C led to concomitant crystallisation of an **unknown phase** and **2** (experiment **e**). Figure 4.3 shows the products of experiment **e**: the yellow material is the **unknown phase** and **2** consists of dark-purple diamond shaped crystals. For the purposes of characterisation, **2** was manually separated from the **unknown phase** under the microscope. In a slightly different experimental setup, experiment **e** was repeated by using anhydrous cobalt (II) nitrate to exclude water molecules. The same products to those in experiment **e** were obtained.

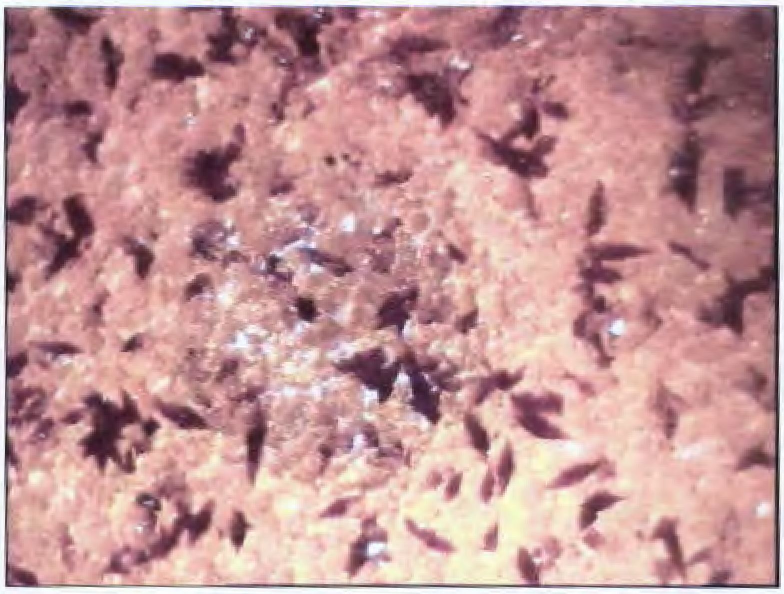

Figure 4.3: Products of experiment **e**. The yellow material is the **unknown phase** while the diamond shaped crystals are compound **2**.

The PXRD patterns of the products synthesised at various temperatures from 75 to 120 °C are depicted in Figure 4.4 and were collected at room temperature. The traces obtained for the compounds synthesised at 105 and 120 °C (traces (e) and (f) respectively) have a good match to the simulated pattern of **1** (trace (d)), thus confirming visual inspection carried under the microscope which revealed very few crystals of **2** for the synthesis carried out at 105°C. The PXRD trace of products obtained at 120 °C is similar to the simulated pattern (d) since **1** is formed exclusively. For compounds isolated at 75 °C (trace (c)), the pattern is very different to the simulated structure of **2** which support that **2** was again formed as a minor phase, however separating **2** from the **unknown phase** gave a PXRD trace (b) which has a close match to the calculated pattern of **2** (a). The powder patterns could not be fitted due to the poor quality of the data.

From these results, one can conclude that **1** is the thermodynamically stable compound (formed at 120 °C) while **2** is a kinetic product (formed at 75 °C). This is based on the fact that high temperatures favour thermodynamic products and kinetic products are generally obtained at low temperatures.[2,3] However in a situation of concomitant crystallisation, it is not easy to confirm which product is the thermodynamic or the kinetic material because they have more or less the same energy. This is ascribed to the fact that concomitant crystals form in a domain in which their area of crystallisation overlaps.

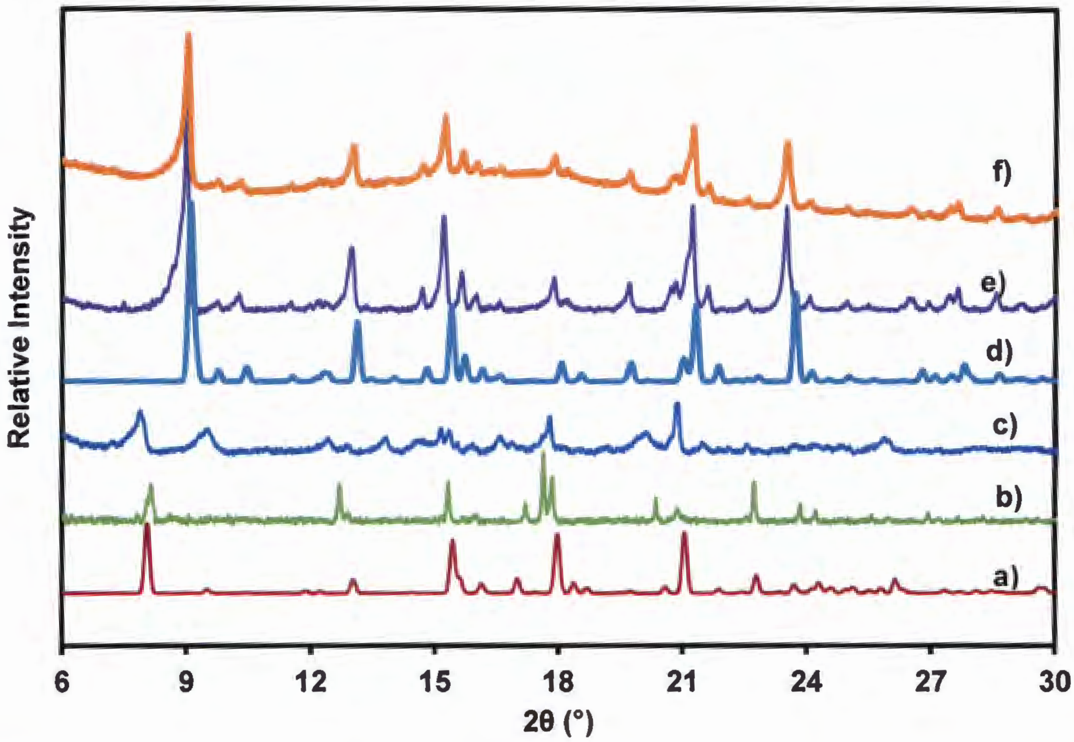

Figure 4.4 a) Simulated pattern of **2** from single crystal data, b) PXRD of **2** after separating it from the **unknown phase** formed at 75 °C, c) raw material obtained at 75 °C containing both **2** and the **unknown phase**, d) simulated pattern of **1** from single crystal data, e) raw material obtained at 105 °C showing **1** as the predominant phase, f) raw material obtained at 120 °C.

4.2 {[Co(34pba)$_2$]·DMF}$_n$ 1 and 2

4.2.1 Single Crystal X-Ray Diffraction

The structure solution and refinement details of non-hydrogen atoms are described in Chapter 2 section 2.7.1. For **1** and **2**, hydrogen atoms were placed into calculated positions using a riding model and were all refined isotropically. The hydrogen atoms were assigned temperature factors that are related to the atoms they are attached to. The hydrogen atoms of the phenyl and pyridyl parts were assigned a temperature factor of 1.2 times the parent atom and 1.5 times was used for the hydrogen atoms attached to the carbon atoms of the

DMF molecules. The crystallographic data and refinement parameters for compound **1** and **2** are given in Table 4.2.

Table 4.2: Crystallographic information and refinement parameters of **1** and **2**

	1	***2***
Empirical Formula	$\{[Co(34pba)_2]\cdot DMF\}_n$	$\{[Co(34pba)_2]\cdot DMF\}_n$
M_r(g·mol^{-1})	528.43	528.43
Temperature (K)	173(2)	173(2)
Crystal size (mm^3)	0.16 x 0.18 x 0.33	0.17 x 0.17 x 0.39
Crystal system	Orthorhombic	Tetragonal
Space group	*Pbca*	$P4_32_12$
a / (Å)	18.0941(7)	11.4957(8)
b / (Å)	14.3903(6)	11.4957(8)
c / (Å)	19.1497(8)	37.257(4)
V/ (Å^3)	4986.2(4)	4923.6(7)
Z	8	8
Calc density/ (g·cm^{-3})	1.408	1.423
F(000)	2184	2176
μ(Mo-K$_\alpha$) (mm^{-1})	0.731	0.740
θ range scanned (°)	2.10- 28.29	1.9-28.3
Index Range	-13:24; -16:19;-18:25	-14:15; -15:15; -29:49
Reflections collected	20171	42251
No. unique data	6183	6166
No. data with $I > 2\sigma(I)$	4642	5272
final R ($I > 2\sigma(I)$)	0.0364	0.0673
final $wR2$ (all data)	0.0949	0.1870
Goodness of fit, S	1.00	1.16
Max, min e density(eA^{-3})	0.43, -0.34	0.35,-0.61

4.2.2 Structural description of 1

Compound **1** crystallises in the orthorhombic crystal system and space group *Pbca.* **1** is a three dimensional neutral MOF. The asymmetric unit consists of two deprotonated ligands (34pba), one cobalt centre and one uncoordinated DMF guest molecule. Two Co(II) ions are bridged by ligand B to form a $Co_2C_2O_4$cluster. The $Co_2C_2O_4$ generated *in situ* can be considered as a secondary building unit (SBU) with carbon and nitrogen atoms being the points of extension. Ligand A and B exhibit different coordination modes: ligand A uses the tridentate μ_2-mode to bridge two Co(II), while ligand B bridges three Co(II) ions using the μ-

syn, syn-carboxylate group and the nitrogen atom. Each Co(II) is bonded to five ligands, two Co(II)-N bonds occupy axial positions, the equatorial positions are occupied by Co-O (carboxylate) bonds (two single Co-O and one chelating Co-O bond) as illustrated in Figure 4.5.

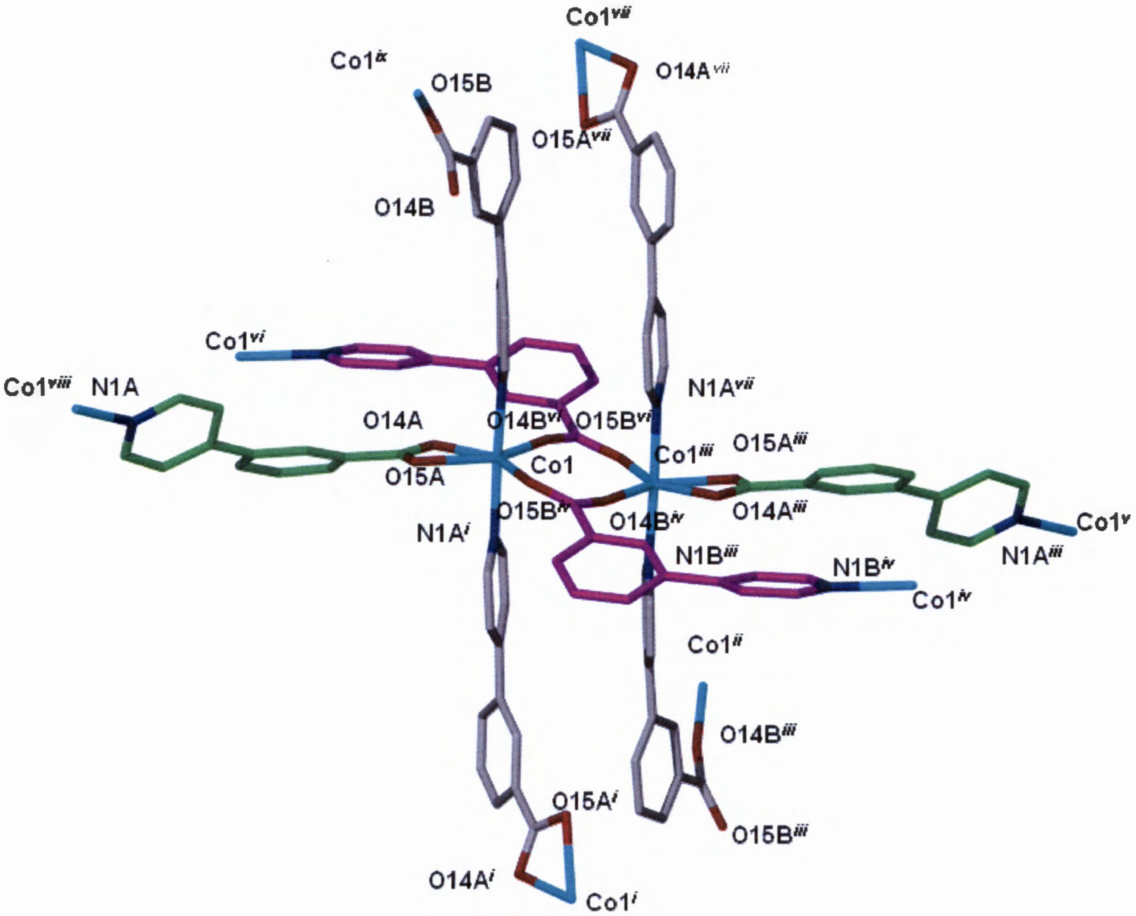

Figure 4.5: Coordination environment of Co(II) ions displaying the Co(II)-N bonds occupying the axial position (these are depicted in grey). The Co(II)-O bonds are in the equatorial position and these are drawn in green and purple. Each Co(II) is bonded to four oxygen atoms and two nitrogen atoms. The two Co(II) centres in the SBU are bridged via O15B – C13B – O14B. Related by symmetry ^{i}1-1/2, y,1/2-z; ^{ii}x-1/2, ½-y, -z; ^{iii}-x,-y,-z; ^{iv}x-1/2, -y-1/2, -z; ^{v}-x-1/2, -y, z-1/2; ^{vi}1/2-x, ½+y, z; ^{vii}1/2-x, -y, z-1/2; ^{viii}1/2+x, y, ½-z; ^{ix}1/2-x, -y-1/2, -z

The Co-O bond length ranges from 2.019(1) to 2.224(1) Å, while the Co-N ranges from 2.136(2) to 2.140(2) Å. Table 4.3 gives the Co-O and Co-N bond lengths. These bond lengths are within the expected range found in the Cambridge Structural Database. The Co(II) metal centre assumes a distorted octahedral geometry with axial-axial, axial-equatorial and equatorial-equatorial bond angles ranging from 87.04(5)° to 176.60(6)°. These are given in Table S4.1 of the supplementary material. The overall structure is a 3D network with micropores in which DMF molecules are trapped.

Table 4.3: Coordination parameters around the Co(II) ion: bond lengths.

Bond type	***Bond length (Å)***	***Bond type***	***Bond length (Å)***
Co1-N1B	2.140(2)	Co1-O15A	2.224(1)
Co1-N1A	2.136(2)[i]	Co1-O14B	2.019(1)[ii]
Co1-O14A	2.171(1)	Co1-O15B	2.065(1)[iii]

Related by symmetry: [i] *½+x, y, ½-x,* [ii] *1/2-x, y-1/2, z; ½+x, -y-1/2, -z*

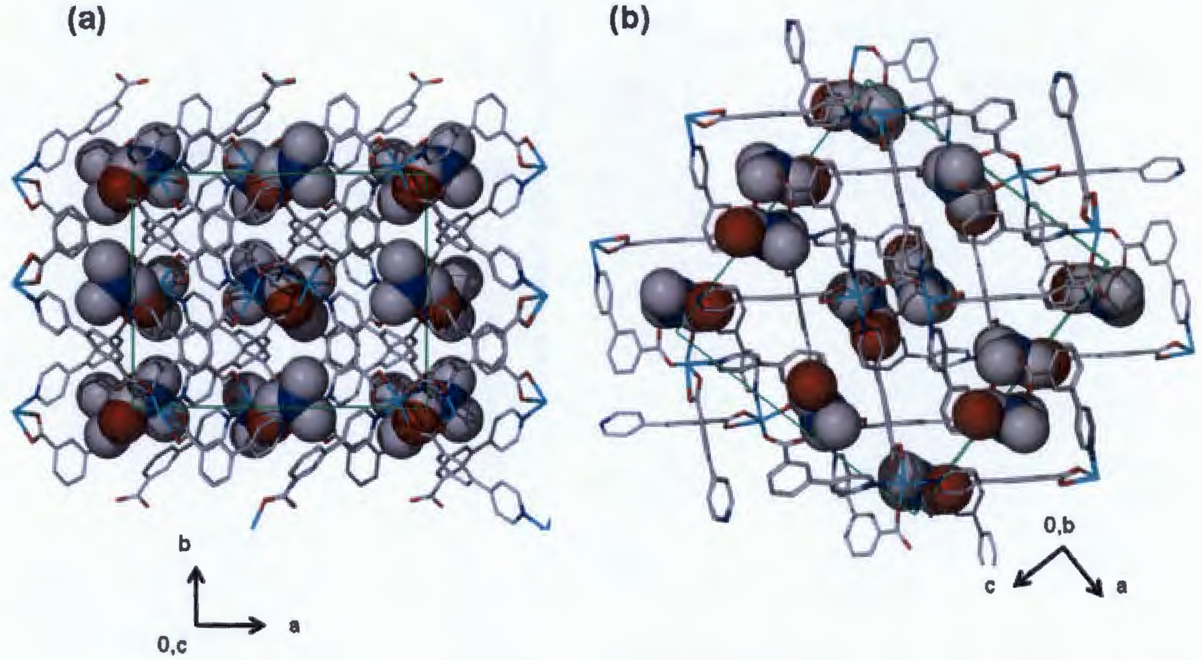

Figure 4.6: (a) Solid state packing of **1** as viewed along the *c*-axis displaying the DMF molecules in van der Waals radii confined in the cavities, (b) packing of **1** viewed down the *b*-axis illustrating the pairwise stacked DMF molecules related by an inversion centre. Hydrogen atoms have been omitted for clarity.

The packing diagram of **1** show that the DMF molecules are trapped within cavities as displayed in Figure 4.6. These guest molecules are pairwise stacked and the interplanar distance between them is 3.62 Å. There are no noticeable interactions between the guest and framework. However, weak intramolecular hydrogen bonding exists within the framework of **1** (Table 4.4). PLATON[4] estimates that the DMF guest molecules occupy 27% of the unit cell volume.

Table 4.4: Weak intramolecular hydrogen bonding parameters found in **1**

	Symmetry operator leading to O(X)`	***d(C···O) (Å)***	***Angle (°)*** **C-H···O**
C12B-H12B···O14A`	½ -x, - ½+ y, z	3.278(2)	169
C9A-H9A···O15A`	½ - x, ½ +y, z	3.200(2)	142
C6A-H6A···O15B`	x, -½ – y, ½ +z	2.967(2)	109
C2B-H2B···O15B`	½ + x, - ½ – y, -z	3.015(2)	119

Figure 4.7 displays the symmetry elements found in compound **1** when viewed along [0 1 0]. The centre of inversion is displayed as a black circle. The inversion centre is located at (0 0 0). The other inversion centres are related by a symmetry of –x, -y, -z

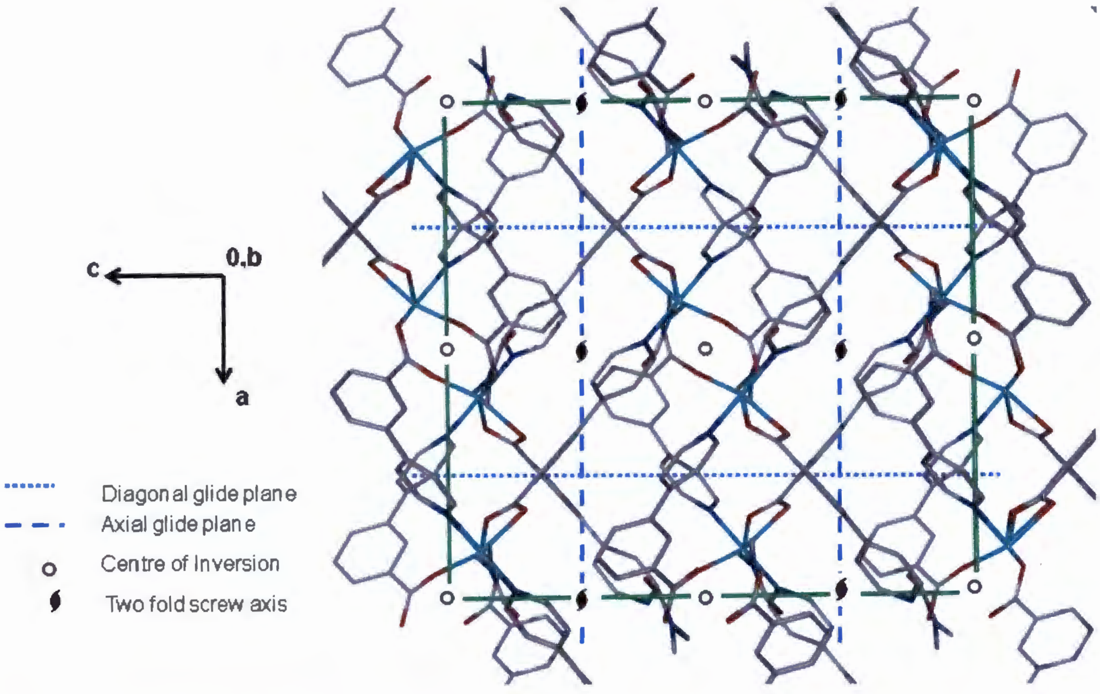

Figure 4.7: The packing diagram of **1** as viewed along the [010] with an overlay of the symmetry elements in the unit cell given in black. The glide planes are displayed in blue.

There are three 2-fold screw axes with directions of [0 0 1], [1 0 0] and [0 1 0], these are located at (¼ 0 z), (x ¼ 0) and (0 y ¼) respectively. The other screw axes are generated by symmetry. The two-fold screw axes located at (¼ 0 z) and (0 y ¼) run between the pyridyl rings, those parallel to the *a*-axes located at (x ¼ 0) run between the phenyl and the pyridyl rings of the network. This implies that there are two chemically different environments around the 2-fold axis.

In the structure of **1**, there exist three glide planes. The glide plane perpendicular to the *c*-direction has a glide component of (½ 0 0), the one perpendicular to *a*-axis has a glide component of (0 ½ 0) and finally the one perpendicular to [0 1 0] has a glide component of (0 0 ½).

Analysis of the network features in **1** by Systre[5] and TOPOS[6] revealed an 8-connected uninodal body centred cubic (**bcu**) net. The centre of the metal cluster in **1** was chosen as the node (Figure 4.8a). The other nodes were symmetrically generated and their coordinates determined by the X-SEED program. The coordinates of the 8-connected node and the nearest 8 nodes were submitted to Systre together with the space group of the compound which confirmed the topology of **1** as a **bcu** net. Topological analysis of the network in TOPOS using the automated cluster method gave the same results. The point symbol and vertex symbol for this net are $4^{24}.6^{4}$ and $4.4.4.4.4.4.4.4.4.4.4.4.4_3.4_3.4_3.4_3.4_3.4_3.4_3.4_3.4_3.4_3.4_3.4_3.^{*}.^{*}.^{*}$ respectively. The net has a topological density value of 2331.

Literature study shows that only a few three dimensional multifunctional frameworks with mineral topologies have been reported so far. The majority of these are based on the use of three, four, five or six connected building blocks. MOFs with connections of five, seven, and eight or higher are very rare. This may be ascribed to limitations in the symmetry or steric hindrance associated with connected nodes. It seems the *in situ* generation of SBU with two or more metal centres gives rise to higher network connectivity.[7-11] In our case the presence of a dinuclear SBU coupled with the nitrogen atom donor of the 34pba ligand provides an alternative way of extending the network with less strain on the linkers, and therefore all the 34pba ligands act as independent linkers. This analysis of the network reduces the structure of **1** to a uninodal 8-connected net and the vertex Figure corresponding to that of a cube (Figure 4.8b and c). Thus, the combination of a cubic node in a uninodal 8-connected net may only be realised in a **bcu** lattice. This topology is rare for MOFs.[12-14]

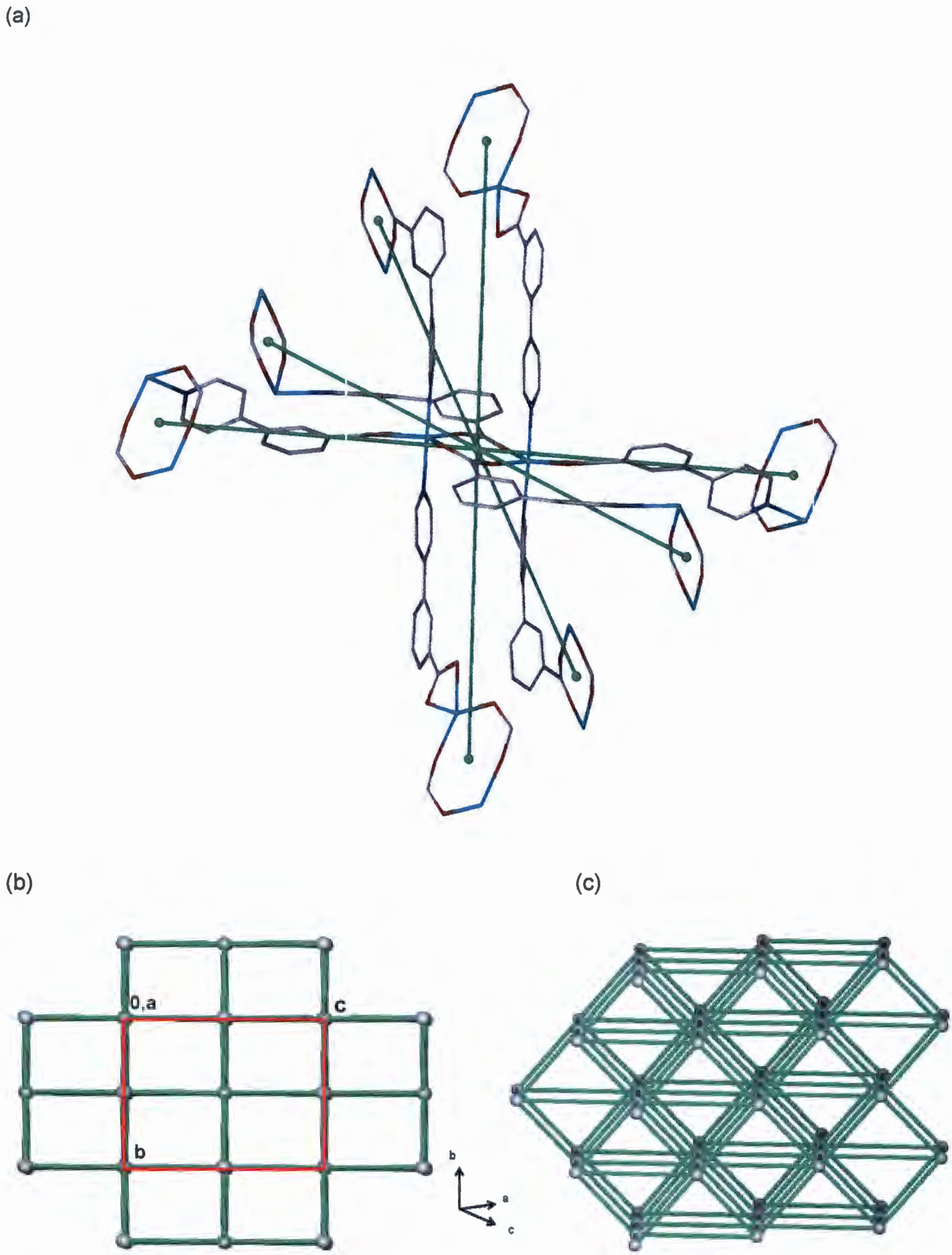

Figure 4.8: (a) Network connectivity of **1**. Placing a node at the centre of the binuclear cobalt cluster generates an 8-connected uninodal net. (b) and (c) Topological representation of the **bcu** net of **1**. Each node represents the 8-connected node at the $Co_2C_2O_4$ cluster.

4.2.3 Structural description of 2

This compound crystallises in the tetragonal crystal system and chiral space group $P4_32_12$. The asymmetric unit comprises of one cobalt centre and two deprotonated ligands (A and B) and one DMF molecule. The oxygen atom of the DMF molecule is disordered over two positions with site occupancy factors of 60% and 40% for O1C2 and O2C2 respectively. The pyridyl part of ligand (A) is disordered over two positions with refined site occupancies of 55% and 45% for fragment A2 and A1 respectively.

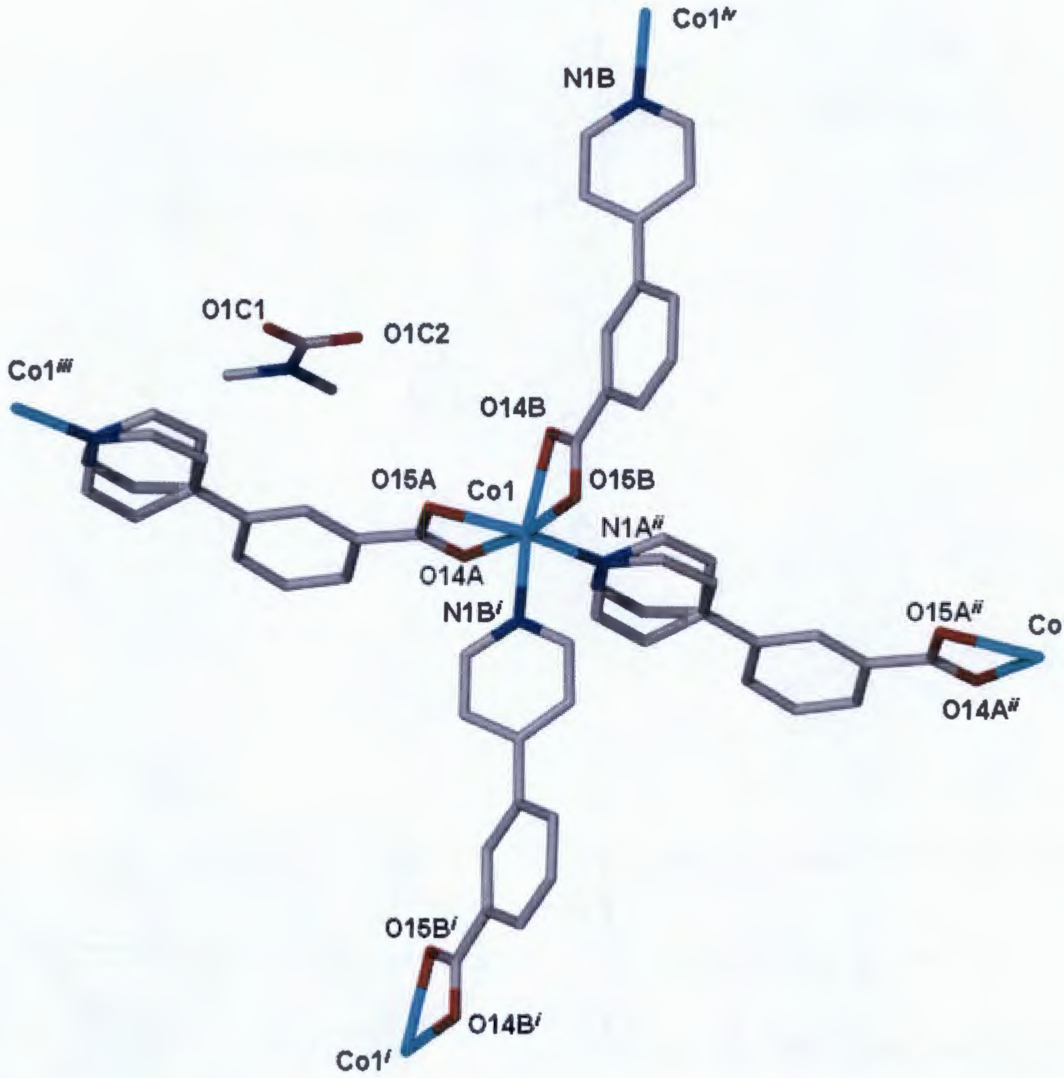

Figure 4.9: Coordination environment of Co(II) in compound **2**. The pyridyl moiety of ligand A and the oxygen atom of the DMF are disordered over two positions as displayed in this Figure. Hydrogen atoms have been omitted for clarity. Symmetry related, ^{i}x, y-1, z; ^{ii}1+x, y, z; ^{iii}x-1, y, z; ^{iv}x, 1+y, z

The Co(II) is coordinated to four ligands through two bidentate Co(II)-O of the carboxylate bonds and two single Co(II)-N(pyridyl) bonds. This gives a distorted octahedral geometry around the metal centre as shown in Figure 4.9. The Co(II)-N bond length varies from

2.106(4) Å to 2.125(5) Å while the Co(II)-O distance is in the range of 2.077(4) - 2.237(4) Å (see Table 4.5). The bond angles around the cobalt centre are within the range of 60.56(14) to 169.50(16)°. These are given in the supplementary material Table S4.1. Four 34pba ligands bridge four Co(II) centres to form a 2D square grid network. The dihedral angles between the pyridyl and phenyl rings in the ligand are 27° for ligand A and 38° for ligand B.

The packing diagram of **2** displays 2D interdigited layers as illustrated in Figure 4.10. The DMF guest molecules are trapped between the 2D layers of the MOF.

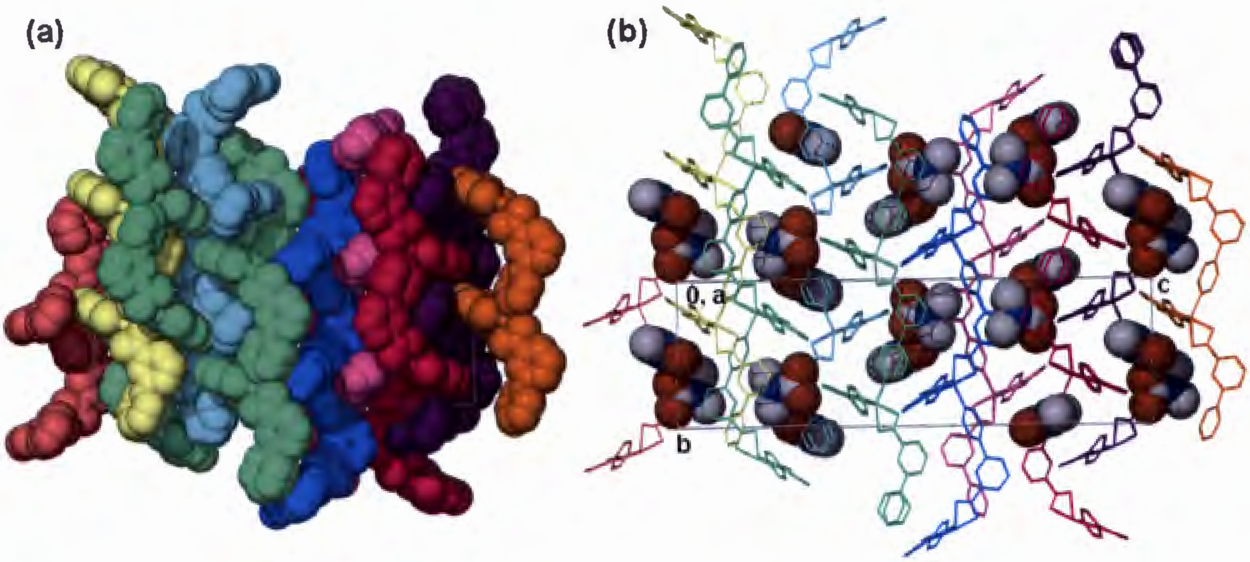

Figure 4.10: Solid state structure of **2** as viewed along [100], hydrogen atoms have been omitted for clarity: (a) Interdigited 2D layers drawn with van der Waals radii, the DMF molecules have been omitted for clarity, (b) the 2D network drawn in stick form and the guest DMF molecules, drawn with van der Waals radii, are residing in the cavities between the 2D layers which are shown in different colours.

Analysis of the interactions between the DMF guest and the 2D network of **2** revealed that there are no noticeable interactions between the two, however the 2D layers are connected by weak intramolecular hydrogen bonds C2(B)-H(2B)···O(15A) with d(C···O) of 3.264(6) Å. The symmetry leading to the generation of these interactions is (½ + x, 3/2 –y, ¼ - z). The volume occupied by the DMF molecules accounts for 23.8% of the unit cell volume as estimated by PLATON.

Table 4.5: Bond distances around the Co(II) in compound **2**

Bond type	***Bond length (Å)***	***Bond type***	***Bond length (Å)***
Co1-N1B	2.125(5)^{i}	Co1-O15A	2.181(4)
Co1-N1A	2.106(4)^{ii}	Co1-O14B	2.237(4)
Co1-O14A	2.107(4)	Co1-O15B	2.077(4)

Related by symmetry: ^{i}*x, 1+y, z;* ^{ii}*x-1, y, z*

The symmetry elements found in compound **2** are displayed in Figure 4.11. There are two four-fold screw axis which all run along the [0 0 1] direction. The symmetry operator for the one located at axis (0 ½ z) is ½-y, ½+x, ¾+z. The other four-fold screw axis is located at axis (½ 0 z) and has a symmetry operator of ½+y, ½-x, ¼+z. These four-fold screw axes are located in environments which are chemically the same (mostly surrounded by hydrogen atoms and oxygen of the carboxylate and the DMF guest)

The two fold screw axes located at (0 0 z) and (¼ y 3/8) are all in a hydrophobic environment and are surrounded by the pyridyl moiety of the framework.

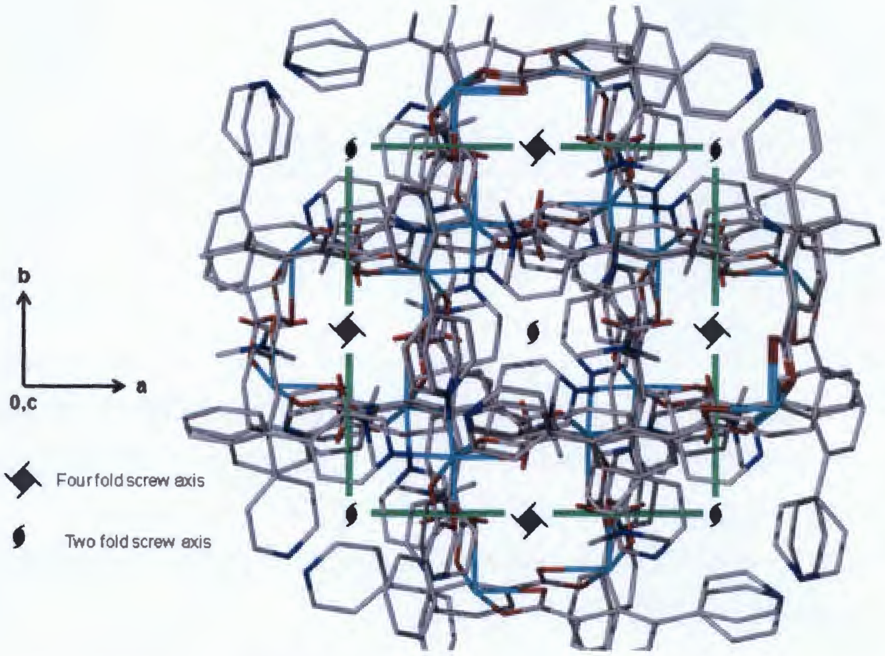

Figure 4.11: The packing diagram of **2** viewed along the [001] axis with an overlay of the symmetry elements in the unit cell in black.

Topological analysis of **2** was performed using Systre and TOPOS computer program. The nodes were placed at the Co(II) ions. The rest of the nodes were symmetrically generated. Each node is four connected. Analysis of the network using the TOPOS automated cluster method revealed an **sql** topology. The point symbol and vertex symbol for this net are $4^4.6^2$ and $4.4.4.4.^{*}.^{*}$ respectively and the net has a topological density value of 221. Figure 4.12 shows the network connectivity and the topological representation of the net in **2**.

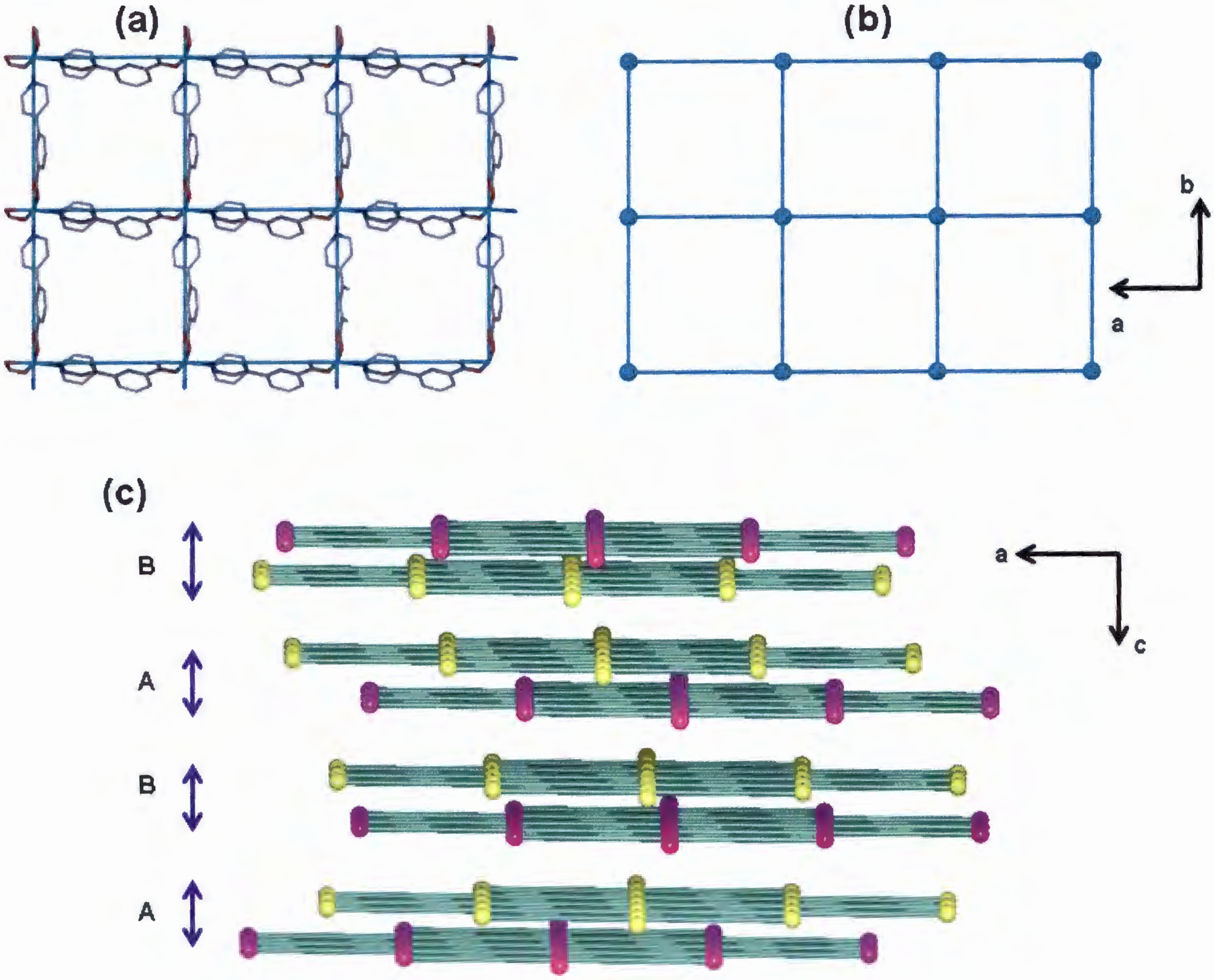

Figure 4.12: (a) Network connectivity in **2**. (b) Topological representation of the **sql** net found in **2**, each blue node is four connected and represents the Co(II) ion, (c) the packing diagram of the **sql** net, showing an ABAB type offset stacks of 2D sheets in **2**. In A the offset of nodes is large, while in there is a slight offset of nodes in B.

An **sql** net is constructed from a square planar node and a ditopic linker, hence it is not surprising that the reaction of 3-(4-pyridyl)benzoic acid with Co(II) can give rise to this network, as already noted, the same reaction components can also generate SBU *in situ* which ultimately leads to concomitant crystallisation of a **bcu** net (compound **1**). This illustrates the difficulty associated with crystal structure prediction. Majority of two-periodic MOFs which are four connected have an **sql** topology.

4.3 Classification of {[Co(34pba)$_2$]. DMF}$_n$: 1 and 2

As seen from the crystal structures of **1** and **2**, these compounds have the same empirical formula but are neither polymorphs nor supramolecular isomers as their coordination entities are different. Although the materials used for the preparation of these compound are the same, the molecular building blocks generated *in situ* are quite different, a dinuclear Co(II) SBU is found in **1** while **2** has a mononuclear Co(II) centre. These compounds may be best described as 'true' molecular building blocks (MBB) structural isomers. 'True' in the sense that the guest type and content is the same in both networks.

4.4 Thermal analysis and thermochromic effects of {[Co(34pba)$_2$]. DMF}$_n$: 1 and 2

The thermal stability of **1** and **2** were investigated by TGA and DSC. Figure 4.13 depicts an overlay of the TGA and DSC of **1** and **2**. Loss of DMF molecules occurs in the temperature range of 100 - 280 °C on the TGA for **1** which suggests that the compound is stable at room temperature. This is associated with a broad endotherm on the DSC trace in the range of 100 - 240 °C. For **2**, guest loss takes place from 50 to 175 °C with an endothermic peak at 134 °C in the DSC. A initial weight loss of 14.3% and 14.2% observed on the TGA of **1** and **2** respectively corresponds to loss of one DMF molecule which was modelled in the asymmetric unit of each compound (calculated 13.8%). The difference in the temperature range of guest loss is ascribed to the difference in the structural features of the compounds. As already noted from the crystal structures, the DMF guests in **1** are confined in cavities of a 3D network which tightly encloses them. For **2**, the guest molecules are sandwiched between the interdigited 2D layers which may easily glide past one another allowing for the easy removal of the DMF molecules, thus resulting in the lower temperature of total guest loss. An exothermic peak is observed at approximately 281 °C for **1** and 347 °C for **2** on the DSC trace. These events which correspond to phase transitions were investigated with hot stage microscopy (HSM) and temperature dependent PXRD studies. After the phase transition, the melting points of **1** and **2** differ by approximately 3 °C irrespective of the heating rate used.

(a)

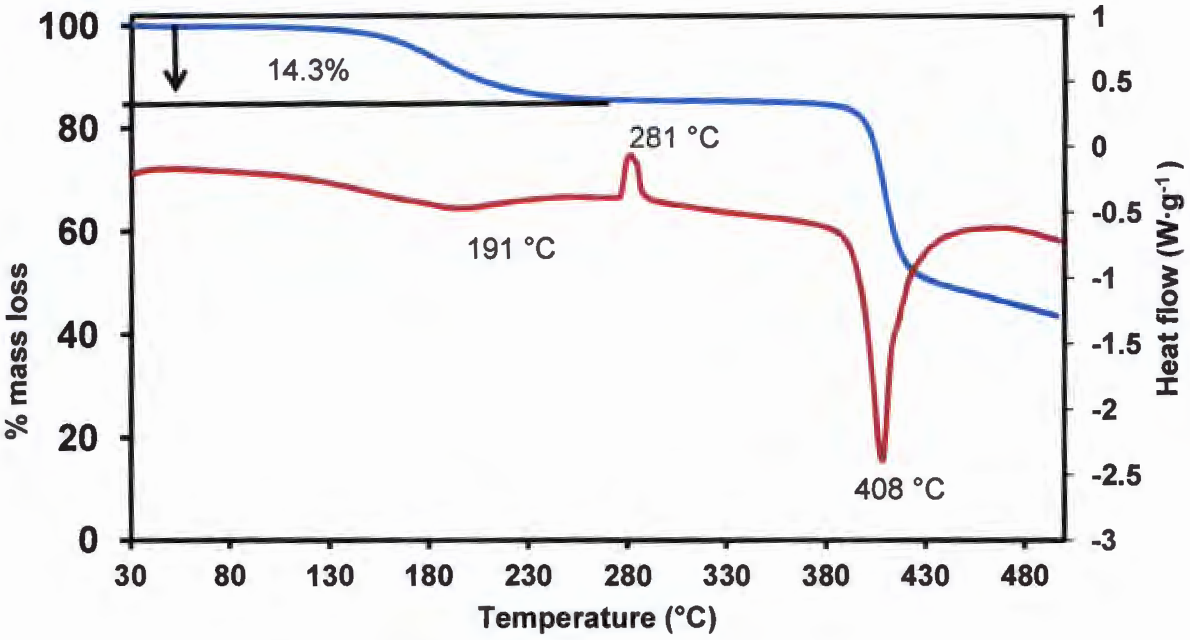

(b)

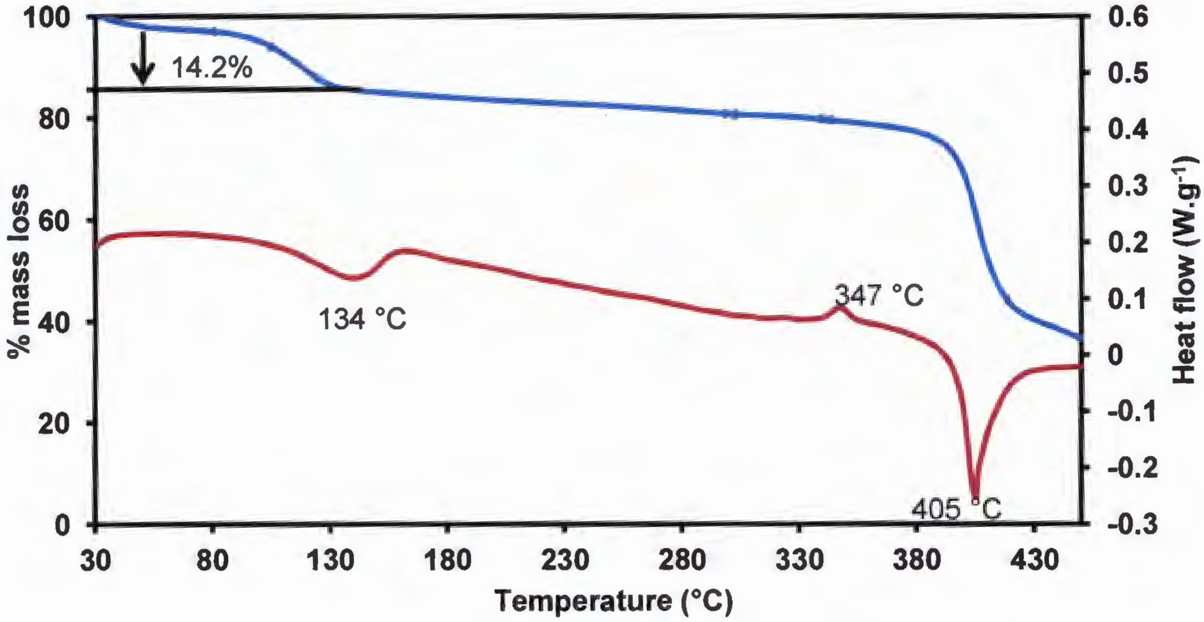

Figure 4.13: (a) Overlay of TGA (blue) and DSC (red) of **1** (b) overlay of TGA (blue) and DSC(red) of **2**.

HSM studies in Figure 4.14 show that the crystals of **1** change colour from dark purple to light purple at about 250 °C which is associated with complete loss of DMF as seen on the TGA (Figure 4.13a). At 300 °C a blue colour is observed and the intensity of the blue colour increases with an increase in temperature. In **2**, the change in colour from dark purple to blue is observed at about 360 °C. It seems reasonable that the exothermic peaks observed in the DSC at about 281 °C for **1** and 347 °C for **2** are associated with the colour change of the crystals. The difference in the temperatures between HSM and DSC is probably due to the different set of geometries under which the experiments were conducted as well as the size of the crystals. The HSM was done on an open geometry while a closed geometry was used for the DSC analysis.

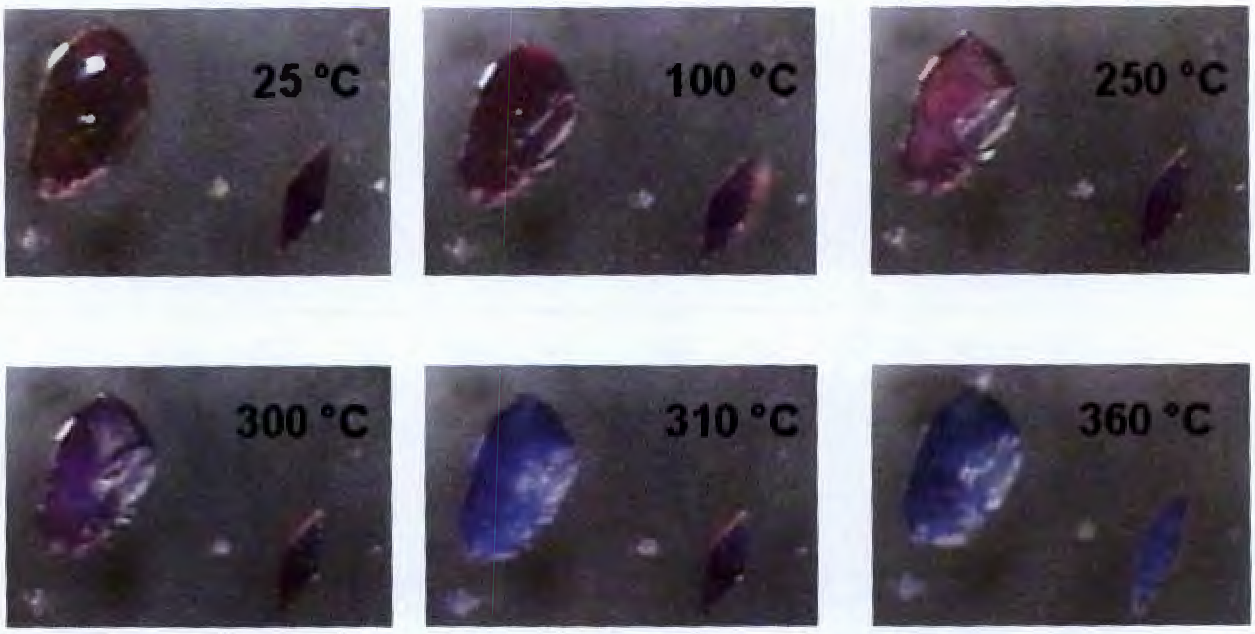

Figure 4.14: Crystals of **1** (large) and **2** (small diamond shaped) under the HSM at different temperatures. A slight colour change is observed for **1** upon complete loss of DMF (250 °C). The observed colour changes at 300-310 °C for **1** and around 360 °C for **2** correspond to the phase transitions which were revealed on the DSC.

The thermal events observed on the DSC and HSM were investigated by temperature dependant PXRD for **1** (Figure 4.15). Subtle changes are observed upon guest loss (240 °C). The peak centred at about 9° in 2θ positions undergoes some splitting from 240 °C upwards. A noticeable feature of this pattern is the decrease in peak intensity (150 – 280 °C). The peak intensity seems to increase above the phase transition with appearance of new peaks at lower 2θ theta angles. Compound **1** undergoes an irreversible phase change above 280 °C with the new phase being retained upon cooling the sample to room temperature. Unfortunately, the mosaicity of the crystals increase above the phase transition precluding single crystal X-ray diffraction analysis. The phase transition observed above 240 °C is in concert with the thermal events observed on the DSC and HSM. Variable temperature PXRD studies of **2** could not be performed due to insufficient material.

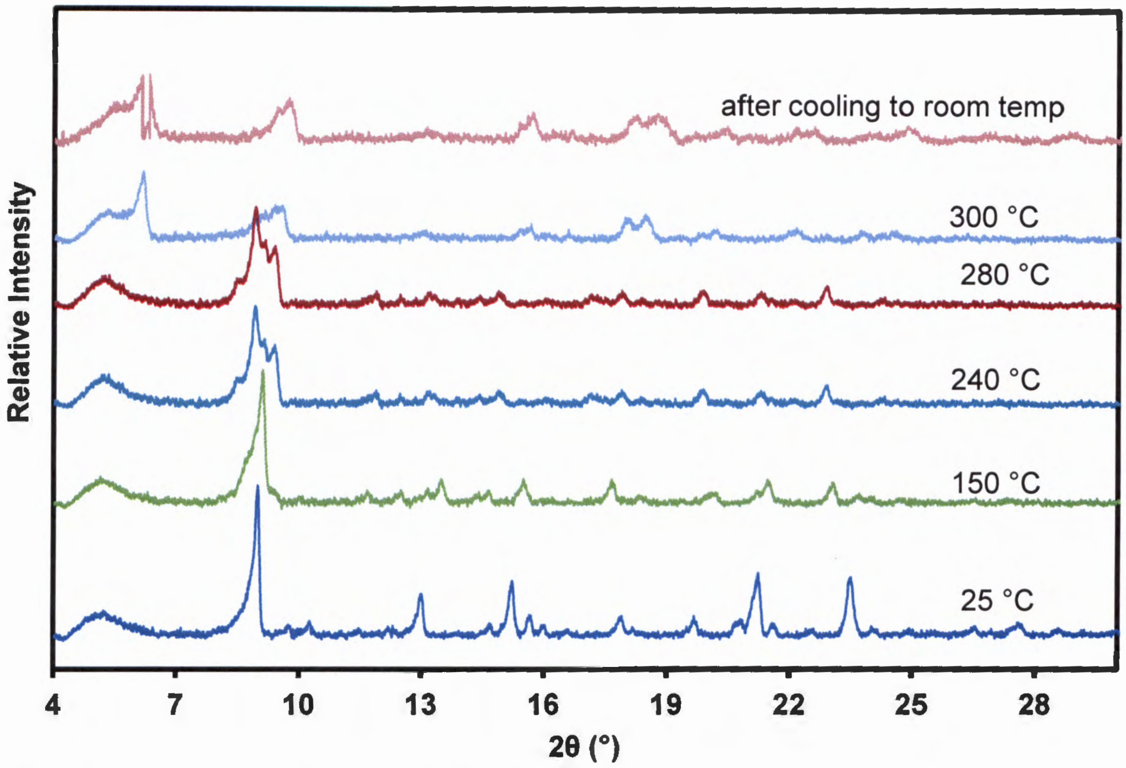

Figure 4.15: Variable temperature PXRD of **1** showing decrease in peak intensity and transformation of **1** to a new phase is observed between 280 and 300 °C.

Cobalt compounds are known to exhibit a wide range of colours. These have been associated with the nature of the coordination geometry around the cobalt centre with blue corresponding to tetrahedral environment.[15] To probe and understand the origins of the colour change in **1** and **2**, the IR spectra of **1**, **1d** (obtained upon desolvation of DMF), **1d-blue** (obtained after **1** is heated above 290 °C), **2** and **2d-blue** (obtained after heating **2** above the phase transition temperature) were compared (Figure 4.16). The (IR) spectrum of **1** displays a band at 1675 cm^{-1} which is assigned to the carbonyl stretch of the DMF molecule. The absence of this band in **1d** and **1d-blue** confirms complete desolvation of the network. The desolvated phase absorbs moisture as evidenced by the broad stretch in the O-H region (not shown). The C-C stretch of the aromatic rings appears at 1613 cm^{-1} in all compounds. The bands at 1550 and 1391 cm^{-1} in **1** and **1d** are assigned to the asymmetric and symmetric stretches of the carboxylate group respectively with a magnitude of separation of 159 cm^{-1}. In **1d-blue**, the asymmetric and symmetric carboxylate bands are located at 1570 and 1394 cm^{-1} respectively with a magnitude of seperation of 176 cm^{-1}. A shoulder is also observed at 1379 cm^{-1} in the IR spectrum of **1d-blue**.

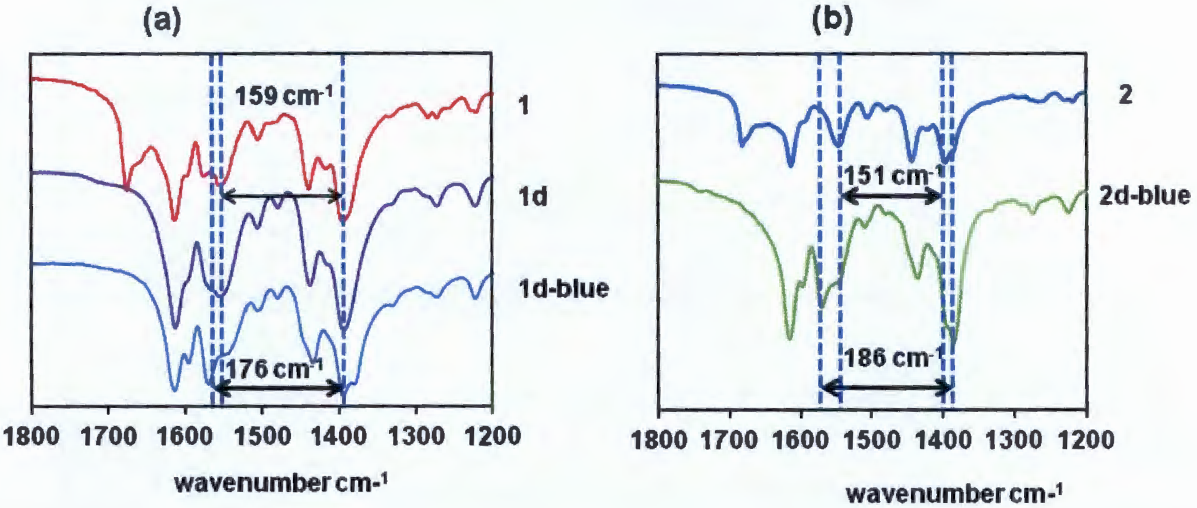

Figure 4.16: (a) IR spectrum of **1**, **1d** and **1d-blue** and (b) **2** and **2d-blue** showing the positions of the bands which allow one to assign the coordination mode of the carboxylate moiety in the framework.

For compound **2**, the band at 1674 cm^{-1} is ascribed to the C=O group of the DMF molecule. The carboxylate asymmetric and symmetric stretches were observed at 1546 and 1395 cm^{-1} respectively, and the energy difference was found to be 151 cm^{-1}. In **2d-blue**, bands are located at 1570 and 1384 cm^{-1} and these correspond to the asymmetric and symmetric stretches of the carboxylates respectively, and the magnitude of separation was found to be 186 cm^{-1}.

Literature documents that the difference in energy between the asymmetric and symmetric carboxylate stretches may be used to derive the coordination geometries of the metals and the mode of carboxylate binding.[16] Generally, the following order has been proposed for divalent metal carboxylates: Δ (chelating) < Δ(bridging) < Δ(ionic) < Δ(monodentate). From the IR results, it may be assumed that the thermochromic effect observed above the phase transition temperature in both **1** and **2** is attributed to the change in geometry from octahedral to tetrahedral (from bidentate bridging mode to monodentate bridging mode of the carboxylate).

4.5 Sorption studies on the activated phase of 1, [Co(34pba)$_2$]$_n$ 1d

To perform solvent sorption studies on **1**, the DMF guest molecules situated in the cavities were evacuated by heating **1** at 150 °C for 10 hours under vacuum to give **1d**. During this process the compound turned from light pink to dark purple. Complete removal of DMF from **1** was confirmed by TGA analysis which showed no weight loss until decomposition. To investigate the solvatochromic behaviour of **1**, powdered samples of **1d** were soaked in dry solvents: methanol, ethanol, acetone, DMF and water for a period of 24 hours to give **1d-MeOH**, **1d-EtOH**, **1d-Acetone**, **1d-DMF** and **1d-water** respectively. The colours of the inclusion compounds formed are displayed in Figure 4.17. The solvatochromic behaviour was investigated by IR analysis which is displayed in Figure 4.18

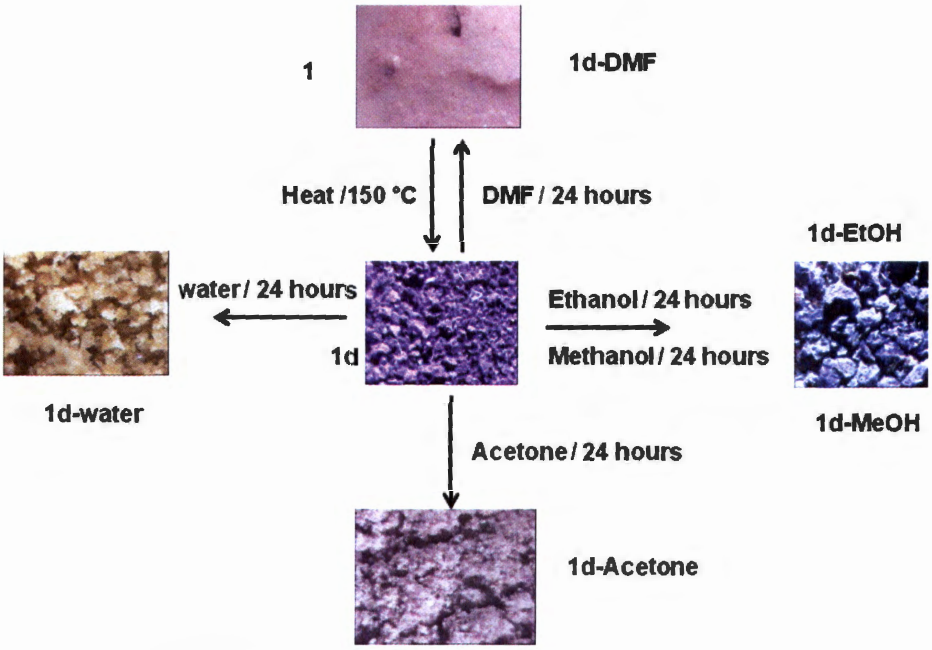

Figure 4.17: Scheme displaying the different colours exhibited by **1d** depending on the nature of the solvent absorbed.

The IR bands which are not affected by the presence of the guest molecules are assigned to the aromatic ring of the 34pba ligand. In contrast, the bands which have been affected relative to **1d** are highlighted in Figure 4.18 and they have been assigned to the asymmetric and symmetric vibration of the carboxylate. The IR spectrum of **1d-DMF**, **1d-EtOH** and **1d-Acetone** exhibits two asymmetric bands which suggest the presence of chelating and bridging coordination modes of the carboxylate as seen in the crystal structure of compound **1**. For **1d**, **1d-water** and **1d-MeOH** these bands are not well resolved and they appear as broad bands. Table 4.6 gives the asymmetric and symmetric carboxylate stretches of the ligand.

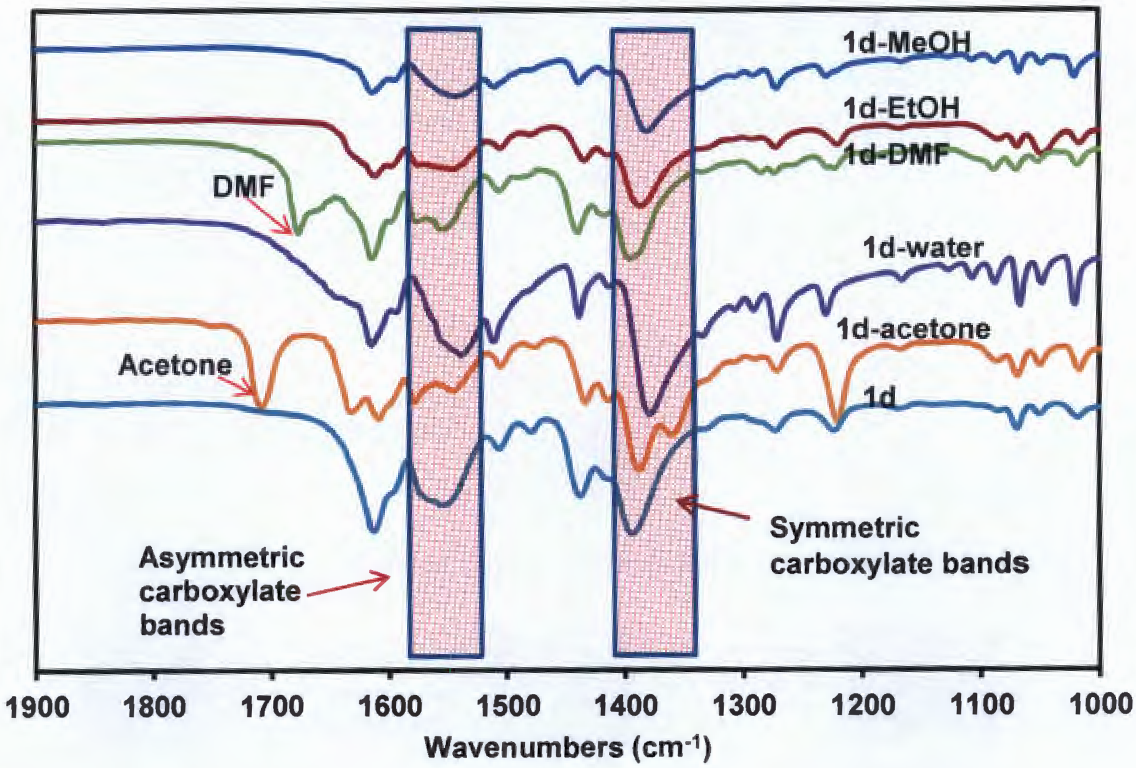

Figure 4.18: IR spectrum of several solvated forms of **1d**.

Table 4.6: Carboxylate band positions in the IR spectrum of the inclusion compounds

Compound	*Asymmetric band /cm^{-1}*	*Symmetric band/cm^{-1}*
1d	1556	1395
1d-acetone	1581, 1544	1386, 1375
1d-water	1540	1380
1d-DMF	1575, 1560	1395
1d-EtOH	1575, 1544	1386
1d-MeOH	1544	1386

The results in Table 4.6 and Figure 4.18 show that absorption of various guest molecules gave rise to changes in the positions of both the asymmetric and symmetric carboxylate bands when compared to **1d**. These changes may be attributed to various interactions between the guest and host framework such as hydrogen bonding or changes in the coordination environment around the Co(II) ions. In other related studies, it has been observed that guest molecules such as methanol may not directly interact with the metal centres, but induce changes in the way molecules interact with each other, which in turn causes a spin transition. Thus the change from high-spin to low-spin or *vice versa* has resulted in colour changes in coordination networks. It is very difficult to draw a conclusion about the origins of the colour changes observed when **1d** absorbs solvents based on the IR results. This is because solvatochromic phenomena in MOFs stems from different mechanisms. Techniques such as Mössbauer spectroscopy and single crystal X-ray diffraction alongside IR studies may provide a greater insight into the solvatochromic effects observed. However, single crystal x-ray diffraction is hampered by the poor diffraction of crystals after desorbing and absorbing guest molecules.

In a different experimental set up, powdered samples of **1d** were exposed to solvent vapours as described in the experimental section. The inclusion compounds formed (**1d-solvent**) were characterised using TGA and DSC to establish the amount of solvent enclathrated by the framework (Table 4.7 and Figure S4.1-S4.6). Thermal analysis by TGA shows that all the inclusion compounds formed lose the guest molecules at room temperature with the exception of **1d-DMF** compound. The slopes of the TGA curves give an indication of the amount of energy that is required to desorb the guest molecules. It seems the removal of methanol requires less energy as its desorption occurs over a small temperature range in comparison to the other inclusion compounds. The DSC profile of **1d-MeOH** compound exhibits a broad endothermic peak from 25 to 94.93 °C associated with the departure of the methanol molecules. For **1d-water** inclusion compound, the initial mass loss from 30 to 75 °C may correspond to loss of loosely bound water molecules. The second mass loss of water occurs over a narrow temperature range and is associated with a steep gradient on the TGA profile which also suggests that less energy is required to desorb the guest molecules, however the DSC shows a broad endotherm from a temperature range of 92 °C to 150 °C. For **1d-EtOH** and **1d-acetone**, the guest loss profiles look very similar except that acetone is lost over a larger temperature range which may suggest stronger interactions of the molecule with the host framework. Just like compound **1**, the **1d-DMF** inclusion compound is very stable at room temperature. This suggests that **1** and **1-DMF** have the same crystal structure. The loss of the DMF is associated with a broad endotherm at about 290 °C. It is noted that all compounds undergo a phase transition at high temperatures before their decomposition. **1d-water** and **1d-EtOH** present phase changes at 263 and 271 °C respectively while the rest of the inclusion compounds exhibit phase changes above 280 °C.

Table 4.7: Thermal analysis of inclusion compounds resulting from vapour sorption studies: **1d, 1d-MeOH, 1d-EtOH, 1d-Acetone, 1d-DMF and 1d-water**

	TG analysis			DSC analysis		
	% weight loss	*[a]network: guest ratio based on $Co(34pba)_2$:x*	*temperature range of weight loss (°C)*	*Solvent desorption endothermic peak (°C)*	*Phase transition temperature (°C)*	*melting point (°C)*
1d					284	407
1d-MeOH	10.3	1:1.6	RT - 90	61	283	406
1d-EtOH	9.9	1:1.1	RT - 175	144	271	not recorded
1d-acetone	8.5	1:0.7	RT - 235	184	283	406
1d-DMF	14.8	1:1.1	100 - 270	190	287	not recorded
1d-water	15.4	1:4.6	92 - 150	120	263	not recorded

[a] The experimental TGA results were used to calculate the network:solvent ratios. The results were modelled on $\{[Co(34pba)_2]\cdot x\ solvent\}_n$ and expressed as 1:x. RT: room temperature.

The PXRD traces of these inclusion compounds were recorded and are displayed in Figure 4.19. Indexing and fitting of the data were not possible owing to the poor quality of the data. The PXRD shows that the network undergoes some structural changes upon desolvation (**1d**) and solvent sorption. This demonstrates some degree of flexibility associated with the framework. None of the PXRDs are the same although the traces exhibit some similarities 'except for **1d-water**'.

Exposure of **1d** to DMF confirmed the resilience of the network as the resulting phase **1d-DMF** exhibits a PXRD trace and colour similar to that of **1**. A drastic colour change from purple to bright yellow is observed upon absorption of water by **1d**. The PXRD of **1d-water** is significantly different from the rest of the inclusion compounds. This suggests that absorption of water leads to significant structural distortion of the network accompanied by reduction in crystallinity. This may be because water molecules have a tendency of attacking open metal sites or disrupting the framework by hydrolysing the carboxylate moiety coordinated to the metal centre.[17] Furthermore, water is capable of forming strong hydrogen bonds with the framework which may cause molecular distortion of the network thus triggering the π-π^* and d-d transitions resulting in some colour changes.[18,19]

Since **1d-water** inclusion compound showed a PXRD that is not similar to the other inclusion compounds, the reversibility of **1d-water** to **1d** was tested by carrying out variable temperature PXRD studies which is shown in Figure 4.20. The PXRD shows that the compound collapses upon loss of water molecules around 120 °C. This suggests that the inclusion of water in the network results in an irreversible phase change accompanied with chromotropism.

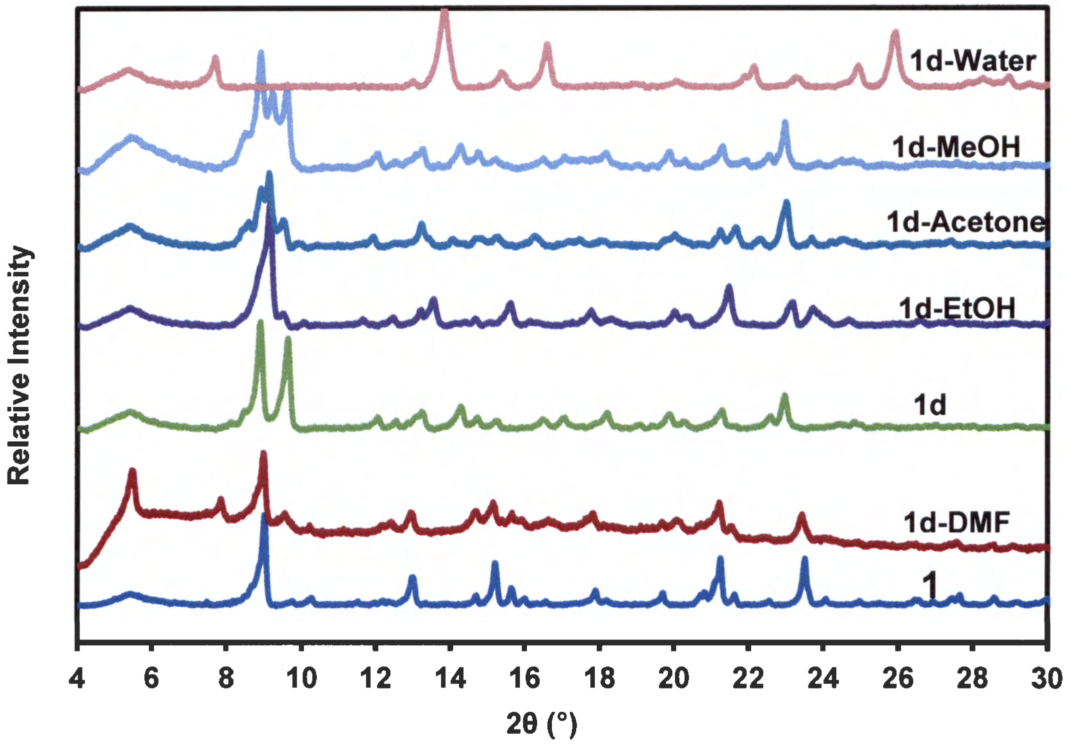

Figure 4.19: PXRD traces of **1**, **1d** and other solvated forms of **1d**

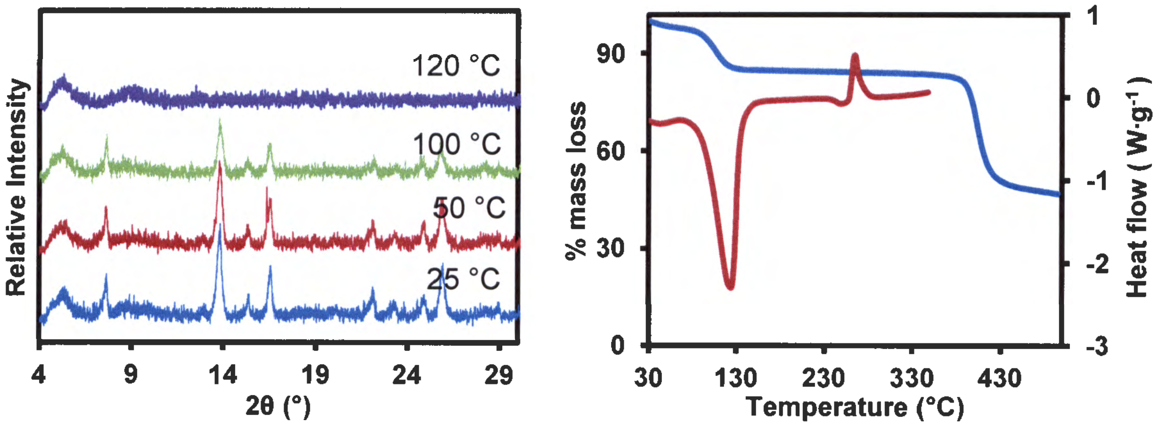

Figure 4.20: (a) Variable temperature PXRD of **1d-water**, (b) an overlay of TGA (blue) and DSC (red) of **1d-water**.The loss in crystallinity observed on the PXRD is associated with complete water loss as seen on the TGA.

To probe and understand the absorption behaviour of the solvents by the empty network **1d**, the geometry and volume of the cavities were modelled (Figure 4.21) in **1** after omission of the DMF molecules. Although the sorption studies of **2** were not carried out due to insufficient material, its cavities were also modelled. The cavities in **1** and **2** are not connected but are in close contact to each other which may allow passage of guest molecules through dynamic motion of the rings in the ligands.

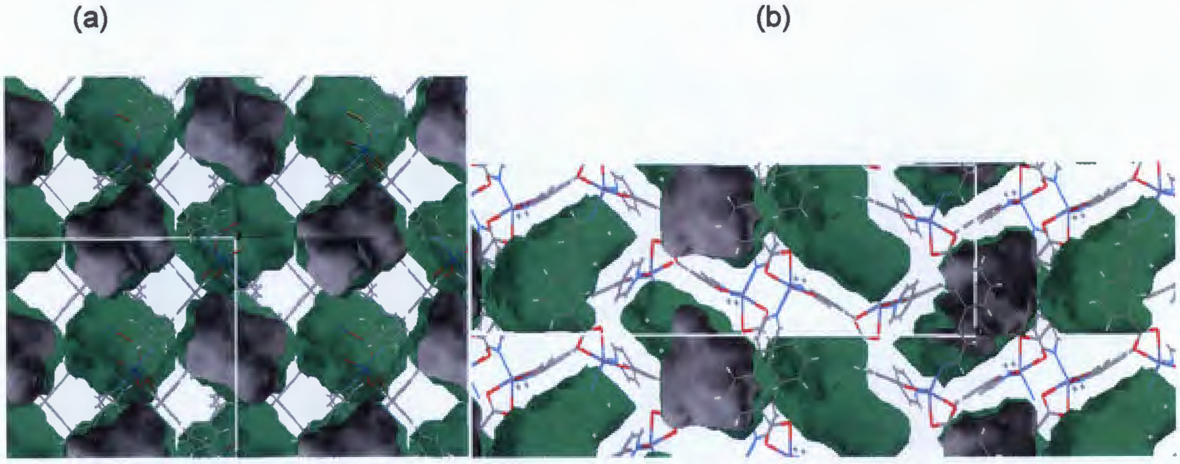

Figure 4.21: Cavities found in (a) **1** and (b) **2** in the absence of DMF, the outside surface and inside surface of the cavities are depicted in green and grey colours respectively

The maximum loading capacity (L_c) of the empty network (cavities in **1**) was estimated using the formula:

$$L_C = (\text{solvent accessible void volume}) / (Z \times \text{molecular volume}) \quad 4.1$$

The solvent accessible void volume of **1** was estimated using Mercury program with a probe radius of 1.2 Å and a grid step of 0.2 Å and was found to be 1387 Å^3. The molecular volumes (M_v) of the solvents were determined from their liquid density:

$$M_v = (\text{molecular weight})/(N_A \times \text{density}) \qquad 4.2$$

The experimental and theoretical solvent loading values are presented in Table 4.7.

Table 4.8: Loading parameters of the cavities in **1**

	% weight loss	network: guest ratio based on $Co(34pba)_2:x^a$	Boiling point of solvent	^bM_v ($Å^3$)	L_c $Co(34pba)_2:x$	% loading
1d-MeOH	10.3	1:1.6	65	67	1:2.6	62
1d-EtOH	9.9	1:1.1	78.4	97	1:1.8	61
1d-acetone	8.5	1:0.7	57	122	1:1.4	50
1d-DMF	14.8	1:1.1	153	128	1:1.4	79
1d-water	15.4	1:4.6	100	30	1:5.8	79

[a]The experimental TGA results were used to calculate the network:solvent ratios. The results were modelled on $\{[Co(34pba)_2]\cdot xsolvent\}_n$ and expressed as 1:x. [b]Solvent molecular volumes M_v were determined from their liquid density.

A plot of the molecular volume of the solvent M_v *vs* the number of moles of each solvent captured in the network reveals a third order polynomial function trend. An overlay of the expected and experimental values shows a similar trend, with the theoretical curve above the experimental curve (Figure 4.22). These curves illustrate that as the molecular volume increases, the network absorbs less solvent molecules. This suggests that big molecules may be excluded from entering the cavities of the host material or could just suggest that fewer large molecules fit into the cavity. Table 4.8 reveals that high percentage loading capacities (79%) are observed with solvents with high boiling points (DMF and water). For solvents with low boiling points such as acetone, methanol and ethanol, the loading of the cavities ranges from 50 to 62%. The results clearly indicate that for solvents with low boiling points, the amount of solvent absorbed is not close to the maximum loading capacity. This poor retention of the solvents in the cavities may be explained in terms of the equilibrium between the solvent in its gaseous phase and its enclathrated phase and we seem to observe that the equilibrium favours the gaseous phase. These results might be expected since the experiments were conducted at room temperature and atmospheric pressure. High loading values for low boiling solvents may be achieved by carrying out the experiment at high pressure and low temperature.

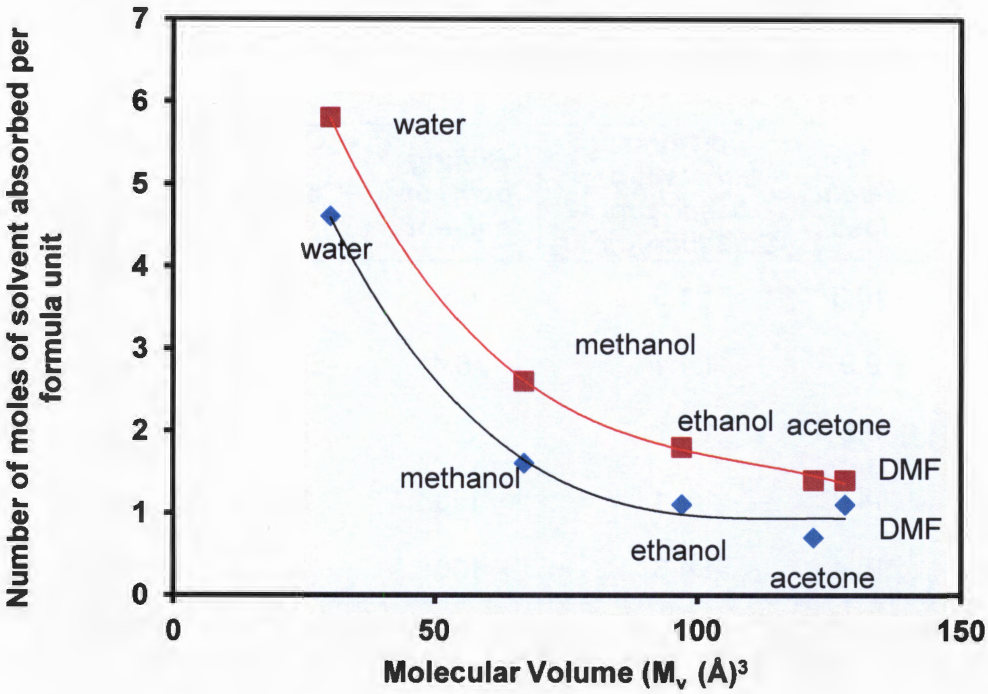

Figure 4.22: Plot of M_v versus the number of moles of each solvent absorbed per formula unit. The red curve represents the theoretical loading values while the black curve is the observed loading capacity for the guest molecules studied.

4.6 Non-isothermal kinetic studies of DMF desorption

The energy associated with the removal of DMF from the cavities of **1** and **2** was determined from non-isothermal kinetic studies which were performed using TGA. The disadvantage of this method is that one cannot identify the mechanism of desorption. A model free method based on the Ozawa, Flynn and Wall was used to determine the activation energy from the non-isothermal experiments as described in Chapter 2.10 of the experimental procedure.[20] The thermogravimetric traces for the desorption of DMF guest molecules are displayed in Figure 4.23. The data from the TGA analysis was run through the Universal speciality program[21] to obtain the percentage conversion level at a given temperature. The data are given in Table 4.9, and allow for the determination of activation energy by plotting log β against 1000/T(K^{-1}) as shown in Figure 4.24.

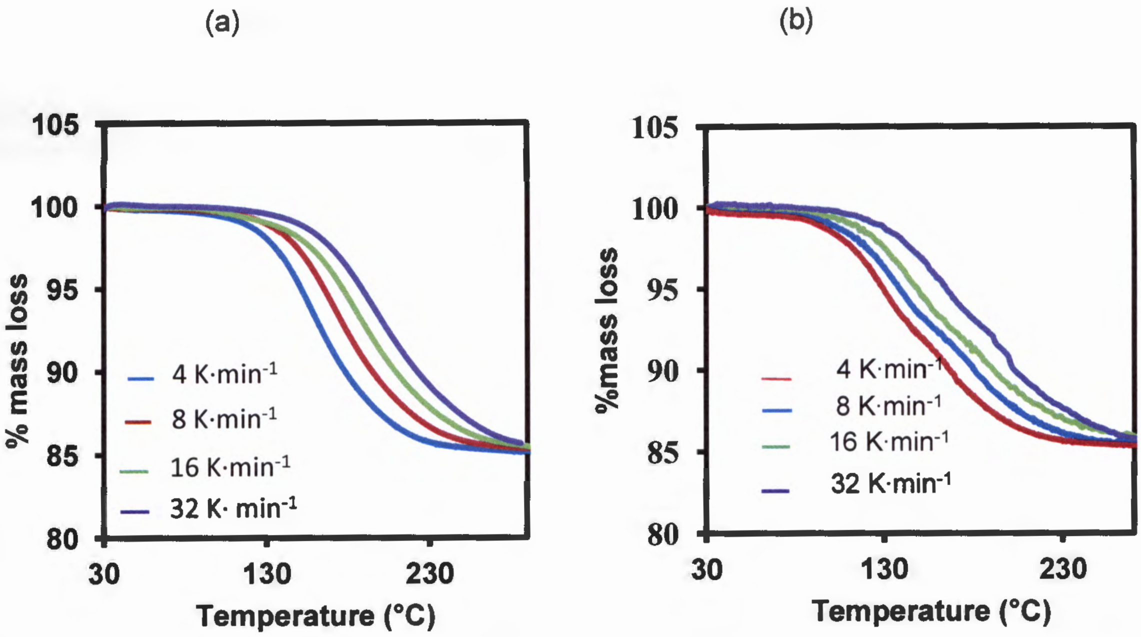

Figure 4.23: Thermogravimetric desorption kinetic profiles of a) **1** and b) **2** obtained from non-isothermal runs.

Table 4.9: The reciprocal temperature values obtained at the various conversion levels for each heating rate for compound **1** and **2**

				1000/T (K^{-1})			
	Heating rate (β) K·min^{-1}	***log β***	***20%***	***40%***	***60%***	***80%***	***95%***
1	4	0.602	2.425	2.331	2.251	2.145	2.004
	8	0.903	2.409	2.304	2.216	2.105	1.968
	16	1.204	2.298	2.200	2.117	2.014	1.89
	32	1.505	2.239	2.148	2.067	1.969	1.865
2	4	0.602	2.699	2.591	2.451	2.321	2.211
	8	0.903	2.566	2.455	2.311	2.221	2.103
	16	1.204	2.465	2.347	2.216	2.093	2.011
	32	1.505	2.367	2.259	2.146	2.047	1.932

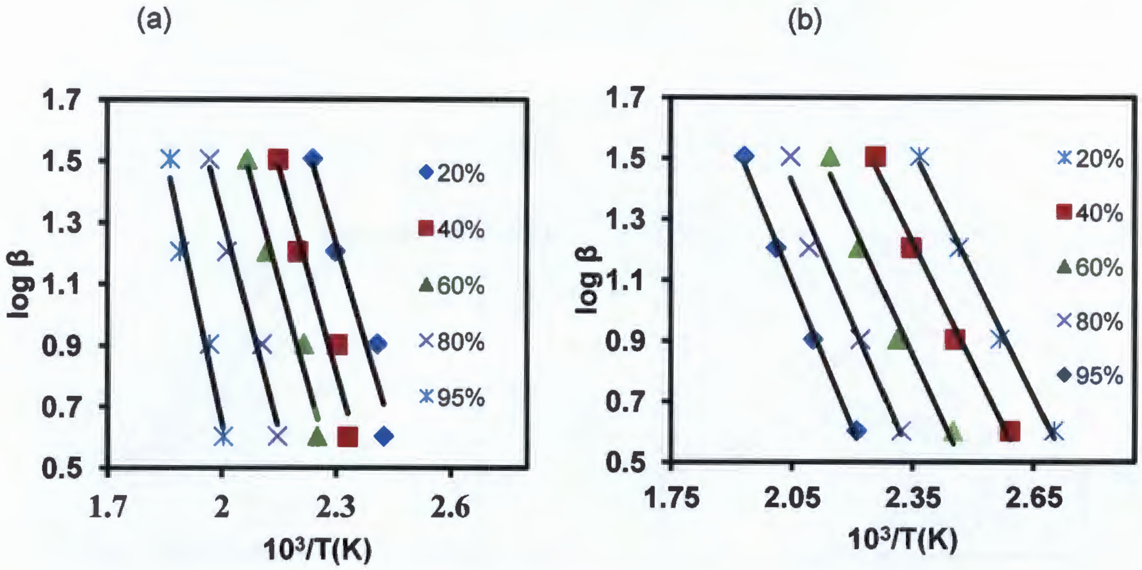

Figure 4.24: Plots of log β versus 1000/T for (a) **1** and (b) **2**

Figures 4.24 (a) and (b) display linear plots which are almost parallel. The activation energies were calculated by equating the gradient of the curves to $-0.457E_a/R$. The values obtained are recorded in Table 4.10. For **1**, the activation energy (E_a) obtained ranges from 76(6) to 106(6) kJ·mol^{-1} for 20 to 95% conversion level, while for **2** the E_a is within the range of 49(3) to 58(3) kJ·mol^{-1} for the same conversion level. The results clearly show that the activation energy increases concurrently with the conversion.

Table 4.10: Activation Energy (E_a) for different conversion levels

	Conversion level	***20%***	***40%***	***60%***	***80%***	***95%***
1	E_a (kJ mol^{-1})	76(6)	80(12)	81(10)	86(9)	106(16)
2	E_a (kJ mol^{-1})	49(3)	49(3)	52(6)	55(7)	58(3)

The activation energies obtained for **1** and **2** correspond to full desorption process of the guest. The fact that the energies obtained have relatively low percentage errors suggest that the desorption mechanism of DMF may be associated with a single process.

The energies for desolvation of DMF in **1** and **2** may be considered with respect to the following factors: (i) the environment of the guest in the host framework (cavities, open or constricted channels or layers), (ii) the nature of interactions between DMF and the framework (hydrogen bonding or other weak dispersion forces) and (iii) the amount of DMF in the network and its boiling point. The results obtained for **1** compare well with those documented in literature, where activation energies are reported over the range of 75 to 160 kJ·mol^{-1}.[22,23] The higher activation energies obtained for **1** in comparison to **2** concur with conclusions drawn from thermal analysis and the crystal packing of the compounds. In **1**, the DMF were described as confined in closed cages which suggest that high energy is required to open the cages through dynamic rotation of the rings of the ligand, while for **2** the DMF are sandwiched between the 2D layers which may easily glide past one another allowing for the easy release of the guest.

Solid state kinetics is a complex area of study associated with many assumptions and mathematical manipulations. If these studies are accompanied by visual techniques such as scanning electron microscopy perhaps one could obtain greater insight into the mechanisms of a certain kinetic process.

4.7 Summary

The two MOFs **1** and **2** exhibit the same composition of the framework, as well as of the guest residing in the cavities. **1** has a **bcu** topology with DMF guest molecules confined in cages, while **2** has an **sql** net with DMF molecules sandwiched between the interdigited the 2D layers. These compounds are assembled from different molecular building blocks generated *in situ*, and have been referred to as molecular building blocks structural isomers.

Optimisation of the reaction conditions lead to the isolation of **1** exclusively at 120 °C, while **2** was produced inclusively with an **unknown phase** at 75 °C. Hence, **1** has been referred to as the thermodynamic product while **2** is a kinetic one.

The change in crystal colour from purple to blue above 300 °C in both compounds was associated with a change in coordination environment of the metal centres. This was confirmed by IR studies. It was also observed that **1** undergoes a subtle change upon desolvation of DMF as revealed by PXRD studies. The activated phase $[Co(34pba)_2]_n$ (**1d**) absorbs methanol, ethanol, acetone and DMF while retaining its pink-purple colour. The solvatochromic behaviour of **1d** was observed upon uptake of water. The compound displayed a dramatic colour change from purple to a bright yellow colour accompanied with reduction in crystallinity.

The ability of **1** to change colour upon heating and on solvent absorption, demonstrates desirable characteristics that could be exploited for the production of sensing materials. The thermochromic and solvatochromic properties of **1** could have been understood well by indexing the PXRD patterns; unfortunately the quality of patterns was not suitable for the study. However, it can be concluded that the thermo-and solvatochromic behaviour is related to the structural changes the compound undergoes upon heating and absorbing the solvent molecules.

The average activation energy for **1** (86.6(9) $kJ \cdot mol^{-1}$) was found to be higher than that of **2** ((53(4) $kJ \cdot mol^{-1}$). These values correspond well with the structural features and thermal behaviours of compounds. There is perhaps a link between the sorption kinetics and the kinetic product/thermodynamic product. One could argue that the lower activation energy is also relevant for the formation of the compounds, unless the crystals are always formed around the solvent molecules. One notable feature is that the Co-L (L=ligand) bond lengths are shorter in **1** compared to **2**, especially the two shortest 2.02 Å *vs* 2.08 Å. This may suggest that bonding interactions in **1** are stronger than in **2** and thus there is greater thermodynamic stability for **1**.

4.8 References

1. H.-R. Wang and G.-T. Li, *Acta Crystallogr. Sect E, Struct. Rep online*, 2011, **67**, 1743.

2. C. Lee, C. Mellot-Draznieks, B. Slater, G. Wu, W. T. A Harrison, C. N. R. Rao, and A. K. Cheetham, *Chem. Commun*, 2006, 2687.

3. A. K. Cheetham, C. N. R. Rao, and R. K. Feller, *Chem. Commun*, 2006, 4780.

4. A. L. Spek, *Acta Crystallogr. Sect A*, 2009, **64**, 148.

5. O. Delgado-Friedrichs and M. O'Keeffe, *Acta Crystallogr. Sect A, Found.Crystallogr*, 2003, **59**, 351.

6. TOPOS 4.0, http://www.topos.ssu.samara.ru/, accessed May 2012.

7. S. Goswami, S. Sanda, and S. Konar, *CrystEngComm*, 2014, **16**, 369.

8. H. Chun and N. Jin, *Bull. Kor. Chem. Soc*, 2009, **30**, 1405.

9. Q.-G. Zhai, J.-P. Niu, S.-N. Li, Y.-C. Jiang, M.-C. Hu, and S. R. Batten, *CrystEngComm*, 2011, **13**, 4508.

10. K. He, Y. Li, Y. Chen, and Z. Chang, *Chin. Chem. lett*, 2013, **24**, 691.

11. Q.-R. Fang, G.-S. Zhu, Z. Jin, M. Xue, X. Wei, D.-J. Wang, and S.-L. Qiu, *Angew. Chem., Int. Ed*, 2006, **45**, 6126.

12. T.-T. Luo, H.-L. Tsai, S.-L. Yang, Y.-H. Liu, R. D. Yadav, C.-C. Su, C.-H. Ueng, L.-G. Lin, and K.-L. Lu, *Angew. Chem., Int. Ed.*, 2005, **117**, 6217.

13. R. J. Hill, D.-L. Long, P. Hubberstey, M. Schröder, and N. R. Champness, *J. Sol. St. Chem*, 2005, **178**, 2414.

14. D. Long, A. J. Blake, N. R. Champness, C. Wilson, and M. Schröder, *Angew. Chem., Int. Ed,* 2001,**113**, 2509

15. L. G. Beauvais, M. P. Shores, and J. R. Long, *J. Am. Chem. Soc*, 2000, **122**, 2763.

16. K. Nakamoto, In *Infrared and Raman Spectra of Inorganic and Coordination Compounds, Applications in Coordination, Organometallic, and Bioinorganic Chemistry*; Hoboken, NJ, USA: Wiley, 2009; 64-66.

17. L. Xie and M. Paik, *J. Eur. Chem*, 2011, **17**, 13653.

18. Z. Lu, R. Zhang, Y. Li, Z. Guo, and H. Zheng, *J. Am. Chem. Soc*, 2011,**133**, 4172.

19. Y. Gong, Y. Zhou, J. Li, R. Cao, J. Qin, and J. Li, *Dalton Trans*, 2010, **39**, 9923.

20. T. Ozawa, *Bull. Chem. Soc. Jpn,* 1965, **38**, 1881.

21. H. J. Borchardt and F. J. Daniels, *J. Am. Chem. Soc*, 1957, **79**, 41.

22. A. Jacobs, N. L. Z. Masuku, L. R. Nassimbeni, and J. H. Taljaard, *CrystEngComm*, 2008, **10**, 322.

23. S. A. Bourne, K. L. G. Nash, and F. Toda, *J. Mol. Struct.* 1999, **474,** 223.

Chapter 5

3-(4-pyridyl)benzoate compounds of Zn(II)

In Chapter 4, the properties of cobalt(II) compounds based on 3-(4-pyridyl)benzoate (**1** and **2:** $\{[Co(34pba)_2]\cdot DMF\}_n$) were described. Chapter 5 deals with 2D MOFs assembled from the 3-(4-pyridyl)benzoate linker and Zn(II) ions. Compounds **3** and **4** both have the empirical formula $\{[Zn(34pba)_2]\cdot DMF\}_n$ but have different structures and topologies. Compound **4** is an analogue of compound **2** described in Chapter 4. The breathing behaviour of this compound upon uptake of linear chain alcohols is presented. The factors responsible for the dynamic motion of the 2D network in **4** are evaluated.

The reaction of 3-(4pyridyl)benzoic acid with zinc nitrate hexahydrate at room temperature or at elevated temperatures afforded two new compounds **3** and **4**: both have structural formula $\{[Zn(34pba)]_2 \cdot DMF\}_n$. Compound **3** is very similar to the reported structure by Niu *et al* but differs in the guest type and β angle.[1] Compound **3** was formed as a colourless material with DMF molecules in the channels while the one reported by Niu *et al* ($\{[Zn(34pba)]_2 \cdot 1.5H_2O\}_n$) is yellow and includes water as guest molecules in the cavities. The PXRD patterns of **3** and **4** simulated from their single crystal data is given in Figure 5.1.

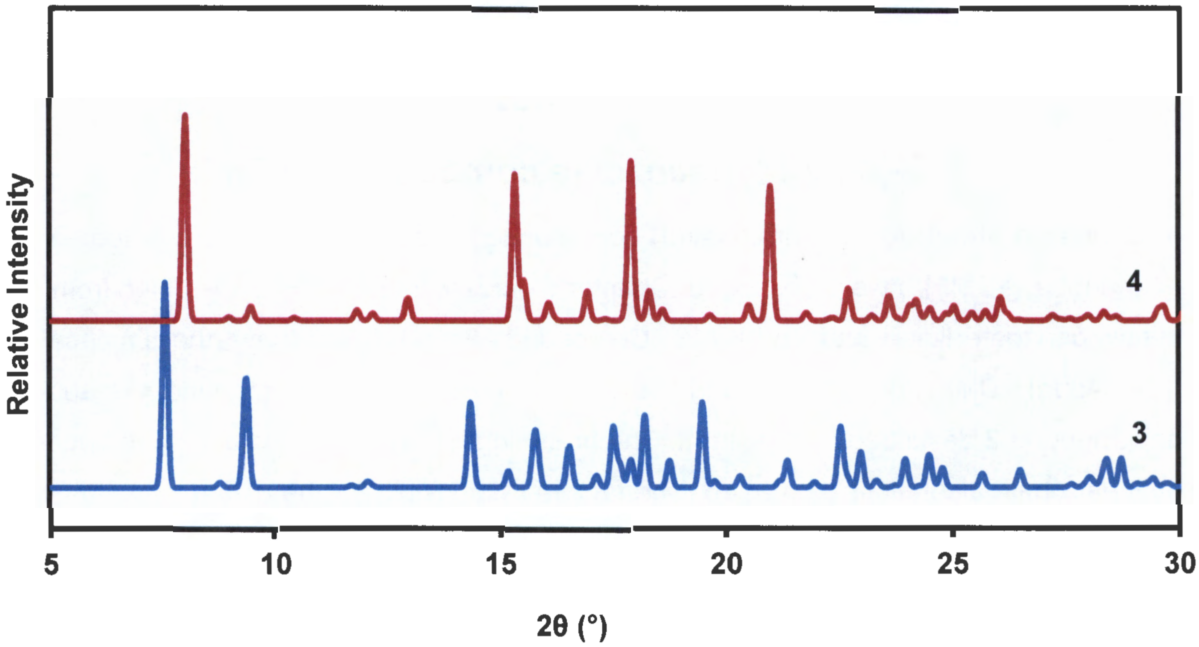

Figure 5.1: PXRD of **3** and **4** calculated from single crystal data

5.1 Synthesis of compounds 3 and 4: $\{[Zn(34pba)]_2 \cdot DMF\}_n$

Table 5.1 gives the experimental conditions that lead to the isolation of **3** and **4**. In experiment ***a***, $Zn(NO_3)_2.6H_2O$ (290 mg, 1 mmol) was dissolved in 4 cm^3 of DMF and 80 mg (0.4 mmol) of 3-(4-pyridyl)benzoic acid was dissolved in 4 cm^3 of DMF. The two solutions were combined in a large vial. The solution was left to evaporate at room temperature. Colourless crystals were formed after two weeks. Two crystal forms were identified based on their shapes (Figure 5.2). The first reaction batch (experiment ***a***) produced compound **3** as the predominant phase which was confirmed by PXRD studies, shown in figure 5.3. Repeating the experiment (experiment ***b***) under the same conditions produced compound **4** as the predominant phase. Altering the reactions conditions to enhance the chances of producing compound **3** did not yield any results. In all experiments the total volume of the solvent used was 8 cm^3 of DMF. Compound **4d**,

$\{Zn(34pba)_2\}_n$ was obtained by removing DMF molecules in **4** at 200 °C for 24 hours under vacuum. Compound **4d-propanol** and **4d-butanol** were obtained as described in Section 2.8

Table 5.1: Experimental Parameters for the preparation of **3** and **4**

Experiment ID	***Metal to ligand ratio***	***Temperature***	***Products***
a	5: 2	room temp	**3** and **4** (**3** major product)
b	5 : 2	room temp	**3** and **4** (**4** major product)
c	5 : 2	80 °C	**4**

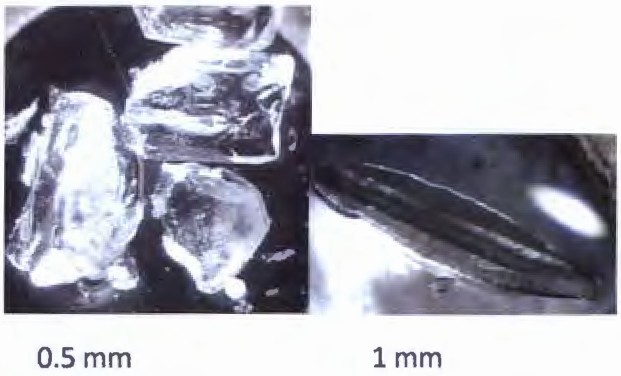

Figure 5.2: Left: crystals of **3**; right: a single crystal of **4**

In Figure 5.3, the PXRD trace of experiment ***a*** shows that compound **3** was the predominant phase as it matches well with the calculated pattern from its single crystal structure. The slight offset observed in the 2θ positions of the peaks is ascribed to the different temperatures at which the experiments were conducted. Single crystal data collection was performed at -100 °C while the PXRD pattern were collected at room temperature. The experimental PXRD of ***a*** was collected using the Huber Diffractometer while ***b*** and ***c*** were collected using the D8 Advance Bruker machine. Repeating the first experiment, experiment ***b***, gave rise to the formation of compound **4** as the predominant phase. The PXRD of this trace shows diffraction peaks from both compound **3** and **4**.

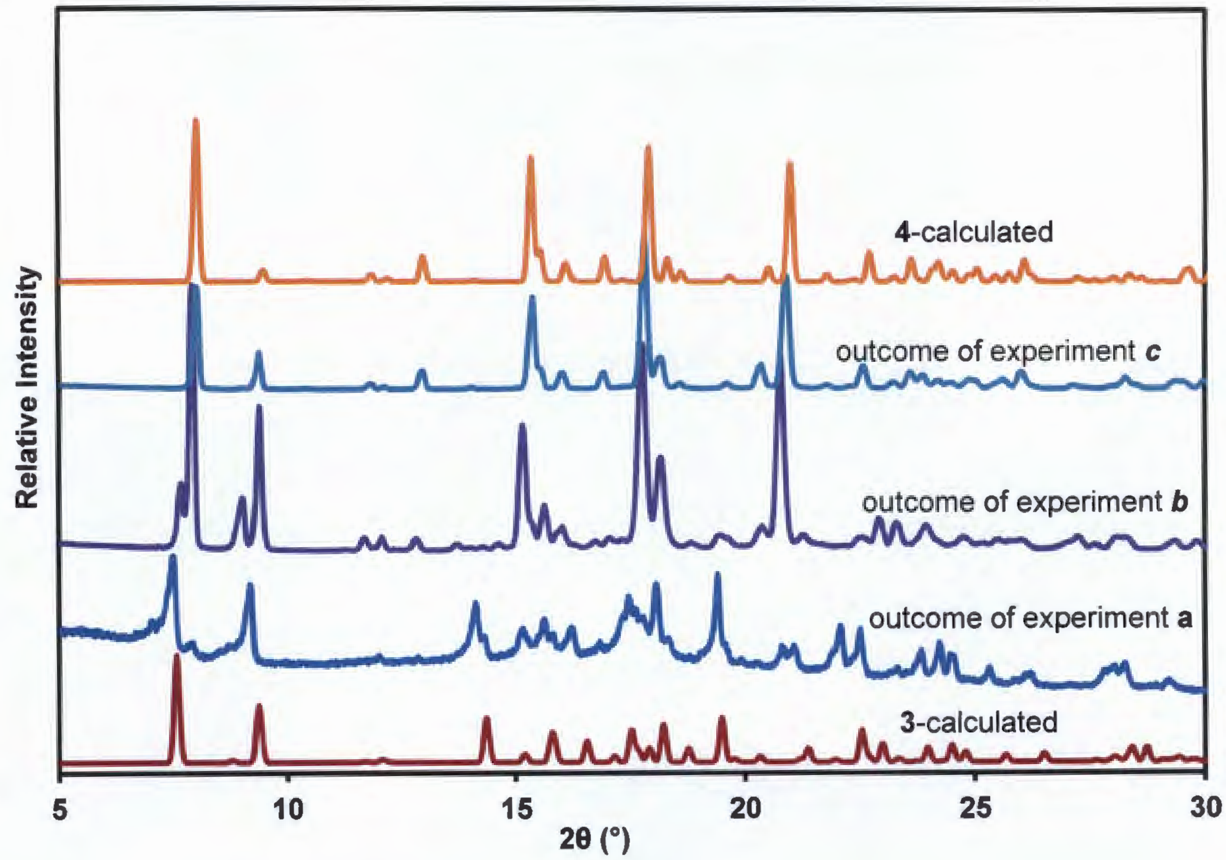

Figure 5.3: PXRD patterns of experiment ***a***, ***b***, and ***c***.

Quantitative Rietveld refinement was carried out on the PXRD outcome of experiment ***b*** (Details for this refinement have been described in Chapter 2). Results obtained shows that 13% of the mixture was compound **3**, while the remaining phase compound **4** was 87%. The result for this analysis is given in Figure S5.1 and the output file is found in the appendix as a text file. Rietveld refinement was not performed on the PXRD outcome of experiment ***a*** because of the poor quality of the pattern. In experiment ***c***, the reaction was carried out in an oven. A comparison of the calculated pattern and the experimental pattern of **4** suggests that the compound was formed exclusively as the two patterns matches very well. The product of this reaction was formed within two days at 80 °C while in experiment ***a*** and ***b*** the crystals were formed after two weeks. Hence, experiment ***c*** was used for the preparation of **4** for further studies. It is worth mentioning that the method ***c*** that produced **4** could not produce its cobalt analogue compound **2** described in Chapter 4

5.2 {[Zn(34pba)$_2$]·DMF}$_n$ (3)

5.2.1 Single crystal X-ray diffraction

Chapter 2 section 2.7.1 describes the structure solution and refinement procedures for all non-hydrogen atoms. The hydrogen atoms were placed in calculated positions in a riding model. All hydrogen atoms were refined isotropically. Temperature factors of 1.2 times and 1.5 times the parent atoms's were assigned for hydrogen atoms on phenyl and pyridyl rings and for methyl groups respectively. The crystallographic parameters and refinement parameters of **3** are given in Table 5.2. For the sake of comparison, the lattice parameters for the compound **3** and Niu's structure[1] are given in Table 5.2.

Table 5.2: Crystallographic and refinement parameters for compound **3**

	3	***Reported***[1]
Empirical Formula	{[Zn(34pba)$_2$]·DMF}$_n$	{[Zn(34pba)$_2$]·1.5H$_2$O}$_n$
M$_r$ (g·mol^{-1})	534.85	
Temperature (K)	173(2)	173(2)
Crystal size (mm^3)	0.2 x 0.25 x 0.33	
Crystal system	monoclinic	monoclinic
Space group	P2$_1$/c	*P*2$_1$/*c*
a / (Å)	11.652(2)	11.623(3)
b / (Å)	19.788(4)	19.684(5)
c / (Å)	10.715(2)	10.774(2)
β/°	90.3	93.452(4)
V/ (Å^3)	2470.7(8)	2460.48
Z	4	
Calc density/ (g·cm^{-3})	1.438	
F(000)	1104	
θ range scanned (°)	1.75-27.49	
h, k, l range	-15:15; -25:25; -13:13	
Reflections collected	9894	
No. unique data	5504	
No. data with *I* >2σ (*I*)	2952	
final *R* (*I* > 2σ (*I*))	0.0684	
final *wR2* (all data)	0.1953	
Goodness of fit, s	1.075	
Max, min e density(eA^{-3})	-0.59, 1.00	

5.2.2 Structural description of 3

Compound **3** is very similar to the reported structure by Niu *et al* but differs in the guest type and β angle.[1] This compound crystallises in a monoclinic crystal system within the space group *P*2$_1$/*c*. The asymmetric unit comprises of one zinc centre, two deprotonated 34pba ligands and one uncoordinated DMF molecule. The carboxylate moiety assumes the monodentate binding mode. The Zn(II) centre is coordinated to two nitrogen atoms of the pyridyl ring and two carboxylate oxygen atoms to furnish a distorted tetrahedral geometry as displayed in Figure 5.4.

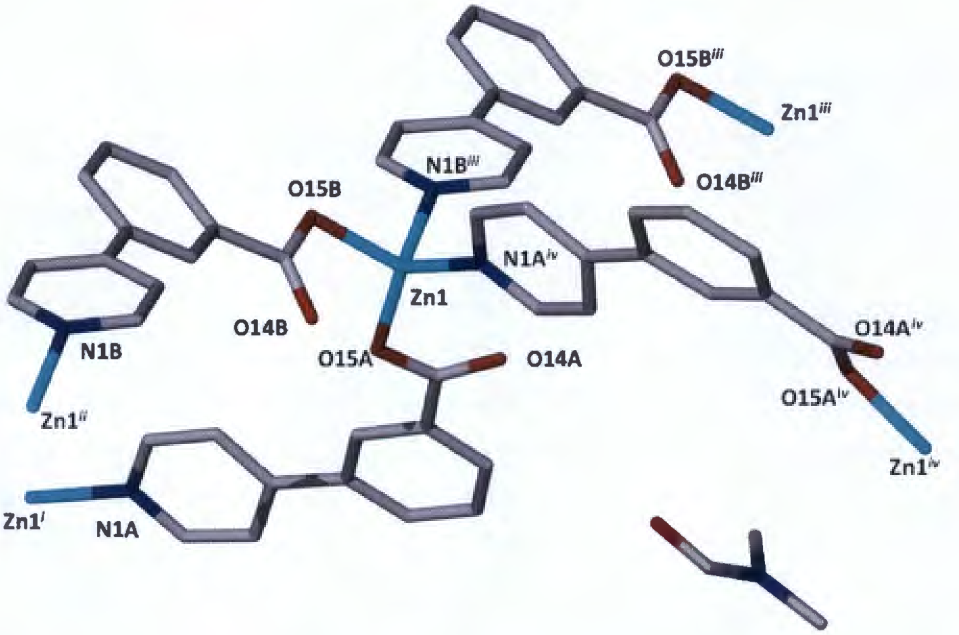

Figure 5.4: Coordination environment of Zn(II). The metal centre is bonded to two nitrogen atoms of the pyridyl moiety and two oxygen atoms of the carboxylate moiety. Symmetry Related: ^{i}-x, y-1/2, ½-z; ^{ii}*x+1, y, z;* ^{iii}*x-1, y, z;* ^{iv}*-x, ½+y, ½-z.*

Four 34pba ligands bridge four zinc centres to form a grid net. Ligand A separates two zinc centres by 9.146 Å and ligand B seperates two metal centres by 11.652 Å. The difference in the distance of separation is attributed to the coordination modes assumed by the ligands. Ligand A links two metal centres *via* the near oxygen atom of the carboxylate group to the pyridyl nitrogen atom and B *via* the far oxygen atom. The Zn-O bond distances are 1.972 Å and 1.942(3) Å while the Zn–N bond distances are 2.024(4) Å and 2.067(4) Å. A comparison of the bond length of **3** and the previously reported structure are given in Table 5.3

Table 5.3: Bond length parameters of compound **3** and Niu's reported structure

Compound 3* *Bond type	***Bond length***	***Reported compound* *Bond type***	***Bond length***
Zn1 - N1A	2.024(4)	Zn - N	2.011(4)
Zn1 - N1B	2.067(4)	Zn - N	2.059(5)
Zn1 - O15A	1.942(3)	Zn - O	1.949(4)
Zn1 - O15B	1.972(3)	Zn - O	1.955(4)

The dihedral angles between the pyridyl and the phenyl ring are 13.8° and 30.7° for the two ligands modelled in the asymmetric unit. The monodentate carboxylate moiety is almost coplanar with the phenyl ring. The structure is stabilised by weak hydrogen bonds between the 2D layers (Table 5.4) and $\pi\cdots\pi$ interactions of the aromatic rings. A distance of 3.728 Å between the DMF molecules and the framework rings suggest the presence of C-H$\cdots\pi$ interactions.

Table 5.4: Hydrogen bond distances and angles of **3**

Donor - H...Acceptor	***H...A (Å)***	***D...A(Å)***	***D - H...A(°)***
C6A - H6A ...O15A	2.33	3.059(3)	133
C6B - H6B ...O14A	2.44	3.334(4)	157
C12A- H12A...O15B	2.48	3.319(4)	147

The packing diagram of **3** depicts 2D interdigited layers with guest molecules residing in the channels. Interestingly the overall structure is three dimensional with channels running along the *c*-axis. The high dimensionality from 2D to 3D arises as a result of the type of interdigitation. A single 2D network interdigitates two adjacent 2D layers; one below and one above as shown in Figure 5.5.a. This type of entanglement is unprecedented for 2D networks to the best of our knowledge. In reported cases, high dimensionality is observed as result of parallel or inclined interpenetration of 2D networks with (square lattice) **sql** topology.[2,3]

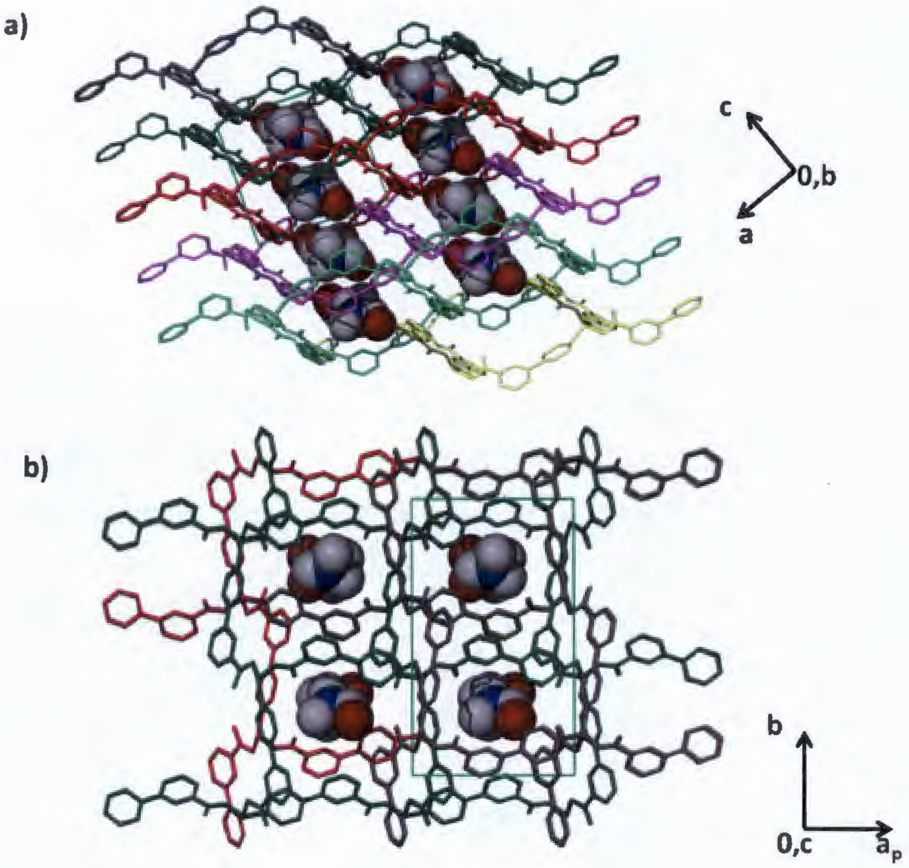

Figure 5.5: a) Packing diagram of compound **3** displaying interdigited 2D layers depicted in different colours. b) Channels found in **3**. The DMF molecules which occupy these channels are drawn in van der Waals radii.

The estimated solvent accessible void volume in the solvent free network was found to be 26.3% of the unit cell volume. This volume is occupied by the DMF molecules. Analysis of the cavities occupied by the DMF molecules using the Mercury program[4] shows that they are interconnected as illustrated in Figure 5.6.

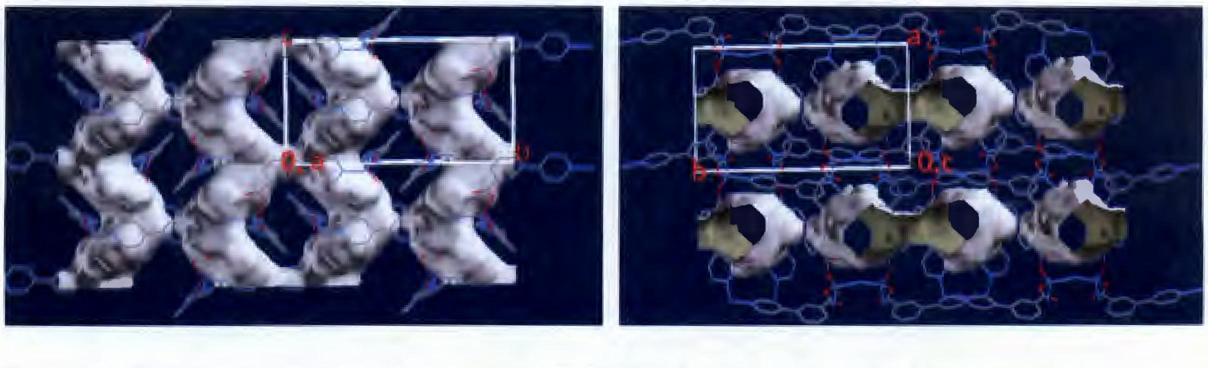

Figure 5.6: Right, view of the channels occupied by DMF viewed along the *a*-axis, Left: view along the *c*-axis

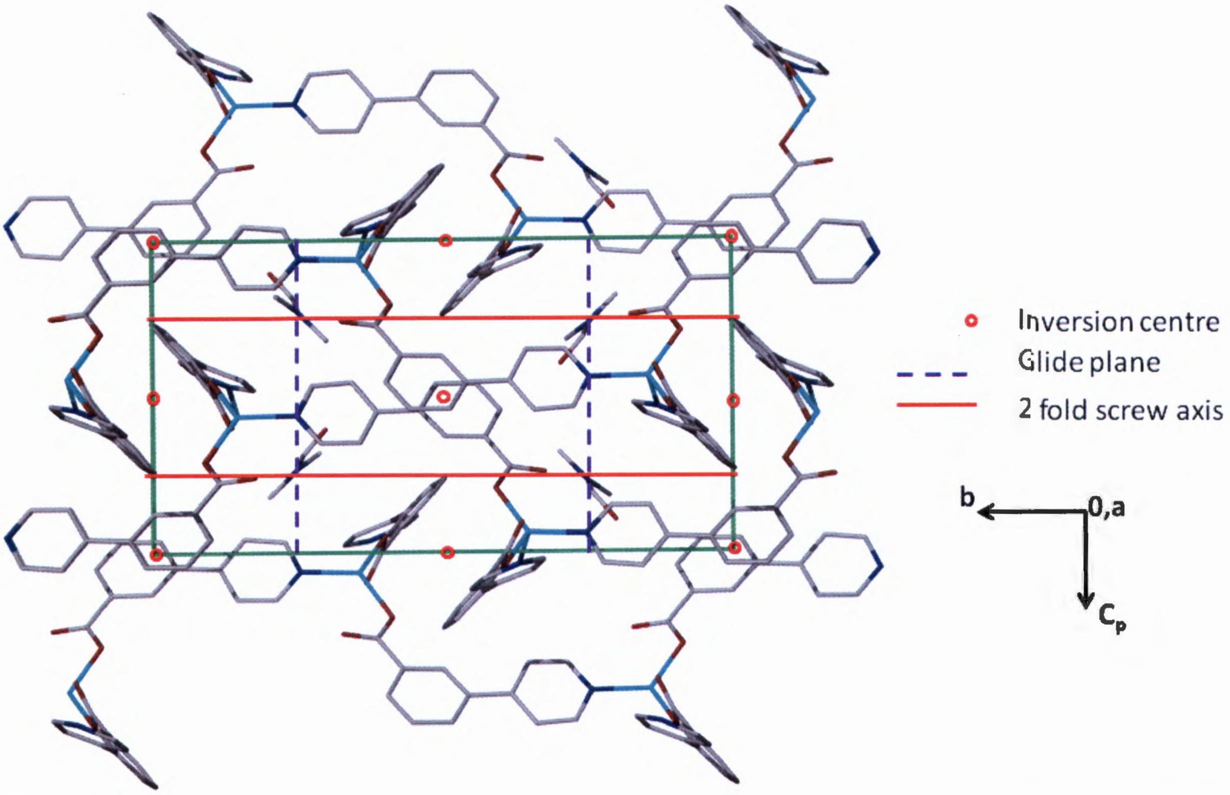

Figure 5.7: The packing of **3** viewed along [1 0 0] shown in stick form. The inversion centres are shown as red circles, the glide plane and the direction of the 2-fold screw axis are depicted as broken purple and solid red lines respectively.

Figure 5.7 depicts the symmetry elements present in **3** when viewed along the [1 0 0] axis. The red circles represent the inversion centres. These are located between the phenyl rings of adjacent 2D layers. There also exists glide planes which are perpendicular to [0 1 0] with a glide component of 0 0 ½. The 2-fold screw axis run along the [0 1 0] direction and is located at (0 y ¼) with a screw component of 0 ½ 0. The other 2-fold screw axes are related by a symmetry of -x, ½+y, ½-z.

To simplify the structure, compound **3** can be viewed as a 4-connected **sql** grid net (Figure 5.8). Unlike the usual square grids assembled from linear bridging ligands and metal centres under the square planar coordination geometry, a zig-zag 2D single layered network parallel to the *ab* crystallographic plane is obtained. Topological representation of the network shows that the metal centres on adjacent sheets are off-setted.

Further studies on this compound were not possible owing to the difficulty in reproducing the material.

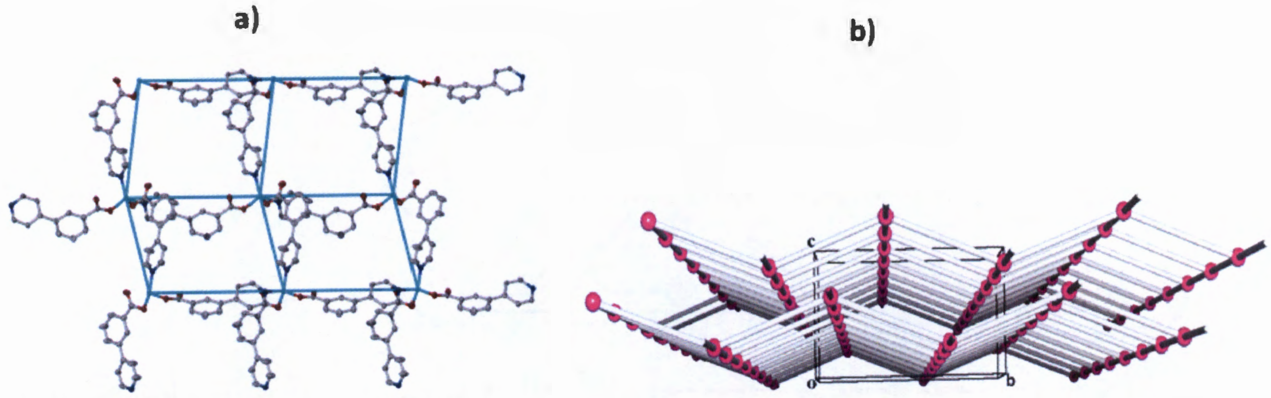

Figure 5.8: Network connectivity of **3**, b) Topological representation of compound **3**, adjacent 2D layers pack in a zig-zag fashion. The picture also illustrates that the metal centres of adjacent sheets are off-setted.

5.3 Structures of {[Zn(34pba)$_2$]·DMF}$_n$ (4), [Zn(34pba)$_2$]$_n$ (4d), {[Zn(34pba)$_2$]·0.4C$_3$H$_8$O}$_n$ (4d-propanol) and {[Zn(34pba)$_2$]·C$_4$H$_{10}$O}$_n$ (4d-butanol)

5.3.1 Single crystal X-ray diffraction

Non-hydrogen atoms were located and refined as outlined in section 2.7.1 of Chapter 2. The phenyl and pyridyl hydrogen atoms were placed in idealised positions and were all refined isotropically. These were assigned temperature factors of 1.2 times the parent carbon atoms. The hydrogen atoms of the guest DMF molecules were also refined isotropically with temperature factors of 1.5 times the methyl carbon atoms. Due to the disorder of the guest propanol molecule in **4d-propanol,** the hydrogen atoms were assigned to their parent atoms. The guest *n*-butanol in **4d-butanol** could not be located due to the poor quality of the diffraction data, the structure could not be refined to acceptable levels. The crystallographic data for compound **4** and its inclusion compounds are given in Table 5.5.

Table 5.5: Crystallographic and refinement parameters for compound **4** and its related structures.

Compound	***4***	***4d***	***4d-propanol***	***4d-butanol***
Emperical Formula	$\{[Zn(34pba)_2]\cdot(DMF)\}_n$	$[Zn(34pba)_2]_n$	$\{[Zn(34pba)_2]\cdot 0.4(C_3H_8O)\}_n$	$(C_{24}H_{16}N_2O_4Zn).(C_4H_{10}O)$
Molecular Mass	534.85	461.78	503.85	539.91
Crystal Size (mm)^3	0.21 x 0.22 x 0.25	0.23 x 0.28 x 0.26	0.13 x 0.16 x 0.20	0.06 x 0.25 x 0.25
Temp. Of collection / K	173(2)	173(2)	173(2)	173(2)
Crystal symmetry	Tetragonal	Tetragonal	Tetragonal	Tetragonal
Space group	$P4_32_12$	$P4_32_12$	$P4_32_12$	$P4_32_12$
a / Å	11.5361(3)	11.5806(3)	11.6638(4)	11.7281(13)
c / Å	37.3168(19)	34.904(2)	36.790(3)	36.977(4)
Z	8	8	8	8
Volume Å^3	4966.2(3)	4681.0(3)	5005.0(5)	5086.2(17)
Dc / g cm^{-3}	1.431	1.310	1.385	1.400
F(000)	2208	1888	2160	
2θ (°) range	1.85 - 27.89	1.85 - 28.39	1.83 - 27.10	2.06 - 26.53
Index range	-15:13, -14:15, -49: 49	-14:15, -13:15, -46:46	-14:14, -14:13, -47:46	
No. of reflections collected	24798	43511	28248	32238
No. Unique reflections	5934	5871	5524	5164
No. Reflections with I> 2σI	5045	5200	4271	
Data/ parameters refined	5934/329	5871/274	5524/297	
Goodness of fit, S	1.059	1.053	1.043	
R (I> 2σI)	0.0429	0.0404	0.0917	

5.4 Structural description

Compound **4** **{[Zn(34pba)$_2$]·DMF}$_n$** is an analogue of compound **2** **{[Co(34pba)$_2$]·DMF}$_n$** described in Chapter 4, hence its full structural description will not be given in this chapter. However a description of the changes that occurs when **4** undergoes desolvation of DMF to give **4d**, and the structures of the inclusion compounds of **4d** will be described. This compound crystallises in a tetragonal crystal system and chiral space group $P4_32_12$. In the asymmetric unit of compound **4,** two 34pba ligands coordinating to one zinc (II) ion, and one uncoordinated DMF molecule were modelled. The two ligands A and B in the asymmetric unit assume bidentate μ_2-bridging coordination mode. In ligand A, the pyridyl moiety is disordered over two positions with equal site occupancies. The oxygen atoms of the DMF are also disordered over two positions and were refined with equal site occupancies. Because the two ligands A and B adopt the same coordination mode, the distance of separation between any two bridged Zn(II) centres by the linkers is the same (11.536 Å) .The mononuclear zinc(II) ion atom is coordinated to four oxygen atoms of the carboxylate moieties and two nitrogen atoms of the pyridyl rings to give a distorted octahedral geometry (Figure 5.9). The Zn - donor atom ranges from 2.026 to 2.388 Å. These bond lengths and those of the subsequent compounds are given in Table 5.6

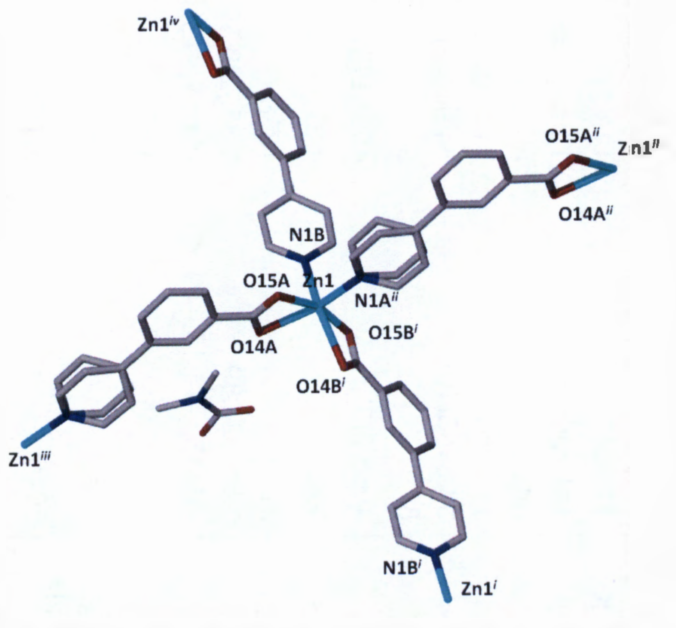

Figure 5.9: (a) Coordination environment around the metal centre in **4**, the labels show the atoms that are coordinated to the zinc centre. The pyridyl part of ligand A is disordered over two positions. The octahedral geometry observed in **4** is retained on desolvation of the DMF guest molecules to give **4d.** Hydrogen atoms have been omitted for clarity. Symmetry operators ^{i}*x, y-1, z;* ^{ii}x-1, y, z; ^{iii}1+x, y, z; ^{iv}x, 1+y, z

Table 5.6: Bond lengths of compounds **4**, **4d** and **4d-propanol**

Compound	***Bond type***	***Bond length***	***Symmetry Operator***
4	Zn1 - O14A	2.268(2)	
	Zn1 - O14B	2.388(2)	*x, y, 1-z*
	Zn1 - O15A	2.081(2)	
	Zn1 - O15B	2.026(2)	*x, y, 1-z*
	Zn1 - N1B	2.114(2)	
	Zn1 - N1A	2.095(2)	*x-1, y, z*
4d	Zn1 - O14A	2.367(2)	
	Zn1 - O14B	2.389(2)	
	Zn1 - O15A	2.031(2)	
	Zn1 - O15B	2.014(2)	
	Zn1 - N1B	2.076(2)	*x, y-1, z*
	Zn1 - N1A	2.090(2)	*1+x, y, z*
4d-propanol	Zn1 - O14A	1.990(8)	
	Zn1 - O14B	1.948(7)	
	Zn1 - O15A	2.459(9)	
	Zn1 - N1A	2.09(1)	*x-1, y, z*
	Zn1 - N1B	2.070(9)	*1+y, z*

The packing diagram of **4** depicts interdigited 2D layers in which DMF molecules are sandwiched (Figure 5.10). The 34pba ligands link Zn(II) centre to form a 2D square grid network. Hydrogen bonding analysis shows that adjacent 2D layers are connected by weak intermolecular C-H···O hydrogen bonds (Table 5.7).

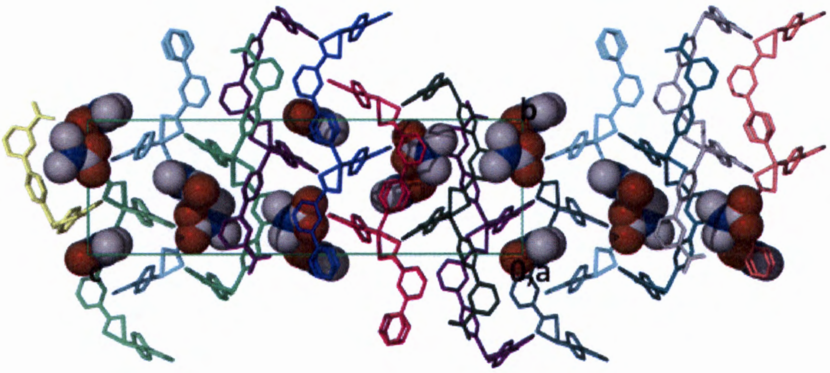

Figure 5.10: Solid state packing diagram of 4 viewed along the *a* -axis, the 2D layers are displayed in different colours and these interdigitate with one another encapsulating the guest DMF molecules drawn in van der Waals radii.

Table 5.7: Hydrogen bonding interactions parameters in **4**

Donor -H...Acceptor	*H...A(Å)*	*D...A(Å)*	*D - H...A(°)*	*Symmetry operator*
C6A - H6A...O15A	2.43	3.193(3)	114	*1+x, y, z*
C6A - H6A...O15A	2.33	3.266(8)	126	*x, 1+y, -z*
C6B - H6B...O14A	2.40	3.219(4)	144	*x-1/2, 1/2-y, ¼-z*
C8B - H8B...O1C2	2.54	3.326(11)	140	*x-1/2, ½-y, ¼-z*
C8B - H8B...O1C1	2.54	3.490(11)	173	*x-1/2, ½-y, ¼-z*

The guest DMF molecules also interact with the framework through weak intermolecular hydrogen bonds (Table 5.7). There are also a number of C-H···π interactions which stabilises the structure.

Upon evacuation of DMF from **4**, the compound undergoes desolvation to give the empty network $[Zn(34pba)_2]_n$, (**4d**). Single crystal x-ray diffraction analysis shows that compound **4** undergoes anisotropic compression upon the loss of DMF. This is evidenced by the slight increase in the lattice parameters along *a*- and *b*- directions and a decrease by 2.4 Å along the *c*-axis. The overall effect is a decrease in the unit cell volume by 5.74%. During this process, the geometry around the Zn(II) ion seen in Figure 5.11 is preserved and there is little change in the Zn-O and Zn-N bond lengths (Table 5.6).

Figure 5.11: The transformation from **4** to **4d** upon guest loss: the major difference is that the disorder observed in **4** on one of the pyridyl rings shown in green is absent in **4d**. During this process of desolvation of DMF, the geometry around the Zn(II) is maintained.

One notable feature of **4d** is that the disorder seen in one of the pyridyl ring in **4** and its cobalt analogue compound **2** presented in Chapter 3 is absent. The torsion angles between the pyridyl and phenyl rings provide evidence of some dynamic motion of the ligand during the desolvation process. Compound **4d** exhibits high torsion angles between the mean planes through the pyridyl and phenyl rings in comparison to **4**. These are 40.15° and 7.29° for **4**, while in **4d**, these angles are 49.00° and 44.30°. The increase in these torsion angles serve to reduce steric effects of the rings upon channel closing as the 2D networks glide towards one another. As observed in **4**, **4d** is also stabilised by weak hydrogen bonding interactions between interdigited 2D layers (Table 5.8).

A significant change is observed in the solvent accessible void volume. Compound **4** has a void space of 24.8% of the unit cell volume in the absence of guest DMF molecules. A 37% decrease in solvent accessible void volume is observed during the desolvation process. This is because **4d** has a potential solvent accessible volume of 15.4% as estimated in PLATON.[5]

Table 5.8: Hydrogen bonding parameters for compound **4d**

Donor - H...Acceptor	*H...A*	*D...A*	*D - H...A*	*Symmetry operator*
C6A - H6A...O15A	2.33	3.062(3)	133	y-1, x, -z
C6A - H6A...O15A	2.92	3.343(3)	109	x-1, y, z
C6B - H6B...O14A	2.44	3.335(4)	157	½+x, 5/2-y, ¼-z
C12A - H12A...O15B	2.48	3.318(4)	147	x-1/2, 3/2-y, ¼-z

The network of $[Zn(34pba)_2]_n$ (**4d**) absorbs *n*-propanol to give $\{[Zn(34pba)2]\cdot 0.4C_3H_8O\}_{n}$, **4d-propanol**. This process appears to be a single crystal to single crystal owing to the insolubility of the framework material. The asymmetric unit of this structure comprises of two deprotonated 34pba ligands exhibiting two different coordination modes of the carboxylate moiety, one zinc(II) centre and a propanol molecule with a modelled site occupancy of 40%. The carboxylate group in ligand A is bound to the zinc(II) centre in chelating fashion while ligand B binds in a monodentate fashion as opposed to the chelating mode observed in **4** and **4d**. Thus, the zinc (II) is bonded to three oxygen atoms and two nitrogen atoms of the pyridyl moiety. This gives rise to a trigonal bipyramidal coordination environment around the metal centre as shown in Figure 5.12.

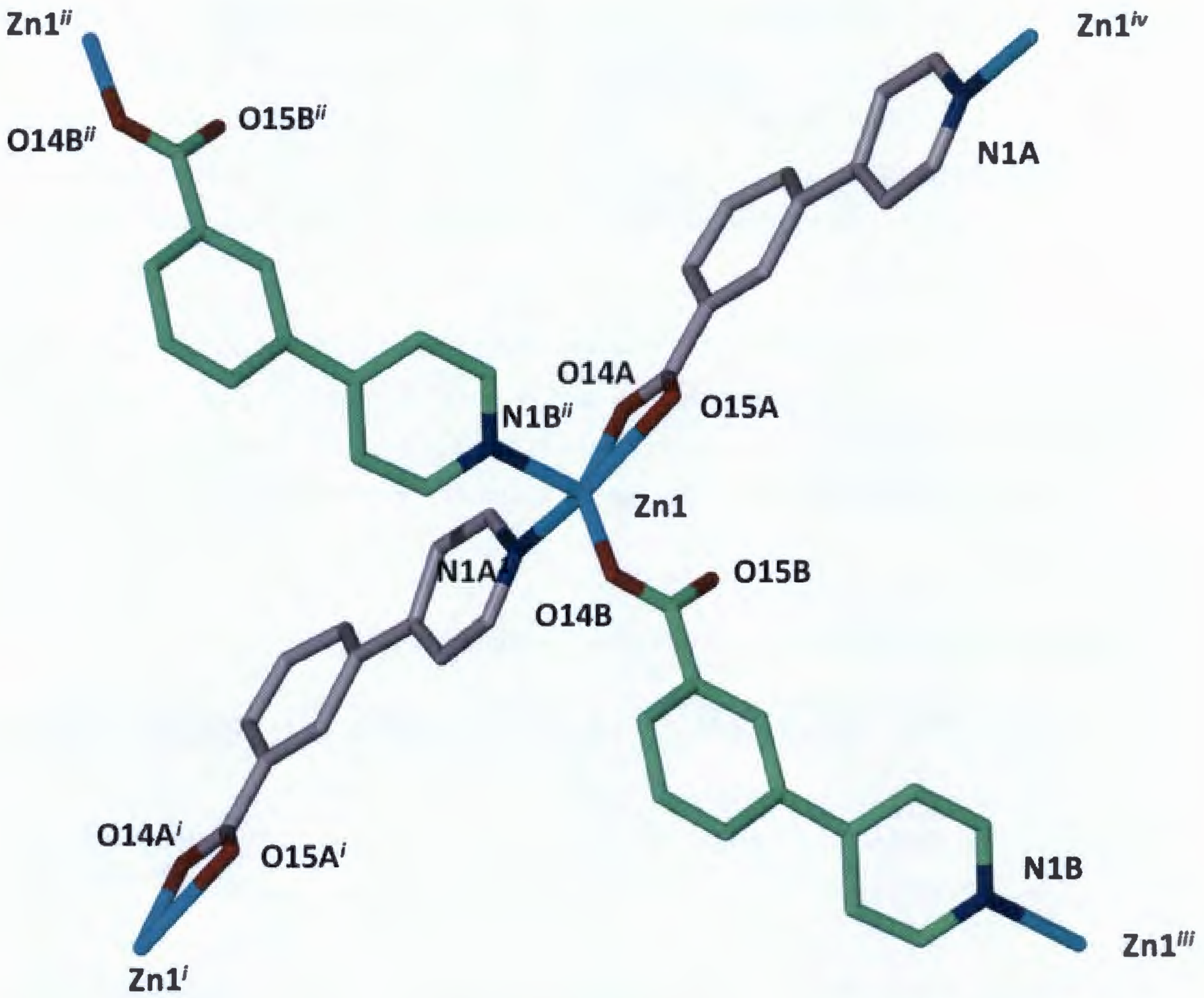

Figure 5.12: Coordination environment of Zn(II) in **4d-propanol**. The ligand which exhibits a monodentate binding mode of the carboxylate has carbon atoms shown in green, while the other carbon atoms are shown in grey for the chelating binding mode. Symmetry operator ^{i}*x-1, y, z;* ^{ii} *x, 1+y, z;* ^{iii} *x, y-1, z;* ^{iv} *1+x, y, z*

The Zn-O15A bond length in **4d-propanol** is significantly longer than any other Zn-O bonds in **4** and **4d**. The bond lengths of this compound are given in Table 5.6 while the bond angles are found in the supplementary material (Table S5.1-5.4). The solid state packing diagram of compound **4d-propanol** is displayed in Figure 5.13. As observed in compound **4** with DMF, the *n*-propanol guest molecules are located between the 2D layers. There are no obvious interactions between the *n*-propanol molecules in the cavities. The solvent accessible void volume occupied by *n*-propanol accounts for 27.9% of the unit cell volume, suggesting an expansion of the cavities as this value is higher than in **4** and **4d**.

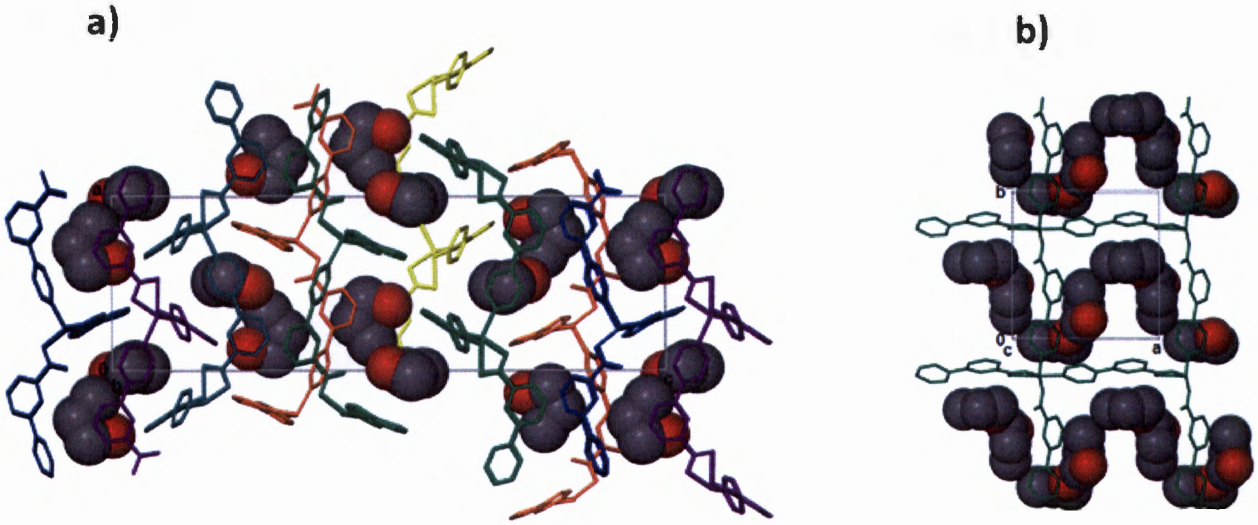

Figure 5.13: Packing diagram of the *n*-propanol inclusion compound **4d-propanol**: a) viewed along [010] and b) viewed along [001].

The symmetry elements present in compound **4**, **4d** and **4d-propanol** have been described for the cobalt analogue compound **2** in Chapter 4 section 4.2.3. These compounds have the same **sql** topology as previously noted with the cobalt analogue.

5.5 Thermal analysis of 4

The thermal stability of compound **4** was investigated by TGA, DSC, HSM and variable temperature PXRD studies. Figure 5.14 is an overlay of the TGA and DSC of compound **4**. The TGA trace of **4** shows that the compound is stable at room temperature. A mass loss of 14.94 % within a temperature range of 100 – 180 °C is observed. This is ascribed to loss of one DMF molecule per formula unit modelled in the structure of **4** (calculated 13.65%). The DSC profile of **4** displays a broad endotherm between 150 °C and 200 °C assigned to the departure of DMF guest molecules which resides in the cavities of **4**. In the cobalt analogue, compound **2**, an exotherm was observed at about 360 °C. The zinc analogue undergoes a phase transition at a slightly lower temperature *ca* 280 °C. Decomposition of the guest free framework occurs above 350 °C.

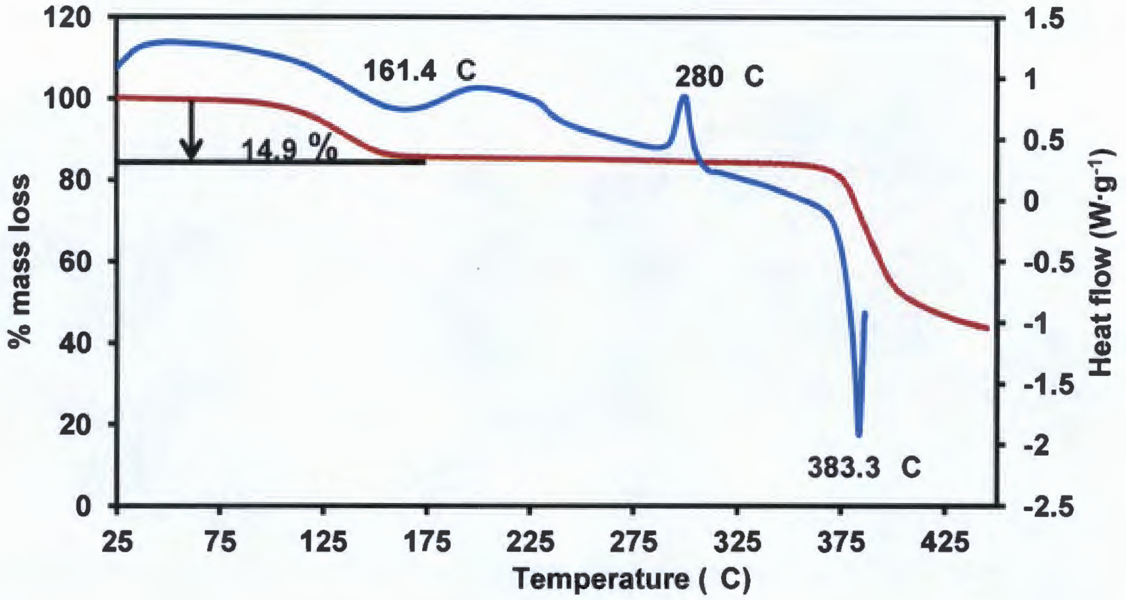

Figure 5.14: An overlay of the TGA (red) and DSC (blue) of **4**

Figure 5.15 shows the crystals of **4** under the HSM. The studies reveal that guest loss is accompanied by a colour change from colourless to a golden-yellow colour on heating from room temperature to 360 °C.

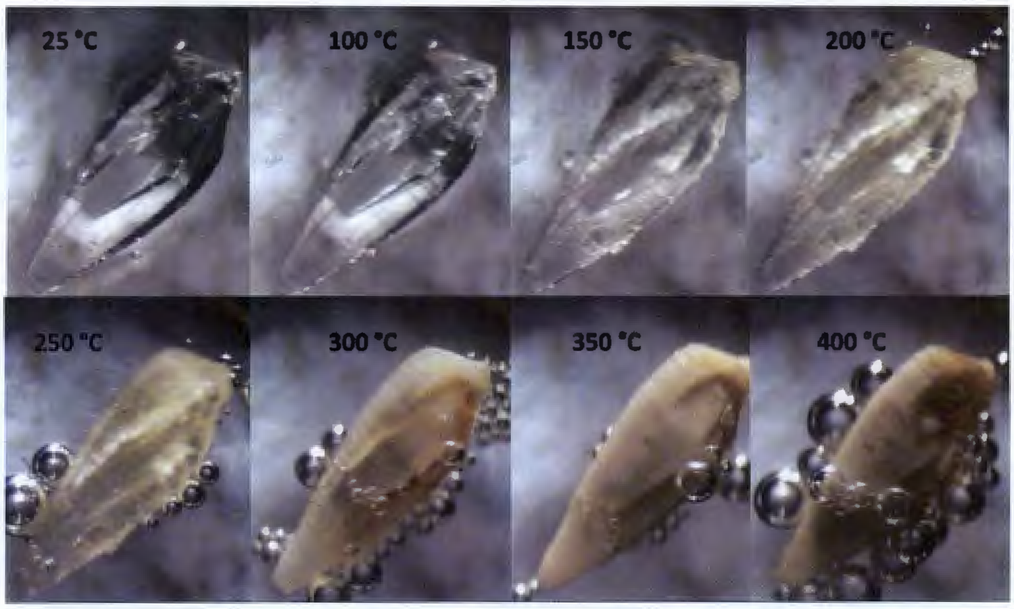

Figure 5.15: Hot Stage microscope images of **4** at different temperatures. Bubbling is observed around 150 °C which is associated with the departure of the guest DMF molecules. As more guest molecules are lost the crystal turns to a golden yellow.

Temperature dependant PXRD studies show that structural integrity is maintained upon loss of DMF molecules as shown in Figure 5.16. This agrees well with single crystal structure of **4d** which only shows minor changes in bond lengths and dihedral angles. Above 210 °C there is a slight change in the PXRD pattern with new peaks appearing at *ca.* 6.5° and 17° indicating a phase change. This is in concert with the exotherm observed in the DSC trace. Furthermore, a notable feature of the PXRD pattern is the evolution of diffraction peaks to higher 2θ angles on heating from 30 to 300 °C. This is attributed to contraction in unit cell volume which is in accordance with single crystal data of **4d**. Compound **4** undergoes an irreversible phase change above 270 °C as the pattern observed at this temperature is maintained on cooling to 30 °C. Unfortunately the crystalline integrity is lost at this point so the structure of the resultant phase could not be determined by single-crystal XRD.

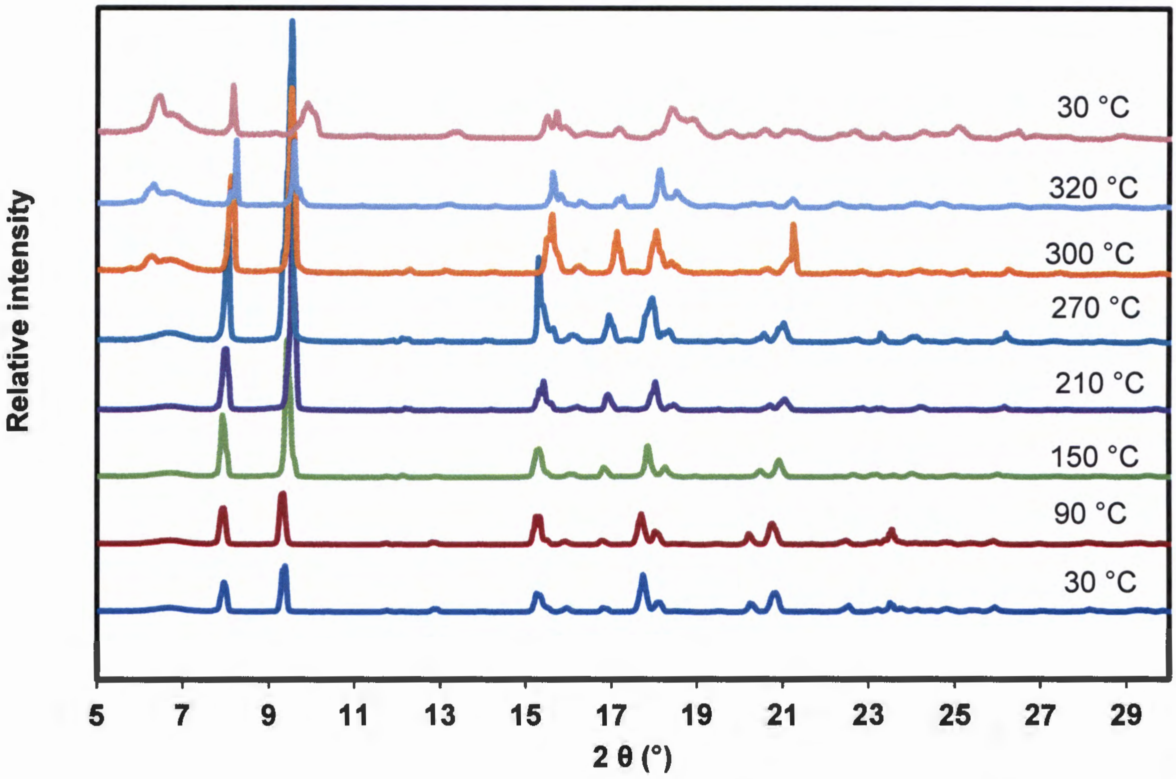

Figure 5.16: Variable temperature PXRD studies of compound **4**. The PXRD traces illustrate that the structure shrinks upon heating from 30 °C to 270 °C as evidenced by the shift of the peaks to higher 2θ values with a phase change occurring around 280 °C.

5.6 Evaluating the dynamic motion of the network upon alcohol uptake

The DMF molecules in **4** were desorbed under vacuum at 200 °C for 24 hours to give the empty network **4d**. Inclusion compounds of **4d-methanol**, **4d-ethanol**, **4d-propanol**, **4d-butanol** **4d-hexanol** and **1d-water** were formed by exposing the activated phase to dry solvents of methanol, ethanol, *n*-propanol, *n*-butanol, *n*-hexanol, and water respectively as described in the experimental section. The TGA traces of the alcohol and water inclusion compounds are given in Figure 5.17. From these results, it can be observed that **4d-hexanol** is the most stable inclusion compound as guest loss occurs above 120 °C. **4d-methanol** is the least stable compound as the initial guest loss occurs rapidly at room temperature. The relative order of stability order was found to be: **4d-hexanol** > **4d-water** > **4d-butanol** > **4d-propanol** > **4d-ethanol** > **4d-methanol.** Table 5.9 tabulates the fundamental parameters associated with the uptake of the alcohols and water by **4d**.

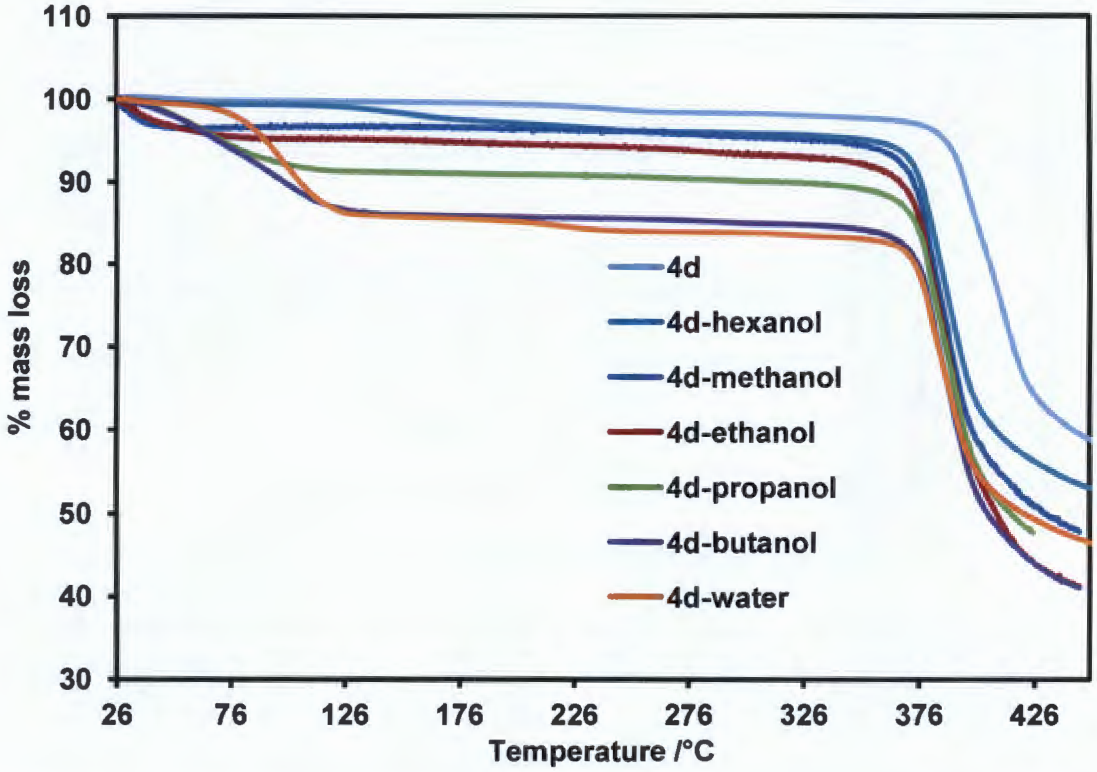

Figure 5.17: Thermogravimetric traces of the inclusion compounds of **4** illustrating the relative stabilities.

Table 5.9: Parameters associated with the absorption of alcohols and water by **4d**

Solvent	*TGA % mass loss*	*Metal: solvent ratio*
Methanol	2.15	1: 0.3
Ethanol	4.23	1: 0.5
n-propanol	9.45	1: 0.7
n-butanol	14.16	1: 1.0
n-hexanol	4.08	1: 0.2
water	14.01	1: 4.2

The largest metal:solvent ratio was observed upon exposure to *n*-butanol; while exposure to *n*-hexanol resulted in very little guest being absorbed per formula unit.

The kinetics of alcohol uptake was studied at 25 °C as described in Chapter 2 section 2.9 to evaluate the rate constant and the model which governs the absorption. Fresh samples of **4d** weighing 75 mg with a uniform particle size between 38 - 45 µm were exposed to alcohol vapours of methanol, ethanol, *n*-propanol and *n*-butanol using the sorption balance described in Chapter 2 section 2.9. Except for methanol and ethanol (due to surface adsorption), the amount of alcohol uptakes closely matched with those obtained from thermogravimetric analysis. The Table S5.5 gives the values associated with the uptake of the alcohols. Figure 5.18.a displays the α-time curves for the uptake of the four alcohols as a function of time. The shapes of curves clearly show that the uptake of alcohols is either governed by a geometrical or a diffusion model. Fitting these curves into the standard kinetic models gave the D2 model as the best fit except for *n*-butanol which fitted the D4 mechanism. Hence, it can be concluded that uptake of alcohols by **4d** is governed by a diffusion model. It seems reasonable that the process of alcohol sorption may be governed by the D2 or D4 model. This arises from the flexibility of the ligands which may allow diffusions from different directions as a result of rotation of the ligand about its connecting points. The D2 mechanism is derived by assuming that the solid particles are cylindrical, and diffusion occurs rapidly through a cylindrical shell with an increasing reaction zone. The D4 model applies to a diffusion reaction which takes place at several nucleation sites forming phase interfaces between the product and the reactant.

(a)

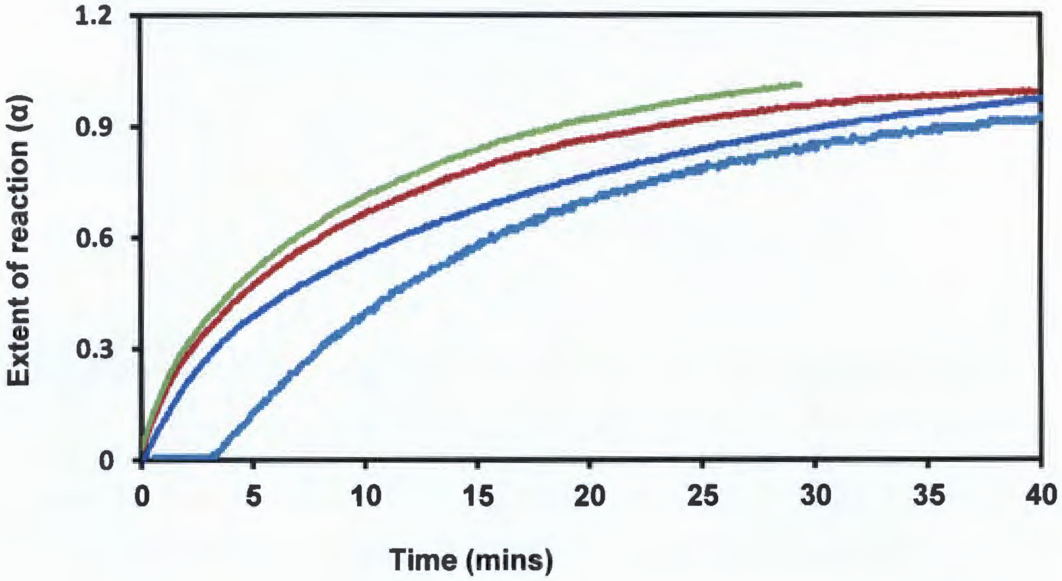

(b)

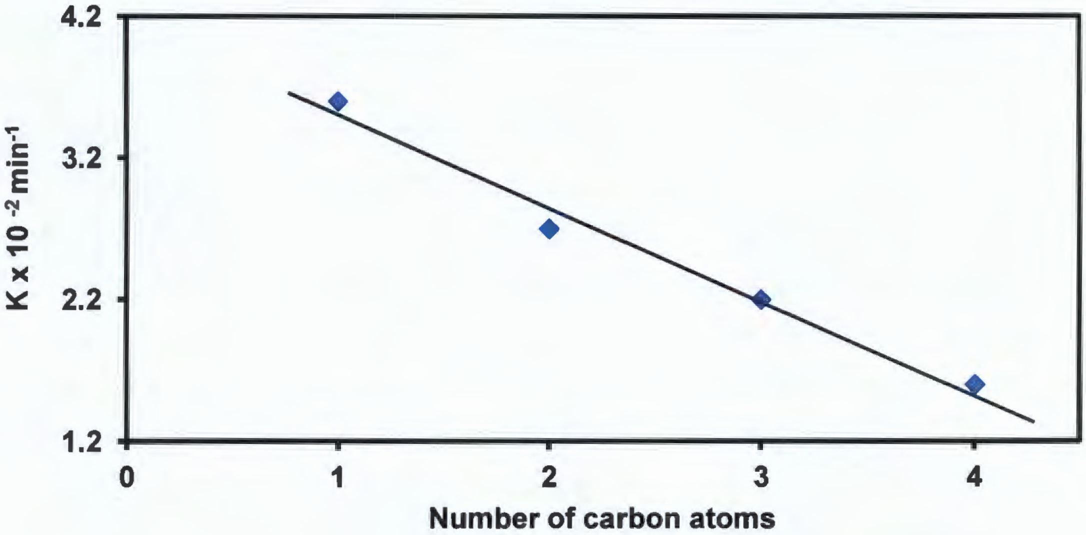

Figure 5.18: (a) kinetics of alcohol uptake by **4d** at 25 °C: the green, red, dark blue and light blue curves correspond to the absorption of methanol, ethanol, *n*-propanol and *n*-butanol respectively, (b) A plot of the number of carbon atoms *vs* the rate constant illustrating a negative linear correlation.

The rate constant for C_1 chain to C_4 chain ranged from 3.6×10^{-2} to 1.6×10^{-2} min^{-1} at 25 °C respectively. When the numbers of carbon atoms in the alcohols were plotted against the rate constant a negative linear relationship was revealed with an R^2 value of 0.98 (see Figure 5.18.b). The rate constant may be considered with respect to the following factors;

(i) the vapour pressure of the alcohols at 25° C
(ii) the size of the cavities in the closed form
(iii) the size of the alcohols
(iv) the motion of the 2D network upon uptake of the alcohols and
(v) the ease with which the guest moves into the host framework.

The sorption curves show that exposure of **4d** to methanol, ethanol and *n*-propanol results in an immediate uptake of the solvent vapours, however, this is not the case with *n*-butanol which shows a dead time of approximately two minutes. This behaviour may be attributed to the large size of *n*-butanol molecules. For *n*-butanol to be enclathrated between the 2D layers of the host, it has to trigger the dynamic motion of the layers first before moving into the host network. This is achieved through the interaction of guest molecules with the network.

5.7 PXRD and single crystal studies of the alcohol inclusion compounds

The PXRD traces of the inclusion compounds formed upon exposure of **4d** to alcohols and water are given in figure 5.19. The single crystal structure of **4d** shows that the 2D framework shrinks along the *c*-axis (Δc = -2.413 Å) and stretches slightly along the *a*- and *b*-axes (Δ *a* and Δ *b* = + 0.116 Å). This phenomenon is reversible upon absorption of methanol, ethanol, *n*-butanol and *n*-propanol as revealed by PXRD studies. Except for *n*-hexanol, the diffraction peaks shift to lower 2θ angles as the size of the alcohol chain increases. Evolution of diffraction peaks demonstrates the breathing behaviour of the 2D network which is consistent with an increase in the unit cell volume. This phenomenon has been observed in several systems.[6-14]

In **4d**, the (0 0 4) reflections are located at 10.10°. The change in the size of the cavities is reflected by the change in the position of the (0 0 4) reflections which is a measure of the length of the *c*-axis (Figure 5.20). The expansion of the cavities upon uptake of alcohols is responsible for the evolution of the Bragg diffraction peaks towards their original 2θ positions (9.34°) in **4**. Hence, as the size of the alcohol increases, the size of the cavities also increases.

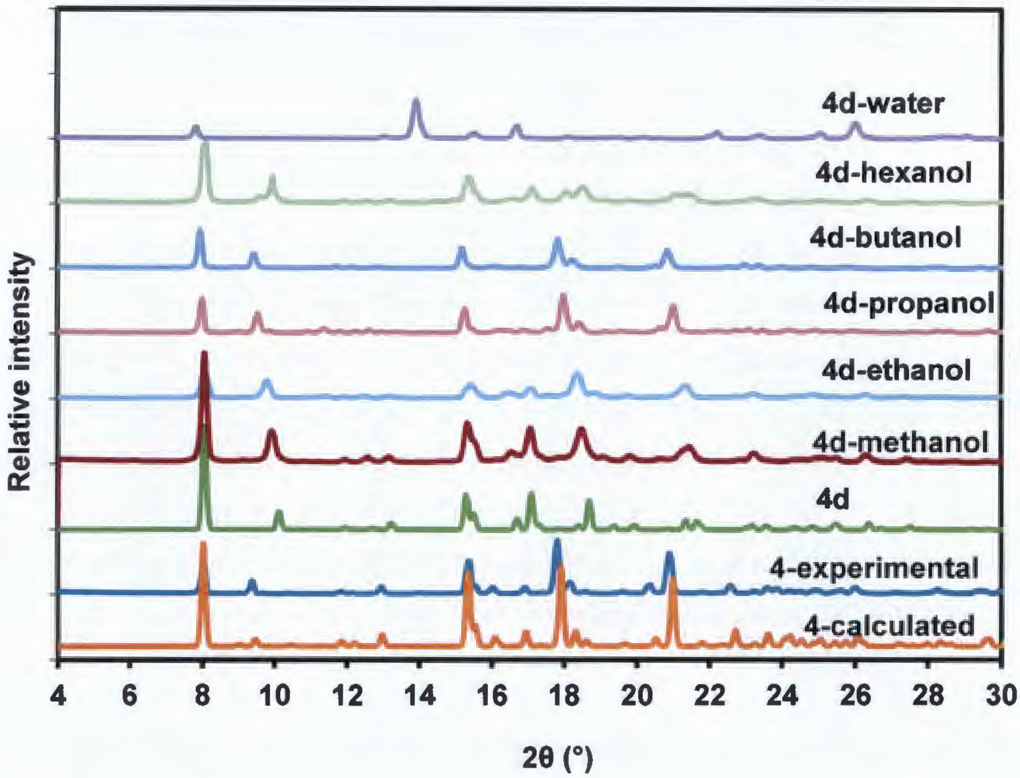

Figure 5.19: a) PXRD of as made **4** and several solvated forms of **4d** at room temperature.

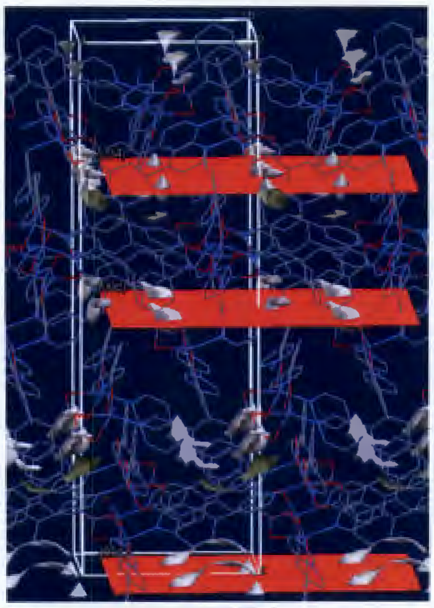

Figure 5.20: An illustration of the [0 0 4], [0 0 1] and [0 0 2] planes in red which slice across the channel cavities, the cavities depicted as grey (outside surface) and dark grey (inside surface) house the guest molecules. On inclusion of the guest molecules, the [0 0 4] plane shifts to lower 2θ angles as a result of the expansion of the cavities.

The unit cell parameters of the alcohol inclusion compounds were determined using the Pawley fitting method[15] in TOPAS[16] as described in Chapter 2 section 2.72. This allows for the determination of the breathing amplitude of the system which is calculated as the difference in lattice parameters between the alcohol inclusion compounds and the dry form (**4d**), expressed as a percentage (Table 5.10).

Table 5.10: Unit cell parameters of the alcohol inclusion compounds

	4	***4d***	***4d-methanol***	***4d-ethanol***	***4d-propanol***	***4d-butanol***
a (Å)	11.580(1)	11.565(3)	11.572 (2)	11.514(4)	11.622(8)	11.677(1)
c (Å)	37.786(3)	35.632(7)	35.466(7)	36.122 (1)	37.103(2)	37.496(4)
V (Å^3)	5066.7(9)	4765.4(2)	4751.7(21)	4788.9(4)	5011.2(75)	5112.6(12)
% VBA[a]			1.510	2.305	7.054	9.220
%c-ABA[b]			1.610	3.490	6.300	7.426

[a]Volumetric breathing amplitude; [b]Axial breathing amplitude

Figure S5.2 and S5.3 shows the calculated and observed peak intensity patterns of the PXRD of the alcohol inclusion compounds and that of **4** and **4d** respectively. By inspecting the two patterns, it is clear that there is a good fit. The difference between the two is depicted in grey. The discrepancies observed as (+) and (-) peaks in the grey line between the calculated and observed pattern is due to the fact that the integration used for R_{Bragg} indices fails when the peaks have significant unmodeled asymmetry. Furthermore, the peak shapes observed are a convolution of both sample (eg. domain size, stress/strain, defects) and instrument (radiation source, geometry, slit sizes etc.), and vary as a function of 2θ. It is very difficult to factor all these aspects in a single peak-shape description, hence compromises are often made.

When the number of carbon atoms in the alcohols was plotted *versus* the *c*-axis and *versus* the unit cell volume, a positive linear correlation was obtained as illustrated in Figure 5.21.

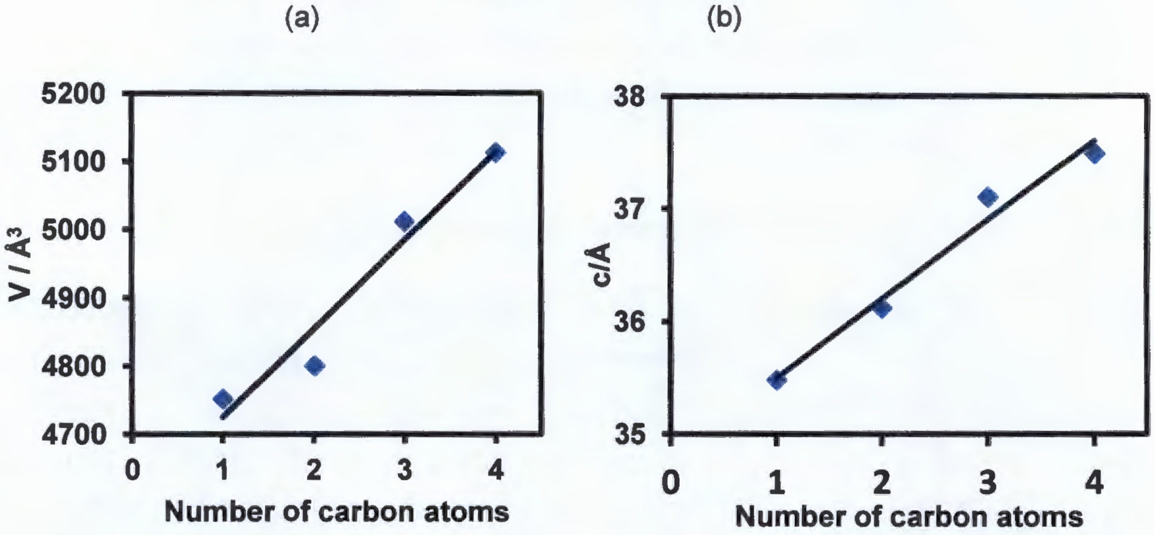

Figure 5.21: Plots revealing positive linear correlation between the length of the alcohol and the unit cell parameters.

The equations defining these plots are:

$$c = 0.7013n + 34.795 \qquad (5.1)$$

$$V = 129.4n + 4595.4 \qquad (5.2)$$

The value of *n* represents the number of carbon atoms in the alcohol. It is evident that the two linear equations above integrate the unit cell parameters of **4d**. In the absence of the guest, $n = 0$, this give a *c*-value of 34.79 Å with a corresponding unit cell volume of 4591.8 Å^3. These values corresponds to the lattice parameters of the desolvated phase **4d** from single crystal analysis but there is a significant difference to those obtained from powder data at room temperature. The value for the unit cell volume is slightly lower due to experimental error. The *c*-axis value is close to the observed value obtained by single crystal diffraction, thus validating the two equations above. These equations may be used to estimate the unit cell parameters one would expect upon inclusion of linear chain alcohols. For example, absorption of *n*-pentanol in the 2D network will give a *c*-axis value of 38.302 Å with a corresponding unit cell volume of 5242.4 Å^3. As would be expected, the calculated volumetric breathing amplitude of the network was found to follow the order: methanol < ethanol < *n*-propanol < *n*-butanol. Compared to volumetric breathing amplitudes observed in some 3D networks, the values are very low, but they are important in demonstrating the effect of the guest size in changing the unit cell dimensions.[17]

Crystal structures of **4d-methanol** and **4d-ethanol** were not obtained due to poor single crystal quality. However, the structures of **4d-propanol** and **4d-butanol** were obtained from single crystal diffraction and were consistent with these PXRD studies. Single crystal X-ray diffraction reveals that upon uptake of *n*-propanol and *n*-butanol by **4d**, the framework breathes in all three crystallographic directions. This gives rise to a unit cell volume of 5005.0(5) Å^3 and 5086.2(2) Å^3 for *n*-propanol and *n*-butanol respectively. These values are comparable to those obtained by Pawley fitting method in Table 5.10. The **4d-butanol** structure could not be refined to acceptable levels due to the poor diffraction. However, it provides useful information on the mechanism of the breathing motion of the 2D framework.

To increase a further understanding of the breathing behaviour, the solvent accessible voids were modelled utilising Mercury[4] with a probe radius of 1.2 Å as delineated in Figure 5.22. Desorption of DMF from **4** results in the contraction of the cavities while absorption of *n*-propanol and *n*-butanol allows for the expansion of these cavities. The solvent accessible void volumes of the cavities were calculated in PLATON and were found to be 15.4%, 24.8%, 27.9% and 28.7% in **4d**, **4**, **4d-propanol** and **4d-butanol** respectively, thus affirming the observed expansion of the channels upon guest uptake.

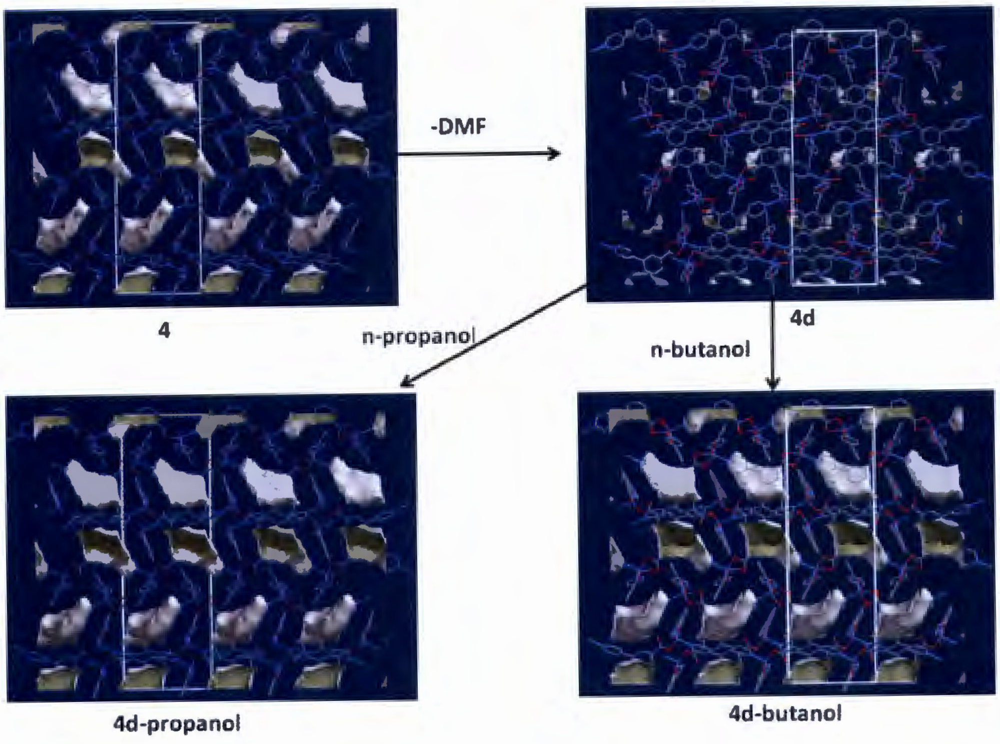

Figure 5.22: The scheme illustrates solvent accessible void volumes found in compound **4** and related structures upon guest loss and inclusion of *n*-butanol and *n*-propanol. The outside surface area of the cavities is depicted in grey while the inside is dark grey. As seen in the scheme, the cavities oscillate between small and large cavities upon guest loss and guest inclusion respectively.

To comprehend the movement of the ligands on absorption of alcohols, it is handy to think about the C-C bond which connects the two rings in every ligand as an adaptable point of rotation. The other possible adaptable point is the orientation of the carboxylate with respect to the phenyl ring; however this torsion angle was discovered to be indistinguishable for most cases, contrasting just in **4d-propanol** and **4d-butanol** for the carboxylate moiety bound in a monodentate fashion. An overlay of the structures of the dry form, **4d** (blue) and the **4d-propanol** (red) (Figure 5.23) shows unmistakably that incorporation of *n*-propanol in **4d** results in some conformational revisions of the ligands. The rotation of ligand A about the C-C single bond is more significant than that in ligand B, which implies that the two ligands in the asymmetric unit display distinctive degrees of breathing. **4d** has the highest dihedral edge of 49° which may demonstrate that it has high conformational energy; subsequently it is more inclined to be unstable. Therefore, its ligands ought to be more inclined to experience a change in conformation under external stimuli to give a low energy compliance structure. Incorporation of guest molecules in the structure diminishes the torsion angles between the phenyl and the pyridyl ring as given in Table 5.11. Therefore the variables answerable for the expansion in the size of the cavities are:

(I) rotation of the ligand at its adaptable bond allowing for cleavage of the Zn-O bond and bringing about stretching of the twisted connecting ligand,

(II) the concertina impact this has in expanding the separation of Zn-Zn detachment inside a 2D layer (along the *a*- and *b*- axis) while diminishing the Zn-Zn separation of contiguous 2D layers along the *c*-axis to oblige an increment in the size of the guest molecule (see Table 5.12).

These two variables account for the anisotropic expansion observed in the crystal structures of **4d-butanol** and **4d-propanol**.

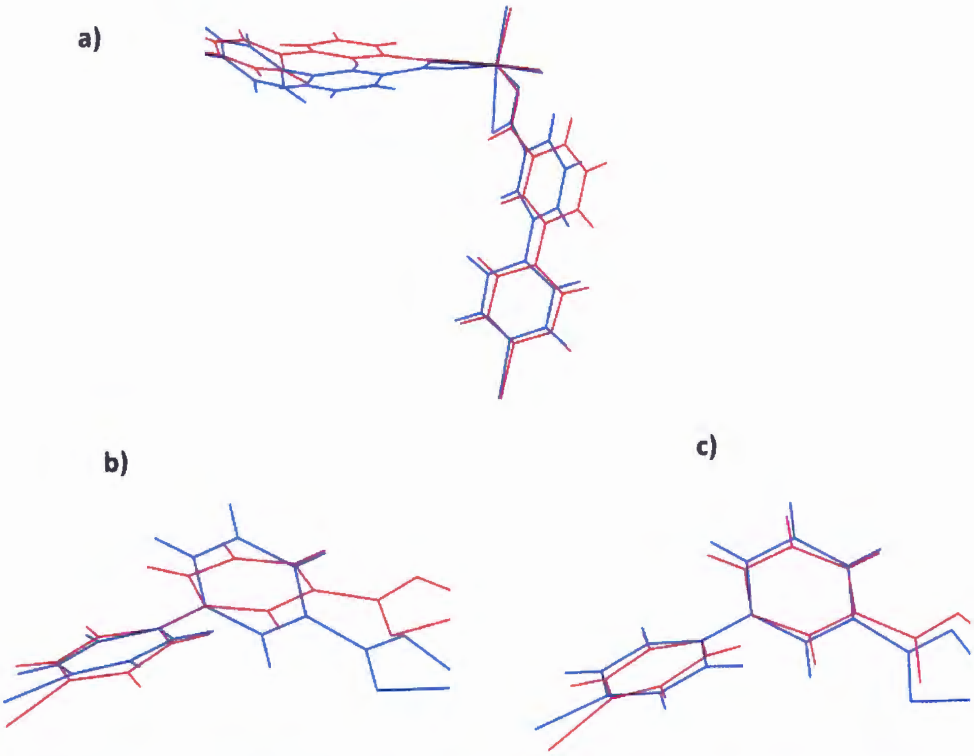

Figure 5.23: An overlay of the fragments of **4d** (blue) and **4d-propanol** (red) illustrating ligand conformational change (a) Local structure variations of the metal-ligand connections, b) conformational change of ligand A and c) conformational change of ligand B upon uptake of *n*-propanol by the desolvated phase **4d**.

Table 5.11: Fundamental parameters of the dynamic motion of the 2D network

Compound	***Guest***	***Dihedral angle Ligand A (°)***	***Dihedral angle Ligand B (°)***
4	DMF	40.15	7.29
4d	guest free	49.00	44.3
4d-propanol	*n*-propanol	38.30	15.56
4d-butanol	*n*-butanol	38.35	11.97

Table 5.12: Breathing parameters of selected compounds

Compound	***Zn-Zn distance inside a 2D layer along a- and b-axis(Å)***	***Zn-Zn distance of adjacent 2D layers along c-axis (Å)***
4d	11.581	6.224
4d-propanol	11.664	6.219
4d-butanol	11.728	6.271

Table 5.11 gives the dihedral angles between the phenyl and the pyridyl ring in selected compounds. These results show that the size of the guest modulates the degree of the movement of the rings as unequivocally indicated by the reduction in the dihedral edges with increase in the size of the guest. The crystal structure of **4** gives more proof of the movement of the rings. The modelled DMF molecule has an oxygen atom disordered over two sites which may be attributed to the thermal motion of the guest molecules (Figure 5.24). This suggests that the molecule may be rotating about the C - N platform by 180° which in turn triggers rotation of the ligand by 29.6°. The movement of the guest is transmitted to the structure, and is responsible for the pyridyl rings disorder over two positions. This is an adaptation change which suits the two positions adopted by the DMF guest molecule. Similar effects were seen on dynamic ultramicroporous frameworks constructed from 34pba ligand and Mn(II). The compound selectively responded to molecular rearrangement of DMF, which prompted conformational reversion of the flexible ligand. These brought about disfigurement of the entire crystal lattice.[18]

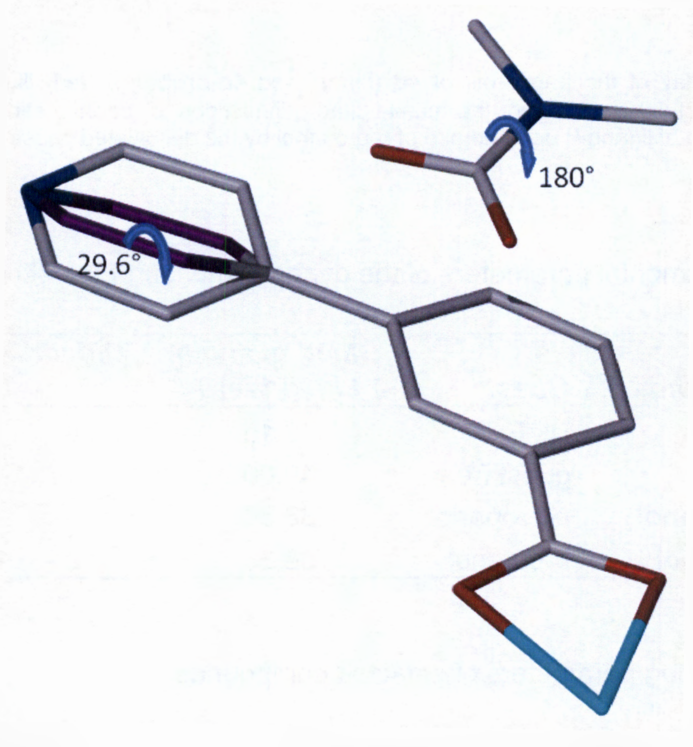

Figure 5.24: Illustration of the positions occupied by the disordered DMF molecule and the pyridyl moiety of compound **4**. The disorder observed in the ring accounts for the two positions occupied by the guest DMF molecule. Due to the absence of the DMF in **4d** (see Figure 5.10), this disorder is absent conforming that the motion of the guest is responsible for the two sites of the ring.

On uptake of *n*-propanol and *n*-butanol **4d** experiences a reconstructive phase transition within the same space group $P4_32_12$ with reversible cleavage of a metal carboxylate bond. The other carboxylate moiety keeps its chelating mode. Reconstructive phase changes are generally scarce in 2D systems and only a few examples have been observed to date, most of which comprise of 3D pillared structures.[19] In comparable alcohol systems reported previously , it has been proposed that the alcohol molecules interact through their hydroxyl groups with the oxygen atoms of the framework. For longer alcohol chains, the alkyl aggregations are required to curve towards the phenyl rings to enhance hydrophobic van der Waals attractions.[20] In this study, it was noted that the hydroxyl moiety on *n*-propanol does not interact with the host system, however the propyl chain is embraced within the system cavity, making various weak dispersion contacts with the aromatic rings of the host system (Figure 5.13). The *n*-butanol structure was not of sufficiently high quality to find the guest molecules, however it was noticed that the unmodelled electron density is located in close vicinity to the host system's aromatic rings.

It appears sensible that the improved uptake of *n*-butanol is due to the increment in hydrophobicity as the carbon chain increases, henceforth the alcohol molecule interacts more with the hydrophobic framework through $CH\cdots\pi$ and other weak interactions. These interactions trigger the opening of the channels. Methanol and ethanol are less hydrophobic and they interact less with the framework. This accounts for the low volumetric breathing amplitudes of 1.5% and 2.4% observed for methanol and ethanol respectively. A comparable effect was seen by Serre *et al.*[21] PXRD and TGA studies give an impression of there being a size cut off that might be imposed by these channels, clarifying why few molecules of *n*-hexanol was absorbed. Absorption of alcohols by the 2D network may be ascribed to the vicinity of the phenyl rings in the structure, giving a hydrophobic impact which attracts in the alkyl chains of the alcohols. Absorption of water prompts poisoning of the framework as proven by the formation of another phase (figure 5.19).[22] Water molecules are very polarised in comparison to the alcohols. It has been suggested that they tend to attack the open metal sites or upset the system by hydrolysing the carboxylate group connected to the metal centres.[23] For these reasons, recent studies have focussed on methodologies that diminish the amount of water that can enter the channels of networks. For the time being, this phenomenon precludes requisition of this material as an alcohol-water separator, since ideal alcohol uptakes and unfavourable water uptakes are the requirements for powerful vapor-phase alcohol separation.[24,25]

IR studies were performed on the alcohol inclusion compounds to comprehend the observed reconstructive phase transitions observed in the single crystal structures of **4d-propanol** and **4d-butanol**. Figure 5.25 shows the IR spectrum of several forms of **4d**. The bands at 1617 cm^{-1} in all traces were assigned to the aromatic stretch of the ligand. The positions of the asymmetric and symmetric carboxylate stretches are given in Table 5.13 and the conclusions drawn about the binding mode of the ligands are also presented in the table. Two asymmetric and symmetric carboxylates bands were observed in the IR spectrum of alcohol inclusion compounds. This is due to the presence of two different binding modes as already seen from the crystal structures of *n*-butanol and *n*-propanol. The O-H region not shown in Figure 5.25 suggests the presence of hydrogen bonding between the framework and the alcohols. When compared to **4d**, significant shifts in the O-H region were observed upon alcohol uptake by the framework.

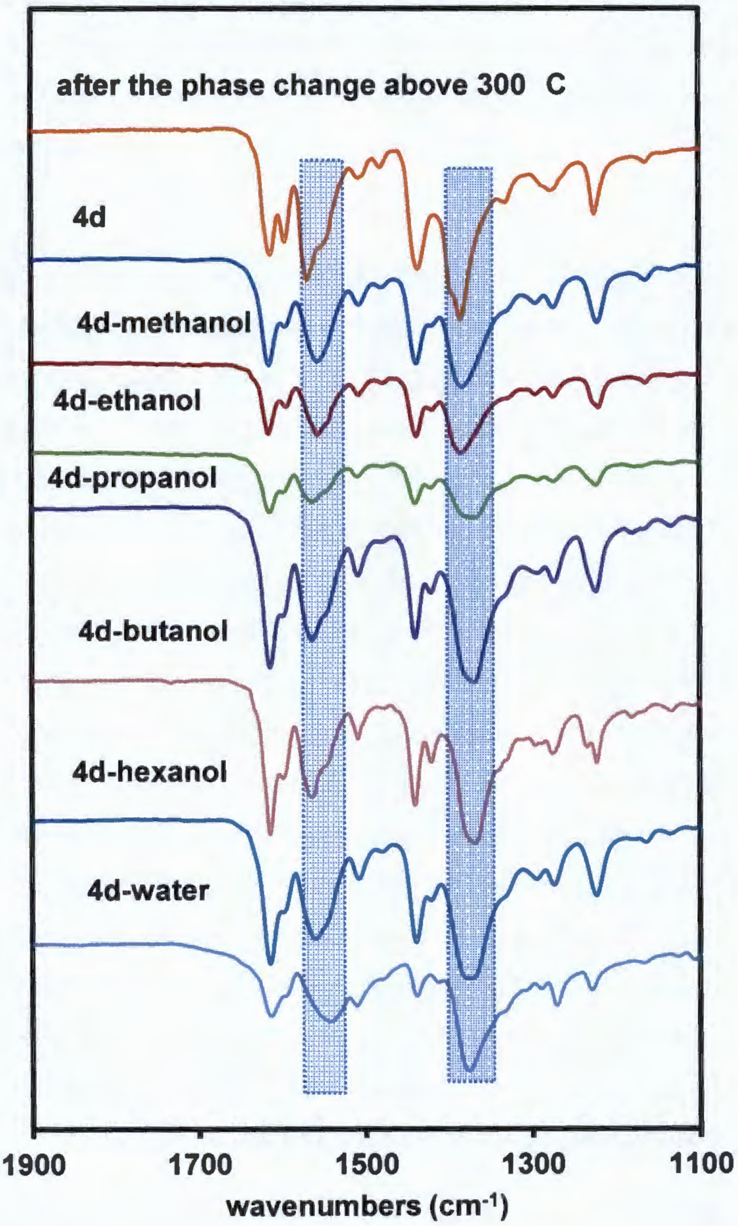

Figure 5.25: FTIR spectrum of several forms of **4d** compounds.

Table 5.13: IR analysis and the conclusions drawn on the binding mode of the carboxylate moiety

Compound	***Asymmetric band/ cm^{-1}***	***Shoulder/cm^{-1}***	***Symmetric band/ cm^{-1}***	***ΔV /cm^{-1}***	***Conclusions***
4d	1556		1384	172	chelating
4d-methanol	1558	1543	1384	174	chelating
4d-ethanol	1562	1544	1384	178	chelating and monodentate
4d-propanol	1564	1546	1382	182	chelating and monodentate
4d-butanol	1564	1544	1379	185	chelating and monodentate
4d-hexanol	1562	1544	1380	182	chelating and monodentate
4d-water	1543		1379	164	chelating or bridging
after phase change	1568	1544	1394	174	chelating and monodentate

5.8 Effects of structural phase change on absorption capacity

On the DSC trace of **4** (Figure 5.14), a phase transition of the framework was observed at high temperature (*ca.* 300 °C) which was confirmed using variable temperature PXRD (figure 5.16). To evaluate the effect of this structural rearrangement on the absorption of water and alcohols, compound **4** was activated at 300 °C for 24 hours to give **4d2**. Exposure of this phase to solvent vapours showed no uptake of water nor alcohols. This suggests that above 300 °C the structure rearranges to form a non-breathing network. Hence, it can be suggested that the dynamic motion of the 2D network is disrupted at high temperatures above the phase transition.

5.9 Competition experiments

With a specific end goal to establish whether one alcohol might be absorbed preferentially, a competition experiment between the two extremes in size, methanol and *n*-butanol was carried out. In the first competition experiment, crystals of **4d** were immersed in a solvent mixture of *n*-butanol and methanol with a molar ratio of 1:1. In the second, polycrystalline material of **4d** was exposed to vapours from the same solvent mixture. PXRD studies were performed to see whether the PXRD acquired matched those of **4d-methanol** or **4d-butanol** compounds (Figure 5.26). Particular consideration was focussed on the position of the (0 0 4) reflections. As previously noted, absorption of *n*-butanol gives a peak centred at 9.3° while incorporation of methanol will give Bragg peaks centred at 10.3°. Results from PXRD studies after immersing the crystals in the solvent mixture for one week demonstrates that *n*-butanol and methanol are both absorbed as proved by the manifestation of two reflection peaks between 9.2° and 10.3° attributable to the presence of both **4d-methanol** and **4d-butanol** phases (figure 5.26 trace c).

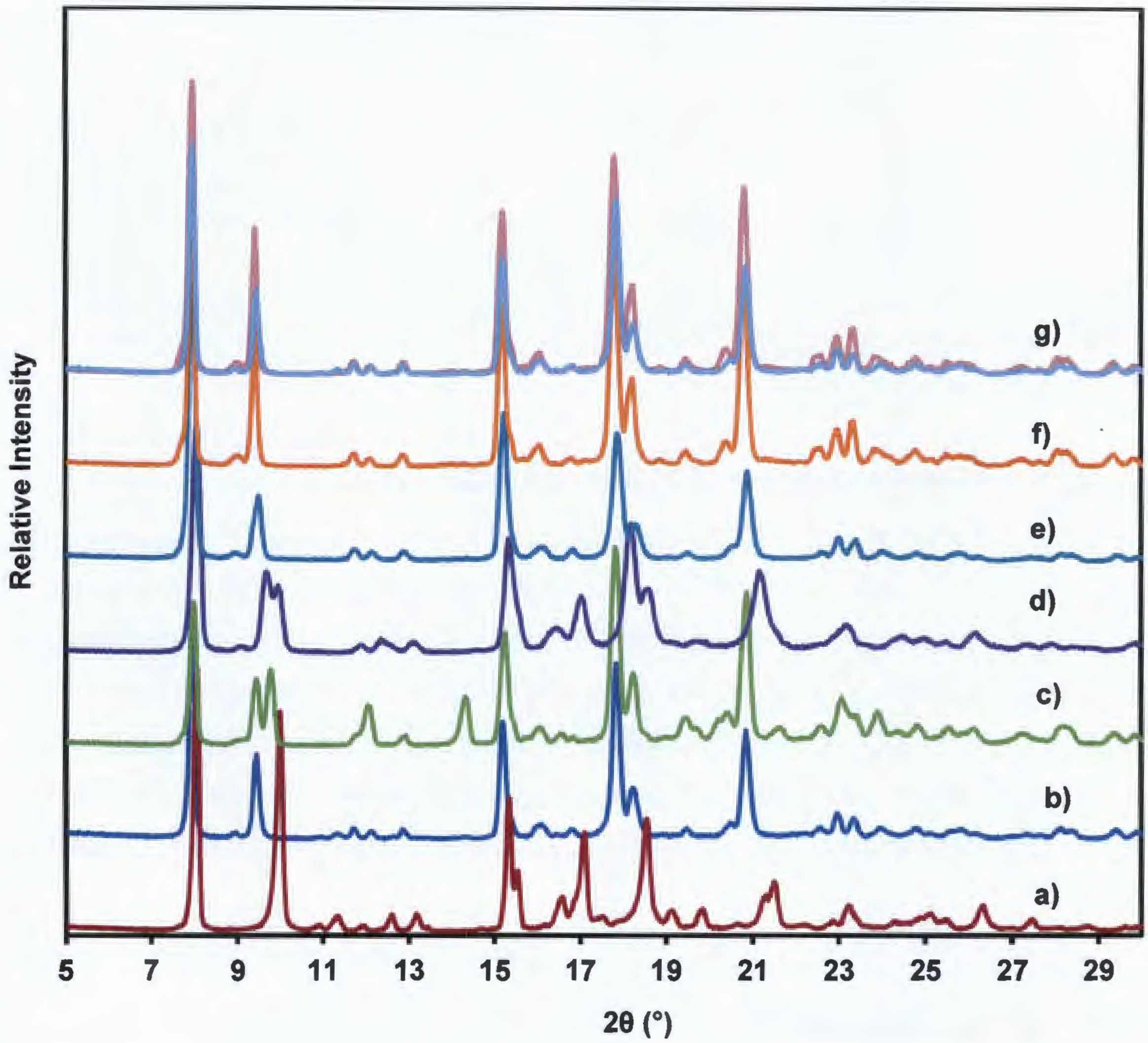

Figure 5.26: PXRD trace of: (a) **4d-methanol**, b) **4d-butanol**, c) obtained after soaking **4d** in a solvent mixture of *n*-butanol and methanol for one week, **d**) obtained after 6 hours of exposure alcohol vapours derived from the 1:1 liquid mixture of n-butanol and methanol, e) after 24 hours exposure to the vapours of the solvent mixture, f) PXRD obtained after 72 hours of exposure to solvent mixture and g) overlay of a) in red and f) in blue.

The incorporation of a specific guest in a crystal appears to demonstrate that under an alternate condition the host system may have the capacity to partition the two alcohols. Having this as a top priority, polycrystalline material of **4d** was exposed at room temperature to the vapours of the solvent mixture. PXRD traces gathered following six hours of exposure to the vapour gave similar results to the ones acquired when soaking the crystals in the 1:1 solvent mixture and in which both alcohols were absorbed by the system. Although the single crystal structure of **4d-methanol** was not obtained, it is presumed that this structure has dihedral angle values close to those of the desolvated phase **4d**, in which torsion angles are high (this is predicated on the assumption that fewer methanol molecules were able to move into **4d**). This may suggest that **4d-methanol** is likely to be less stable than the **4d-butanol** compound with low torsion angles between the rings. The PXRD traces were collected over an extended time to check whether the most stable compound might prevail over the less stable one. The PXRD studies performed after 24 hours and 72 hours of exposure to the vapours show only one reflection peak centred at 9.34° (Figure 5.26.e and f). When compared with the PXRD trace of **4d-butanol**, there is a perfect match. A 1:1 molar ratio of methanol and *n*-butanol gives a higher vapour pressure of methanol than butanol. Despite the high vapour pressure of methanol, the PXRD shows that the two solvated phases are obtained at the start of the reaction. As time advances, *n*-butanol dislodges the absorbed methanol to give a single phase of **4d-butanol** as confirmed by PXRD traces following 72 hours of exposure. In this respect, it is presumed that the selectivity of the compound is thermodynamically determined despite the fact that different variables, for example, nature of interactions, the packing energy and entropy might additionally play a role.[26]

5.10 Desorption kinetics of *n*-propanol and *n*-butanol

To investigate the energy associated with the removal of *n*-propanol and *n*-butanol in **4d-propanol** and **4d-butanol** respectively, non- isothermal desorption kinetics were performed as described in chapter 2.10. The desorption kinetics of *n*-propanol and *n*-butanol from the network was followed by thermogravimetric analysis. Figure 5.27 displays the thermogravimetric traces for the loss of *n*-propanol and *n*-butanol. The reciprocal temperature values at each conversion level were determined using the Universal analysis speciality library[27] and these are given in Table 5.14. Plots of log β versus 1000/T are given in Figure 5.28. The gradient of the slopes of the plots were equated to $-0.457E_a/R$ which allowed for the determination of the activation energy at each given % conversion level.

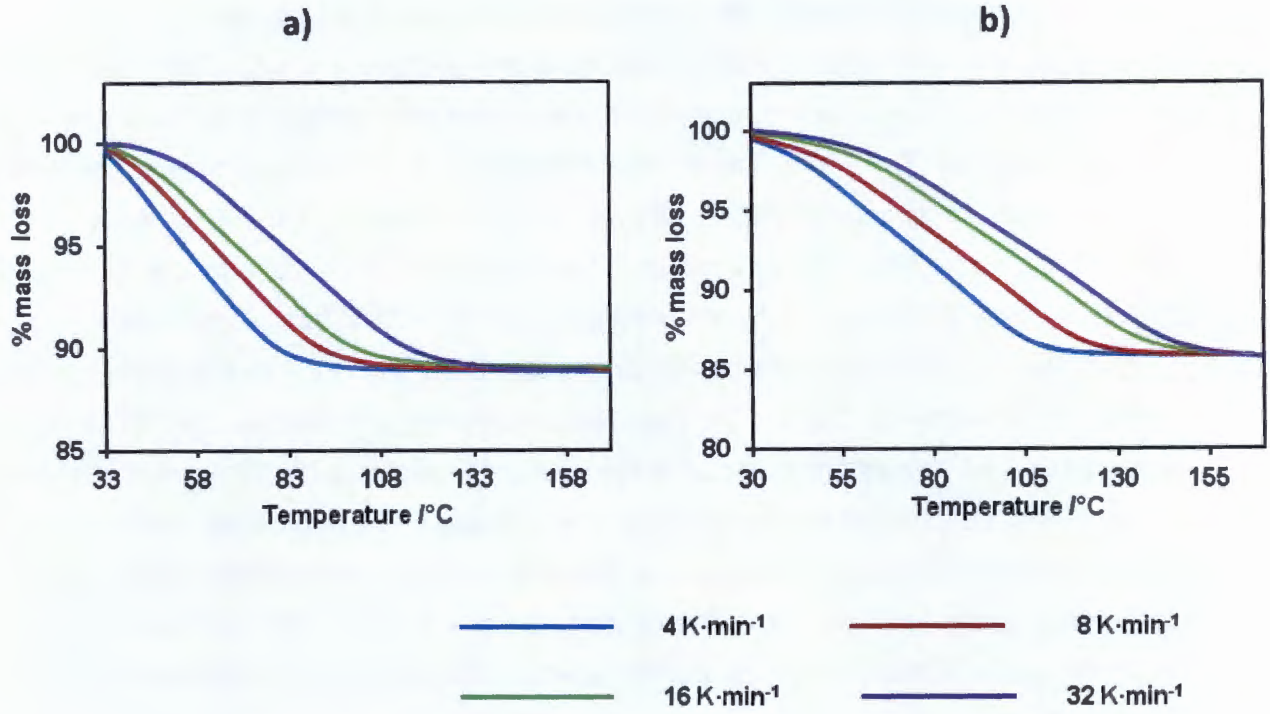

Figure5.27: Desorption kinetic profiles of: a) **4d-propanol** and b) **4d-butanol** at different heating rates.

Table 5.14: Desorption kinetic parameters of **4d-propanol** and **4d-butanol**

			1/T x 1000				
	Heating rate (β) K· min^{-1}	***log β***	***20%***	***40%***	***60%***	***80%***	***95%***
4d-propanol	4	0.6021	3.16	0.602	2.986	2.898	2.803
	8	0.9031	3.115	0.903	2.907	2.809	2.683
	16	1.2041	3.05	1.204	2.849	2.754	2.647
	32	1.5051	2.973	1.505	2.748	2.647	2.532
4d-butanol	4	0.602	3.077	2.945	2.825	2.719	2.623
	8	0.903	3.002	2.861	2.734	2.626	2.523
	16	1.204	2.919	2.77	2.639	2.529	2.425
	32	1.505	2.873	2.724	2.592	2.481	2.375

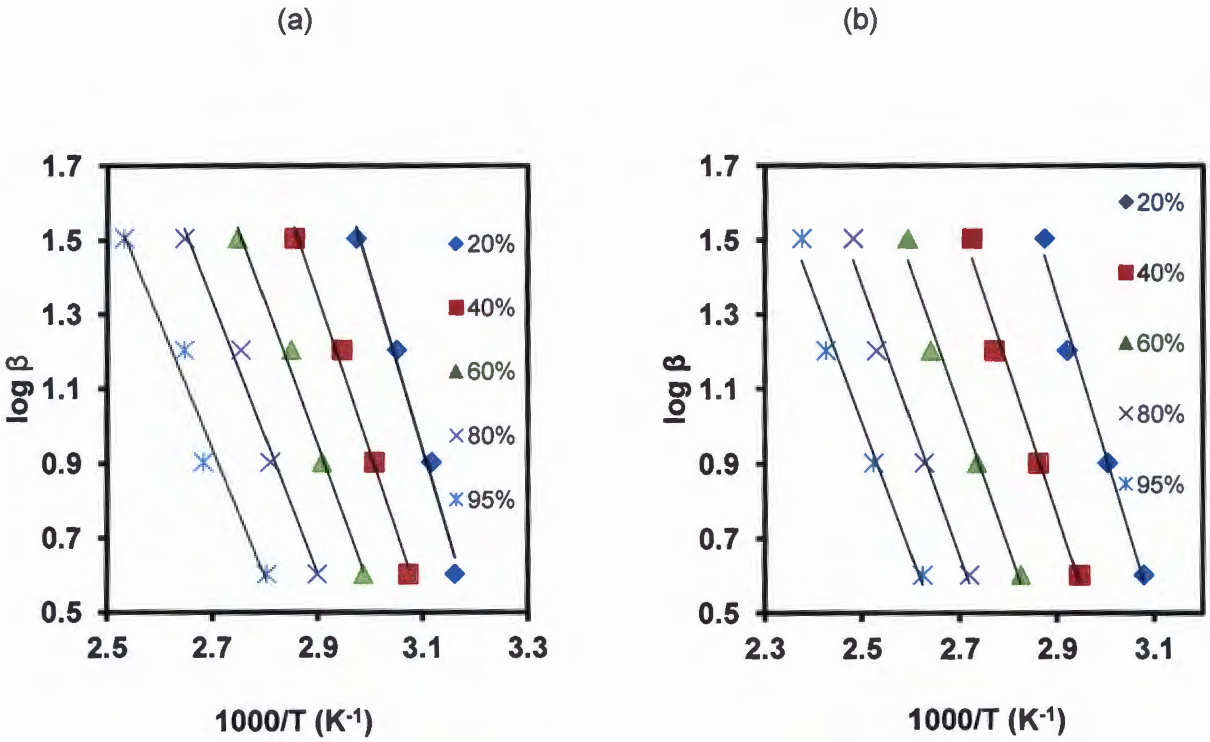

Figure 5.28: Plots of 1000/T versus log β which allowed for the determination of the gradient equated to -0.457Ea/R;

The activation energy for the desorption of both *n*-propanol and *n*-butanol was found to decrease with an increase in the percentage conversion level (Table 5.15). This is in contrast with many findings which generally show an increase in the energy of activation with an increase in conversion level.[28] Our results suggest that once the first molecule is removed from the channels of the network, less energy will then be required to remove the remaining molecules. This may suggest that a single mechanism is responsible for the desorption of both *n*-propanol and *n*-butanol. The energy associated with the removal of the guest *n*-propanol ranged from 86(7) to 62(8) kJ·mol^{-1}. while that of *n*-butanol ranged from 78(6) to 64(6) kJ·mol^{-1} The fact that the desorption of *n*-butanol and *n*-propanol have comparable energies may suggest that both guest molecules are located in the same chemical environment and have the same orientation relative to the host framework. As already noted from the sorption kinetics, the uptake of both guest molecules is governed by a diffusion model. It is not surprising that the desorption will have similar energy values suggesting a single mechanism for the desorption of the two alcohols. The kinetic profile in Figure 5.27 of guest loss shows that *n*-propanol is lost at a lower temperature when compared to *n*-butanol. This difference is attributed to the difference in the boiling points of the alcohols.

Table 5.15: Activation energy at different conversion levels

	Conversion level	*20%*	*40%*	*60%*	*80%*	*95%*	*Average*
4d-propanol	E_a (kJ·mol^{-1})	86(7)	76(5)	70(5)	69(6)	62(8)	73(8)
4d-butanol	E_a (kJ·mol^{-1})	78(6)	71(7)	68(7)	66(7)	64(6)	69(5)

5.11 Summary

Compound **3** and **4** were obtained in the same reaction pot. These compounds have the same molecular formula but differ in their coordination entities. Compound **3** crystallised in a monoclinic crystal system and space group $P2_1/c$ while **4** crystallised in a chiral space group $P4_32_12$. The overall structure of **3** is 3D while that of **4** is 2D. Although compound **3** was produced as the major phase in the first experiment, repeating the experiment under the same conditions lead to the isolation of **4** as the major phase. Attempts to optimise the reaction conditions to enhance the changes of producing **3** were unsatisfactory as compound **4** was formed in most cases.

The 2D coordination system $\{[Zn(34pba)_2].DMF\}_n$ **4**, undergoes a single crystal to single crystal transformation change on desolvation of the DMF molecules accompanied by a displacive phase change. The desolvated material $[Zn(34pba)_2]_n$ **4d**, shows a reconstructive phase change on incorporation of alcohol vapours as proven by cleavage of one the zinc-oxygen bond. This behaviour was confirmed by single crystal diffraction and infrared analysis

The breathing effect of **4d** was assessed from single crystal data and powder information. The unit cell volume was found to directly increase with an increment in the amount of carbon atoms in the alcohol. However uptake of *n*-hexanol brought about low volumetric breathing amplitude because of a geometrical limit above which expansion/opening of the cavities is not conceivable. The kinetics of breathing was assessed at 25 °C. Methanol, ethanol and *n*-propanol were absorbed instantly on introduction to the host compound. A dead time *(ca* 2 minutes) was seen before uptake of *n*-butanol. This was ascribed to the small size of the cavities in the closed form of **4d**; consequently *n*-butanol needed to interact with the host framework to trigger the movement of the 2D layers before it could move into the cavities. Previously reported breathing systems typically use high guest pressure which is regularly alluded to as the gate opening pressure. Remarkably, the framework here under study breathes at room temperature and pressure and the extent of breathing is controlled by the size and hydrophobicity of the alcohol guest molecules.

Vapour phase competition studies between methanol and *n*-butanol show that the 2D network selectively absorbed *n*-butanol in the presence of a high vapour pressure of methanol. The observed selectivity may be predicated on factors that permit the MOF inclusion compound to assume the most relaxed conformation.

Although the structure of **4d-butanol** could not be refined to acceptable levels, the desorption kinetics of *n*-propanol and *n*-butanol suggests that both guest molecules are located in the same chemical environment. Hence, it was concluded that *n*-butanol has the same conformation as *n*-propanol in the host framework.

5.12 References

1. C.-Y. Niu, X.-F. Zheng, Y. He, Z.-Q. Feng, and C.-H. Kou, *CrystEngComm*, 2010, **12**, 2847.

2. J.-Q. Liu, Y.-Y. Wang, L.-F. Ma, G.-L. Wen, Q.-Z. Shi, S. R. Batten, and D. M. Proserpio, *CrystEngComm*, 2008, **10**, 1123.

3. S. Wang, D. Wang, J. Dou, and D. Li, *Acta Crystallogr. C.*, 2010, **66**, 141.

4. C. F. Macrae, I. J. Bruno, J. A. Chisholm, P. R. Edgington, P. McCabe, E. Pidcock, L. Rodriguez-Monge, R. Taylor, J. van de Streek, and P. A. Wood, *J. Appl. Crystallogr.*, 2008, **41**, 466.

5. A. L. Spek, *Acta Crystallogr. D. Biol. Crystallogr.*, 2009, **65**, 148.

6. P. K. Thallapally, J. Tian, M. Radha Kishan, C. A Fernandez, S. J. Dalgarno, P. B. McGrail, J. E. Warren, and J. L. Atwood, *J. Am. Chem. Soc.*, 2008, **130**, 16842.

7. S. Henke, A. Schneemann, A. Wütscher, and R. A Fischer, *J. Am. Chem. Soc.*, 2012, **134**, 9464.

8. F. Millange, C. Serre, N. Guillou, G. Férey, and R. I. Walton, *Angew. Chem. Int. Ed. Engl.*, 2008, **47**, 4100.

9. L. Chen, J. P. S. Mowat, D. Fairen-jimenez, C. A. Morrison, S. P. Thompson, P. A. Wright, and T. Du, *J. Am. Chem. Soc.*,2013, **135**, 15763

10. S. Sanda, S. Parshamoni, and S. Konar, *Inorg. Chem.*, 2013, **52**, 12866.

11. Z. Wang and S. M. Cohen, *J. Am. Chem. Soc.*, 2009, **131**, 16675.

12. S. Sanda, S. Parshamoni, and S. Konar, *Inorg. Chem.*, 2013, 12866.

13. P. G. Yot, Q. Ma, J. Haines, Q. Yang, A. Ghoufi, T. Devic, C. Serre, V. Dmitriev, G. Férey, C. Zhong, and G. Maurin, *Chem. Sci.*, 2012, **3**, 1100.

14. J. Xiao, Y. Wu, M. Li, B.-Y. Liu, X.-C. Huang, and D. Li, *Chemistry*, 2013, **19**, 1891.

15. G. S. Pawley, *J.Appl. Crystallogr.*, 1981, 14, 357.

16. A. A. Coelho, *TOPAS-Academic, version 4.1 (Computer software)*, Coelho Software, Brisbane, 2007

17. Y.-S. Wei, K.-J. Chen, P.-Q. Liao, B.-Y. Zhu, R.-B. Lin, H.-L. Zhou, B.-Y. Wang, W. Xue, J.-P. Zhang, and X.-M. Chen, *Chem. Sci.*, 2013, **4**, 1539.

18. H.-L. Zhou, R.-B. Lin, C.-T. He, Y.-B. Zhang, N. Feng, Q. Wang, F. Deng, J.-P. Zhang, and X.-M. Chen, *Nat. Commun.*, 2013, **4**, 2534.

19. G. Férey and C. Serre, *Chem. Soc. Rev.*, 2009, **38**, 1380.

20. G. F. de Lima, A. Mavrandonakis, H. A. de Abreu, H. A. Duarte, and T. Heine, *J. Phys. Chem. C*, 2013, **117**, 4124.

21. C. Serre, C. Mellot-Draznieks, S. Surblé, N. Audebrand, Y. Filinchuk, and G. Férey, *Science*, 2007, **315**, 1828.

22. L.-H. Xie and M. P. Suh, *Chemistry*, 2011, **17**, 13653.

23. J. J. Gutiérrez-Sevillano, D. Dubbeldam, L. Bellarosa, N. López, X. Liu, T.J.H. Vlugt and S. Calero, *J. Phys. Chem. C*, 2013, 117, 20706.24. K. Zhang, R. P. Lively, M. E. Dose, A. J. Brown, C. Zhang, J. Chung, S. Nair, W. J. Koros, and R. R. Chance, *Chem. Commun.*, 2013, **49**, 3245.

25. J. C. Saint Remi, T. Rémy, V. Van Hunskerken, S. van de Perre, T. Duerinck, M. Maes, D. De Vos, E. Gobechiya, C. E. a Kirschhock, G. V Baron, and J. F. M. Denayer, *ChemSusChem*, 2011, **4**, 1074.

26. M. Lusi and L. J. Barbour, *Angew. Chem. Int. Ed. Engl.*, 2012, **51**, 3928.

27. H. J. Borchardt and F. Daniels, *J. Am. Chem. Soc.*, 1957, **79**, 41.

28. G. Mehlana, S. A. Bourne, G. Ramon, and L. Öhrström, *Cryst. Growth Des.*, 2013, **13**, 633.

Chapter 6

4-(4-pyridyl)benzoate compounds of Co(II) or Ni(II)

Two isostructural compounds of Co(II) and Ni(II) assembled using a linear ditopic linker 4-(4-pyridyl)benzoate (44pba) are presented in this chapter. These compounds differ in their solvent content. Both compounds display water induced phase transformation with chromotropism which has been studied using TGA and PXRD analysis. Solvatochromism is evident in this class of compounds with crystals exhibiting a range of colours depending on the solvent included in the channels. Techniques such as TGA, PXRD and UV-Vis spectroscopy have been used to characterise the two isostructural compounds and their subsequent inclusion compounds formed by exposing their activated phases to a wide range of solvent molecules.

6.1 4-(4-pyridyl)benzoic acid (5)

Single crystals of the compound 4-(4-pyridyl)benzoic acid (**5**) were obtained after slow evaporation of dimethylformamide (DMF) for a period of two weeks. The compound could also be crystallised in solvents like dimethylsulfoxide (DMSO) and dimethylacetamide (DMA). Compound **5** was used for the synthesis of compounds **6** and **7**.

PXRD studies shows that bulk of the material was compound **5**. The calculated pattern matches well with the experimental pattern (Figure 6.1)

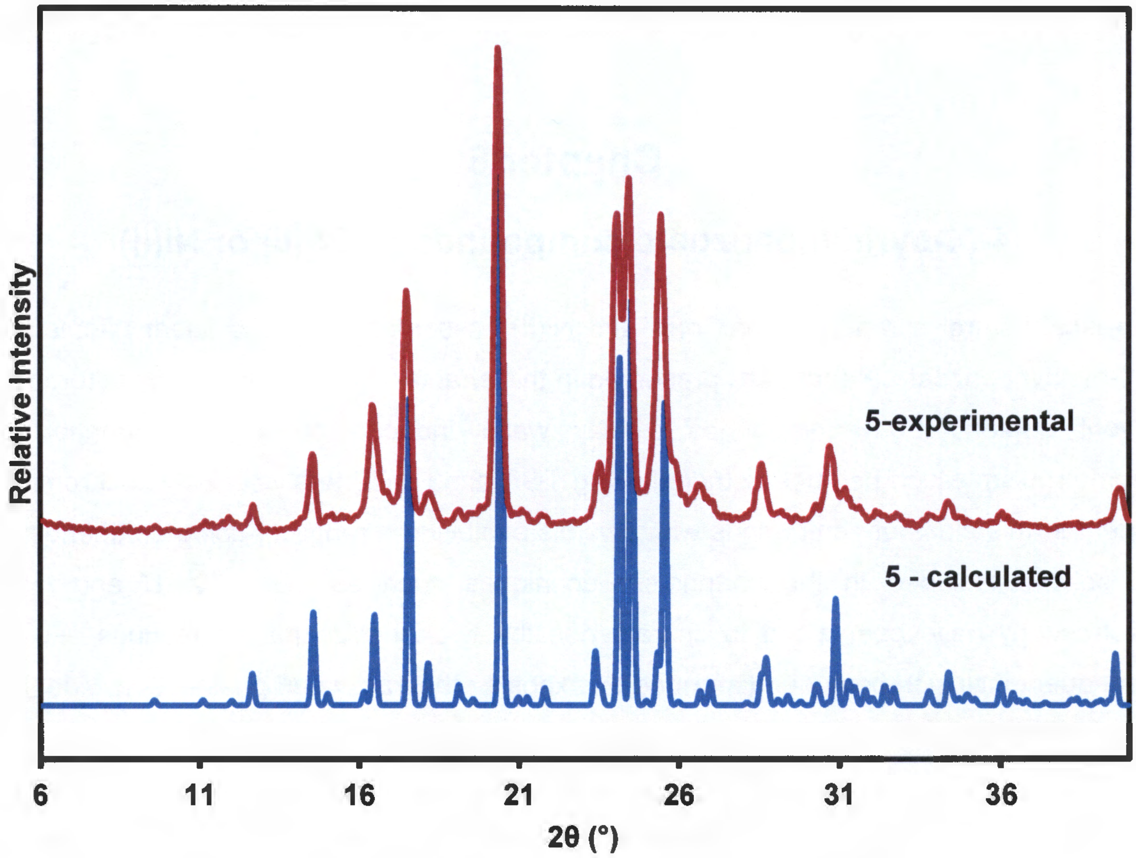

Figure 6.1: PXRD of compound **5**: the calculated pattern from single crystal data matches the experimental pattern which confirms that bulk material was compound **5**.

6.1.1 Single crystal X-ray diffraction

Structure solution and refinement details are given in Chapter 2 section 2.7.1. Hydrogen atoms were located on the Fourier electron density map and were refined isotropically with temperature factors of 1.2 times the parent atoms they were attached to. Table 6.1 lists the crystallographic and refinement parameters of **5**.

Table 6.1: Crystallographic and refinement parameters of **5**

	5
Empirical Formula	$C_{12}H_9NO_2$
M_r (g·mol^{-1})	199.2
Temperature (K)	173(2)
Crystal size (mm^3)	0.13 x 0.08 x 0.03
Crystal system	Orthorhombic
Space group	$P2_12_12_1$
a (Å)	10.748(1)
b (Å)	11.800(1)
c (Å)	14.728(2)
V(Å^3)	1867.9(3)
Z	8
Calculated density/ (g·cm^{-3})	1.417
F(000)	832
(Mo-K$_\alpha$) (mm^{-1})	0.098
θ range scanned (°)	2.21 – 27.17
Index h, k, l range	-9:13, -15:13, -17:18
Reflections collected	6844
No. unique data	4121
No. data with $I > 2\sigma(I)$	2564
final R ($I > 2\sigma(I)$)	0.0549
final $wR2$ (all data)	0.1151
Goodness of fit, s	0.970
Max, min e density (eÅ^{-3})	0.20, -0.21

6.1.2 Structural description of 4-(4-pyridyl)benzoic acid

X-ray crystal structure diffraction revealed that the compound crystallises in the orthorhombic space group $P2_12_12_1$. The asymmetric unit consists of two anti-parallel crystallographically independent molecules as shown is Figure 6.2a. The dihedral angles between the pyridyl and phenyl ring are 40° and 34.9° for ligand A and B respectively. The two molecules in the asymmetric unit show little variation in the torsion angle of the carboxylate group relative to the phenyl ring. The carboxylate group is almost co-planar with the phenyl ring. Solid state packing of the compound shows that intermolecular hydrogen bonds link neighbouring molecules into infinite chains which grow along the *b*-axis as depicted in Figure 6.2.b.

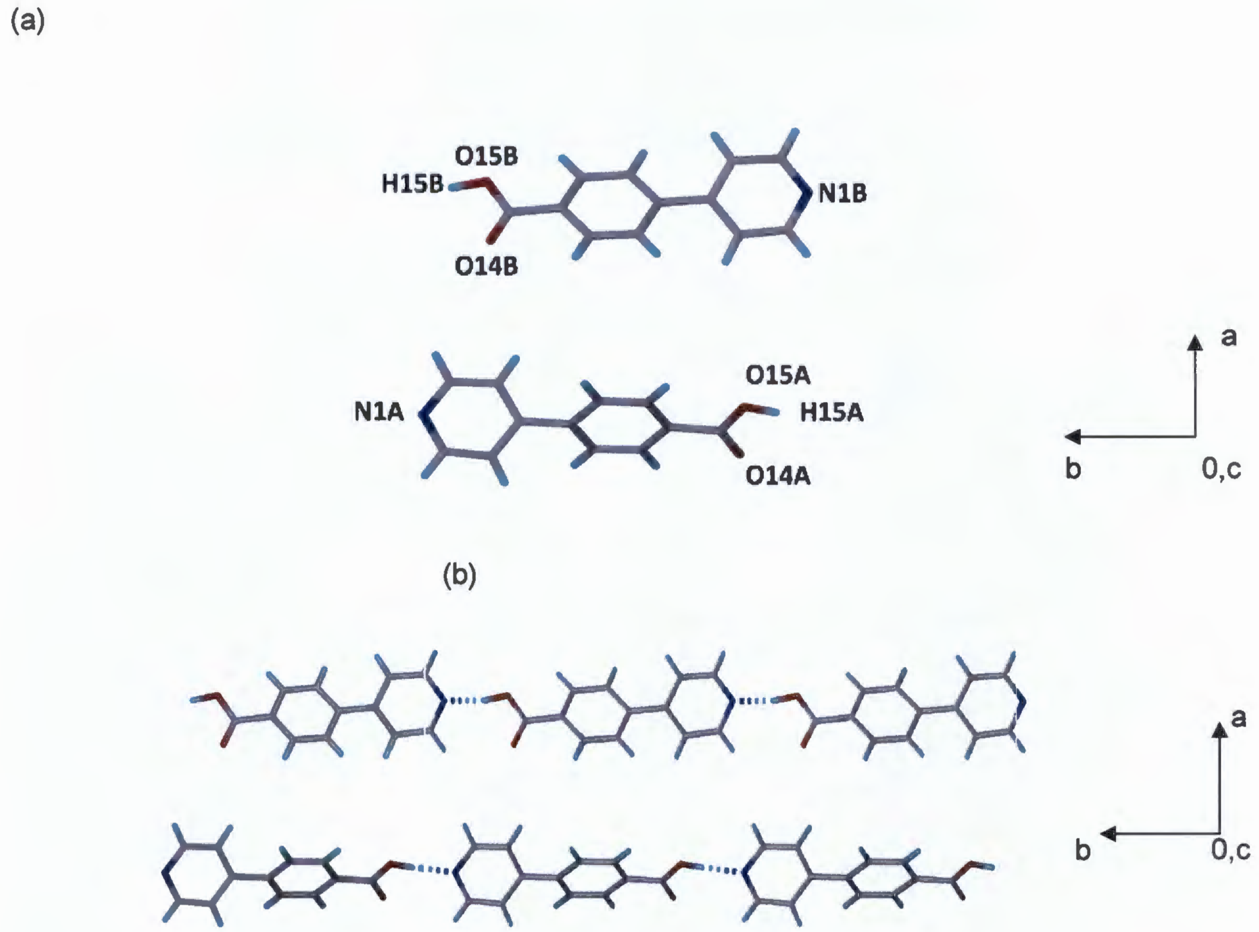

Figure 6.2: (a) Two molecules are modelled in the asymmetric unit of **5**; (b) packing diagram of **5** demonstrating hydrogen bonding interactions. The hydrogen bonded chains grow along the *b*-axis.

Adjacent anti parallel chains are linked by weak hydrogen bonding interactions. Table 6.2 lists some hydrogen bonding parameters of compound **5**. The hydrogen bonding interactions ranges from 2.612(3) to 3.511(4) Å with angles of 135 - 175°. Hydrogen bonding angles in the range of 135° to 175° show that medium to strong hydrogen bonds prevail in this structure. The distance of 3.633 Å on adjacent offset phenyl rings indicates the presence of π – π stacking interactions.

Table 6.2: Geometric parameters for O-H...N and C-H...O hydrogen bonds

Donor - H...Acceptor	***d(H...A)/Å***	***d(D...A)/Å***	***<(D-H...A)/°***	***Symmetry operator***
O15A - H15A...N1A	1.71	2.623(3)	175	x, -1+y, z
O15B - H15B...N1B	1.60	2.612(3)	166	x, 1+y, z
C2A - H2A...O14A	2.45	3.189(4)	135	½+x, 3/2-y, -z
C9A - H9A...O14B	2.58	3.511(4)	165	1-x, -½+y, ½-z
C12B - H12B..O14A	2.34	3.190(4)	148	½-x, 1-y, ½+z

6.2 Thermal analysis of 5

The thermal stability of the compound was evaluated by TGA, DSC and HSM studies. The TGA and DSC trace of compound **5** are displayed in Figure 6.3. The two profiles show that no guest was included as they are featureless until decomposition above 200 °C. In the DSC trace, a double endotherm is observed at about 342 and 370 °C which correspond to melting and decomposition respectively. HSM studies were conducted within a temperature range of 25 to 340 °C. HSM images of **5** were captured at different temperatures as shown in Figure 6.4. Crystals turned opaque on heating to high temperatures and melting was observed at about 340 °C. This concurs with the thermal events observed on the DSC.

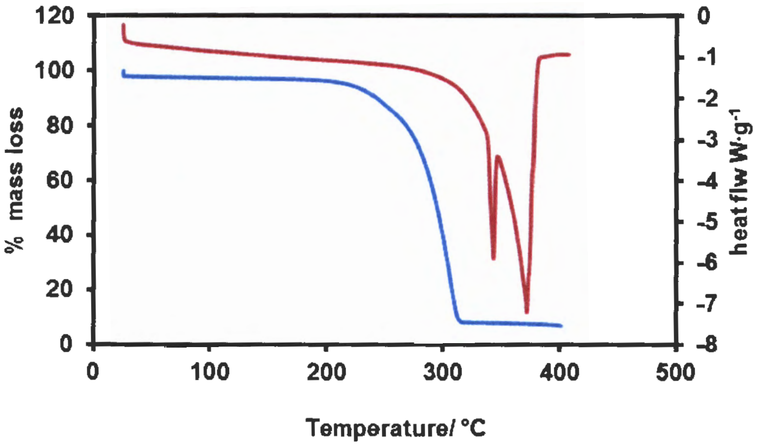

Figure 6.3: An overlay of the DSC(red) and TGA (blue) of the compound **5**

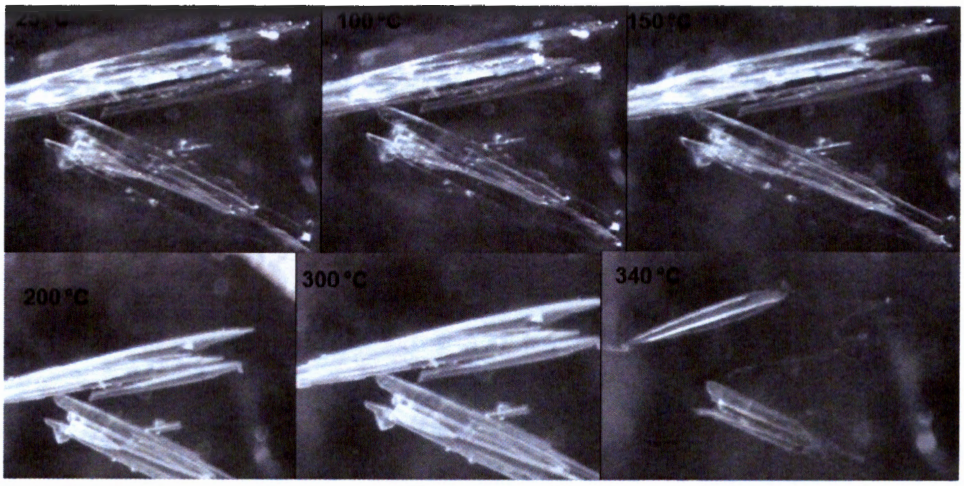

Figure 6.4: Hot Stage Images of compound **5**. Crystals of **5** melts at about 340 °C. This is in agreement with the endothermic peak observed on the DSC of **5**

6.3 Synthesis of compound $\{[Co_4(44pba)_8]\cdot4DMF\cdot0.5EtOH\cdot4H_2O\}_n$ (6) and $\{[Ni_4(44pba)_8]\cdot4DMF\cdot0.5EtOH\cdot3H_2O\}_n$ (7)

Compound **6** and **7** were synthesised under the same conditions (44pba in the formula represents 4-(4-pyridyl)benzoate). The two compounds are isostructural and comprise of different guest content in their channels. Figure 6.5 displays the PXRD patterns for these compounds calculated from their single crystal structures.

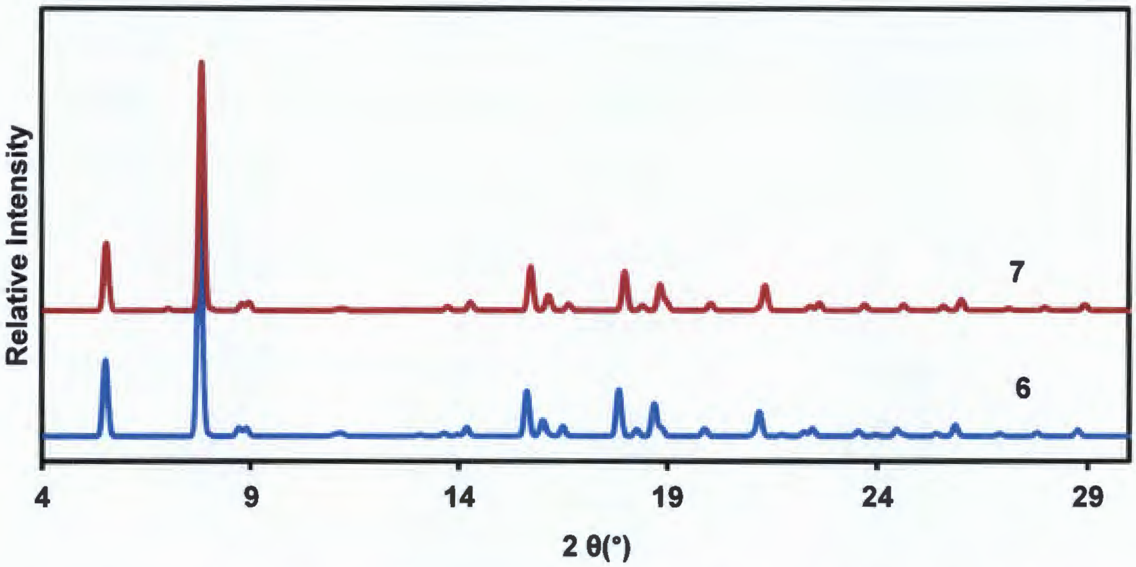

Figure 6.5: Simulated PXRD patterns of compound **6** and **7**. The two traces are the same which illustrates that the compounds are isostructural.

Crystals of **6** and **7** were obtained under solvothermal conditions. Compound **6** was prepared by dissolving 80 mg (0.4 mmol) of 4-(4-pyridyl)benzoic acid in 5 cm^3 of DMF with heating and stirring. 29 mg (0.1 mmol) of $Co(NO_3)_2.6H_2O$ was dissolved in $2cm^3$ of ethanol with stirring. The two solutions were mixed and sealed in a 15 cm^3 Teflon - lined bomb and placed for three days in an oven which was preset at 105 °C. Purple prismatic crystals were obtained. The same method was used to prepare green crystals of compound **7** using $Ni(NO_3)_2.6H_2O$. It was noted that the compounds could be made over a temperature range of 105 to 130 °C. High yields were obtained at 130 °C while temperatures below 105 and above 130 °C resulted in the formation of powdered samples. Compound **6** and **7** could also be obtained from metal salts of cobalt acetate and nickel acetate respectively. Figure 6.6 displays a comparison of the experimental and calculated PXRD patterns of **6** and **7**. The experimental PXRD of both compounds matches their respective calculated patterns which indicate that both **6** and **7** were produced as the bulk phase. The slight offset in peak positions is ascribed to the different temperatures at which the experiments were performed.

Single crystal data was collected at -100 °C while the PXRD was done at room temperature. Reliable elemental analysis for **6** and **7** to confirm the given formula was impeded by rapid loss of the guest molecules upon removing the crystals from their respective mother liquor.

Compounds $[Co(44pba)_2]_n$ **(6d)** and $[Ni(44pba)_2]_n$ **(7d)** were prepared by drying crystals of **6** and **7** under vacuum at 200 °C for 10 hours. Elemental analyses of **6d** and **7d** agrees well with the proposed formulae. Found for **6d**: C 62.89; H 4.08; N 5.84%. Calculated for **6d** ($CoC_{24}H_{16}O_4N_2$): C 63.31; H 3.54 N 6.15%. Found for **7d**: C 63.12; H 3.72; N 5.98. Calculated for **7d** ($NiC_{24}H_{16}O_4N_2$): C 63.34; H 3.54; N 6.16%

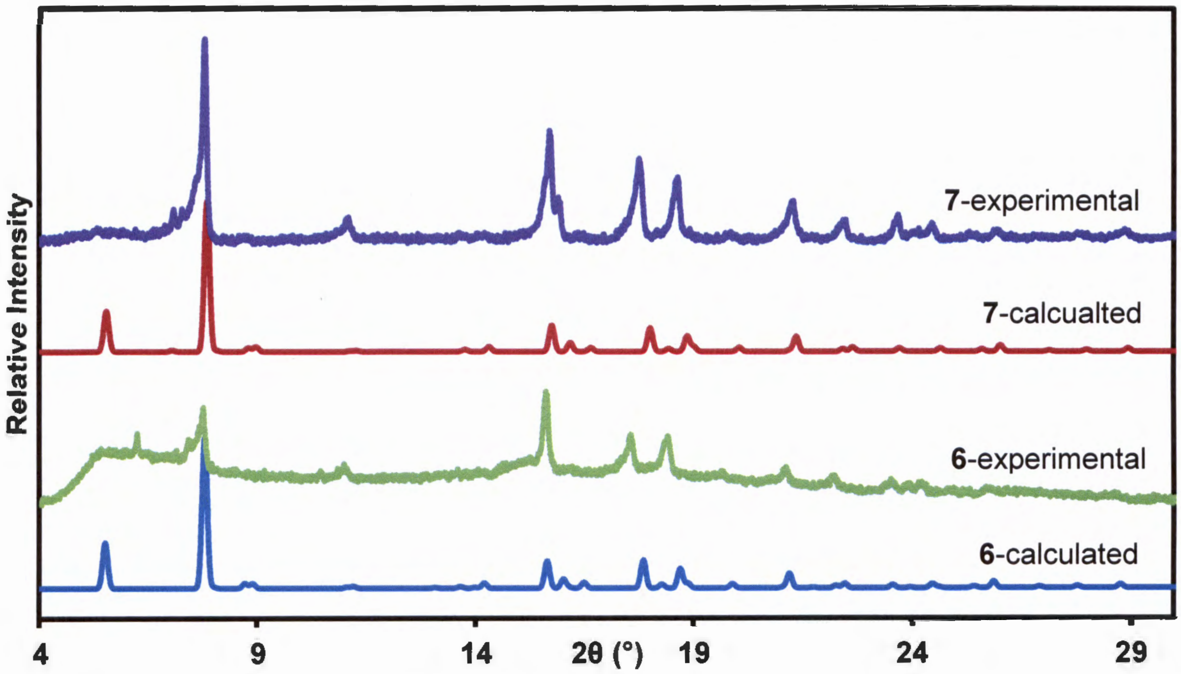

Figure 6.6: A comparison of the calculated patterns from single crystal structure with the experimental data obtained by powder diffraction studies.

6.4 Single crystal X-raydiffraction of 6 and 7

6.4.1 Refinement procedures

The general structure solution and refinement details are described in chapter 2 section 2.7.1. All the carbon atoms of the frameworks were refined with an anisotropic temperature factors. Due to solvent disorder that is normally encountered in highly porous metal organic frameworks, some of the non hydrogen atoms of the guest molecules were refined isotropically. All hydrogen atoms were refined isotropically with temperature factors that are 1.2 times their parent atoms in the framework and 1.5 times for those attached to the guest molecules. Hydrogen atoms for the water guest molecules could not be modelled satisfactorily.

The N – C (methyl carbon atoms), C – O, and N – C (carbonyl carbon atoms) bond distance of the DMF molecules were restrained to bond distances of 1.445 Å, 1.230 Å and 1.321Å respectively with a standard deviation of 0.005 Å. A total of 29 and 38 restraints were applied to the refinement of the guest molecules in the channels of compound **6** and **7** respectively.

Crystals of **6** and **7** exhibited merohedral twinning. The BASF factor for this twinning was determined in PLATON[1] and was found to be 0.49 and 0.46 for **6** and **7** respectively. For compound **6**, the twin law (0 -1 0) (-1 0 0) (0 0 -1) was used after locating all the atoms and the refinement brought down the R-factor from 14% to values below 9%. However, refinement of **7** with the twin law could not bring down the R-factor to acceptable values, hence only the TWIN command was used for **7**. The crystallographic and refinement parameters for compound **6** and **7** are given in Table6.3.

Table 6.3: Crystallographic and refinement parameters for compound **6** and **7**

	6	**7**
Empirical Formula	$\{[Co_4(44pba)_8]\cdot 4DMF\cdot 0.5EtOH\cdot 4H_20\}_n$	$\{[Ni_4(44pba)_8]\cdot 4DMF\cdot 0.5EtOH\cdot 3H_20\}_n$
M_r ($g\cdot mol^{-1}$)	2208.82	2189.83
Temperature (K)	173(2)	173(2)
Crystal size (mm^3)	0.26 x 0.26 x 0.25	0.30 x 0.26 x 0.25
Crystal system	tetragonal	tetragonal
Space group	*I4*	*I4*
a (Å)	31.982(1)	31.820(2)
c (Å)	25.332(1)	25.115(2)
V ($Å^3$)	25911(1)	25429(3)
Z	8	8
density/ ($g\cdot cm^{-3}$)	1.1323	1.1438
F(000)	9160	9112
(Mo-K_α) (mm^{-1})	0.565	0.646
θ range scanned (°)	1.64-27.34	1.64-28.29
Index range	-41:41, -31:24, -32:19	-38:42, -42:41, -33:33
Reflections collected	47724	90225
No. unique data	21374	31528
No. data with $I > 2\sigma(I)$	11366	17448
final R ($I > 2\sigma(I)$)	0.0803	0.1400
final $wR2$ (all data)	0.2911	0.4337
Goodness of fit, s	1.025	1.072
Max, min e density(eA^{-3})	1.10, -0.85	2.03, -1.99*

*the peak 2.03 and deepest hole -1.99 are located close to Ni3 and N1A atoms respectively in the crystal structure of **7**

6.4.2 Structural description of compound 6 and 7.

Compound **6** and **7** are iso-structural and crystallise in the same space group *I4*. Hence the full structural description of compound **7** is not given. The asymmetric unit of **6** contains four crystallographically independent cobalt centres. Each Co(II) centre is bonded to four 44pba ligands via four Co – O and two Co – N bonds as illustrated in Figure 6.7. The Co – O bond length ranges from 2.032(11) to 2.371(12) Å while the Co – N is within the range of 1.984(15) to 2.122(10) Å. The overall geometry around each metal centre is a distorted octahedron due to the bidentate binding mode of the carboxylate moieties. The bond lengths around each metal centre are very similar and are given in Table S6.1 - 6.2. The average bond lengths for Co – O and Ni – O in **6** and **7** were found to be 2.161 ± 0.12 Å and 2.117 ± 0.08 Å respectively. The average metal to nitrogen donor atom bond distance is longer in **6** (2.058 ± 0.45 Å) in comparison to that of **7** (2.037 ± 0.20 Å)

The torsion angles between the pyridyl and phenyl rings in all 8 ligands are different. (Table 6.4). This accounts for the observed four crystallographically independent M(44pba)$_2$ (where M is Co(II) or Ni(II)) units which make up the framework.

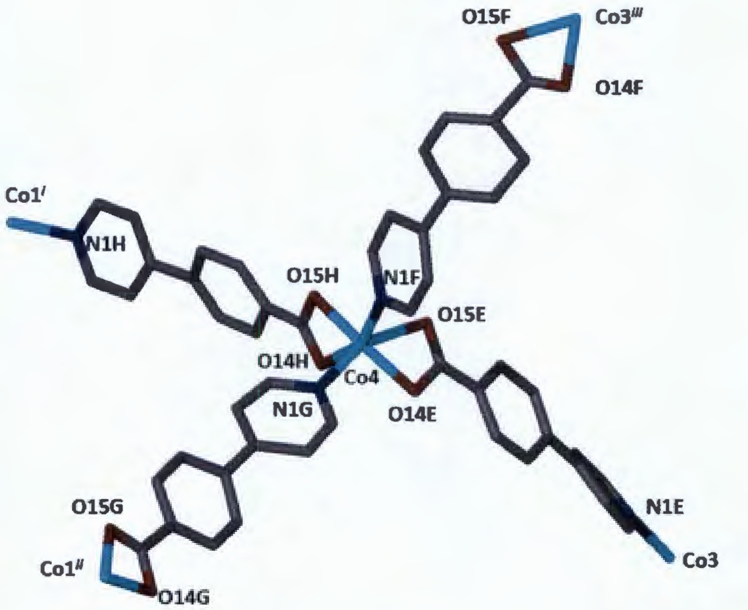

Figure 6.7: Coordination environment of the Co(II) in **6** showing some of the atom labels used. The other ligands not shown in this structure are labelled with suffices, A, B, C and D. Hydrogen atoms have been omitted for clarity. Symmetry operator ^{i}5/2-x, ½-y, ½+z; ^{ii}1+x, 1+y, z; ^{iii}5/2-x, 3/2-y, ½+z

Table 6.4: Torsion angles between the pyridyl and phenyl ring in compounds **6** and **7**

Atom labels	*A*	*B*	*C*	*D*	*E*	*F*	*G*	*H*
Compound **6**								
C5 - C4 - C7 - C8 (°)	27(2)	31(2)	21(2)	3(2)	36(2)	43(2)	27(2)	22(2)
Compound **7**								
C5 - C4 - C7 - C8 (°)	25(1)	22(2)	23(1)	24(2)	27(2)	39(2)	21(1)	29(1)

The overall structure of the network in **6** is constituted by the assembly of 4 diamond nets with large hexagonal channels which form helical chains parallel to [001] (Figure 6.8.a). In each diamond net, the distance of separation between two Co(II) centres is about 13.2 Å. The maximum dimension of a single diamondoid cavity is 26.9 Å (measured from one cobalt centre to the opposite cobalt centre). As a result of the void present with large hexagonal channels found in one single net, four individual nets interpenetrate each other. They fill all the hexagonal channels to give rise to channels running along the *c*-axis as illustrated in Figure 6.8.b and c.

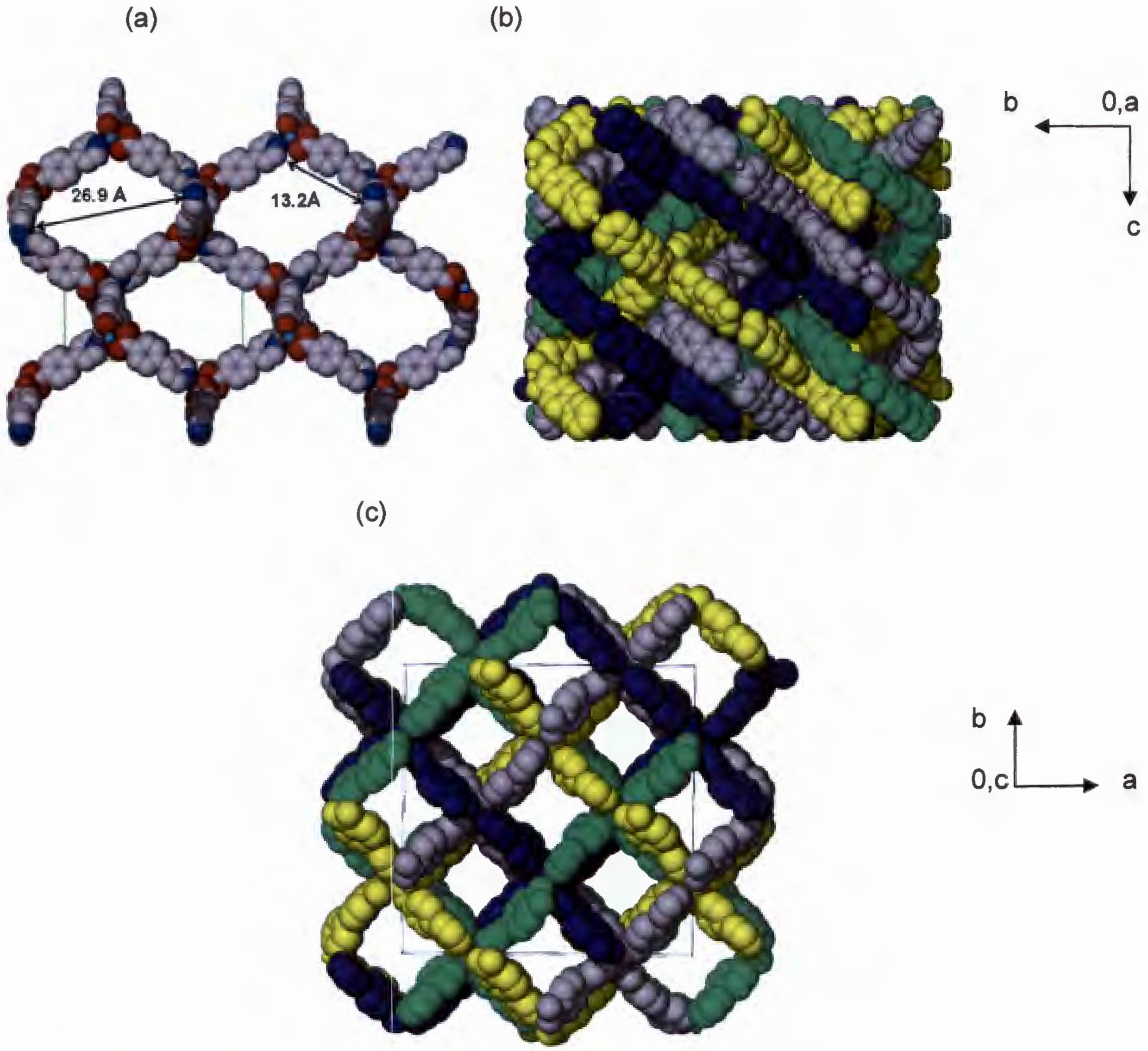

Figure 6.8: (a) Single net found in **6** showing large hexagonal channels as viewed along the [100] direction, (a) is the yellow network in (b), (b) the large hexagonal channels are completely filled up by the four interpenetrating networks, (c) despite this interpenetration, channels running along the *c*-axis are observed. These channels are occupied by guest molecules and account for 47% of the unit cell volume in both **6** and **7**.

Hydrogen bonds exist between adjacent diamond nets and between helical chains in the *a* and *b* plane. These are in the range of 2.782(19) - 3.35(2) Å with angles of 100 - 148° (Table 6.5) for compound **6** while for **7** they are in the range of 2.982(15) to 3.382(18) with angles of 121 -157° (Table 6.6). Hydrogen interactions observed in this structure also account for the high thermal stability[2] which will be discussed in section 6.5.

Table 6.5: Hydrogen bonding parameters in **6**

Donor -H...Acceptor	*H...A(Å)*	*D...A(Å)*	*D - H...A(°)*	*Symmetry Operator*
[a]C2D - H2D...O14F	2.45	*3.30(2)*	*148*	2-y,-1+x,z
[a]C2H - H2H...O15D	2.56	3.20(2)	125	1+x,y,z
[a]C2H - H2H...O15H	2.45	3.30(2)	150	1+y,2-x,z
[b]C3A - H3A...OK1	2.52	3.42(2)	158	2-y,-1+x,z
[b]C3E - H3E...OM1	2.59	3.46(2)	151	3/2-y,-1/2+x,-1/2+z
[a]C3G - H3G...O15F	2.48	3.35(2)	152	3/2-y,-1/2+x,-1/2+z
[b]C5A - H5A...O14D	2.45	3.35(2)	157	3/2-y,-1/2+x,-1/2+z
[a]C5C - H5C...OJ1	2.46	3.37(3)	162	
[a]C5E - H5E...O14H	2.53	3.35(2)	144	2-y,-1+x,z
[a]C5F - H5F...O14G	2.52	3.34(2)	145	1/2+y,5/2-x,1/2+z
[b]C5G - H5G...OL1	2.47	3.41(2)	169	
[a]C6B - H6B...O14F	2.45	3.09(2)	124	x,-1+y,z
[a]C6B - H6B...O14B	2.54	3.33(2)	140	1+y,1-x,z
[a]C6F - H6F...O15H	2.35	2.98(2)	123	
[a]C6F - H6F...O15D	2.54	3.35(2)	143	2-y,x,z
[a]C9A - H9A...O14A	2.43	2.75(2)	100	
[a]C9B - H9B...O14B	2.54	2.86(2)	100	
[a]C11G - H11G...O15G	2.47	2.79(2)	100	
[b]CK4 - HK4A...OK1	2.32	2.74(2)	105	
[b]C12G - H12G...OL1	2.46	3.37(3)	161	
[b]CL4 - HL4C...OL1	2.39	2.75(3)	100	
[b]CL5 - HL5B...OK1	2.59	3.51(3)	156	

[a]Framework-framework interactions; [b]guest-framework interactions

Table 6.6: Hydrogen bonding parameters in **7**

Donor - H...Acceptor	***H...A(Å)***	***D...A (Å)***	***D - H...A(°)***	***Symmetry Operator***
[a]C2A - H2A...O15D	2.52	3.11(1)	121	7/2-x,3/2-y,1/2+z
[a]C2B - H2B...O14F	2.40	3.24(2)	147	2-y,x,z
[a]C2B - H2B...O14H	2.37	2.99(2)	123	5/2-x,3/2-y,-1/2+z
[a]C2C - H2C...O14A	2.59	3.16(2)	119	
[a]C2E - H2E...O14F	2.53	3.14(2)	122	
[a]C2H - H2H. ..O14H	2.45	3.28(2)	145	1+y,1-x,z
[a]C2H - H2H...O14F	2.35	2.98(2)	123	5/2-x,1/2-y,1/2+z
[b]C3A - H3A...O1K	2.39	3.32(2)	166	
[a]C3C - H3C...O15H	2.52	3.38(2)	151	2-y,x,z
[b]C3E - H3E...O1J	2.49	3.41(2)	162	3/2-y,-1/2+x,-1/2+z
[a]C3G - H3G...O14B	2.42	3.31(2)	156	y,2-x,z
[a]C3H - H3H...O14C	2.57	3.38(2)	143	y,2-x,z
[a]C5A - H5A...O15F	2.49	3.34(2)	149	1+y,2-x,z
[b]C5C - H5C...O1M	2.4	3.33(2)	169	
[a]C5E - H5E...O14D	2.45	3.35(2)	157	1/2+y,5/2-x,1/2+z
[a]C5F - H5F...O15A	2.55	3.36(2)	144	2-y,-1+x,z
[b]C5G - H5G...O1L	2.55	3.45(2)	157	-1/2+x,-1/2+y,1/2+z
[b]C5J - H5J3...O1J	2.34	2.76(2)	105	
[a]C6C - H6C...O15B	2.53	3.13(2)	121	
[a]C6D - H6D...O15B	2.37	3.00(2)	124	
[a]C6D - H6D...O15D	2.46	3.31(2)	148	1+y,3-x,z
[a]C6E - H6E...O15G	2.58	3.15(1)	119	
[a]C6F - H6F...O15D	2.43	3.05(2)	122	-1+x,y,z
[a]C6F - H6F...O15B	2.49	3.36(2)	151	2-y,-1+x,z
[a]C6G - H6G...O14H	2.54	3.14(2)	121	
[b]C8A - H8A...O1K	2.57	3.47(2)	159	
[b]C4L - H4N...O1L	2.36	2.77(2)	104	
[b]C12C - H12C...O1M	2.54	3.42(2)	154	
[b]C4M - H4M2...O1M	2.37	2.78(3)	104	

[a]Framework-framework interactions; [b]guest-framework interactions

There exist three distinct channels in **6** which differ in their guest contents. Figure 6.9 displays the crystal packing diagram of compound **6** with channels labelled A, B and C.

These channels account for 47% of the unit cell volume estimated using the PLATON. Channel A centred at (0 ½ z) contains ethanol molecules and several disordered water molecules. Channel B, centred at (¼ ¼ z) contains DMF and water while channel C centred at (½ ½ z) contains water molecules only. Compound **7** exhibits a similar guest arrangement in its channels except that channel C comprises of ethanol and water molecules.

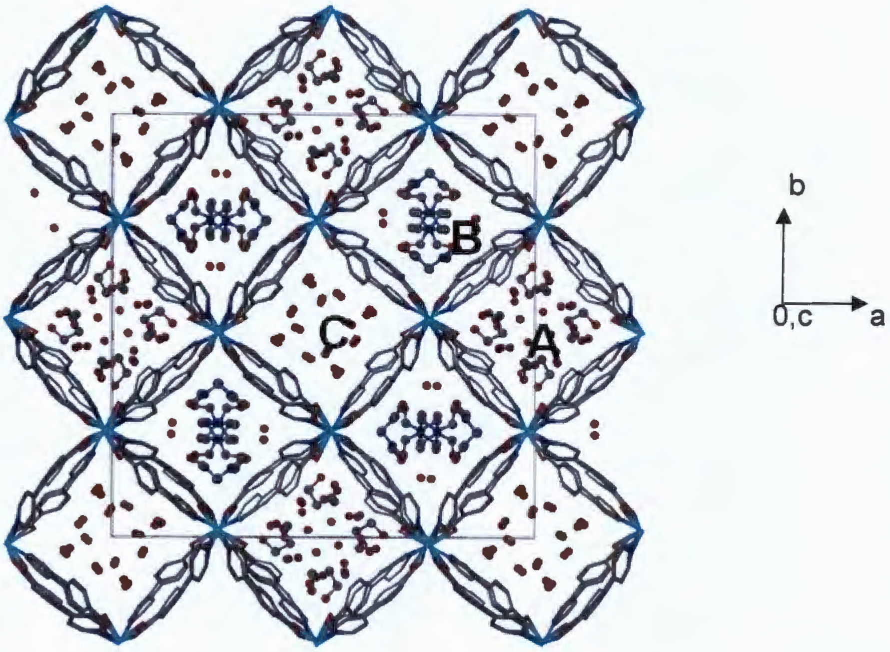

Figure 6.9: Crystal packing of compound **6** displays three distinct channels. The framework has been drawn in stick form while the guest ethanol and DMF are displayed in ball and stick form. The water molecules are drawn as red spheres. Channel A comprises ethanol and water, B is occupied by water and DMF and C comprises of water molecules alone.

The total solvent content in the channels was estimated from TGA and was used to model the relevant site occupancies of the guest molecules. It is expected that the solvent content may differ from crystal to crystal owing to the large channels found in this compound. For the selected crystal, a total of 4 DMF molecules were modelled in **6** and were disordered over four positions, a total of 4 water molecules disordered over sixteen positions and two ethanol molecules were located, each with a refined site occupancy of 0.25. All the DMF molecules in the channels interact with the framework through weak to moderate C – H ...O hydrogen bonding interactions. These range from 2.75(3) – 3.46(2) Å with angle of 100 - 158° (Table 6.5).

In the crystal structure of **7**, a total of 4 DMF molecules were modelled and were disordered over four positions. Two ethanol positions were located each with a site occupancy of 0.25

and 11 positions were modelled for a total of 3 water molecules per asymmetric unit. The relevant site occupancies of the guest molecules were modelled from TGA analysis. As noted in the structure of **6**, all DMF guest molecules in compound **7** interact with the host framework through hydrogen bonding interactions ranging from 2.982 – 3.382 Å (Table 6.6)

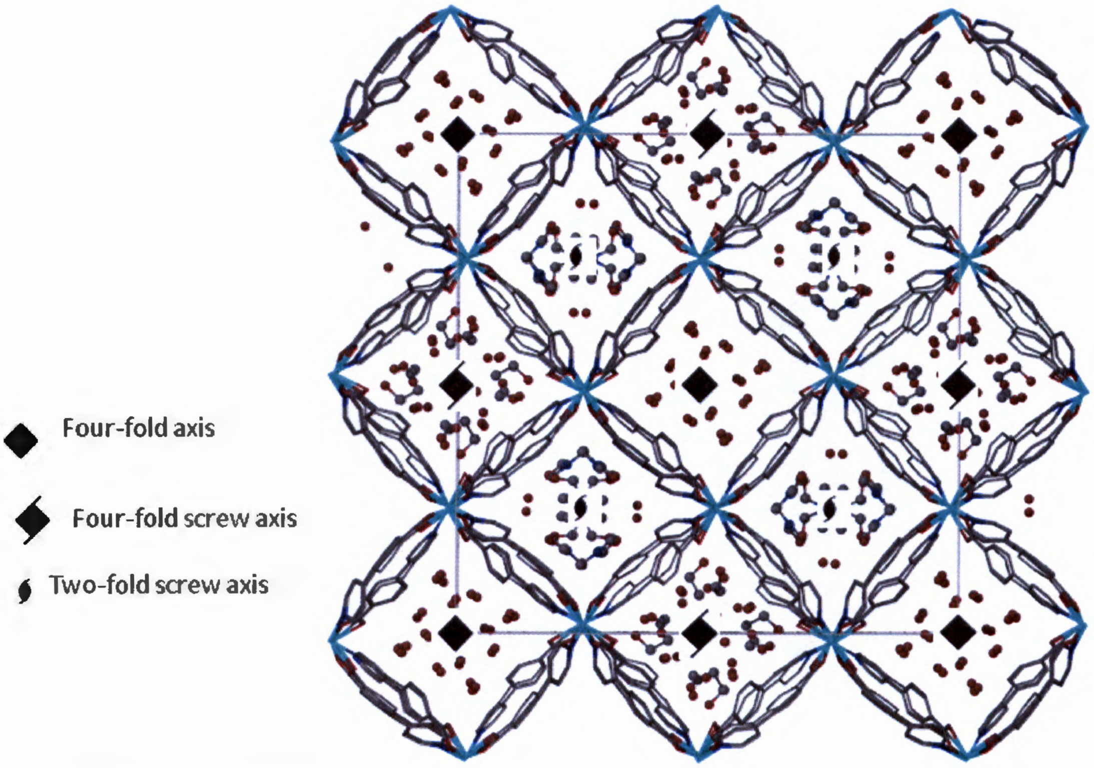

Figure 6.10: Symmetry elements found in the *I4* space group. The structure of **6** is given as an example.

Figure 6.10 displays the symmetry elements in the space group *I4*. The four-fold screw axis at (0 ½ z) which run along the [0 0 1] direction is surrounded by water and ethanol molecules. The two-fold screw axis is at (¼ ¼ z) and also runs along the *c*-direction and passes through the DMF molecules. A four-fold rotational symmetry operator running along the [0 0 1] direction located at (½ 0 z) and is surrounded by water molecules only. The channel selectivity observed in **6** and **7** may be explained in terms of the shape, crystallographic environment and the nature of interaction present on the surface of their channels. Channel A and C have a four-fold screw axis and four-fold rotational axis at the centre of the channels respectively while channel B has a two-fold screw axis. This gives rise to different geometries of the channels as illustrated in Figure S6.1. Furthermore, the packing diagram of **6** and **7** shows that the π···π interactions are more prominent along the walls of channel B. This implies that there are different electrostatic interactions present in these channels. These interactions arise as a result of the non-translating interpenetration symmetry elements and translating interpenetration vectors that construct the four-fold interpenetrated networks in the iso-structural compounds.

Topological analysis of **6** and **7** in TOPOS[3] revealed a four-fold uninodal **dia** network. The vertex symbol and point symbol for this net is $6_2.6_2.6_2.6_2.6_2.6_2$ and 6^6 respectively. Figure 6.11 displays the topological representation of the net found in **6** and **7**. Four-fold interpenetration of the nets is observed as a result of the large channels found in a single **dia** net.

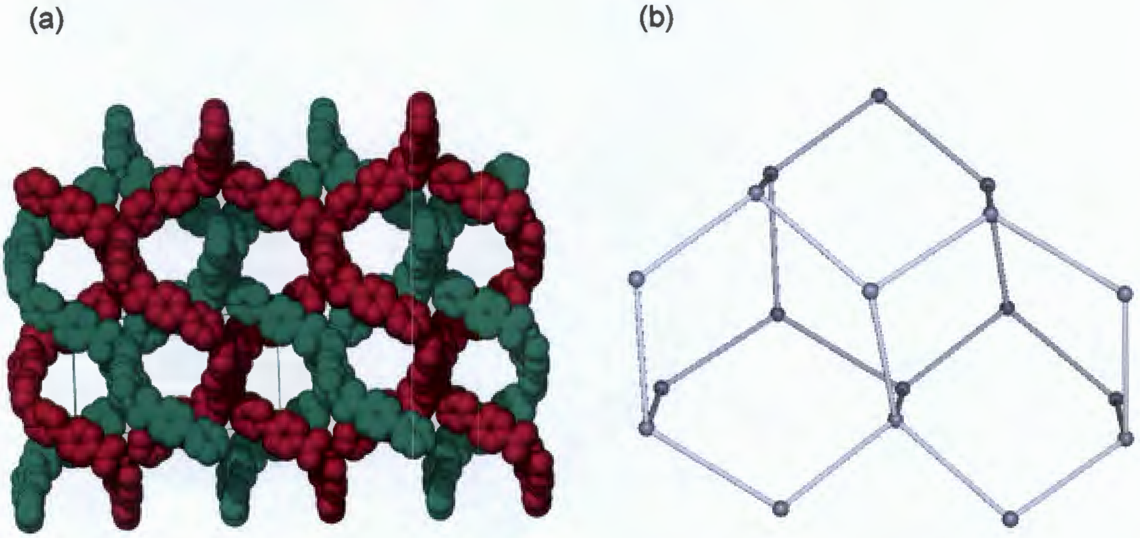

Figure 6.11: (a) Two-fold interpenetrating dia nets. The overall interpenetration is four-fold as displayed in Figure 6.8. (b) Topological representation of the dia net found in **6** and **7**. Each grey node represents the metal centres which are 4-connected.

A study conducted by O'Keeffe and co-workers revealed that the **dia** net is the most encountered net in 4-connected 3D networks.[4] They concluded that the most important nets are regular with one kind of node, edge, face, tile and of high symmetry. The authors substantiate high symmetry criteria based on the fact that the preparation of MOFs involves employing simple components that have maximum degrees of freedom and highly symmetric binding environments, thus these components would assemble to give nets of the highest possible symmetry. This assumption explains why the **dia** net is the most frequently encountered form of net in 4-connected 3D systems.

In consequence, the reaction of 4-(4-pyridyl)benzoic acid and Co(II) or Ni(II) could have been expected to give a **dia** network. This is because the Co and Ni can easily adopt an octahedral geometry, but because of the chelation of the carboxylate groups these metal centres function as tetrahedral nodes in the network when coordinated to a ditopic linker.

6.5 Thermal Analysis of 6 and 7

Figure 6.12 shows the TGA and DSC analysis of compound **6** and **7**. Attempts were made to distinguish between losses of different solvents by using lower heating rates. However, no distinct mass losses were obtained. The TGA profile of **6** shows a total weight loss of 16.4% within a temperature range of 26 to 134 °C. This total mass loss corresponds to the release of the guests: ethanol, water and DMF molecules from the channels in the crystal structure (calculated 17.5%). The DSC trace of **6** displays two endothermic peaks at 95 and 120 °C which correspond to multistep guest loss observed on the TGA. It is most likely that the first endothermic peak at 95 °C is attributed to the associative loss of ethanol and water, while the one observed at 120 °C is due to release of high boiling point solvent DMF. An exothermic peak in the DSC trace of **6** is observed at 312 °C which may be associated with a phase change before decomposition of the guest free network at about 456 °C.

Thermal analysis of **7** is very similar to that of **6**. The TGA of **7** shows a single step, total mass loss of 17.3 % within a temperature range of 26 – 156 °C. This is attributed to loss of ethanol, water and DMF molecules which were modelled in the asymmetric unit (calculated 16.9%). The DSC analysis of **7** shows a broad endothermic peak from 100 to 170 °C which is associated with the departure of the guest molecules from the host framework. Similarly to compound **6**, which displayed an exothermic peak at a 312 °C, compound **7** exhibits an exothermic peak at higher temperature (333.4 °C). Furthermore, the guest free compound of **7** has a lower decomposition temperature (429.7 °C) than **6** which decomposes above 450 °C. The two peaks observed above 400 °C correspond to melting and decomposition of the compound.

Compared to other reported MOFs, these two compounds have high thermal stabilities. The majority of MOFs reported in literature decompose at temperatures which are below 400 °C, and only a few compounds have been reported to decompose at temperatures above 450 °C.[5] The high stability of these compounds arises from their diamondoid topology. As noted in the topological analysis of these compounds, the 3D **dia**- networks are catenated and they exhibit a four-fold interpenetration. This makes the compounds thermally stable. In addition to that, the difference in the temperature of decomposition of the two compounds is probably attributed to the difference in the strength of hydrogen bonding interactions. Stronger hydrogen bonding interactions prevail between adjacent diamondoid nets in **6** than in **7**. Such type of interactions may restrict the movement of individual nets.

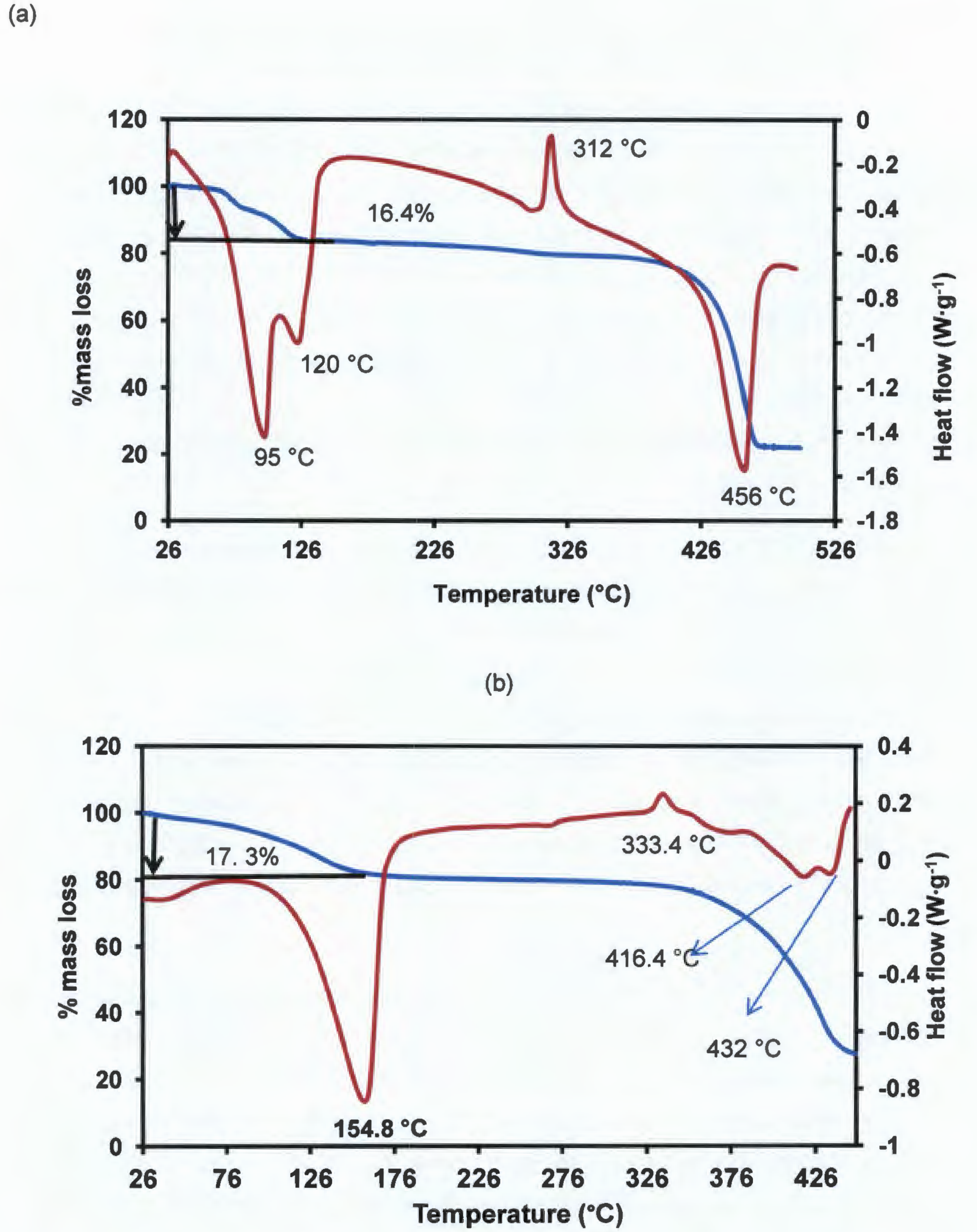

Figure 6.12: An overlay of the DSC (red) and TGA (blue) of a) compound **6** and b) compound **7**.

Both compound **6** and **7** were subjected to HSM studies within a temperature range of 25 to 400 °C. As displayed in Figure 6.13, the HSM images of **6** show bubbling around 300 °C.

This does not correlate with the guest loss temperature observed on the DSC and TGA of **6**. At approximately 320 °C the crystals of **6** start to change to a blue colour, this event is in concert with the observed exothermic peak at 312 °C on the DSC trace which may be associated with a phase transition. By 400 °C, a complete colour change from a purple to blue is observed.

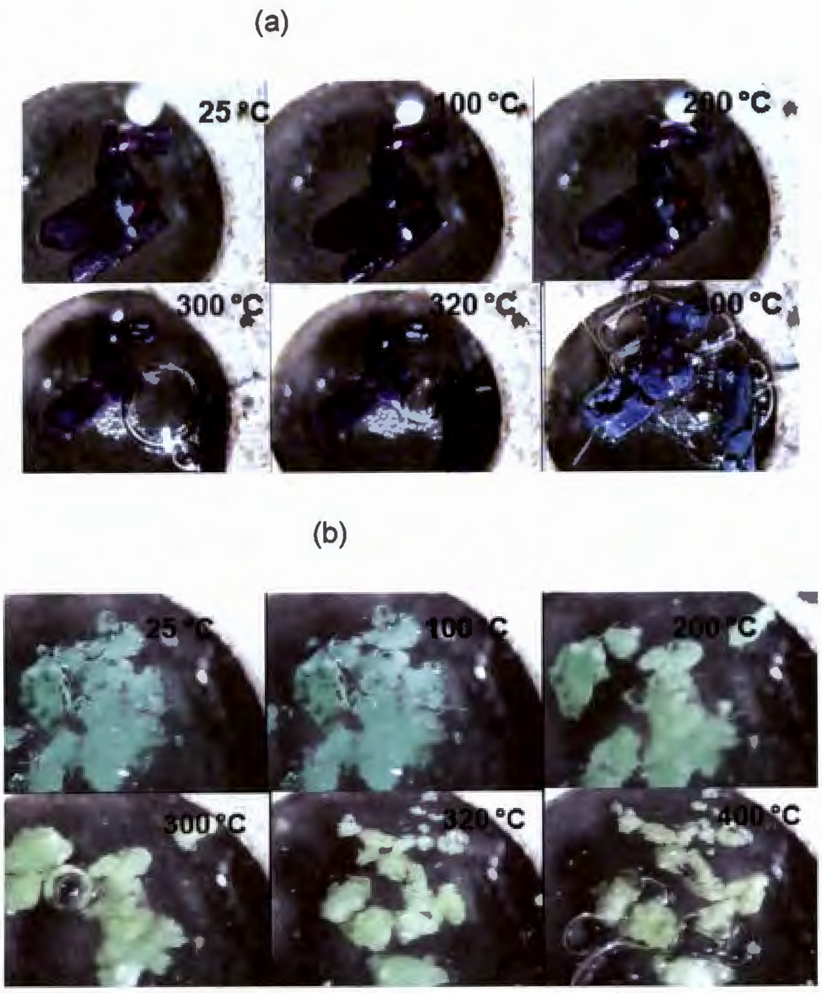

Figure 6.13: HSM studies of a) **6** and b) **7** at different temperatures. The images illustrate the thermochromic behaviour of the compounds at high temperatures. These events may be correlated with the phase transitions (exothermic peaks) observed from their DSC curves

HSM studies of **7** illustrate that the crystals change from darker green to a light green colour when heated from 25 °C to 200 °C. The light green colour fades with continued heating to a whitish brown colour at about 320 °C. The thermochromic behaviour observed in **7** could also be correlated to the exothermic event witnessed on the DSC trace of **7** at 333.4 °C.

Variable temperature PXRD studies were performed to assess the structural integrity of these two compounds over a temperature range of 25 – 340 °C. Figure 6.14 and Figure S6.2 show the PXRD traces obtained. These studies gave similar results in both compounds;

hence the variable temperature of **7** is used for the description of the structural changes that occur when compounds are subjected to thermal treatment. There is no change in the PXRD traces from 25 to 200 °C which suggests that structural integrity is maintained on loss of the solvent molecules. There is a significant decrease in the intensity of the peaks located at 7.715° 2θ positions as temperature is raised from 220 to 340 °C. These peaks are due to the (2 2 0) reflections which pass through the guest molecules and the organic ligand, hence it is expected that the intensity of the peak will decrease after guest loss. Bragg peaks located at about 15.5° do not show any significant change in the intensity as the compound is heated above its phase transition temperature (Figure 6.12). These peaks correspond to the (4 0 0) plane which bisects the channels occupied by the DMF molecules cutting through the metal centres and is parallel to the *c*-axis. For **6**, there is significant loss in crystallinity at about 300 °C which concurs with the exothermic event observed on the DSC at about 312 °C. Both **6** and **7** undergo a crystalline to amorphous phase transformation above 350 °C.

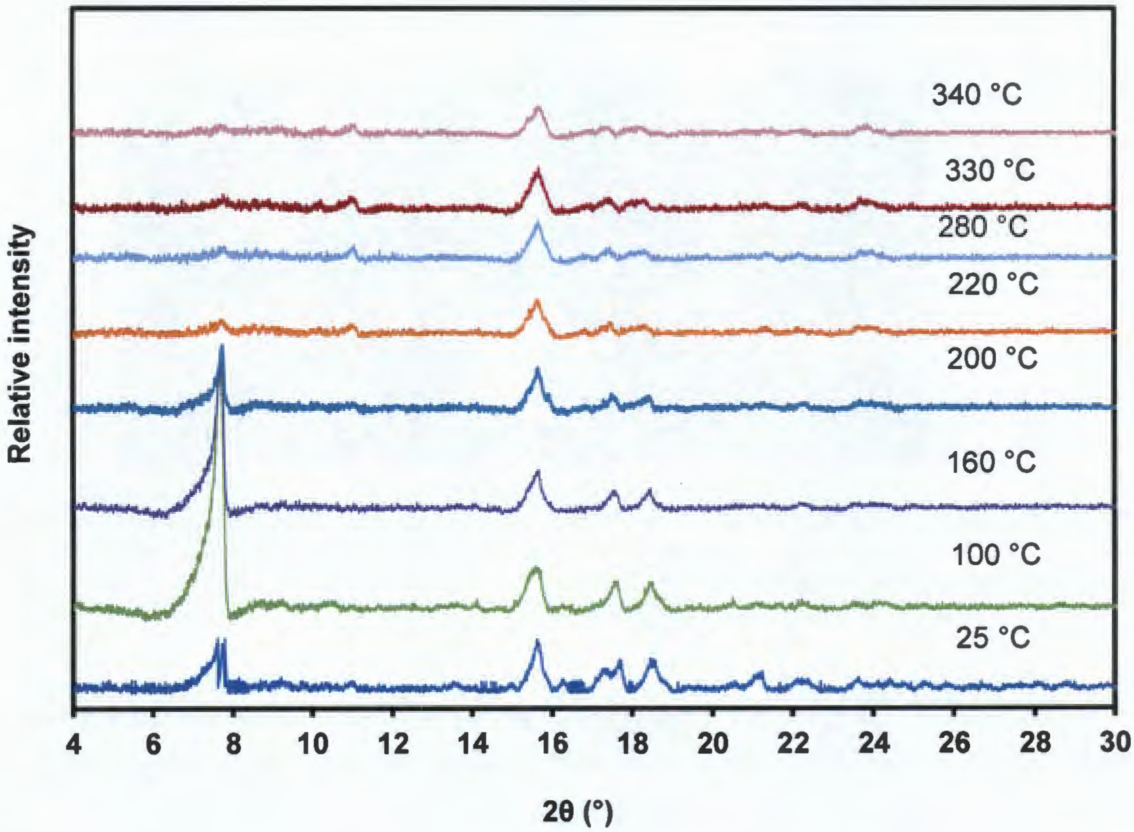

Figure 6.14: Variable temperature PXRD studies of **7**. The pattern demonstrates that the structure is retained upon total guest loss at 200 °C. A significant decrease in peak intensity for diffraction peaks located at about 7.7° is observed at temperatures above 220 °C.

6.6 Thermochromic behaviour of 6 and 7

To evaluate the thermochromic effects observed in the HSM, crystals of compound **6** and **7** were heated at 330 °C (above their phase transition temperature as seen from their DSC curves) until they turned blue and whitish-grey respectively. IR analyses were performed on the as-made crystals and on crystals which changed colour upon heating. Figure 6.15 displays the IR spectra of the two compounds.

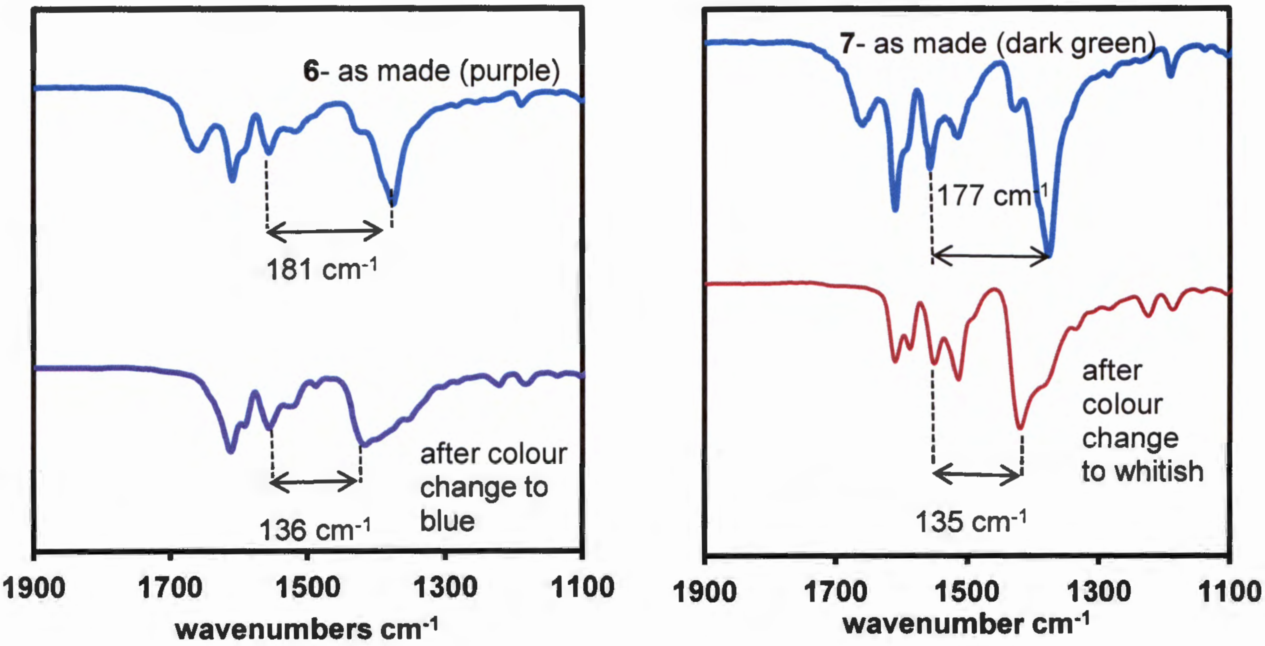

Figure 6.15: Left: Infrared spectrum of **6**; Right: infrared spectrum of **7**

It is well documented that the energy difference between the asymmetric and symmetric vibrations of the carboxylate moiety depends on the coordination mode.[6] Bearing this in mind, IR spectra of **6** and **7** before and after the colour changes were collected to investigate the thermochromic effect observed. Generally unidentate carboxylate will have highest differences between asymmetric and symmetric vibrations, whereas the chelating compounds will exhibit the lowest values. The bridging modes are normally associated with intermediate values. Figure 6.16 displays some of the coordination modes that the 4-(4- pyridyl)benzoate ligand can assume when binding to the metal ions. Both compound **6** and **7** exhibit a carbonyl band at approximately 1658 cm^{-1} which is due to the presence of DMF in the channels. The bands observed at about 1614 cm^{-1} before and after colour change in **6** and **7** are assigned to the aromatic ring vibrations. There is a significant shift in the position of the symmetrical bands to higher wavenumbers upon colour change in both compounds. As seen in the crystal structures of **6** and **7**, the carboxylate moiety exhibits a chelating binding mode. The magnitude of separation between the asymmetric and symmetric carboxylate stretches are 181 and 177 cm^{-1} for **6** and **7** respectively. It is observed that after the colour change (above the phase transition temperature) there is a significant decrease in the magnitude of separation of these stretches (136 and 135 cm^{-1} for **6** and **7** respectively). These results do not follow the general rules; one would expect the magnitude of separation to increase as the carboxylate moiety binding mode changes from chelating (in **6** and **7**) to bridging or unidentate. These results may suggest that different compounds have been formed after the phase transition. The presence of shoulders at about 1360 cm^{-1} and 1386 cm^{-1} for **6** and **7** respectively may indicate that the new phase formed exhibits more than one binding modes of the carboxylate.

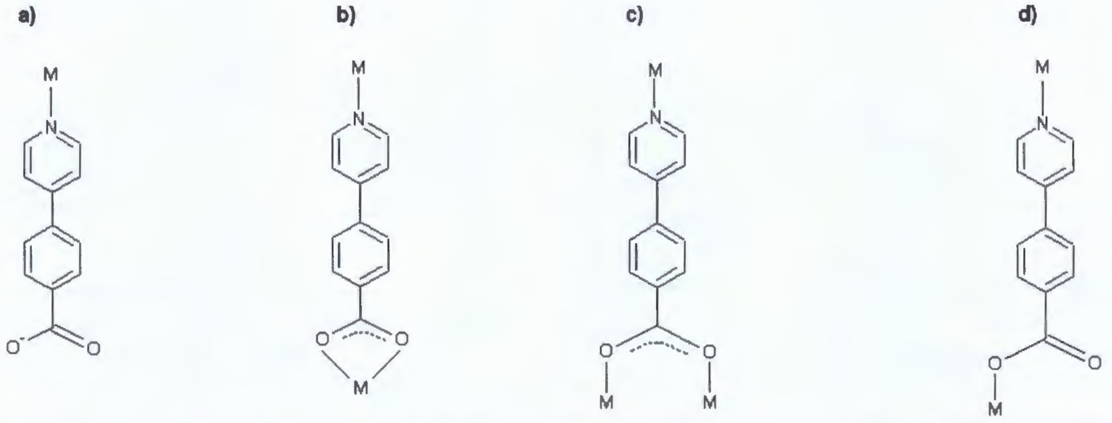

Ionic (1κ-*N*) **Chelating (μ_2-1κ-*N*, 2κ-*O*, 2κ-*O'*)** **Bridging (μ_3-1κ-*N*, 2κ-*O*, 3κ-*O'*)** **Unidentate (μ_2-1κ-*N*, 2κ-*O*)**

Figure 6.16: Some coordination binding modes that can be found when the ligand binds to the metal centre

6.7 Water Induced phase transformations with chromotropism

When single crystals of **6** and **7** are exposed to air for about 10 minutes, they exhibit an irreversible phase transformation to a polycrystalline phase which is accompanied by a colour change. Crystals of **6** change from purple to yellow while crystals of **7** from green to white. Figure 6.17 depicts a single crystal of **6** undergoing this phase transformation. The transformation results in a crystalline powder phase which precludes single crystal analysis. It was noted that the time frame for a complete colour change depends on the relative humidity of the crystal environment. Shorter times (8 minutes) of complete colour change were observed when crystals were exposed to water vapour in a controlled environment.

Exposure of the crystals to 'dryer' air resulted in a longer duration (20 minutes) for a complete colour change.

Figure 6.17: Left , Single crystal of **6**; Right , single crystal of **6** undergoing an irreversible phase transformation. The reaction starts from the outer surface of the crystal and it advances towards the centre of the crystal.

The PXRD of the yellow powder formed when **6** was exposed to air was collected. It was replicated on the crystals that were dried under vacuum at 200 °C for 10 hours to give **6d**, and then exposed to water vapour at 25 °C for a period of 24 hours to give **6d-water**. The PXRD from this study are displayed in Figure 6.18. These results indicate that the formation of a yellow material upon exposure to air is a result of a guest exchange of DMF for water molecules from the atmosphere. **6** and **6d** have similar patterns, showing that the structural integrity is preserved upon desorption of the solvent.

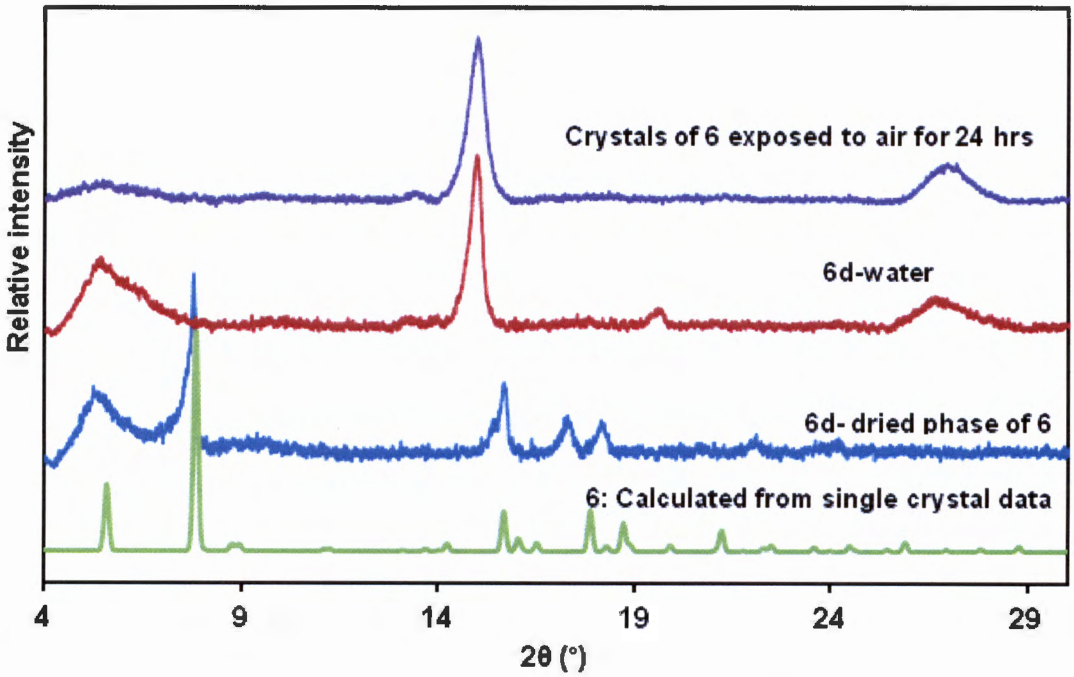

Figure 6.18: A comparison of the PXRD of **6**, **6d**, **6d-water** and of the yellow phase formed by exposing crystals of **6** to air for 24 hours: The PXRD demonstrates that the yellow phase formed upon exposure of the as-made material to air can be replicated by activating crystals of **6** followed by exposure to water vapour.

Thermal analysis by TGA of **6d-water** showed a mass of 14.96% over a temperature range of 25-150 °C (Figure 6.19). This corresponds to 4.5 water molecules per formula unit or to a proposed structure $\{[Co(44pba)_2]\cdot 4.5H_2O\}_n$ (calculated mass loss 15.22%). Elemental analysis Found: C 54.12; H 4.54; N 5.46%. Calculated for $CoC_{24}H_{25}N_2O_{8.5}$: C 53.74; H 4.70; N 5.22%. The elemental analysis results are comparable to the calculated values. Interestingly, when **6d-water** is heated, loss of the absorbed water from the channels is accompanied by a colour change to a deep purple which is similar to the dry compound **6d** (Figure 6.20). Variable temperature PXRD studies displayed in Figure S6.3 show that complete loss of water from the channels is accompanied by loss in crystallinity (crystal to amorphous transformation).

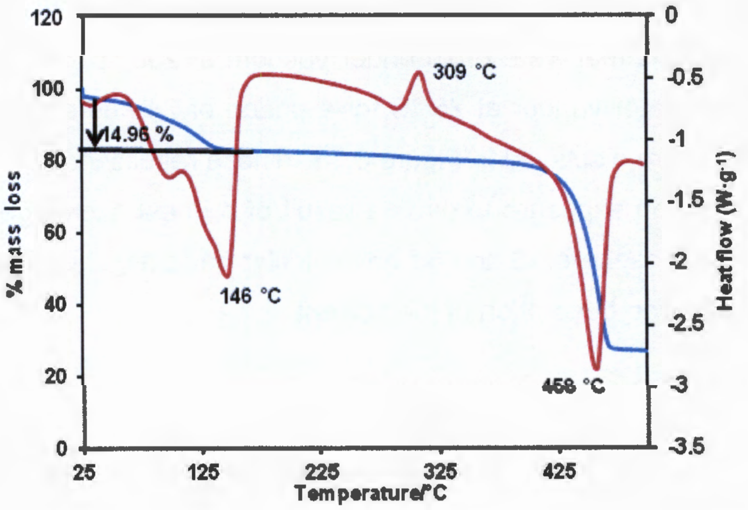

Figure 6.19: TGA (blue) and DSC (red) of **6d-water**. TGA shows that water is lost within a temperature range of 25- 150 °C. The total loss of water molecules is accompanied by loss in crystallinity as seen on the variable temperature PXRD of this compound in Figure S6.3.

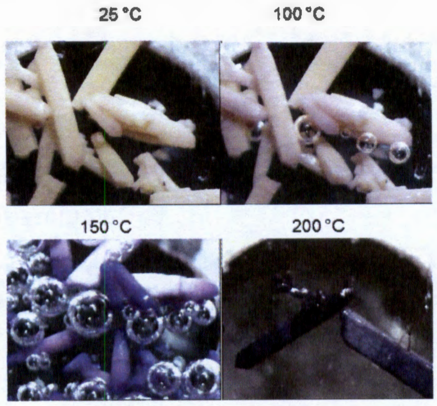

Figure 6.20: crystalline material of **6d-water**: Upon heating, water is released from the channels as evidenced by bubbles at about 100 °C and the sample reverts to a purple colour similar to that of **6d**.

Similar chromic effects were also observed with crystals of compound **7**. The material changes colour from green to white on exposure to moist air or to water vapour. However, the change in colour in crystals of **7** is a slow process compared to its cobalt analogue. A comparison of the real time images of **6** and **7** undergoing colour change when exposed to air are given in Figure 6.21. Drying compound **7** under vacuum for 10 hours at 200 °C affords green crystals of **7d**. Exposure of these desolvated crystals to water vapour for 24 hours gives **7d-water**. PXRD studies of **7d-water** show similar results to those obtained with the cobalt analogue suggesting that the water inclusion compounds are isostructural (Figure S6.4). TGA results showed a mass loss of 13.96% within a temperature range of 25 – 177 °C, corresponding to a proposed structure $\{[\mathrm{Ni(44pba)_2}]\cdot 4\mathrm{H_2O}\}_n$ (calculated mass loss of 13.67%). As noted with the cobalt analogue, white crystals of **7d-water** also change colour to light green upon loss of water from the channels (Figure 6.22). Variable temperature PXRD studies of **7d-water** were not performed. The thermal behaviour of this compound is expected to be very similar to that of **6d-water** which transforms to an amorphous phase upon complete loss of water.

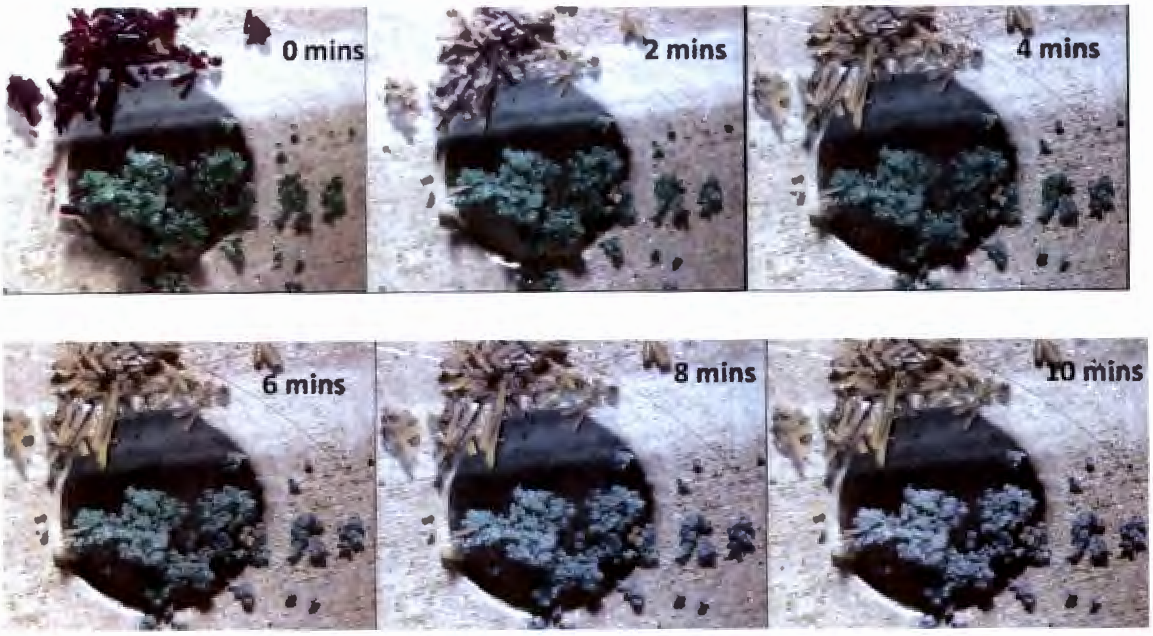

Figure 6.21: A real time comparison at the rate at which the colour change takes place in **6** and **7** when exposed to the atmosphere. Single crystal of **6** (purple-yellow) and **7** (green-white) exposed to air undergoing a phase transition. It was noted that the desolvated phases (**6d** and **7d**) are more stable in air than the as-made solvated forms (**6** and **7**).

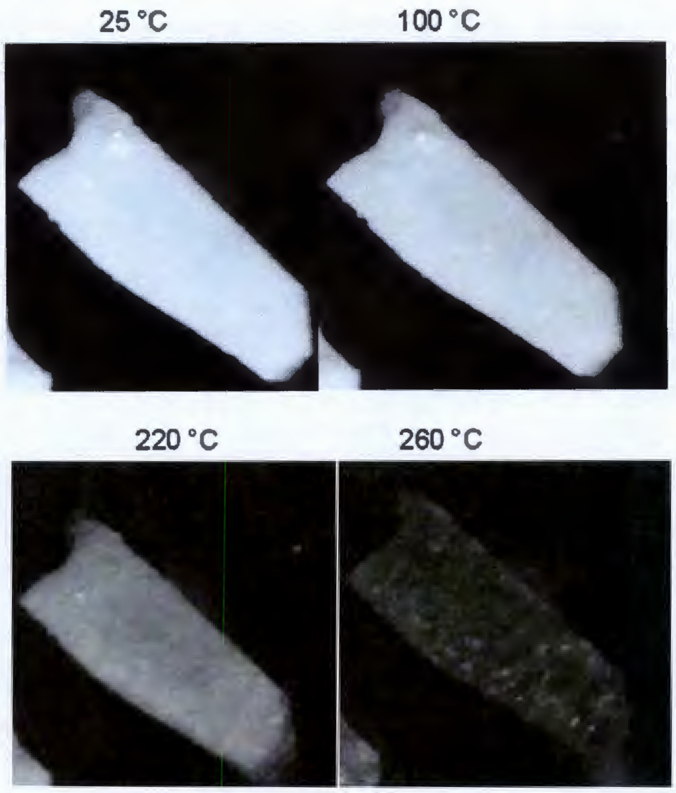

Figure 6.22: Polycrystalline material of **7d-water** changing from white to light green upon loss of water from the channels. The colour change is observed at a higher temperature compared to the cobalt analogue.

6.8 Modelling the kinetics of water vapour uptake

Chapter 1.7 describes the general equations used to study the kinetics of a solid state process under isothermal conditions. Kinetic studies of guest sorption in the solid state pose a number of challenges when dealing with MOFs because of their functionality and flexibility. MOFs or functional coordination polymers can be highly flexible materials that respond to external stimuli such as heat and solvent vapour. It is for this reason that the amount of water vapour absorbed by compound **6d** and **7d** will depend on how they behave at that particular temperature. A change in the dihedral angle between the pyridyl and the phenyl ring is a function of the thermal energy that the atoms possess at a given temperature and such behaviour may regulate the amount of water vapour absorbed. Because the rotation of the ligand is associated with the dynamic pore size and shape, this should affect the absorption property of the compound thus accounting for different kinetic models that fit the experimental data obtained at different temperatures. It is for the stated reasons above that low temperatures were used to study the kinetics of water sorption.

(a)

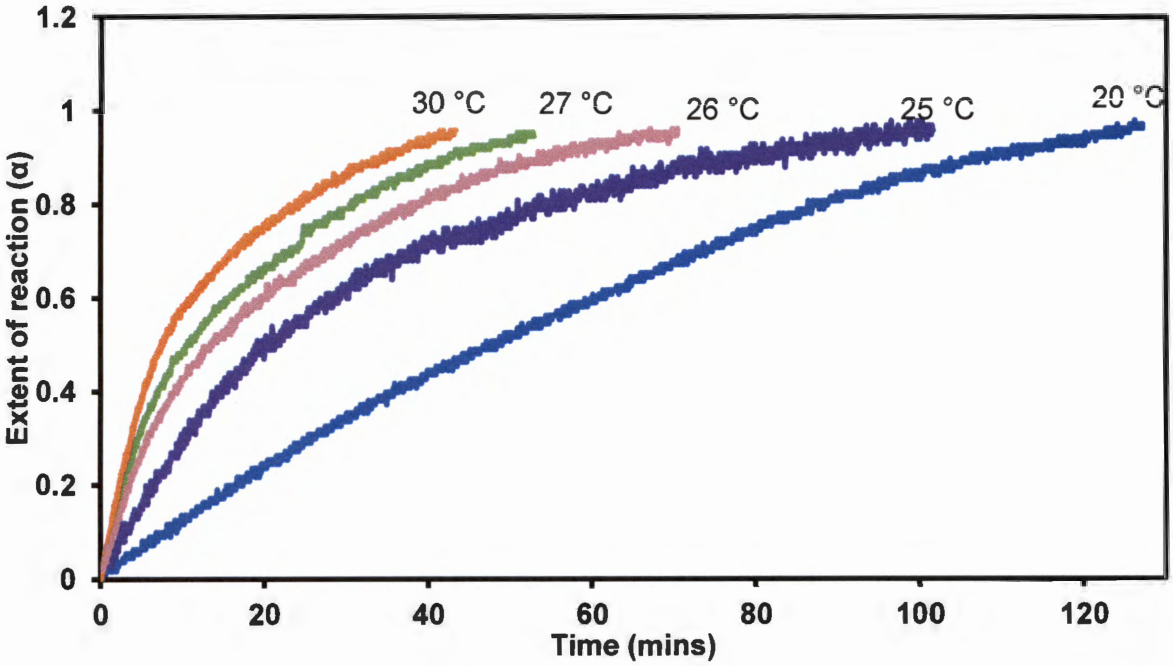

(b)

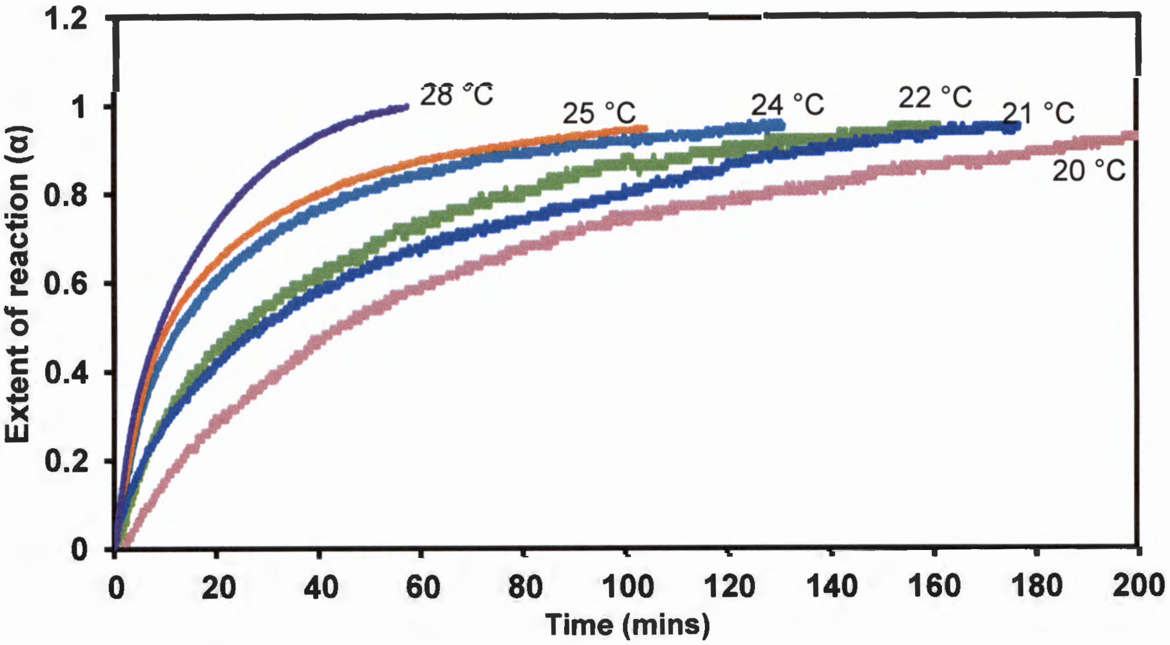

Figure 6.23: Selected α-time curves for the absorption of water by (a) **6d** and (b) **7d**. These curves demonstrate that the sorption of water by the two compounds follows a deceleratory rate law.

The kinetics of water vapour uptake was followed as described in Chapter 2.9. Fresh samples with a particle size of 38 - 45 μm were used for this study. For compound **6d**, the sorption was carried out at temperatures 20, 25, 26, 27 and 30 °C while for **7d** the experiment was performed at 20, 21, 22, 24, 25 and 28 °C. Table S6.3 gives the parameters for the uptake of water by **6d** and **7d**. The amount of water uptake closely matches the mass loss on the TGA of these compounds. The sorption curves were converted into α-time curves and fitted into standard kinetic models. Figure 6.23 displays α-time curves for compound **6d** and **7d** upon water vapour uptake. From Figure 6.23, it is clear that the reaction should follow a rate law that is one of the deceleratory types. This strongly suggests that the reaction could obey an order diffusion-controlled, or geometric type rate law. Table 6.7 gives a summary of kinetic models that fit the experimental data at different temperatures.

Table 6.7: Kinetic parameters for the uptake of water vapour at different temperatures by **6d** and **7d**

	Temp(°C)	***1000/T(K^{-1})***	***Kinetic Model***	***K.min^{-1}***	***ln k***	***R-Value***
6d	20	3.412	D2[a]	7.66×10^{-3}	-4.87	0.9805
			D4[b]	2.23×10^{-3}	-6.11	0.9652
	25	3.356	D2	1.27×10^{-2}	-4.37	0.996
			D4	3.90×10^{-3}	-5.55	0.998
	26	3.344	D2	1.32×10^{-3}	-6.63	0.9965
			D4	4.08×10^{-3}	-5.50	0.9985
	27	3.333	D2	1.58×10^{-2}	-4.15	0.998
			D4	4.89×10^{-3}	-5.32	0.998
	30	3.300	D2	2.35×10^{-2}	-3.75	0.996
			D4	7.04×10^{-3}	-4.96	0.990
7d	20	3.412	D2	3.35×10^{-3}	-5.70	0.990
			D4	9.85×10^{-4}	-6.92	0.995
	21	3.401	D2	4.54×10^{-3}	-5.39	0.997
			D4	1.35×10^{-3}	-6.61	0.998
	22	3.390	D2	4.76×10^{-3}	-5.35	0.989
			D4	1.47×10^{-3}	-6.52	0.996
	24	3.367	D2	5.92×10^{-3}	-5.13	0.971
			D4	1.92×10^{-3}	-6.25	0.983
	25	3.355	D2	6.41×10^{-3}	-5.05	0.990
			D4	1.97×10^{-3}	-6.23	0.994
	28	3.322	D2	9.45×10^{-3}	-4.66	0.987
			D4	2.77×10^{-3}	-5.89	0.992

[a]two-dimensional diffusion; [b] three-dimensional diffusion

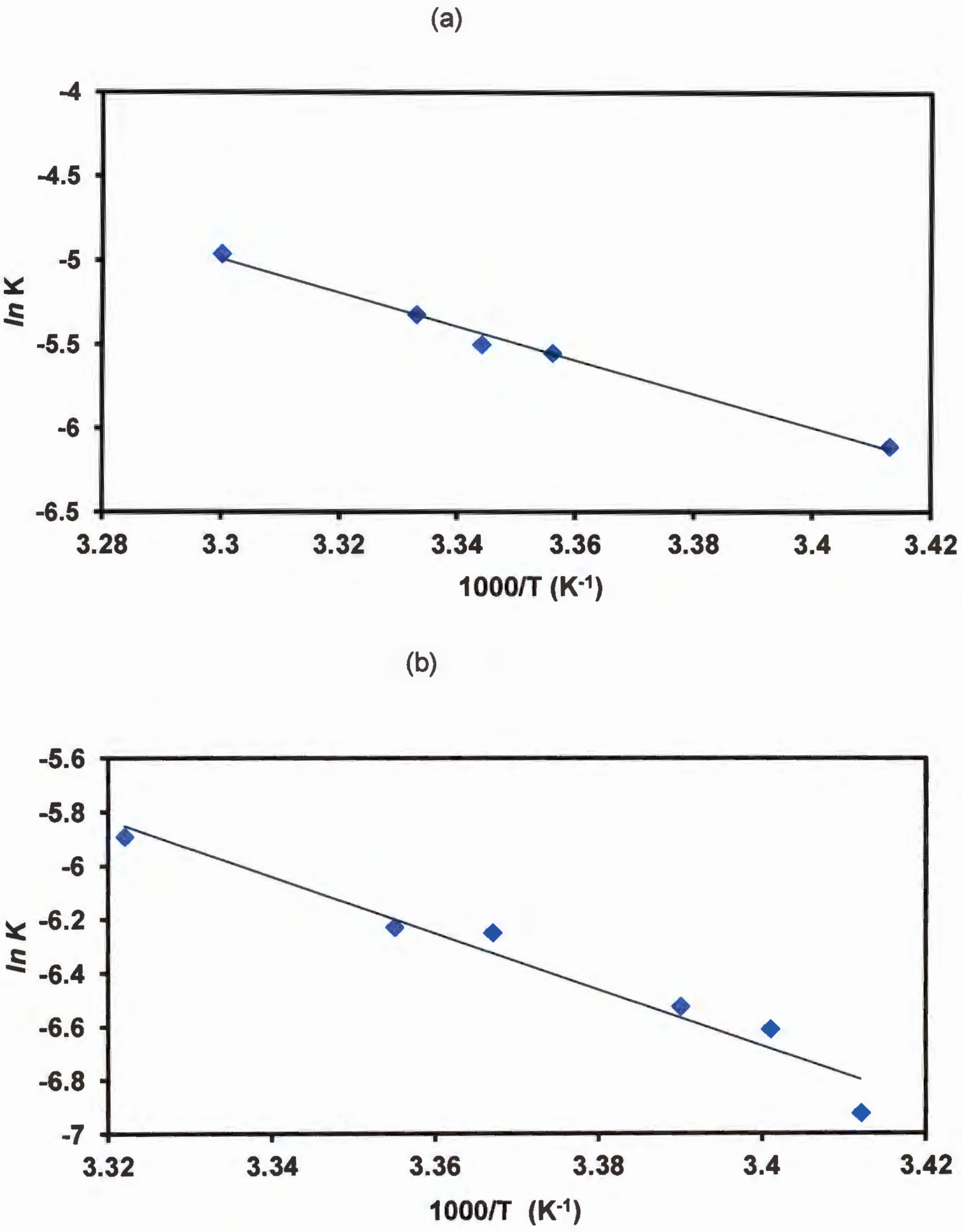

Figure 6.24: Arrhenius plots for sorption of water vapour: (a) **6d** and (b) **7d**

Table 6.7 shows that both the two-dimensional diffusion (D2) and three-dimensional diffusion (D4) models gave some good correlation to the experimental data. The D2 and D4 models are defined by the functions $[(1 - \alpha) \ln (1 - \alpha) + \alpha]$ and $[1 - 2\alpha/3] - (1 - \alpha)^{2/3}]$ respectively. The physical meaning of these two models has been discussed in chapter 5.6. The D2 mechanism is derived by assuming that the solid particles are cylindrical, and diffusion occurs rapidly through a cylindrical shell with an increasing reaction zone while the D4 model applies to a diffusion reaction which takes place at several nucleation sites forming phase interfaces between the product (**6d-water** or **7d-water**) and the reactant (**6d** or **7d**). The two rate laws have very similar mathematical forms that involve the function of (1 – α). Applying these equations to experimental data obtained on solid state reactions may result in more than one of the equations giving equally good fit to the data as already noted in Table 6.7.

A comparison of the correlation coefficients between the D2 and D4 rate laws shows that the D4 mechanism has the best fit. The rate constant for absorption of water by **6d** ranged from 2.23×10^{-3} (at 20 °C) to 7.06×10^{-3} min^{-1} (at 30 °C) while that of **7d** was within the range of 9.85×10^{-4} (at 20 °C) to 2.77×10^{-3} min^{-1} (at 28 °C). The activation energy for the sorption of water was determined from the Arrhenius plots given in Figure 6.24. These plots yielded activation energy values of 83.7 $kJ\cdot mol^{-1}$ and 87.2 $kJ\cdot mol^{-1}$ for **6d** and **7d** respectively. It is apparent that the activation energies obtained for the cobalt (**6d**) and nickel (**7d**) analogues are almost identical and suggest that the kinetics of this process is similar for these isostructural compounds. Based on the crystal structures of **6** and **7**, one would expect a 1D mechanism to govern the rate of water uptake, this is because both structures have one dimensional channels which run along the *c*-axis. However, the D4 mechanism governs the uptake of water. This is ascribed to the flexibility of the ligand which can rotate about the C-C bond that links the phenyl and pyridyl ring allowing for entry of water into the channels from different directions. Furthermore, the individual networks in the four-fold **dia** network may undergo some dynamic motion under external stimuli, thus unlocking the closed hexagonal channels found in a single net.

A comparison of the activation energies obtained for the two systems is not simple, as there are not many kinetic studies of enclathration processes in MOFs. In some studied systems, activation energies ranging from 20 to 140 $kJ\cdot mol^{-1}$ have been reported for the uptake of small solvent molecules by organic and some coordination frameworks.[7,8]

6.9 Non-isothermal kinetics of water desorption in 6d-water and 7d-water

The desorption kinetics of water in **6d-water** and **7d-water** was performed as described in Chapter 2.10. For compound **6d-water**, heating rates of 4, 8, 16 and 32 $K\cdot min^{-1}$ were used while for **7d-water**, heating rates of 1, 2, 4 and 5 $K\cdot min^{-1}$ were applied. Low heating rates were used for **7d** to avoid overlapping of the TGA traces which were observed when heating rates similar to those used for **6d-water** were applied. When the TGA traces obtained using different heating rates overlap, such results may not be applied to the OZAWA method to determine the kinetic energy. Figure 6.25 shows the desorption kinetic profiles of water from the host frameworks. Comparison of the desorption kinetic profiles of water from **6d** and **7d** suggests that loss of water from the two systems may be governed by different mechanisms. The TGA traces for the desorption of water from **7d-water** display two distinct mass losses. The data from these curves were analysed in the Universal analysis program[9] to determine the percentage conversion level at each given temperature and these are given in Table 6.8. Plots of log β versus 1/T (Figure 6.26) allowed for the calculation of the activation energies as described in section 2.10 of Chapter 2. Table 6.9 gives the activation energies of the two systems at different conversion levels.

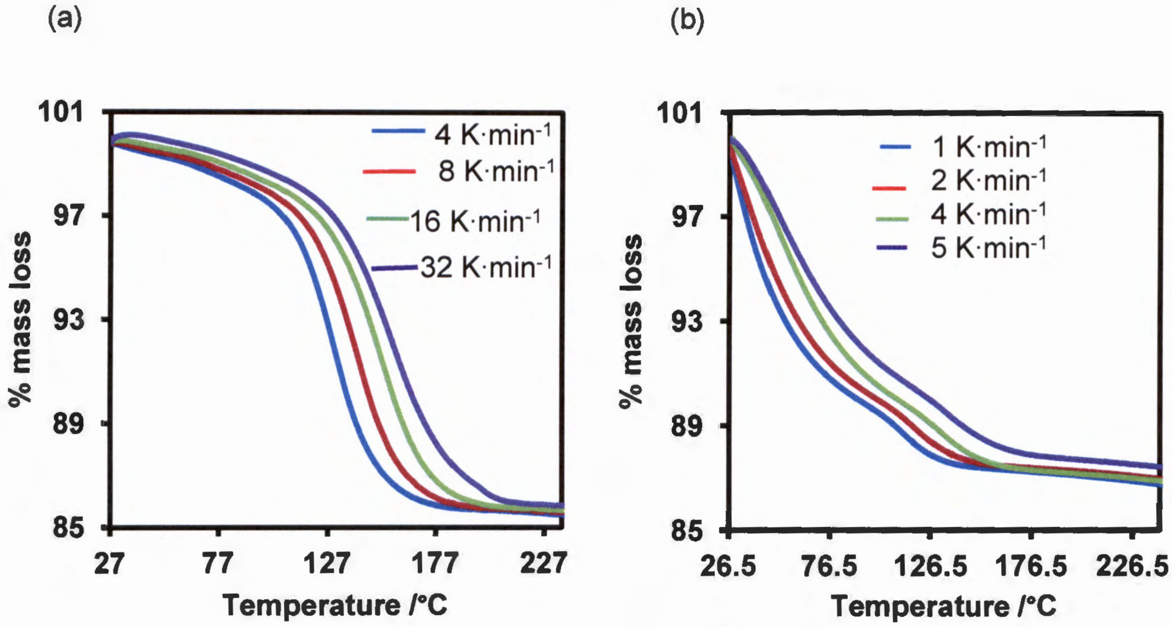

Figure 6.25: Non-isothermal TGA traces for water desorption for (a) **6d-water**, (b) **7d-water**

Table 6.8: Kinetic parameters of water desorption from **6d-water** and **7d-water**

			1/T x 1000			
	Heating rate (β) K· min⁻¹	***log β***	***20%***	***50%***	***70%***	***90%***
6d-water	4	0.6021	2.653	2.503	2.446	2.356
	8	0.9031	2.603	2.449	2.392	2.309
	16	1.2041	2.545	2.390	2.333	2.261
	32	1.5051	2.518	2.367	2.308	2.238
7d-water	1	0.000	3.254	3.082	2.875	2.568
	2	0.3010	3.219	3.026	2.818	2.524
	4	0.6021	3.149	2.952	2.767	2.489
	5	0.6990	3.148	2.938	2.743	2.459

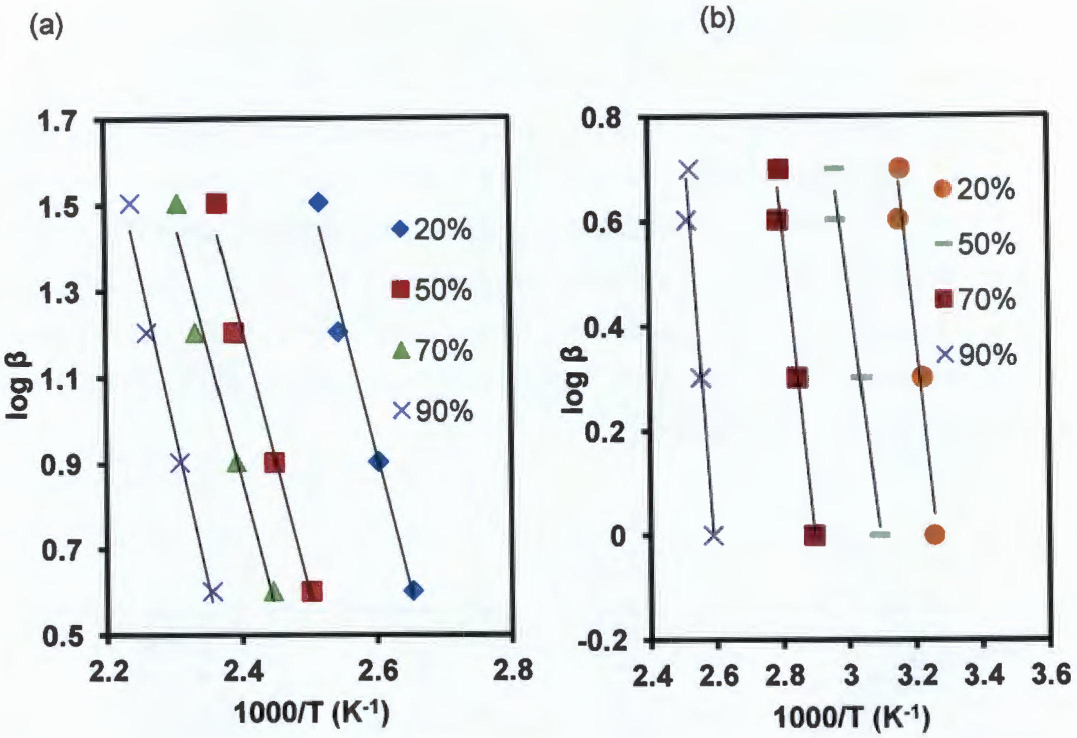

Figure 6.26: Plots of 1000/T versus log β for the kinetics of desorption for(a) **6d-water**, b) **7d-water**

Table 6.9: Activation energies for the desorption of water from **6d-water** and **7d-water**

	Conversion level	*20%*	*50%*	*70%*	*90%*	*Average*
6d-water	E_a (kJ mol^{-1})	116	114	113	133	119(9)
7d-water	E_a (kJ mol^{-1})	107	85	98	121	102(15)

Although the two systems exhibited the same mechanism of water sorption, it is clear from the desorption profiles and the activation energies that the desorption mechanism in these two isostructural compounds is different. The activation energies of **6d-water** show little variation at different conversion levels which may suggest that loss of water follows a single process. In contract to **6d-water**, **7d-water** exhibits a large variation of energies at different conversion levels. This may indicate the existence of different mechanisms being associated with water loss from the channels. One may argue that the different heating rates used may account for the different mechanisms for the guest loss.

6.10 Solvatochromic effects in the two compounds

The dramatic colour change observed upon uptake of water by **6** and **7** prompted the investigation of the behaviour of these compounds under different solvent environments. **6** was dried under vacuum at 200 °C for 10 hours to give **6d**. The compound was then immersed in dry solvents of methanol, DMF, DMSO, ethanol, benzene and water to give **6d-methanol**, **6d-DMF**, **6d-DMSO**, **6d-ethanol, 6d-benzene** and **6d-water** respectively. The resulting inclusion compounds had different colours depending on the solvent included. The inclusion compounds of **6d-methanol** and **6d-ethanol** were not stable upon removing them from their respective solvents. They changed colour to yellow which suggests that these compounds were losing the alcohol guest molecules in favour of water vapour being absorbed from the atmosphere. Figure 6.27 shows the PXRD patterns of these inclusion compounds.

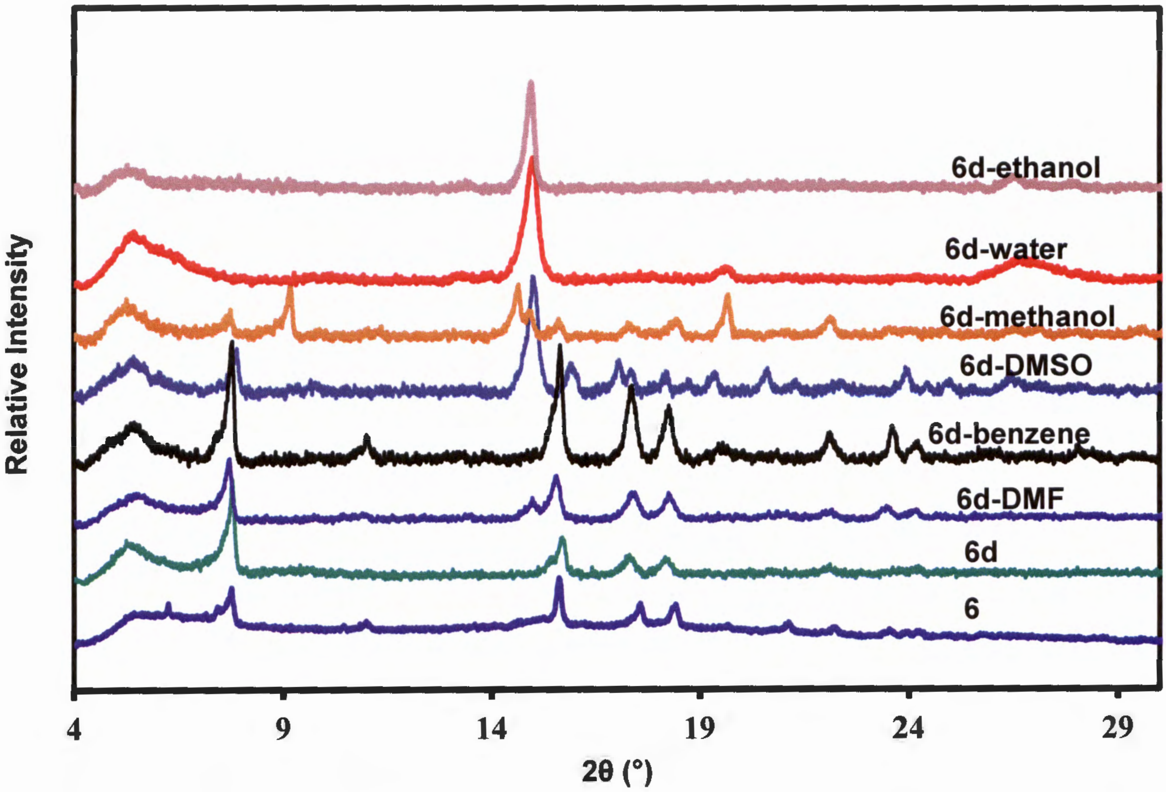

Figure 6.27: PXRD of solvated forms of **6d** upon sorption of different solvents.

It is worthy to note that a similar crystalline phase as **6** is regenerated upon absorption of DMF and benzene. This suggests that these solvents may play a role in templating the formation of the framework in **6**. PXRD studies of the inclusion compounds revealed that inclusion compounds which had a purple colour had similar PXRD patterns and these are inclusion compounds of hydrogen bond acceptors. For hydrogen bond donors, ethanol and water inclusion compounds had a similar PXRD pattern and were a brown and yellow upon inclusion of each solvent. The methanol inclusion compound was pink and its PXRD pattern is completely different from the other inclusion compounds. The most significant changes are the decreased peak intensities at 7.5, 17 and 18° and the shift to lower 2θ of the peak at 16° on exposure to polar protic solvents. Absorption of ethanol and water by **6d** results in a significant loss of crystallinity compared to either **6** or **6d**. Similar effects were observed on a 3D framework $[In_2(OH)_2(TBAPy)]\cdot$ (guests) where TBAPy is 1,3,6,8-tetrakis(*p*-benzoic acid)pyrene.[10] The authors attributed significant loss in crystallinity to structural disorder and distortion in the framework upon absorption of water.

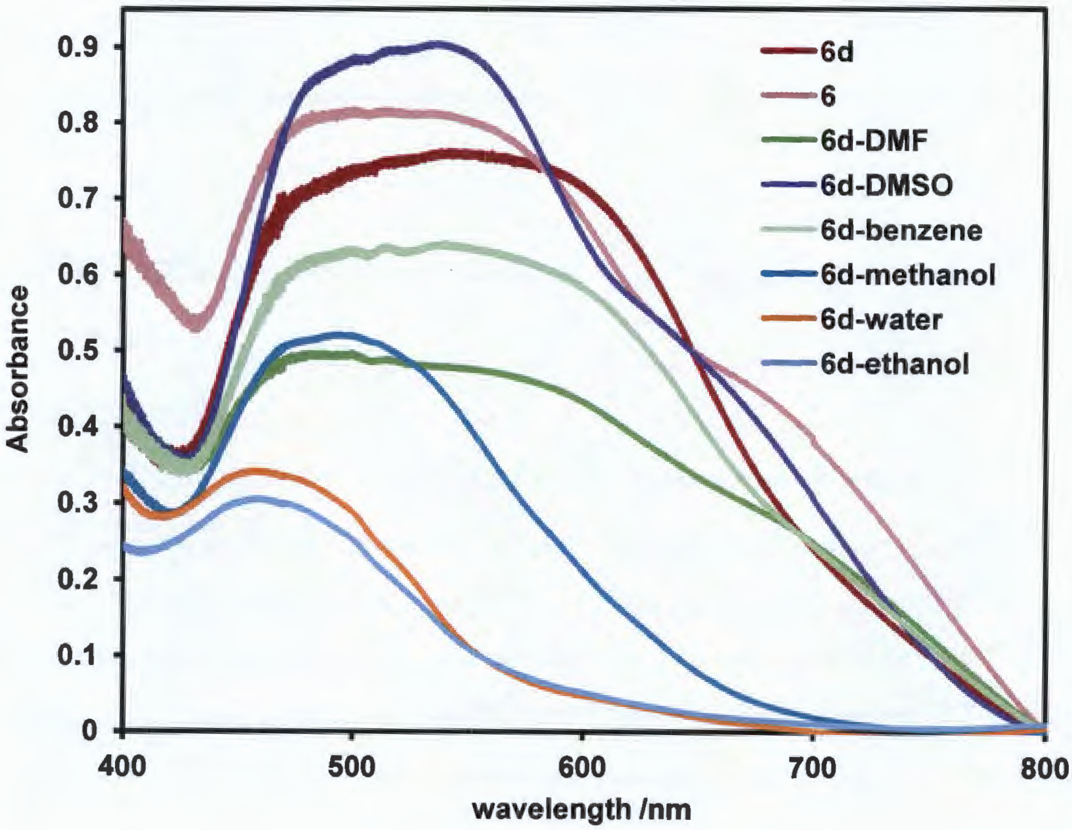

Figure 6.28: UV-vis spectra of **6** and other several solvated forms of **6d**. Inclusion compounds of polar protic solvents absorb at a lower wavelengths, while non-polar and polar aprotic absorb over a wide wavelength

UV-Vis absorption spectra of the inclusion compounds of **6d** (shown in Figure 6.28) correlate well with the PXRD studies. As may be expected, the UV-Vis absorption bands are very similar for **6**, **6d** and **6d-DMF** and **6d-DMSO** as these compounds are all purple in colour. These inclusion compounds comprise of non-polar or polar aprotic solvents and none capable of acting as hydrogen bond donors. Their absorption occurs over a broad wavelength (450 - 750 nm) in the UV-Vis spectrum. Contrary to this, polar protic solvents capable of acting as hydrogen-bond donors and acceptors (ethanol, water and methanol) when loaded to **6d** cause the material to change colour to pink (methanol), orange brown (ethanol) or yellow (water). The absorption bands in the UV-Vis spectra of **6d-water**, **6d-methanol** and **6d-ethanol** are narrower and centred at lower wavelength (450 -500 nm) consistent with their colours.

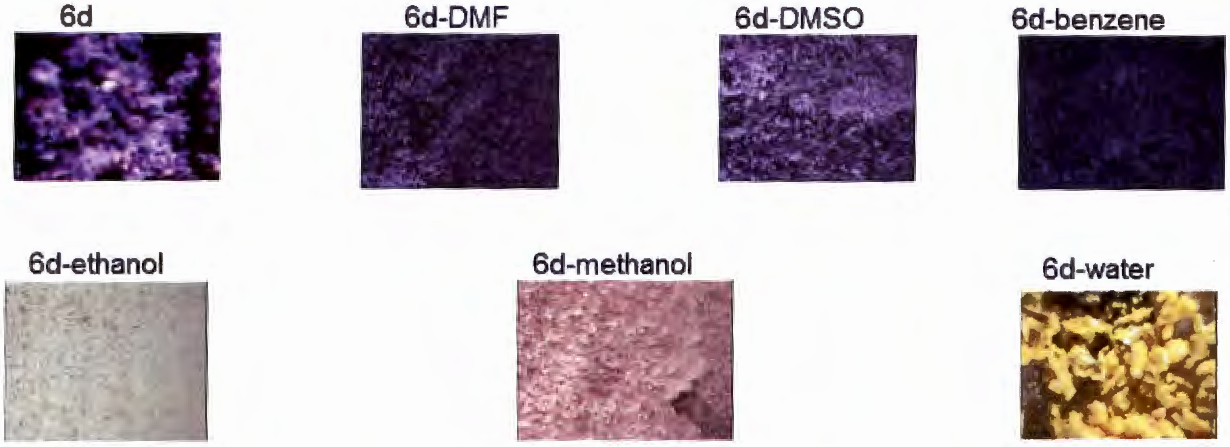

Figure 6.29: Photographs of crystalline powders of several solvated forms of **6d**.

The observed solvatochromic behaviour of compound **6** was investigated by IR analysis (Figure 6.30). The results from this study show that the spectra of the solvated phases are identical in the positions of the asymmetric and symmetric carboxylate bands, thus it is most likely that the carboxylate moiety maintains its bidentate binding mode. The bands at about 1610 cm^{-1} in all compounds are attributed to the ring vibrations of the framework. In **6** and **6d-DMF** the carbonyl stretch of the DMF is observed at approximately 1668 cm^{-1}. The absence of this band in **6d** confirms complete removal of DMF from **6**.

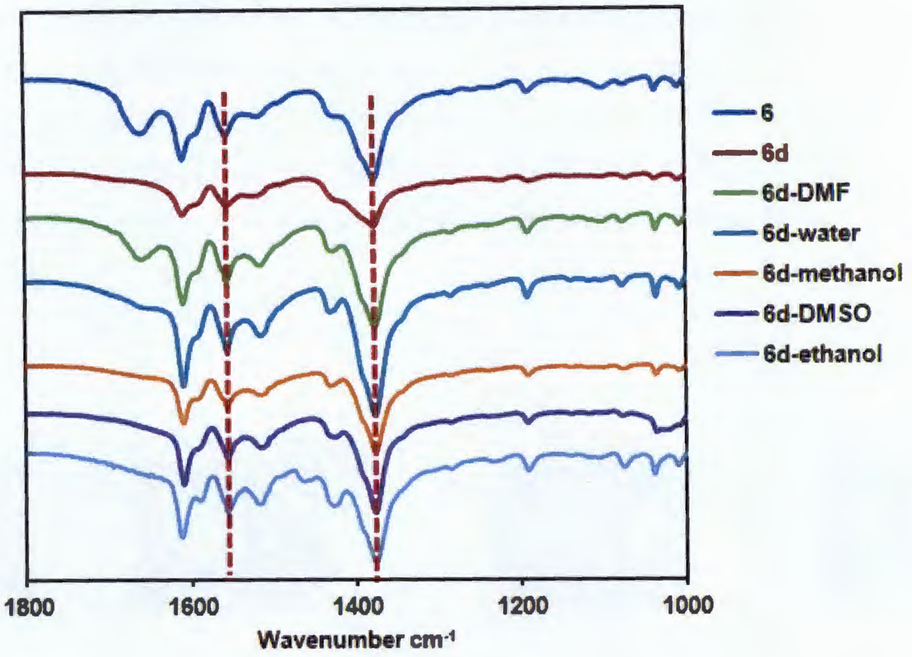

Figure 6.30: IR spectrum of selected solvated phases of **6**. The position of the asymmetric and symmetric carboxylate bands are indicate by dotted red lines. These spectra show that the position of the carboxylate stretches are not affected by solvation. Hence, the possibility of colour resulting from change in coordination geometry is ruled out.

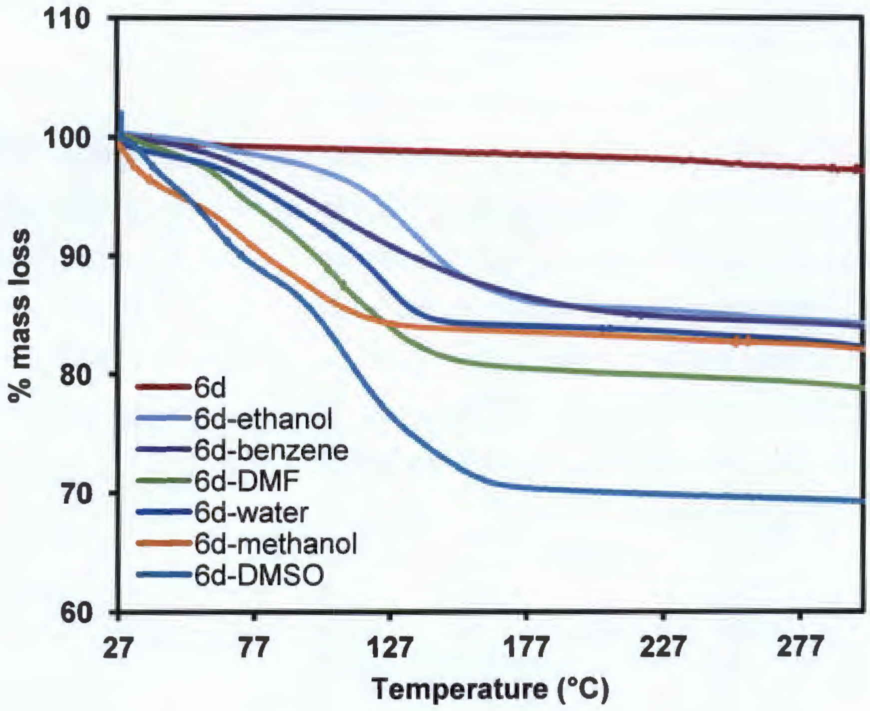

Figure 6.31: TGA analysis of several solvated forms of **6d**. The guest weight loss (listed in Table6.10) observed were used to model the amount of solvent in the proposed formula {[Co(44pba)$_2$]·xsolvent}$_n$.

Figure 6.31 displays the thermal analysis of the inclusion compounds of **6d**. The amount of guest loss is given in Table 6.10. Complete solvent removal in **6** was confirmed by the TGA trace of **6d** which does not show a mass loss in the temperature range of 27 to 250 °C. **6d-methanol** and **6d-DMSO** are the least stable compounds as illustrated on the TGA. These compounds lose their guest molecules at a faster rate than other inclusion compounds as supported by the steep gradient of their curves in the temperature region of their mass loss. The **6d-benzene** compound is the most stable owing to a possibility of the $\pi\cdots\pi$ interactions of the guest with the aromatic framework.

Table 6.10: Solvent sorption results for compound **6d**

Solvent Code	***TGA mass loss***	***L_C[a] (x in $\{[Co(44pba)_2]\cdot xsolvent\}_n$***	***ML_C[b]***	***% L_c***	***Colour***
6d-water	14.96	4.5	12.9	35	yellow
6d-methanol	13.80	2.3	5.9	40	pink
6d-ethanol	13.27	1.5	4.0	38	brown
6d-DMF	21.95	1.8	3.0	60	purple
6d-DMSO	29.00	2.4	3.3	73	purple
6d-benzene	15.50	1.1	2.6	42	purple

[a]L_C: Loading Capacity; [b]ML_C: Maximum Loading Capacity

Table 6.10 lists the solvent sorption results of **6d**. The loading values were calculated from TGA analysis (Figure 6.31) and compared to theoretical maximum loading capacities. In all systems, the loading capacity (L_C) in the proposed formula $\{[Co(44pba)_2]\cdot x$ solvent$\}$ is less than the maximum loading capacity (calculated from the crystallographically derived void volume and the liquid density of the respective solvents).

The maximum loading capacity (L_c) for the empty network (channels in **6** and **7**) was estimated using the formula:

$$ML_c = (solvent\ accessible\ void\ volume)/(Z \times 4 \times molecular\ volume) \qquad 6.1$$

The constant value of 4 ensures that the ML_C is determined for each metal ion as there are four independent crystallographic centres in the asymmetric unit of each compound. The solvent accessible void volume of **6** and **7** was estimated using Mercury with a probe radius of 1.2 Å and a grid step of 0.2 Å and was found to be 12408.12 Å^3 and 12050.58 Å^3

respectively. The molecular volumes (M_v) of the solvents were determined from their liquid density:

$$Mv = (molecular\ weight)/ (N_A X\ density) \qquad 6.2$$

Except for water, benzene and ethanol with loading capacities below 50%, the rest of the solvents have loading capacities above this value. The inclusion of water or ethanol possibly blocks access to regions of the pores giving rise to the observed lower loading values compared to the theoretical values. The solvent loading in most solvated forms of **6d** is associated with retained crystallinity of the network which is confirmed by their PXRD traces.

The observed solvatochromic effects in **6** are most likely derived from molecular distortions in the framework induced by solvent hydrogen bonding. Similar effects have been observed in several systems.[11-13] The yellow colour observed upon uptake of water may suggest coordination of water molecules to the cobalt metal centre. However, the IR results do not support this assumption. The interaction of absorbed water molecules with the framework through hydrogen bonding may trigger the π to π* transition resulting in the observed colour change. During the course of this work, two compounds assembled from Zn(II) and 3-(4-pyridyl) benzoate described in Chapter 5 were found to have different colours depending on the nature of the guest included. $\{[Zn(34pba)_2]\cdot1.5H_2O\}_n$ was yellow and has guest water molecules which were not coordinated to the Zn(II) centre and was previously reported by Niu *et al.*[14] Extensive hydrogen bonding between the water molecules and the framework existed in the 3D structure. The colourless compound $\{[Zn(34pba)_2]\cdot DMF\}_n$ had DMF molecules in its cavities with very weak interactions between the guest and the framework. Such a result may further support the observed IR results which suggest that the solvatochromic properties are not directly related to solvent molecules coordinating to the metal centre.

The solvatochromic properties of **7** were also investigated by immersing the desolvated phase **7d** in several solvents. Crystals of compound **7** were activated by soaking them in methanol for 24 hours followed by heating at 100 °C under vacuum. Soaking of crystals in methanol allows an easier guest removal without damaging the crystals. Complete solvent removal was confirmed by TGA. Sorption studies were carried out by immersing the activated phase **7d** in dry solvents for 24 hours. Figure 6.32 depicts the images of the inclusion compounds. The colours ranged from dark green to white upon inclusion of solvents. Thermal analysis of the inclusion compounds are given in Figure 6.33.

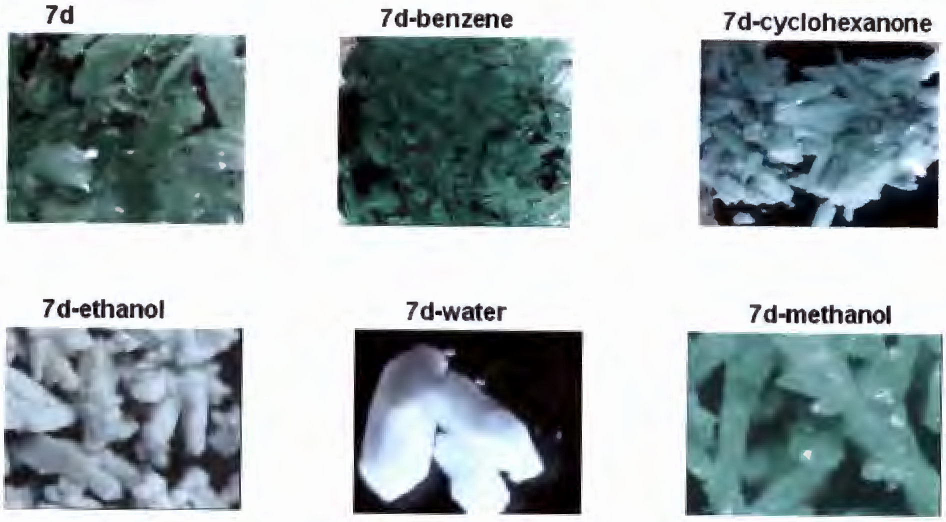

Figure 6.32: Crystal images of solvated forms of **7d**. The colour ranges from green to white.

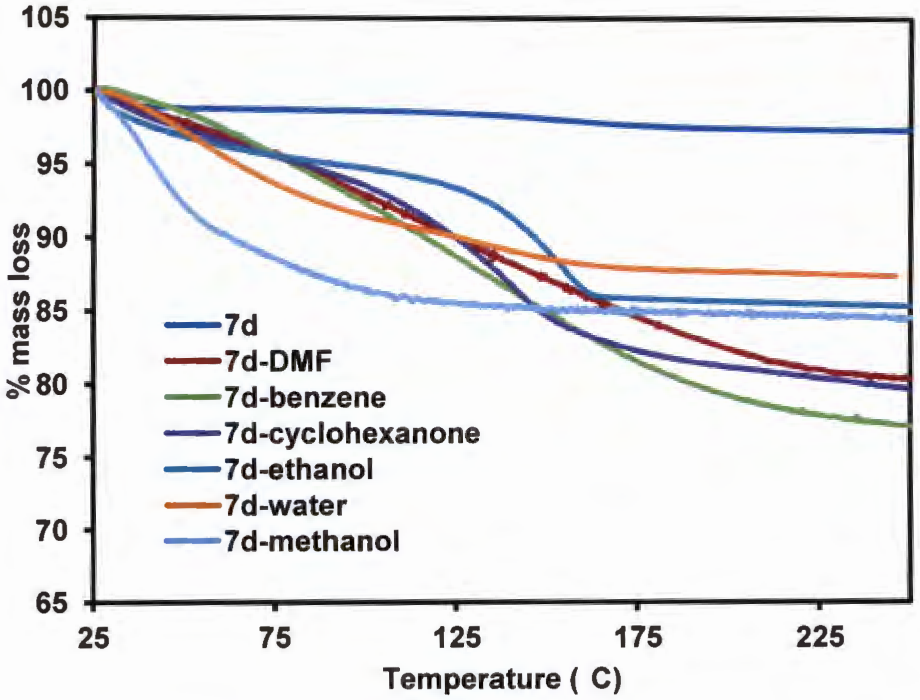

Figure 6.33: Thermal analysis of the several solvated forms of **7d**. The TGA were all performed using a heating rate of 10 K·min^{-1}.

The guest free compound **(7d)** is featureless over the temperature range recorded indicating complete removal of the molecules in the channels of **7** upon heating. From the thermal analysis, it can be observed that majority of the inclusion compounds are not stable at room temperature as seen by the immediate mass loss at the beginning of the analysis. The thermal behaviour of the **7d-inclusion** compounds are very similar to those of the cobalt analogue. **7d-methanol** is the least stable compound as evidenced by rapid guest loss at low temperatures.

Figure 6.34 shows the PXRD traces of the inclusion compounds. As previously noted with the cobalt analogue, a phase change is observed upon inclusion of water and ethanol. Although dry ethanol was used, we noted that the PXRD of **7d-water** and **7d-ethanol** are very similar. It may be concluded that the sample of **7d-ethanol** absorbed water from the air during the PXRD analysis. Absorption of methanol does not result in a phase change as observed in the cobalt analogue which suggests that the framework is not altered by this solvent.

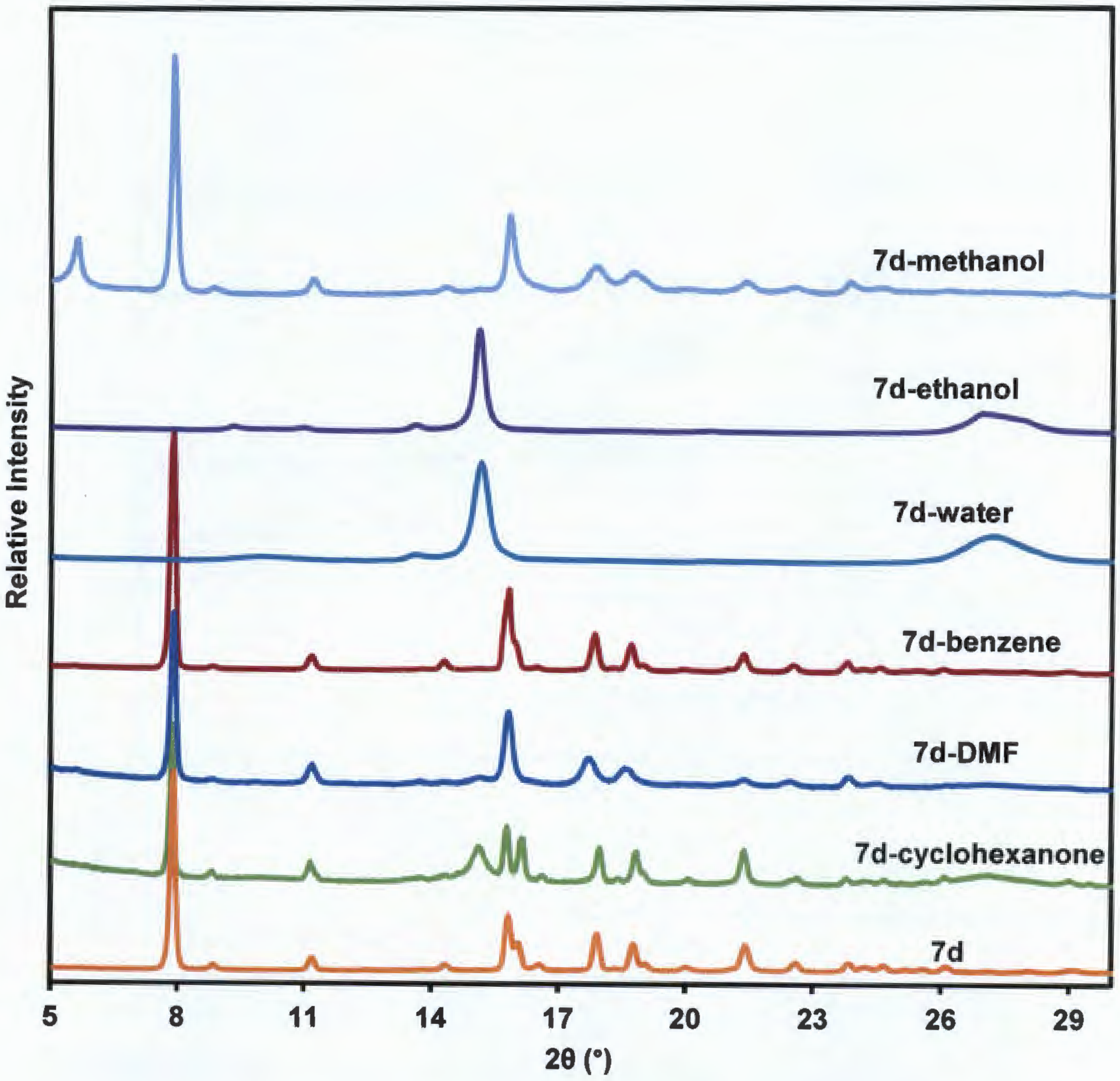

Figure 6.34: PXRD traces of inclusion compounds of **7d**.

Table 6.11 lists the fundamental properties associated with the loading of the 1D channels found in **7**.

Table 6.11: Solvent sorption results of $\{[Ni(44bpa)_2] .x\ solvent\}_n$

Solvent loaded	*TGA mass loss (%)*	*L_c (x in proposed formula): $\{[Ni(44bpa)_2] \cdot x\ solvent\}_n$*	*ML_C*	*% L_C*	*Colour*
water	14.4	4.2	12.6	33	whitish
benzene	23.4	1.7	2.6	65	green
cyclohexanone	18.9	1.1	1.8	61	green-whitish
DMF	19.1	1.5	2.9	52	green
methanol	13.1	2.1	5.6	38	green
ethanol	12.8	1.5	3.9	38	whitish

The PXRD traces of **7d-cyclohexanone**, **7d-DMF**, **7d-methanol** and **7d-benzene** are very similar to the activated phase **7d**, which suggest that the framework is not altered by absorption of these solvents. In all studied systems, the loading capacity after 24 hours does not reach the maximum loading capacity as shown in Table 6.11. Although the compound is responsive to water it has the lowest loading capacity of 33%. Benzene and cyclohexanone have loading capacities above 50% while the rest of the solvents studied are below this value. This may be explained in terms of the nature of interactions between the solvent molecules and the framework. Both benzene and cyclohexanone are capable of interacting with the framework through π···π interactions of the aromatic rings. These interactions are generally weak and may allow the movement of molecules in the channels thus allowing more molecules to enter the channels. On the other hand, DMF, water and ethanol are capable of forming hydrogen bonds with the host framework, and depending on the strength of the interactions, the first molecules to enter the channels may provide a barrier to other molecules to access the channels. The solvent loading behaviour of this material is very similar to the cobalt analogue compound **6d**; however it was noted that the desolvated nickel compound **(7d)** is more stable in air than the cobalt compound **(6d).**

The IR spectrum of **7d** inclusion compounds are displayed in Figure 6.35. Stretches located at 1610 cm^{-1} in all compounds are ascribed to the vibrations of the aromatic framework. A carbonyl stretch is observed at 1664 and 1702 cm^{-1} in **7d-DMF** and **7d-cyclohexanone** respectively confirming the inclusion of the guest molecules in the framework. The IR trace of **7d** and **7d-benzene** are very similar except for the symmetric carboxylate stretches which appears at 1390 and 1378 cm^{-1} for **7d** and **7d-benzene** respectively suggesting that the inclusion of benzene has no great effect on the structure of the framework as already noted with PXRD studies. The down shift observed is probably induced by the π···π interactions of the framework with benzene.

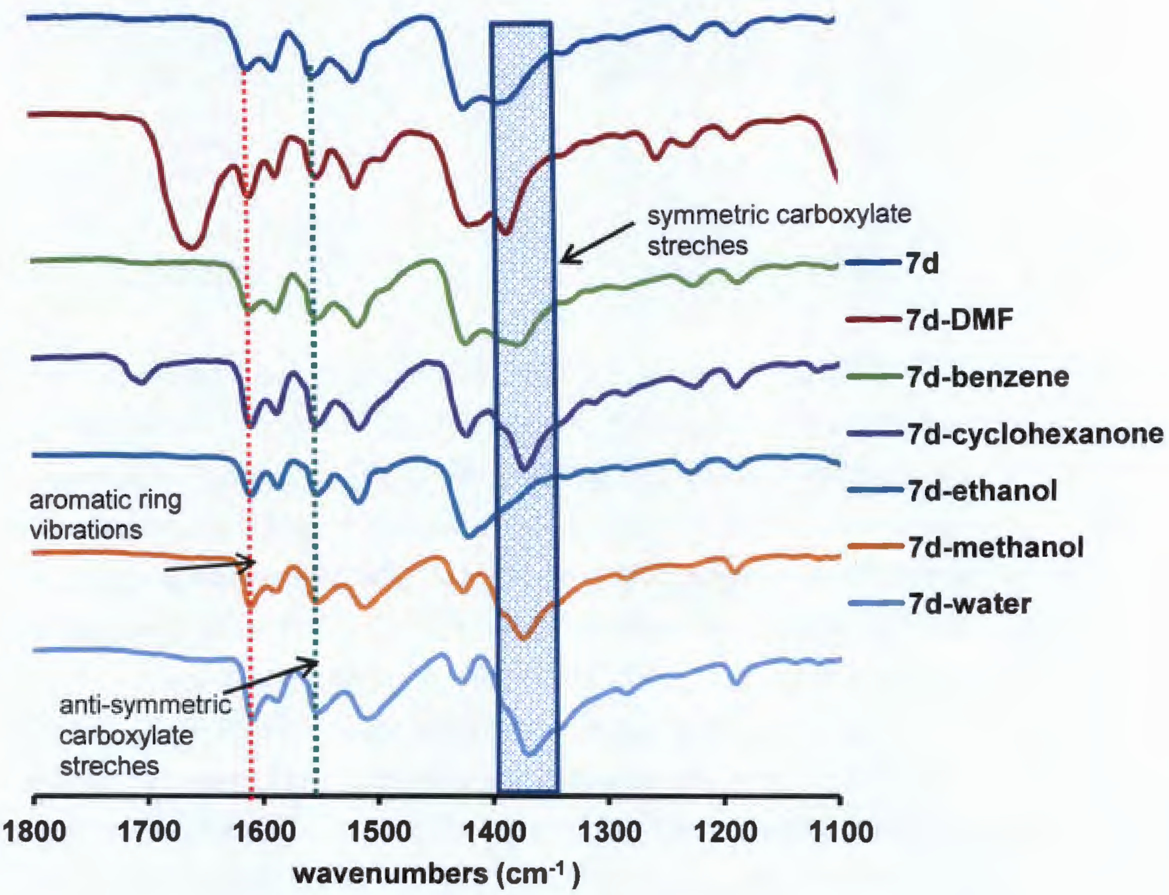

Figure 6.35: IR spectrum of several solvated forms of **7d**

Unlike in compound **6d** in which the positions of the asymmetric and symmetric stretches were unaffected upon solvent loading. Loading of **7d** with polar protic solvents gave rise to some significant changes in the positions of the symmetric carboxylate bands. In contrast to **7d-ethanol** in which the symmetric stretch shifted from 1390 in **7d** to 1423cm^{-1} upon absorption of ethanol, absorption of water and methanol shows a down shift by 15 cm^{-1}. The changes observed may be attributed to a change in the binding mode of the carboxylate supported by the increase in the energy difference between the anti-symmetric and symmetric carboxylate stretches (Table 6.12). Hydrogen bonding interactions have also been reported to cause a down shift in the frequency of absorption of the C = O group.[15]

Hence, there is a possibility that the downshift observed in **7d-water** and **7d-methanol** may be a result of hydrogen bonding interactions of the framework with these solvent molecules. Participation of solvent molecules in hydrogen bonding with the framework has been reported to alter the crystal structure, magnetic and spin cross over properties with some dramatic colour changes.[16,17] Without further data to support the IR results it is difficult to conclude whether or not the coordination geometry or metal centre is affected.

Table 6.12: Carboxylate band positions in the IR spectrum of **7d** inclusion compounds

Compound	***Asymmetric stretch (cm^{-1})***	***Symmetric stretch (cm^{-1})***	***Δ/cm^{-1}***
7d	1552	1390	164
7d-DMF	1552	1390	162
7d-benzene	1552	1378	178
7d-cyclohexanone	1556	1373	183
7d-ethanol	1552	1423	129
7d-methanol	1558	1375	183
7d-water	1558	1375	183

6.11 Summary

Compound **5** was found to crystallise in a chiral space group (*P*$2_12_12_1$). The thermal stability of the compound was evaluated by TGA and DSC. Its melting point was found to be around 340 °C as suggested by DSC and HSM studies. This compound was used for the preparation of compound **6** and **7**.

Compound **6** and **7** are isostructural compounds synthesised under solvothermal conditions. These compounds crystallised in a tetragonal crystal system and space group *I4*. Variable temperature PXRD studies of the two compounds show similar behaviour. Their structural integrity is not affected by the loss of solvent molecules residing in the channels. However thermal analysis by DSC shows that these compounds undergo a phase transition at about 312 and 333.4 °C for **6** and **7** respectively. Both compounds present high thermal stability decomposing at approximately 456 and 416 °C for **6** and **7** respectively. High thermal stability has been ascribed to the four-fold **dia**-network found in these compounds. Hexagonal rings in the four-fold network are catenated thus providing some form of extra thermal stability. Furthermore, the presence of hydrogen bonding interactions between adjacent **dia** networks may prevent the nets from sliding under external stimuli such as heat.

The kinetics of water uptake by activated phases, **6d** and **7d** yielded similar activation energies of 83.7 and 87.2 kJ·mol^{-1} respectively. The rate law which governed the uptake of water was found to be a D4 model in both systems. However, the desorption of water from the two analogues yielded different activation energies. For **6d-water**, an average value of 119(9) kJ·mol^{-1} was associated with the loss of water, while its analogue **7d-water** exhibited a lower activation energy value of 102(15) kJ·mol^{-1}. The difference in the energies has been attributed to the different packing arrangements and interactions of the water molecules with the host framework; this manifested in their TGA profiles which exhibited different kinetic profiles.

Both **6** and **7** exhibit an irreversible phase transformation with chromotropism when exposed to air. This arises from the exchange of guest molecules in the channels for water molecules from the atmosphere. Solvatochromic properties of **6** and **7** were studied by soaking the activated phases of these materials in various solvents. Inclusion of non-hydrogen donor solvents in **6d** (purple) gave colours similar to **6** (purple). However the inclusion of H-bonding donating solvents gave rise to formation of new phases whose colours are different from the former phase. These effects were confirmed by solid-state UV-Vis diffuse reflectance spectra for the inclusion compounds of **6d.** The results obtained were consistent with the observed colours. The mechanism of the solvatochromic behaviour is mostly likely to be derived from molecular distortions induced by strong hydrogen bonding. Such framework distortions may give rise to changes in the d-d transitions. Furthermore hydrogen bonding interactions tend to change the crystal packing of the compound which may also explain the observed colour change, although metal to ligand charge transfer transitions and π to π* transitions in the 44pba ligand may also play a significant role. The solvatochromic behaviour of **7** was very similar to that of **6**, with colours ranging from dark green to white upon inclusion of non-hydrogen donor solvents and hydrogen donating solvents respectively. The solvatochromic properties of **7d** are likely to stem from different mechanisms namely change in the binding mode of the carboxylate moiety or change in crystal packing of the compound induced by interaction of the solvent molecules with the host compound.

6.12 References

1. A. L. Spek, *Acta Crystallogr. D. Biol. Crystallogr.*, 2009, **65**, 148.
2. Z. Yin, Q.-X. Wang, and M.-H. Zeng, *J. Am. Chem. Soc.*, 2012, **134**, 4857.
3. TOPOS 4.0, http://www.topos.ssu.samara.ru/, accessed May 2012
4. N. W. Ockwig, O. Delgado-Friedrichs, M. O'Keeffe, and O. M. Yaghi, *Acc. Chem. Res.*, 2005, **38**, 176.
5. M. Usman, C.-H. Lee, D.-S. Hung, S.-F. Lee, C.-C. Wang, T.-T. Luo, L. Zhao, M.-K. Wu, and K.-L. Lu, *J. Mater. Chem. C*, 2014, **2**, 3762.
6. M. Cortijo, S. Herrero, R. Jiménez-Aparicio, J. Perles, J. L. Priego, M. J. Torralvo, and J. Torroba, *Eur. J. Inorg. Chem.*, 2013, **2013**, 2580.
7. A. Coetzee, L. R. Nassimbeni, and K. Achleitner, *Thermochim. Acta.*,1997, **298**, 81.
8. A. J. Fletcher, E. J. Cussen, T. J. Prior, M. J. Rosseinsky, C. J. Kepert, and K. M. Thomas, *J. Am. Chem. Soc.*, 2001, **123**, 10001.
9. H. J. Borchardt and F. Daniels, *J. Am. Chem. Soc.*, 1957, **79**, 41.
10. K. C. Stylianou, R. Heck, S. Y. Chong, J. Bacsa, J. T. A Jones, Y. Z. Khimyak, D. Bradshaw, and M. J. Rosseinsky, *J. Am. Chem. Soc.*, 2010, **132**, 4119.
11. Y. Gong, Y. Zhou, J. Li, R. Cao, J. Qin, and J. Li, *Dalton Trans.*, 2010, **39**, 9923.
12. Z.-Z. Lu, R. Zhang, Y.-Z. Li, Z.-J. Guo, and H.-G. Zheng, *J. Am. Chem. Soc.*, 2011, **133**, 4172.
13. J. Zhang, Y.-S. Xue, J. Bai, M. Fang, Y.-Z. Li, H.-B. Du, and X.-Z. You, *CrystEngComm*, 2011, **13**, 6010.
14. C.-Y. Niu, X.-F. Zheng, Y. He, Z.-Q. Feng, and C.-H. Kou, *CrystEngComm*, 2010, **12**, 2847.
15. A. Barth, *Biochim. Biophys. Acta*, 2007, **1767**, 1073.
16. B. Li, R.-J. Wei, J. Tao, R.-B. Huang, L.-S. Zheng, and Z. Zheng, *J. Am. Chem. Soc.*, 2010, **132**, 1558.
17. G. J. Halder, C. J. Kepert, B. Moubaraki, K. S. Murray, and J. D. Cashion, *Science*, 2002, **298**, 1762.

Chapter 7

Guest exchange studies in metal organic frameworks of Co(II) and Ni(II) assembled from 4-(4-pyridyl)benzoate

This chapter deals mainly with the structural transformations triggered by guest exchange when compound **6** assembled from Co(II) and 4-(4-pyridyl)benzoate is soaked in methanol for about four weeks. The process of transformation was characterised using DSC, TGA, PXRD and single crystal X-ray crystallography. Single crystal structural characterisation of the transformed MOFs clearly showed how solvent molecules and metal coordination environments influence changes in the properties of the metal organic frameworks such as crystal colour and structural topologies. The last section of this chapter discusses the iodine uptake by the desolvated phase of compound **7**. The nature of interactions between the iodine molecules is unveiled by single crystal structure analysis.

Methanol induced structural transformations on compound $\{[Co_4(44pba)_8]\cdot 4DMF\cdot 0.5EtOH\cdot 4H_2O\}_n$ **(6)** were studied by thermal analysis and X-ray diffraction methods. The phase changes were monitored on a weekly basis by powder X-ray diffraction and X-ray single crystal diffraction. Figure 7.1 shows a schematic illustration of the framework transformations. Inserted in the scheme is a single crystal monitored over a period of four weeks. Single crystal X-ray diffraction revealed that upon soaking **6** in dry methanol the guest DMF and ethanol molecules are easily exchanged for methanol molecules as there are weak hydrogen bonding interactions between the guest molecules and the host framework in **6**. This occurs via a single crystal to single crystal transformation process.

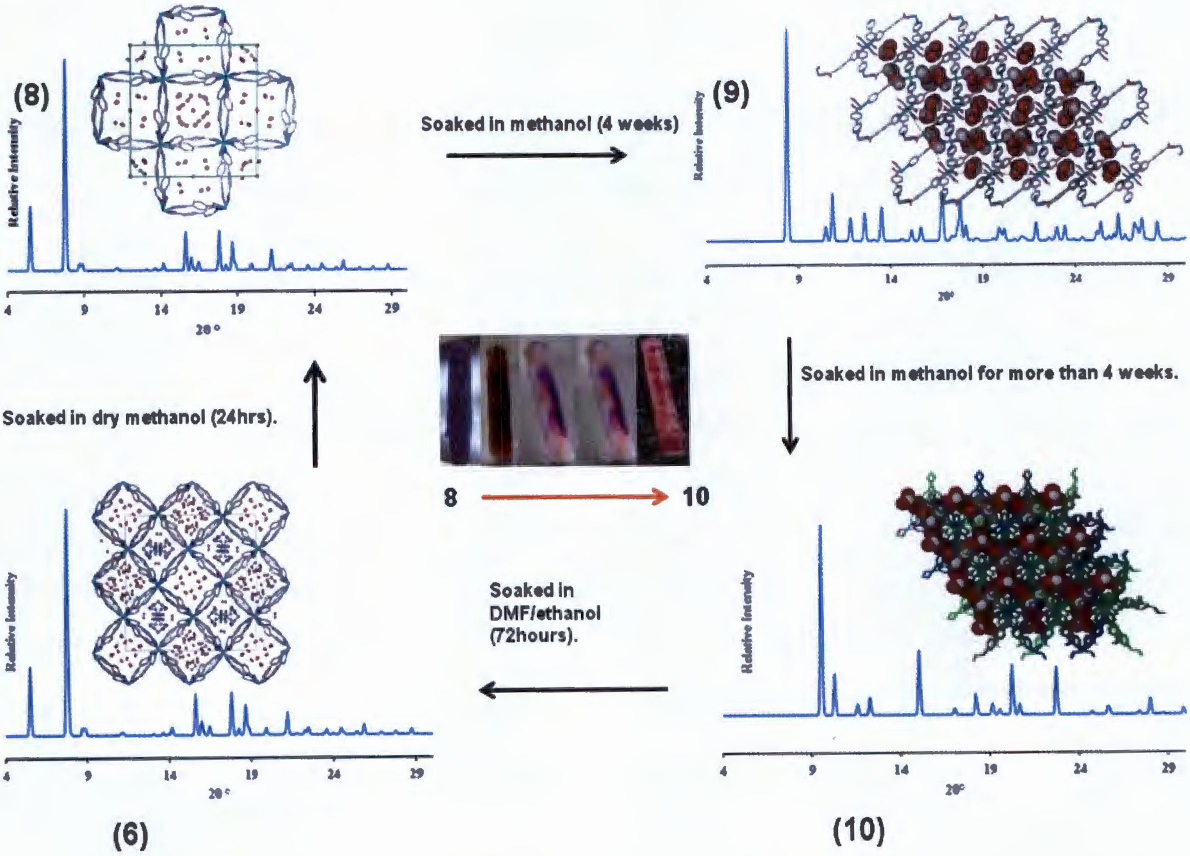

Figure 7.1: Scheme illustrating the phase transformations in **6**. Inserted is a crystal captured over a period of 4 weeks showing changes in its physical appearance.

Figure 7.2 displays the PXRD patterns of the compounds $\{[Co(44pba)_2]\cdot 2.5CH_3OH\cdot H_2O\}_n$ **(8)**, $\{[Co(44pba)_2(CH_3O)_2]\cdot 2CH_3OH\cdot 0.5H_2O\}_n$ **(9)**,

$\{[Co_{0.5}(44pba)(CH_3OH)]\cdot 0.5CH_3OH\cdot 0.25H_2O\}_n$ **(10)** that were obtained after soaking compound **6**, $\{[Co_4(44pba)_8]\cdot 4DMF\cdot 0.5C_2H_5OH\cdot 4H_2O\}_n$ in methanol for four weeks.

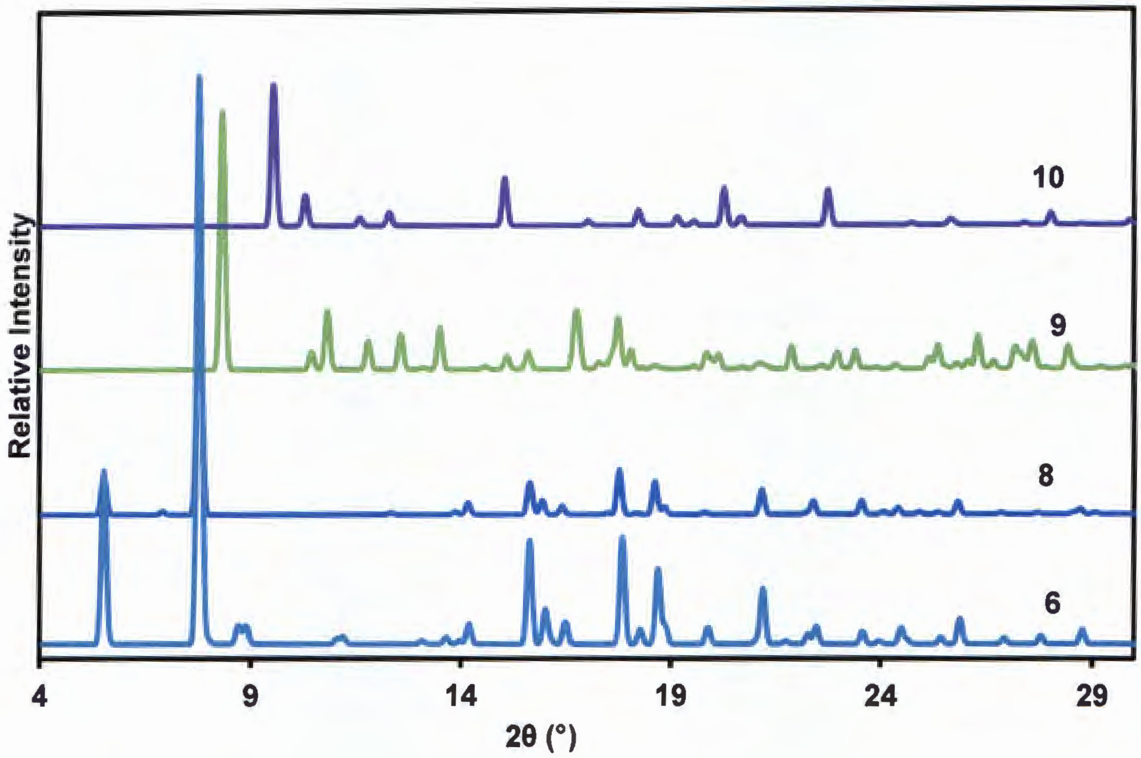

Figure 7.2: PXRD patterns of compounds **6**, **8**, **9** and **10**. The traces were simulated from their single crystal structures

7.1 Preparation of $\{[Co(44pba)_2]\cdot 2.25CH_3OH\cdot 1.25H_2O\}_n$ (8), $\{[Co(44pba)_2(CH_3OH)_2]\cdot 2CH_3OH\cdot 0.5H_2O\}_n$ (9), $\{[Co_{0.5}(44pba)(CH_3OH)]\cdot 0.5CH_3OH\cdot 0.25H_2O\}_n$ (10)

Crystals of **8** were obtained by soaking crystals of compound **6** in dry methanol for 24 hours. Compound **9** and **10** were obtained concomitantly after soaking crystals of **6** in methanol for four weeks. These were identified based on their colours; crystals of **9** were light pink, while those of **10** were dark pink. Elemental analysis for these compounds are given in Table 7.1. Crystals of **9** could not be isolated from their mother liquor for further studies as there was insufficient material.

Table 7.1: Elemental analysis of **8** and **10**

Compound		Calculated	Found
8	% C	57.28	57.27
	% H	5.05	4.99
	% N	5.10	5.13
10	% C	58.17	59.81
	% H	4.71	4.03
	% N	5.03	5.13

7.2 Single crystal X-ray diffraction

The non-hydrogen atoms were located in the difference electron maps and were refined anisoptropically. Due to solvent disorder some non-hydrogen atoms of the guest molecules were refined isotropically. All hydrogen atoms of the 44pba ligand and coordinated methanol were placed with geometric constraints and refined with isotropic temperature factors. Temperature factors of 1.2 times and 1.5 times the parent atom's were assigned for hydrogens on phenyl and pyridyl rings and for methanol methyl groups respectively. Hydrogen atoms of the guest water and methanol molecules could not be located from the Fourier electron density map. The crystallographic and refinement parameters for compounds **8**, **9** and **10** are given in Table 7.2

Table 7.2: Crystallographic and refinement parameters of compounds **8**, **9** and **10**

	8	***9***	***10***
Molecular Formula	**$\{[Co(44pba)_2]\cdot 2.25CH_3OH\cdot 1.25H_2O\}_n$**	**$\{[Co(44pba)_2(CH_3O)_2]\cdot 2CH_3OH\cdot 0.5H_2O\}_n$**	**$\{[Co_{0.5}(44pba)(CH_3O)]\cdot 0.5CH_3OH\cdot 0.25H_2O\}_n$**
Molecular Mass	553.46	590.50	277.72
Crystal Size (mm)	0.22 x 0.21x 0.20	0.45 x 0.27 x 0.20	0.14 x 0.13 x 0.08
Temp. of collection / K	173(2)	173(2)	173(2)
Crystal symmetry	tetragonal	monoclinic	trigonal
Space group	$P42_12$	$P2/c$	$P3_212$
a / (Å)	22.659(1)	17.0218(5)	10.7022(4)
b / (Å)	22.659(1)	10.5990(3)	10.7022(4)
c / (Å)	12.704(1)	18.3064(5)	22.874(2)
α / (°)	90	90	90
β / (°)	90	106.073(1)	90
γ / (°)	90	90	120
Z	8	4	6
Volume/ $Å^3$	6522.4(8)	3173.6(2)	2268.9(2)
Dc / g cm^{-3}	1.12	1.236	1.219
F(000)	2288	1232	861
2θ range	1.60 – 28.32	1.45 – 28.29	2.20 – 24.77
Index ranges (h, k, l)	-30:30; -25:30; -16:16	-22:22; -14:14; -28:28	-12 :11; -8 :12; -26 : 26
No. of reflections collected	43 343	57 286	9 746
No. Unique reflections	8130	17872	2603
No. Reflections with $I > 2\sigma(I)$	6087	6686	1865
Goodness of fit, S	1.12	1.13	1.08
Final R indices	0.064	0.050	0.081
Final wR_2	0.2156	0.1658	0.2522
Min, Max e density / $eÅ^{-3}$	-1.08;1.02	-0.43; 1.27	-0.72; 0.51

space. Adjacent diamondoid nets are linked by weak hydrogen bonding interactions. The hydrogen bonding parameters between adjacent nets are given in Table 7.4.

Table 7.4: Hydrogen bonding interactions between adjacent diamondoid nets in compound **8**

Donor - H...Acceptor	*H...A(Å)*	*D...A(Å)*	*D - H...A(°)*	*Symmetry Operator*
C4A - H4A...O14B	2.57	3.376(5)	143	y-1/2, 1/2-x, z
C5B - H5B...O15A	2.5	3.365(5)	150	1/2-y, 1/2+x, z
C6A - H6A...O14A	2.48	3.328(5)	148	y-1/2, 1/2-x, z
C6A - H6A...O14A	2.44	3.074(6)	123	x-1/2, 1/2-y, 1-z

The structure is stabilised by the four-fold interpenetrating helical nets which form a spiral parallel to the c-axis. The interpenetration preserves the channels (**A** and **B**) which only run along the *c*-axis and are very similar to those of compound **6** (Figure 7.5). Compound **6** had three channels which differ in their guest content. Channels in **8** occupy 46.5% (3029.9 Å) of the unit cell volume (6522.4 Å) as calculated by PLATON[1] using a probe radius of 1.2 Å.

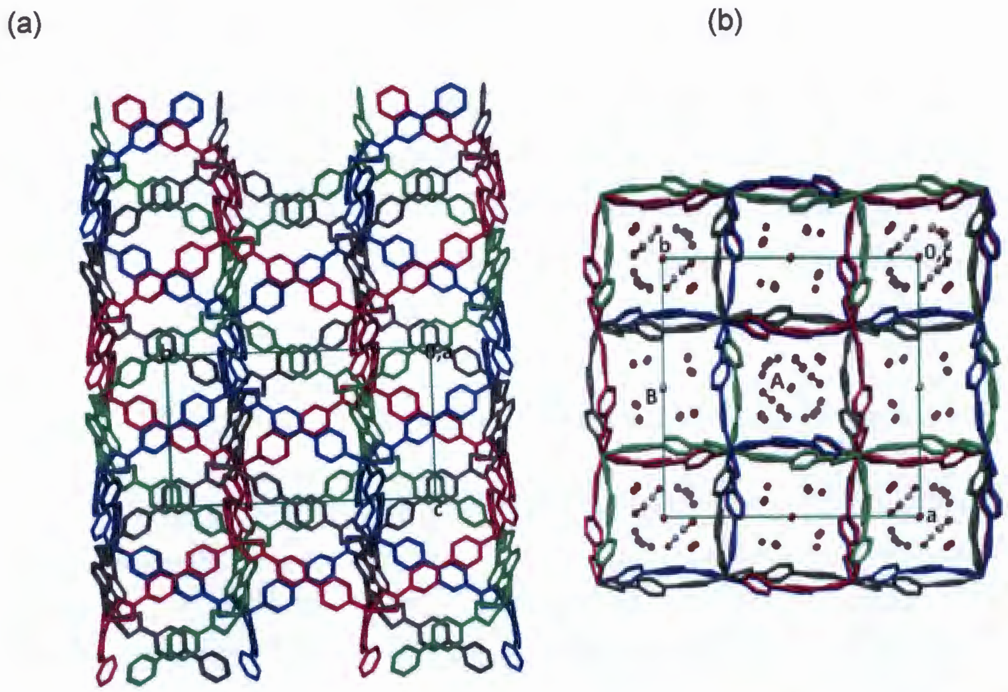

Figure 7.5: (a) Four-fold interpenetrated helical nets which construct the channels **A** and **B** observed along the [0 0 1] direction, (b) packing diagram of **8** viewed along the *c*-axis showing the channels occupied by guest water and methanol molecules drawn in ball and stick form.

Thermal analysis by TGA was used to model the relevant site occupancies of the solvent molecules found in the channel of **8**. A total of 2.25 methanol molecules were located and were disordered over four positions. There are two methanol molecules with full site occupancy while the remaining one has 25% site occupancy. One of the methanol molecules with ¼ site occupancy is located at a Wyckoff position *c*. Three water molecules disordered over three positions were modelled each with site occupancy of 0.25. One of the water molecules is located at a Wyckoff position *c*. A further water molecule located in a general position was refined with partial site occupancy of 0.5

Figure 7.6 shows the packing diagram of **8** viewed along the [001] axis. Overlaid are the symmetry elements present in the $P42_12$ space group. There are two different locations of the four-fold rotation axis parallel to [001]. These are located at (0 ½ z) and (½ 0 z) with symmetry operator of ½-y, ½+x, z and ½+y, ½-x, z respectively. The four-fold rotation axis located at (0 ½ z) passes through a methanol molecule.

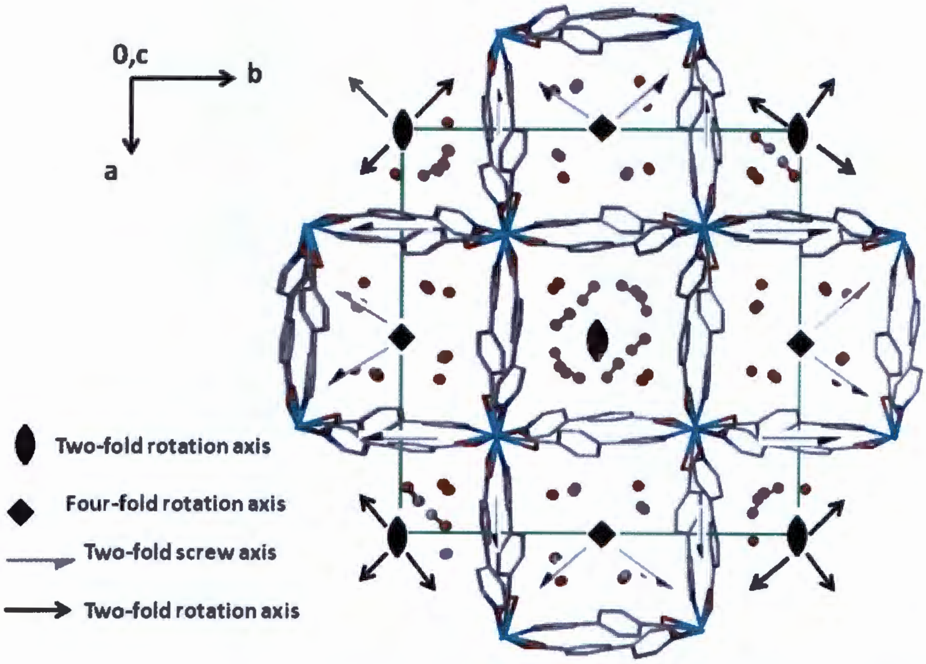

Figure 7.6: The packing diagram of **8** viewed along the [001] axis with an overlay of the symmetry elements given in black.

Present in this space group also are two-fold rotation axes at (0 0 z), (x y 0) and (x,-1 0) parallel to [001], [110] and [1-10] respectively. The two-fold rotation axis located at (0 0 z) passes through a water molecule. Two crystallographically different locations of two-fold screw axis are at (x ¼ 0) and (¼ y 0) with symmetry operators of ½+x, ½-y, -z and

½-x, ½+y, -z respectively. The one located at (x ¼ 0) which run along the [100] axis is centred between independent 44pba ligands which connects the metal centres.

Compound **8** has the same **dia** topology as that found in compound **6**, hence its topological description will not be given.

7.2.2 Crystal structure description of 9

Compound **9** crystallises in the monoclinic space group *P2/c.* Two crystallographically independent Co(II) centres (Co1 and Co2) were modelled in the asymmetric unit each with a site occupancy of 0.5. Both Co1 and Co2 are located at special positions of (½ y ¼) and (0 ½ -½) respectively. These differ in their coordination environments as depicted in Figure 7.7. Co1 is bonded to four 44pba ligands via two nitrogens of the pyridyl moiety and two oxygen atoms of the carboxylate in a monodentate fashion. The two pyridyl moieties are coordinated to the metal ion in a *cis* fashion while the carboxylate groups are *trans* to each other. Two methanol molecules are coordinated to Co1 in a *cis*-fashion and these act as terminal ligands. Co2 is similarly coordinated to four 44pba ligands and two methanol molecules but in this case the methanol molecules and pyridyl groups are *trans* to each other while the carboxylate groups remain in the same configuration as in Co1. The Co – N bond distance range from 2.133(2) to 2.161(2)Å while the Co – O bond length is within a range of 2.033(2) to 2.158(2)Å (Table 7.5). Majority of the bond angles around the two metal centres are close to 90°. The overall geometry around the cobalt centre is a distorted octahedron.

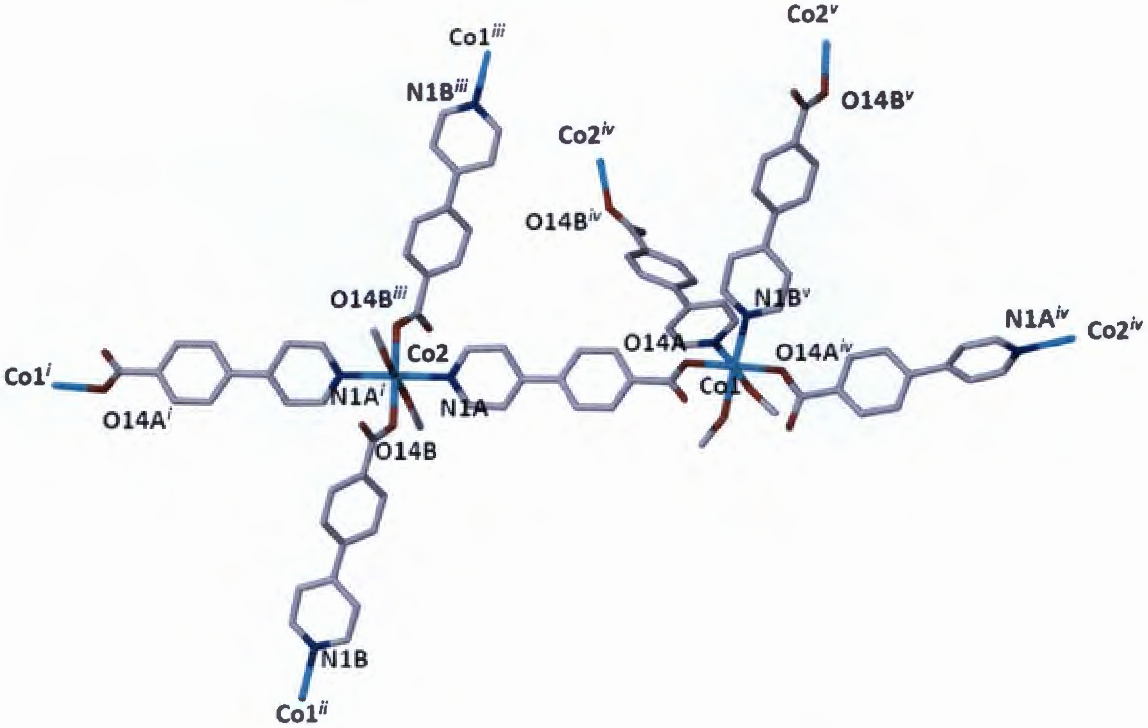

Figure 7.7: Coordination geometry around the two metal centres of **9** showing a distorted octahedral geometry. Symmetry operator: ^{i}*-x, 1-y, -z-1;* ^{ii}*x-1, 1+y, z-1;* ^{iii}*1-x, -y, -z;* ^{iv}*1-x, y, ½-z;* ^{v}*1+x, y-1, 1+z;* ^{vi}*-x, y-1, -z-1/2*

Table 7.5: Bond length parameters around the metal centres of compound **9**

Bond Type	***Bond length(Å)***	***Bond type***	***Bond length(Å)***
^{a}Co1 - O1D	2.158(2)	^{c}Co2 - N1A	2.161(2)
^{a}Co2 - O1C	2.155(2)	^{b}Co2 - O14B	2.033(2)
^{b}Co1 - O14A	2.048(2)	^{c}Co2 - N1B	2.133(2)

^{a}terminal ligand(methanol); ^{b} carboxylate of 44pba; ^{c}pyridyl of 44pba

The 44pba ligands link neighbouring Co(II) centres to form a 3D network . Due to the spacious nature found in a single net, two independent 3D nets interpenetrate to stabilise the overall network (Figure 7.8). Adjacent nets are involved in hydrogen bonding interactions (Table 7.6)

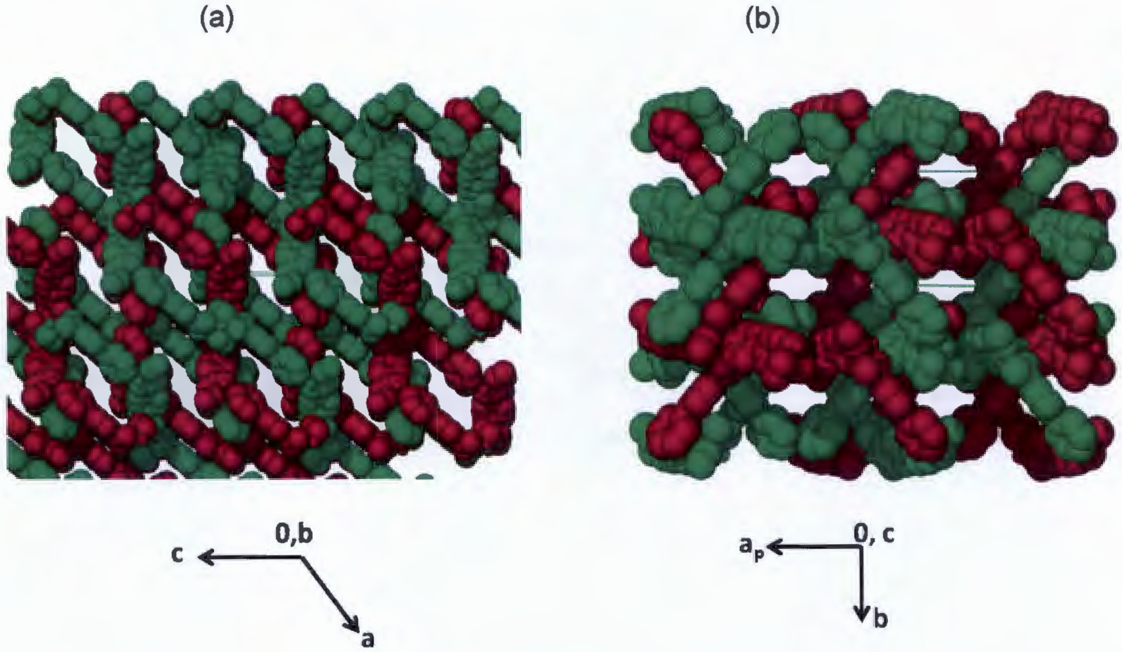

Figure 7.8: Two independent interpenetrating nets found in compound **9** depicted in different colours (a) viewed along the *b*-axis, (b) along the *c*-axis.

Table 7.6: Hydrogen bonding parameters in compound **9**

Donor - H...Acceptor	*H...A (Å)*	*D...A (Å)*	*D - H...A(°)*	*Symmetry Operator*
C2B - H2B...O14A	2.56	3.038(4)	111	-x, 1+y, -1/2-z
C6A - H6A...O14B	2.55	3.057(3)	113	

In the asymmetric unit of **9**, a total of two uncoordinated methanol molecules were modelled and were disordered over seven positions. Two positions were located for a total of 0.5 water molecules. However, it must be noted that the guest content modelled in the asymmetric unit of **9** may be inaccurate due to the absence of TGA results which is usually used to model the amount of guest present. Both coordinated and uncoordinated solvent molecules occupy 44.7% of the unit cell volume as estimated in PLATON. Figure 7.9 displays the packing diagram of compound **9** illustrating the guest free network and the one with guest molecules.

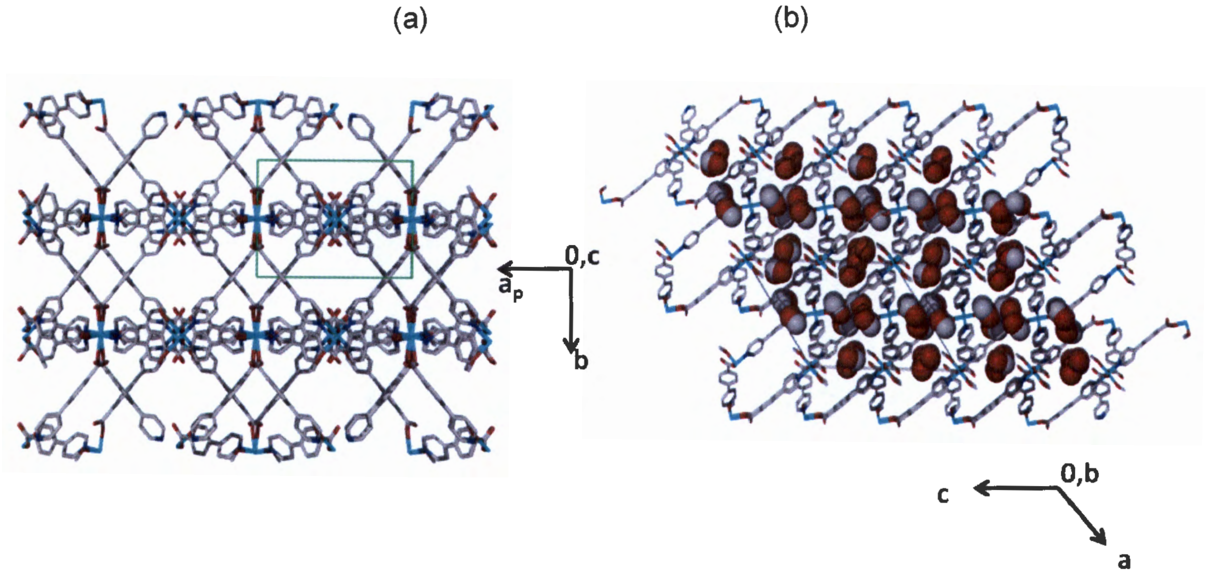

Figure 7.9: (a) Solid state structure of **9** viewed along the *c*-axis. The hydrogen atoms and guest molecules have been omitted. (b) Solid state structure drawn with the guest molecules shown in van der Walls radii and the framework in stick form

Figure 7.10 displays the packing diagram of compound **9** and an overlay of the symmetry elements present in *P2/c* space group. The centres of inversion are shown as black circle while the two-fold rotation axes are depicted in black. The (0, 0, 0) centres of inversion with a symmetry operator of –x, -y, -z are located at the metal centres. The (0 y ¼) two-fold rotation axes which run along [010] pass through a water molecule. There also are glide planes not shown on the diagram which are perpendicular to [010] with a glide component of 0 0 ½ related by a symmetry operator of x, -y, ½+z.

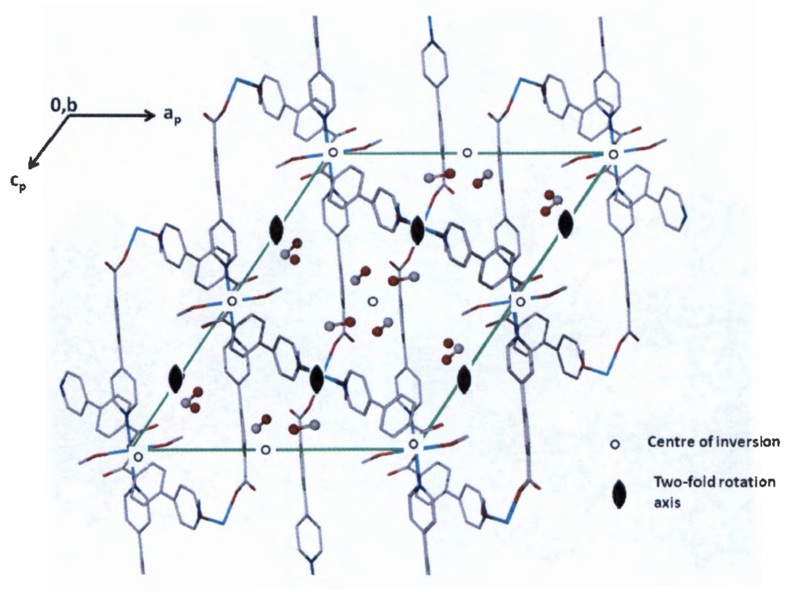

Figure 7.10: The packing diagram of **9** viewed along the [010] axis with an overlay of the symmetry elements given in black.

Network analysis in TOPOS revealed a 4,4–connected binodal net with a **pts** topology. Topologically each cobalt centre can be considered as 4-connected. Due to the different configuration of the coordinated methanol molecules, the Co1 centre results in a tetrahedral node while the Co2 gives a square planar node. The vertex symbols for each of these nodes are different; Co1 has a vertex symbol of $4.4.8_7.8_7.8_7.8_7.8_7$ while that of Co2 is $4.4.8_2.8_2.8_8.8_8$ all having the same point symbol $4^2.8^4$. Figure 7.11 displays several representations of the **pts** net found in **9**. The 3D net is generated by alternating connecting square planar nodes and distorted tetrahedral nodes to those in adjacent layers above and below. Furthermore, 8-membered rings can be identified in the projection shown in Figure 7.11, these rings represent the largest circuit of the essential rings that define the topology. When tetrahedral nodes and square planar nodes are linked in a single net, three topologies may arise. These are **pts** (platinum sulphide), **ppt** (PtS twisted) and **mog** (moganite). In a **pts** net the ratio of the square planar to tetrahedral nodes is equal. The **mog** net has a 1:2 ratio of the square planar to tetrahedral nodes, while a **ptt** net has two types of square planar nodes , hence it may be regarded as a trinodal net. In compound **9**, the square planar node arises as a result of the *trans* geometry exhibited by all the ligands around the Co2 centre. In contrast, the Co1 centre has methanol and the pyridyl moiety in a *cis* geometry. This results in a distorted tetrahedral geometry. Methanol molecules act as terminating ligands and are not considered in the topological geometry. Despite the fact that methanol molecules are not considered in deriving the topology of compound **9**, these molecules play an important role in directing the overall topology of this compound. For example if all the methanol molecules in the two metal centres were *cis* to each other, then it would be possible to obtain a uninodal **qtz** (quartz) net since the two centres would be topologically equivalent.

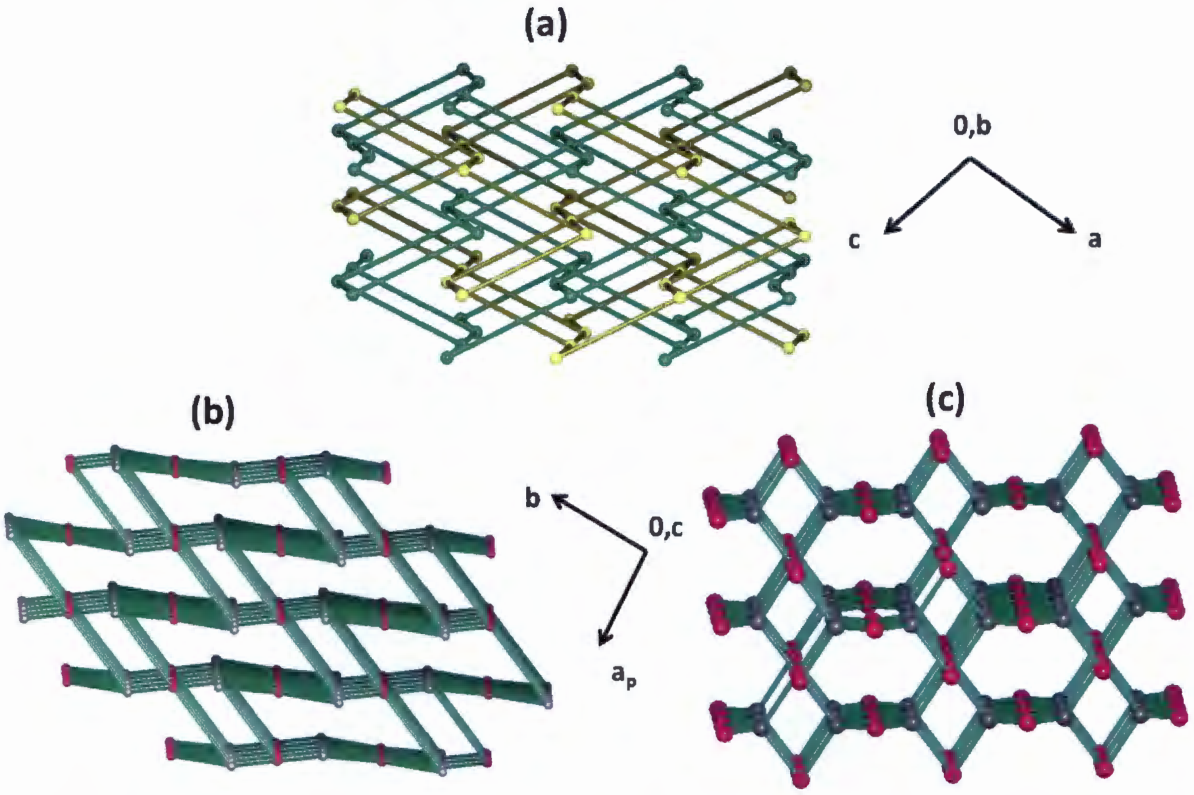

Figure 7.11: (a) two-fold interpenetrating nets found in **9.** (b) Topological representation of the **pts** net found in **9**, (c) ideal form of the net of high symmetry and low density.

7.2.3 Crystal structure description of 10

Single crystal X-ray diffraction revealed that compound **10** crystallises in a trigonal crystal system and chiral space group *P3₂12*. In the asymmetric unit, the Co(II) centre is located at position (x, y, 0) with a site occupancy of 0.5, one coordinated 44pba ligand and one coordinated methanol molecule were modelled. The Co(II) metal ion adopts a similar geometry as Co1 centre in **9** (Figure 7.6 and 7.12). The Co – N bond distance of 2.143(8)Å is within expected range. Coordinated methanol and oxygen atoms of the carboxylate group to the Co(II) centre have bond lengths of 2.128(6) and 2.065(8)Å respectively. The bond lengths are given in Table 7.7. Majority of the bond angles around the metal centre are in the range of 89 to 92° with a few in the range of 176 -178° giving rise to a distorted octahedral geometry.

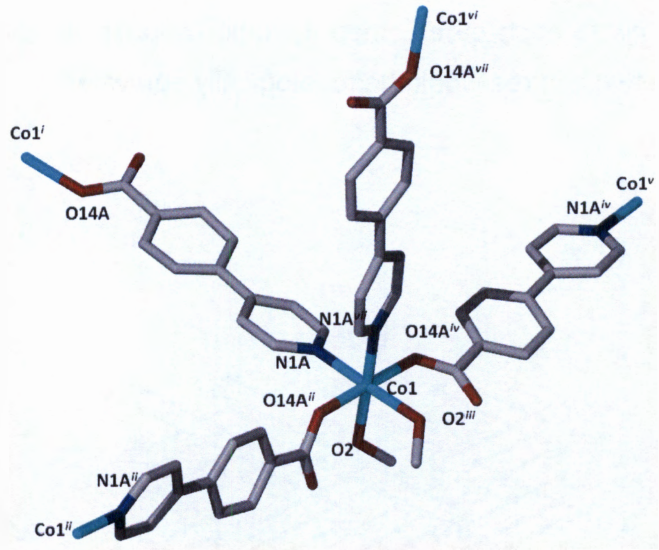

Figure 7.12: Coordination geometry around the Co(II) metal centre in compound **10**. Symmetry operator: ^{i}*2-y, 2+x-y, z-1/3;* ^{ii}*-x+y, 2-x, 1/3+z;* ^{iii}*-x+y-1, -x, 1/3+z;* ^{iv}*-y, 1+x-y, z-1/3.*

Table 7.7: Parameters for bond lengths around the Co(II) centre in **10**.

Bond Type	*Bond length(Å)*	*Bond type*	*Bond type(Å)*
[a]Co1 - N1A	2.143(8)	[b]Co1 – O14A	2.065(8)
[b]Co1 - O2	2.128(6)		

[a] terminal ligand (methanol); [b]44pba ligand. The other bonds which make the overall octahedral geometry are symmetrically generated

In the packing diagram of **10** (Figure 7.13), adjacent symmetry generated independent nets are connected by weak hydrogen bonds. The geometric parameters of these interactions are given in Table 7.8.

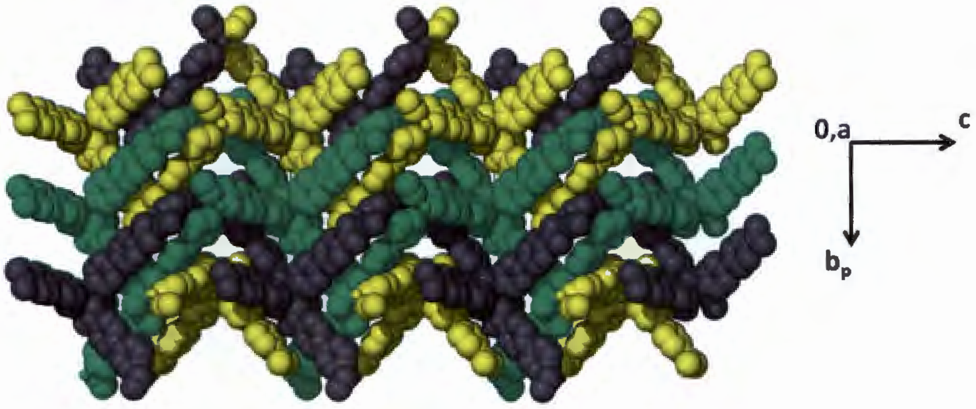

Figure 7.13: Packing diagram of compound **10** drawn with van der Waals radii. Solvent molecules have been omitted for clarity. Independent nets are shown in different colours.

Table 7.8: Intramolecular hydrogen bonding interactions in the framework of **10**

Donor - H...Acceptor	*H...A(Å)*	*D...A(Å)*	*D - H...A(°)*	*Symmetry Operator*
C2A - H2A...O14A	2.47	3.076(17)	122	1-y, 2+x-y, -1/3+z
C6A – H6A...O14A	2.44	3.015(14)	119	1-y, -x, 1/3-z

In addition to the modelled coordinated solvents, a number of uncoordinated solvent molecules were also located in the asymmetric unit. One water molecule with a site occupancy of 0.25 was located as well as two methanol molecules with site occupancy of ¼. PLATON estimates a void volume of 37.1% in the absence of both bound and unbound solvent molecules.

Compound **10** is a 3D network with interconnected cavities. The cavities are occupied by methanol and water molecules. There are two types of cavities in **10** which differ in their dimensions (Figure 7.14). The large triangular channels have dimensions of 27 x 22 x 27 Å^3 while the small triangles have approximately equal sides of 13.4 x 13.4 x 13.4 Å^3. As a consequence of the large channels present in a single net, extra stability of the network is provided through the three-fold interpenetration of independent nets.

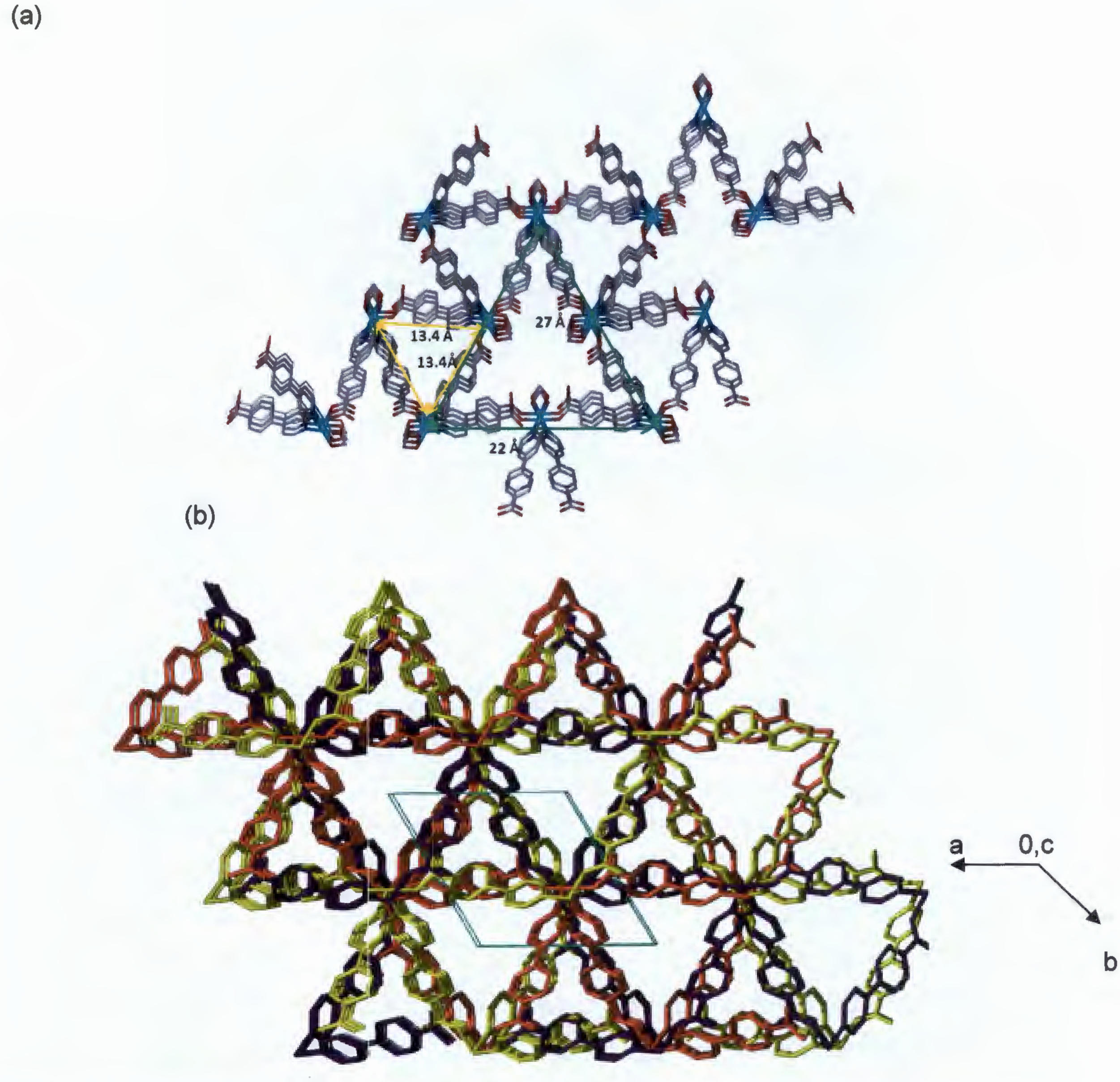

Figure 7.14: (a)Single net found in compound **10** showing dimensions of large and small triangular channels. (b) because of the large channels found in a single net, three independent nets (shown in different colours) interpenetrate each other closing the space, however interconnected channels are observed in which methanol and water molecules reside. Both coordinated and uncoordinated solvent molecules have been omitted for clarity.

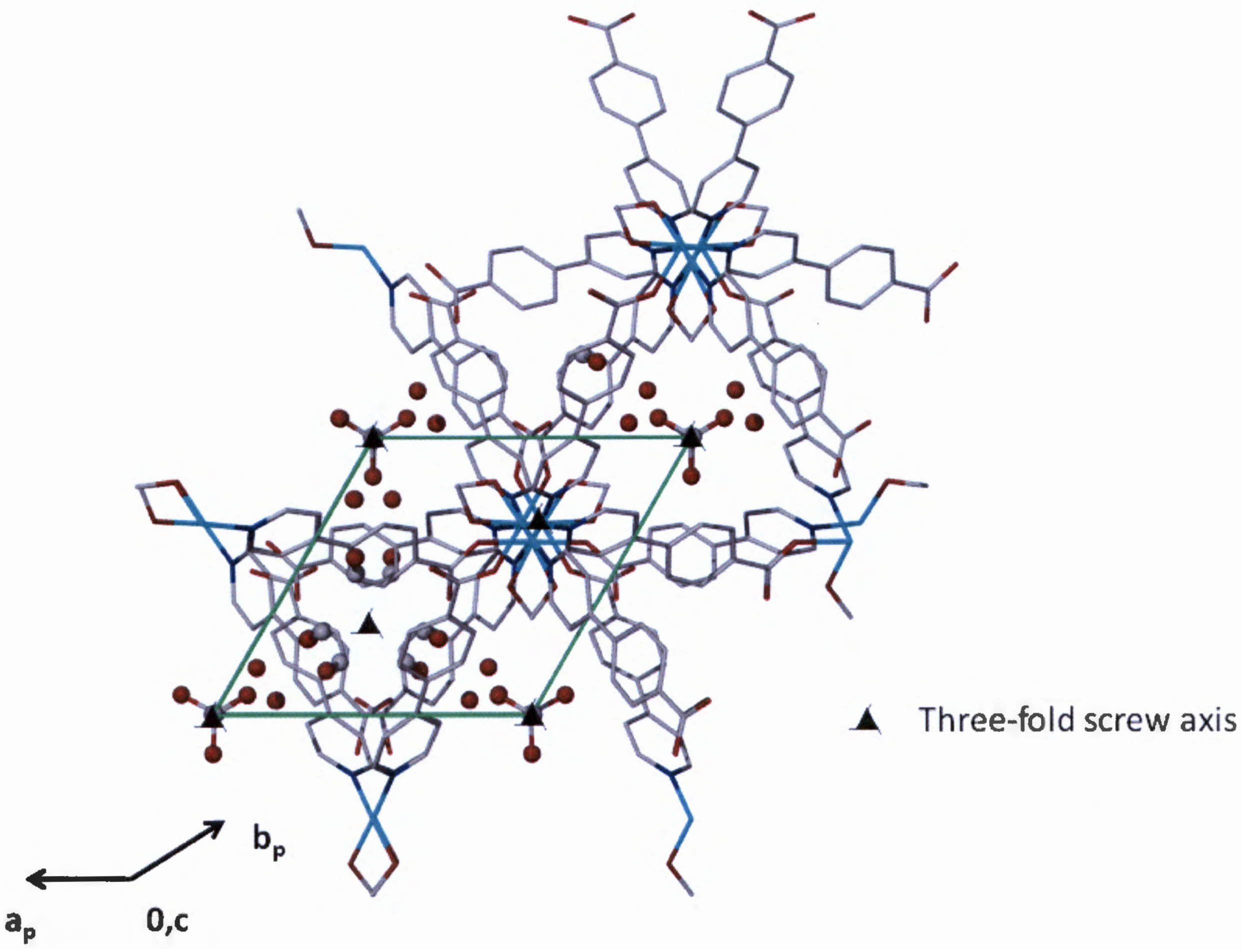

Figure 7.15: An overlay of the structure of **10** and the three- fold screw axis. The framework shown in stick form while the guest is displayed in ball and stick form. Some of the symmetry elements have been omitted.

Figure 7.15 displays the symmetry elements present in $P3_212$. Not shown in Figure 7.15 are two-fold rotation axes. There are three locations of the two-fold rotation axes. These are located at (x, -x, 1/6), (x, 2x, 1/3) and (2x, x, 0) and run along the [1-1 0], [1 2 0] and [2 1 0] respectively. The two-fold rotation axis located at (2x, x, 0) with a symmetry operator x, x-y, -z passes through the metal centre, hence the metal sits on a two-fold axis. In addition to the two-fold rotation axes, there are three-fold rotation screw axes located at (0 0 z) which run along the [0 0 1] direction with different screw components. The one with a symmetry operator of –y, x-y, 2/3+z has a screw component of (0 0 2/3) while the other one with a symmetry operator of –x+y, -x, 1/3+z has a screw component of (0 0 1/3).

Compound **10** can be reduced to a simple net by considering each metal centre as a 4-connected node. Each cobalt centre is connected to the other cobalt centre by the linear 44pba bridges to produce a **qtz** (quartz) network (Figure 7.14). The geometry around each node is a highly distorted pseudo-tetrahedral geometry. The Co – Co – Co are 85.1, 87.2, 89.0 and 174.8°. The calculated point symbol and vertex symbol are $6^4.8^2$ and $6.6.6_2.8_7.8_7$ respectively. Figure 7.16 displays the topological representation of the net found in **10** and the ideal form of the net.

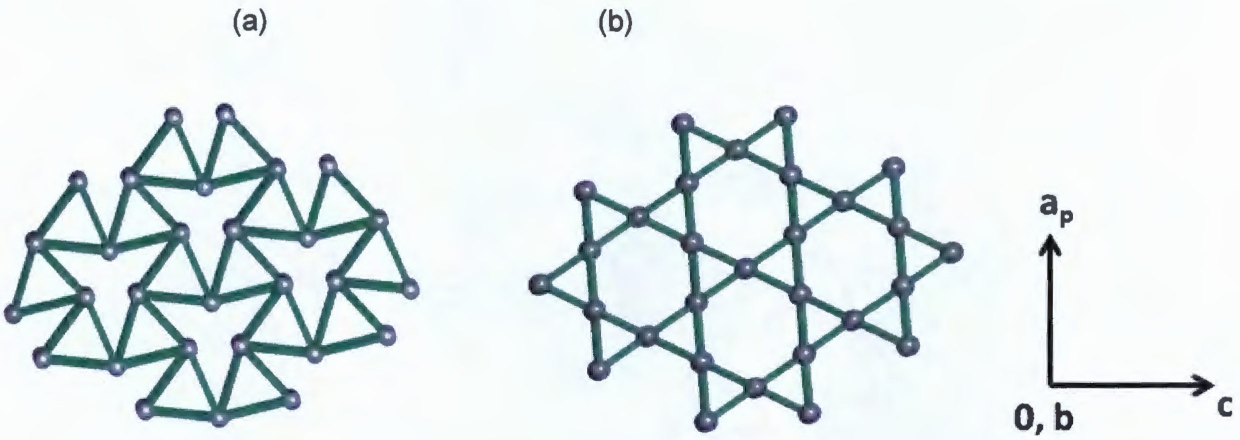

Figure 7.16: a) Topological representation of the net found in **10**; b) ideal form of the net of high symmetry and low density.

MOFs with a **qtz** topology are closely related to the ones with a **mog** topology. In a **qtz** there are no 4-membered rings that are comparable to those found in a **mog** net. Both **qtz** and **mog** nets comprise of only three vertices in the repeat unit, one more than is found in the simplest 4-connected nets such as **dia** and **$CdSO_4$**

7.3 Thermal analysis

An overlay of TGA and DSC analysis of compound **8** is displayed in Figure 7.17a. A total mass loss of 17.6% is observed from 23 – 123 °C. The mass loss corresponds to release of guest water and methanol molecules modelled in the crystal structure (calculated 17.1%). DSC analysis shows endothermic peaks at about 36.5 °C, 60.2 °C and 108 °C within a temperature range of 23 – 123 °C. These events correspond to successive release of the guest water and methanol molecules. The DSC trace exhibits an exothermic peak at approximately 316 °C which suggests a phase change.

Thermal analysis of compound **9** could not be performed as only a few crystals were observed and there was not sufficient material for further analysis.

Thermal analysis of compound **10** is shown in Figure 7.17.b. The TGA shows rapid loss of guest molecules within a temperature range of 25 – 125 °C. A broad endothermic peak (25 – 125 °C) is observed on the DSC trace of the compound which concurs with the mass loss seen on the TGA. The total mass loss of 17.5% observed on the TGA corresponds to simultaneous loss of coordinated and uncoordinated solvent molecules modelled in the crystal structure (calculated 18.6%). An exothermic peak is observed around 314 °C which may be associated with a phase transition as already noted with other compounds presented in this thesis. The guest free compound decomposes above 425 °C as suggested by both TGA and DSC analysis.

Both **8** and **10** decompose at temperatures above 400 °C. The high thermal stability may be associated with their structural features. Interpenetration of independent networks and hydrogen bonding interactions of the nets may account for the observed high thermal stabilities of the compounds.

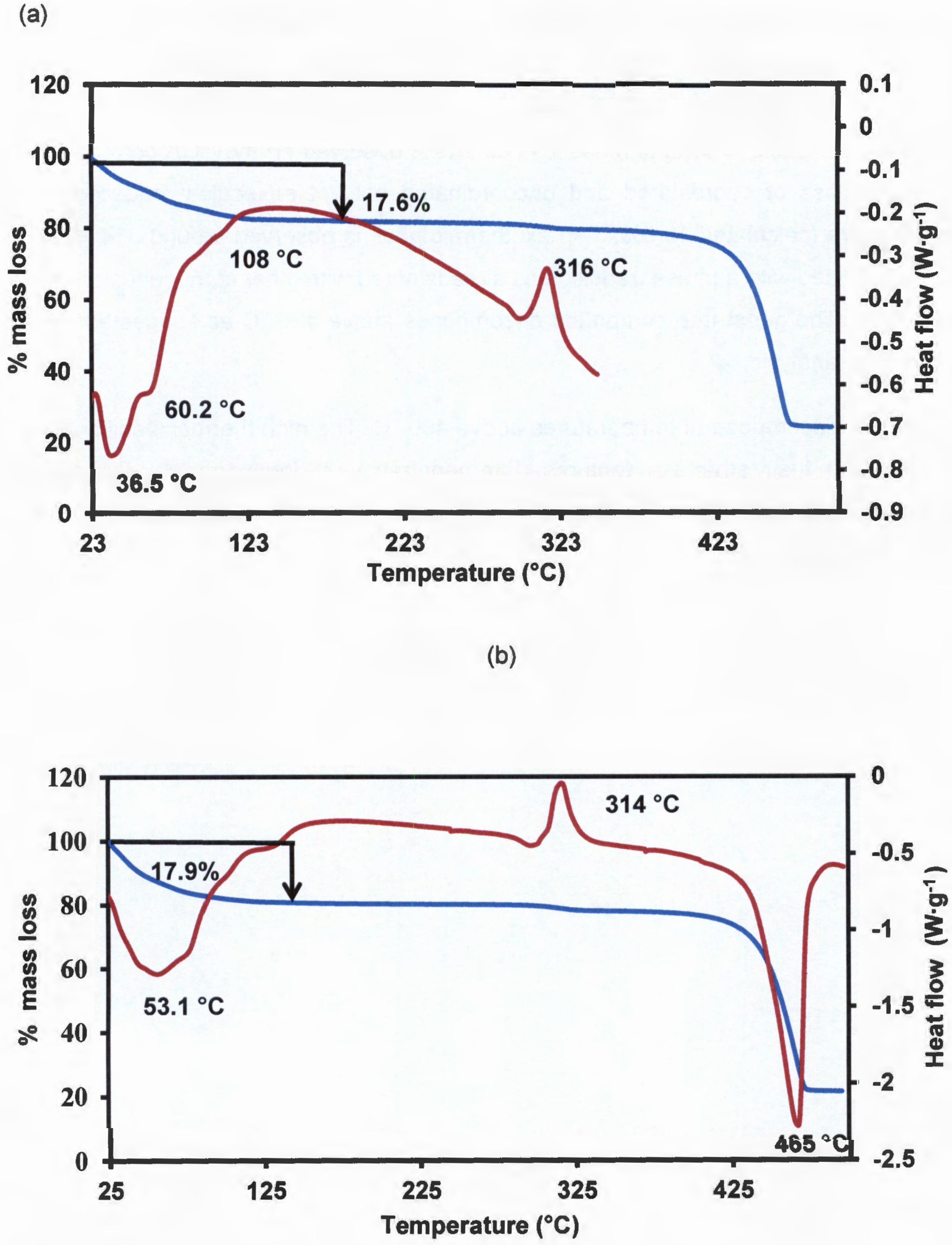

Figure 7.17: TGA (blue) and DSC (red) analysis of compound **8** (a) and **10** (b).

7.4 Phase transformations

Single crystal X-ray diffraction showed that the guest molecules in **6** are easily replaced by methanol molecules to give **8** upon soaking crystals of **6** in dry methanol. This can be explained by the weak hydrogen bonding interactions between the host and the guest in **6**. The process of guest exchange occurs through a single crystal to single crystal process. There is a change in the space group from *I4* in **6** to $P42_12$ in **8** and a minor modification of the framework from the starting material **6** to the subsequent structure **8** which does not affect the network topology. Table 7.8 gives a comparison of the dihedral angles between the phenyl and pyridyl ring in compound **6** and **8**.

Table 7.8: A comparison of the dihedral angles between the pyridyl and phenyl ring found in compound **6** and **8**

Atom labels	*A*	*B*	*C*	*D*	*E*	*F*	*G*	*H*
Compound **6**								
C5 - C4 - C7 - C8 (°)	27	31	21	3	36	43	27	22
Compound **8**								
C5 - C4 - C7 - C8 (°)	33	28						

The maximum dihedral angle between the pyridyl and the phenyl ring in **6** is 43° while that in **8** is 33°. More differences are observed in the Co-O bond distances, **6** exhibits the longest distance of 2.371(12) Å while **8** has a maximum Co-O bond length of 2.302(3) Å. All this information provides enough evidence that the transformation from **6** to **8** was accompanied by dynamic motion of the pyridyl and the phenyl ring, as well as bond length adjustment facilitating the exchange of guest molecules. Figure 7.18 displays the PXRD patterns that were obtained from day one up to day 28. At day 21, a mixture of purple (compound **8**) and other crystal forms was identified based on the different crystal colours. At day 28, two crystal forms (compound **9** and **10**) were identified owing to the difference in their colours, **9** was light pink and **10** exhibited a dark pink colour.

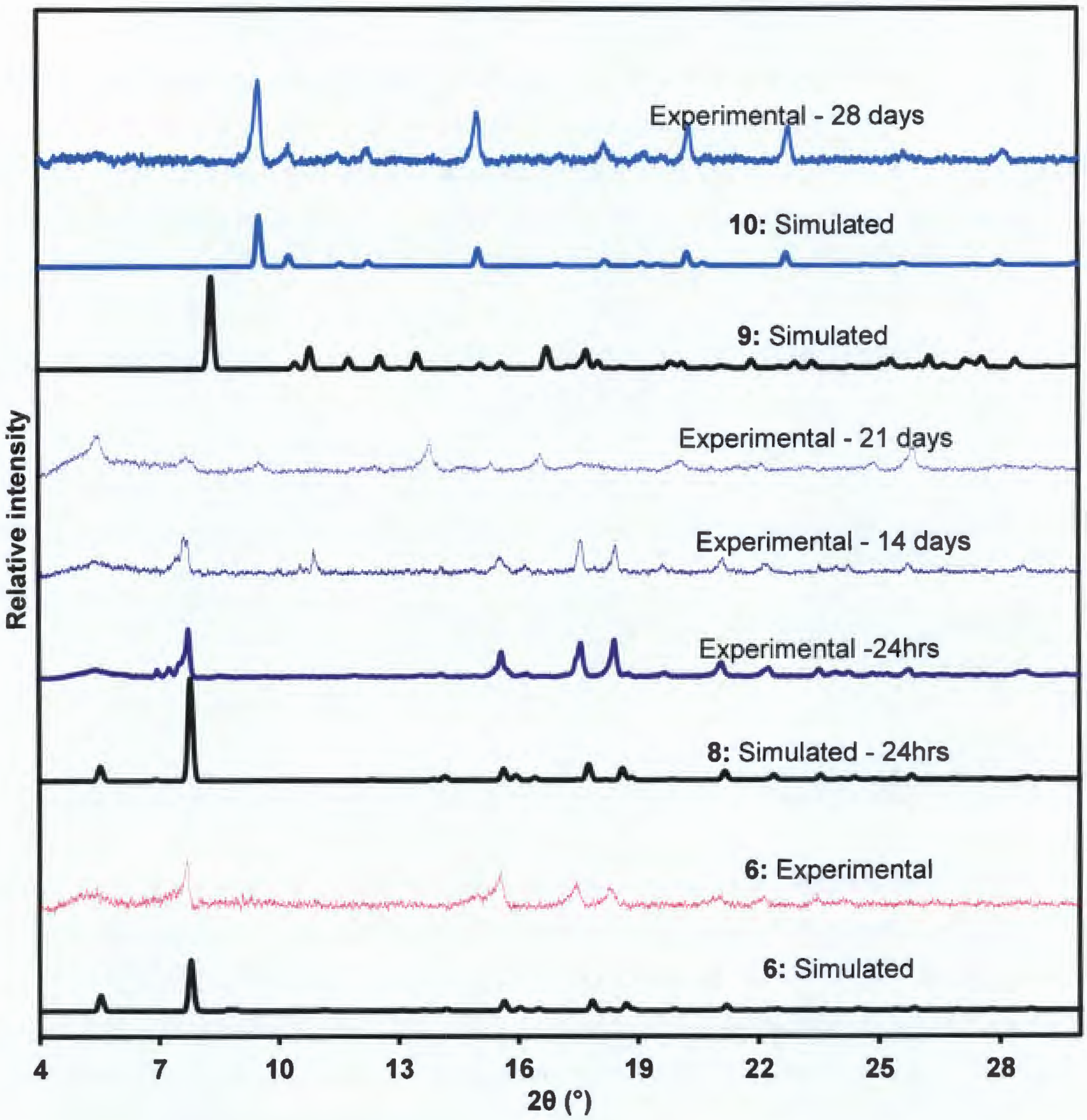

Figure 7.18: PXRD patterns collected as a function of time during the structural transformation of **6** when soaked in methanol

The PXRD suggests that at the end of the experiment (28 days) the major phase was **10** as it matches well with the simulated PXRD pattern of the single crystal diffraction data. The most notable change from **8** to **9** and **10** are the methanol molecules which become coordinated to Co(II) ion and the carboxylate moiety which switches from a chelating binding mode in **8** to a monodentate mode in both **9** and **10**. This suggests that the structural transformation occurs *via* a cooperative motion of atoms that involves breaking of two metal oxygen bonds and formation of two new metal-oxygen bonds with the methanol molecules. This process results in change of the physical appearance of the compound as well as the network connectivity as evidenced by network analysis. Furthermore, such changes are expected to influence other properties such as luminescence, magnetism and catalytic activity. The generation of coordinatively unsaturated metal sites by removal of bound guest molecules has received great attention. Open metal sites promise very specific control over host-guest chemistry and this has been recognised as having potential applications in hydrogen storage.[2] Hence, compound **9** and **10** may find application in this area since they posses bound guest molecules. Although **9** and **10** were obtained concurrently, we believe that **9** is an intermediate phase undergoing a transformation to **10**. This is due to the fact that **9** has two cobalt centres and one of the centres has a similar coordination to the Co(II) in **10** (see precceding section on structural description). In this regard, it is likely that the methanol molecules coordinates first to the cobalt centre in a *trans* fashion followed by rotation of the methanol molecules around the metal centre to give a *cis*-conformation in **10**. This may be influenced by the nature of the other ligands in the coordination sphere or the metal centre itself. It seems this process would require a lot of energy to change from *trans* conformation to a *cis* conformation. Due to steric hindrance effects, one would expect the *trans* form to be the most favourable configuration. However, analysis of the torsion angles between the phenyl and the pyridyl ring shows that compound **9** exhibits high torsion angles compared to **10**. Thus compound **9** is likely to be unstable and should transform to a favourable form (**10**). An overlay of the ligand fragments found in **9** and **10** is depicted in Figure 7.19. The phenyl and the pyridyl rings in **9** are heavily twisted while those in **10** are almost coplanar to each other (Table 7.9). The orientation of the carboxylate moiety in **9** is very unusual and is highly strained, hence this should transform to a less strained geometry.[3] All this information gives evidence that compound **9** is an intermediate phase between compound **8** and **10**.

Table 7.9: Torsion angles in **9** and **10**

		Ligand A (°)	***ligand B (°)***
Compound **9**	PP[a]	38	38
	CP[b]	26	24
Compound **10**	PP[a]	13	
	CP[b]	1.7	

[a]torsion angle between the phenyl and pyridyl ring; [b]torsion angle of the carboxylate moiety relative to the phenyl ring.

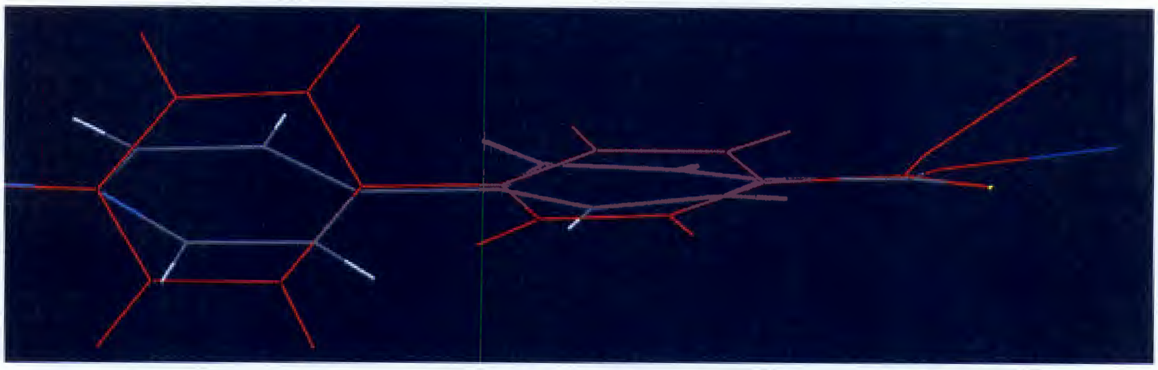

Figure 7.19: Ligand conformation at the phenyl and pyridyl junction as well as the orientation of the carboxylate group. The red fragment is compound **9** while the grey fragment is compound **10**.

The framework in compound **6** can be re-established by soaking the final phase **10** in DMF/ethanol mixture for 72 hours at room temperature. This is confirmed by the PXRD (Figure 7.20). Unfortunately the resulting crystals were of poor quality and no unit cell checks were done to confirm the cell dimensions.

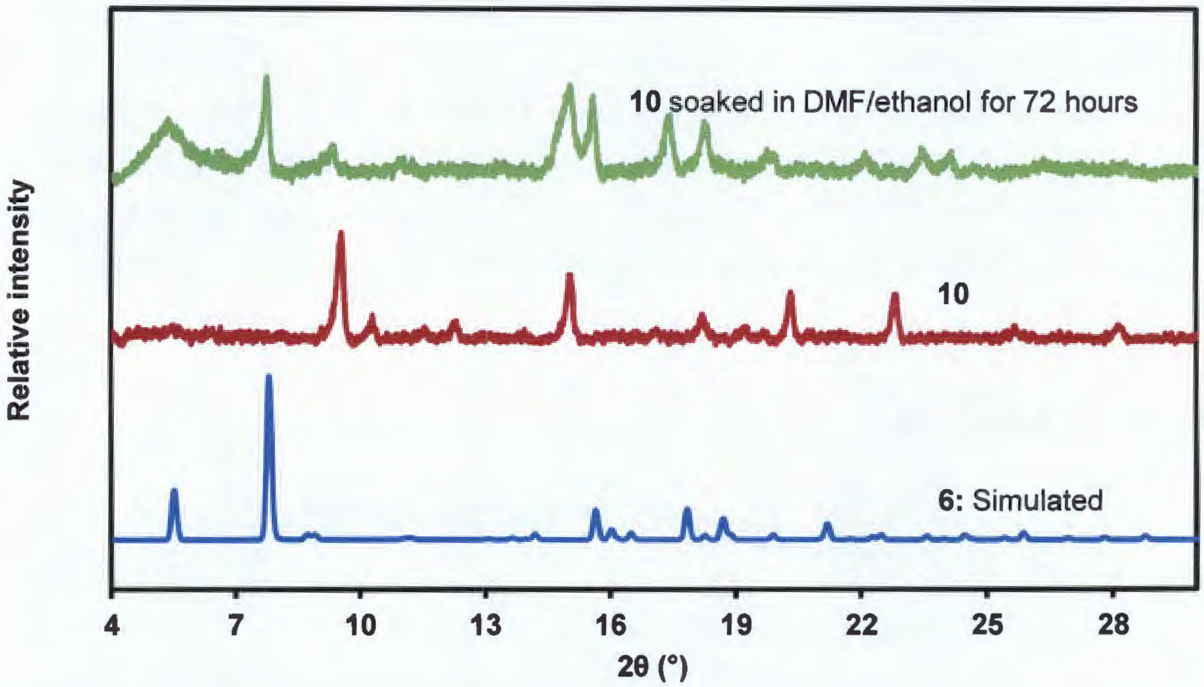

Figure 7.20: PXRD patterns of **6**, **10** and after soaking **10** in a 5:2 DMF/ethanol solvent mixture over a period of 72 hours.

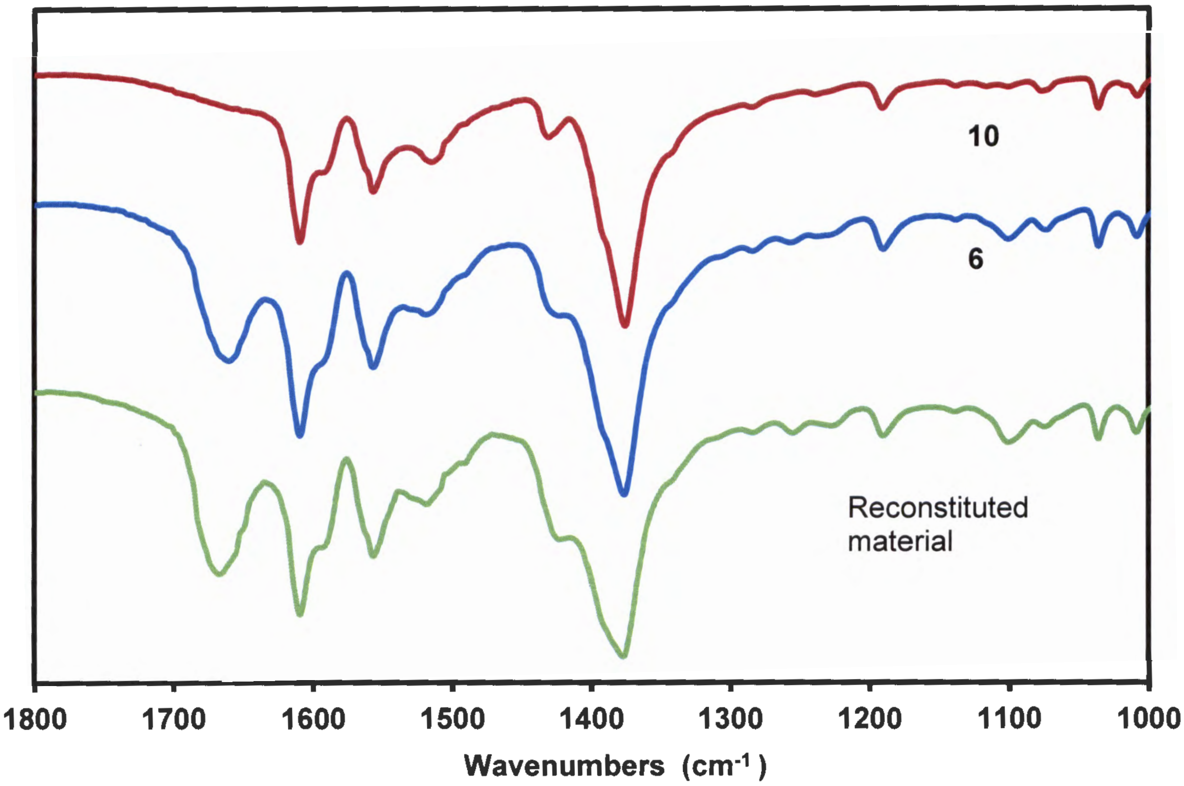

Figure 7.21: IR spectra of **6** (blue), **10** (red) and the reconstituted material (green).

The IR spectra of the compounds **6**, **10** and the reconstituted material after soaking **10** in DMF/ethanol mixture is displayed in Figure 7.21. The successful incorporation of DMF in the reconstituted material is evidenced by the presence of a carbonyl stretch at about 1666 cm^{-1} which is not present in **10** since it does not contain DMF molecules. Similar absorption bands to **6** are observed after the soaking process which reinforces the reestablishment of the framework in **6**.

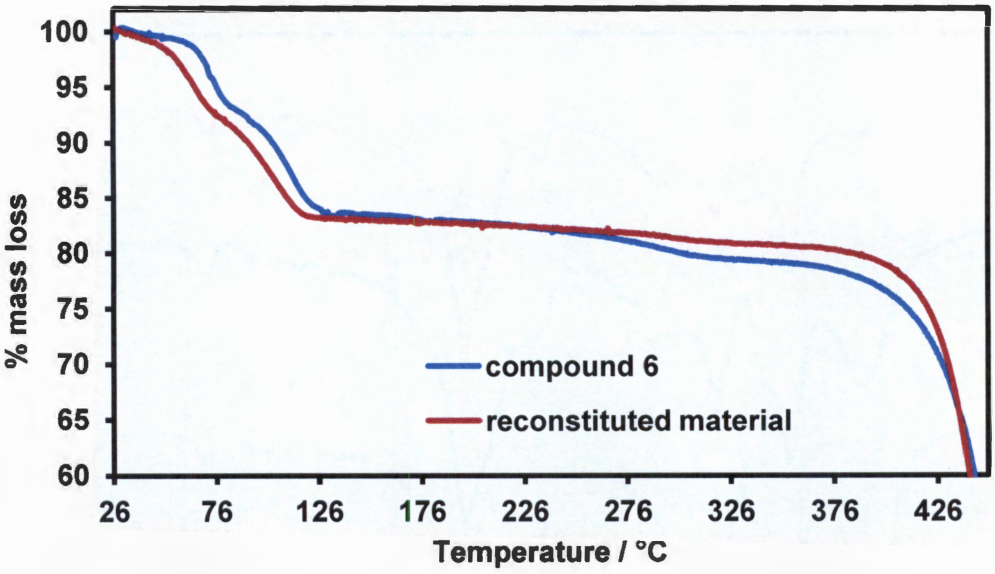

Figure 7.22: A comparison of the TGA of compound **6** and the reconstituted material after soaking **10** in DMF/ethanol mixture.

The amount of solvent encapsulated during the reversible transformation of **10** to **6** was quantified by TGA analysis (figure 7.22). The thermal behaviour of the reconstituted material is very similar to that of **6**. A total mass loss of just less than 17% is observed for both compounds and the guest free compounds decomposing at approximately the same temperature. A similar reversible guest uptake was reported by Chen *et al* for a hydrogen bonded complex.[4]

7.4.1 Guest topology studies

Network analysis of the guest molecules in a host compound has not been explored extensively with only a few literature reports on that kind of studies.[5,6] Some of the questions that might be asked are:

(i) *If studied, can it provide insights associated with reversible structural rearrangement which is triggered by guest molecules?*

(ii) *Is there any topological information exchange that exists between the guest molecules and the host compound upon structural transformation?*

It is assumed that the guest topology in compound **10** may have contributed to the reformation of **6**. This has prompted the analysis of the guest topology in compound **10**.

Such a study is not easy to perform because the guest molecules may be arranged in a manner that will make it difficult where one has to opt to place the node. The hydrogen bonded water and methanol guest molecules in compound **10** form a hexameric network (Figure 7.23.a). Based on the packing of the guest molecules in **10,** the centres in blue shown in Figure 7.23.b were defined as the nodes and the rest of the nodes were symmetrically generated and are topologically identical.

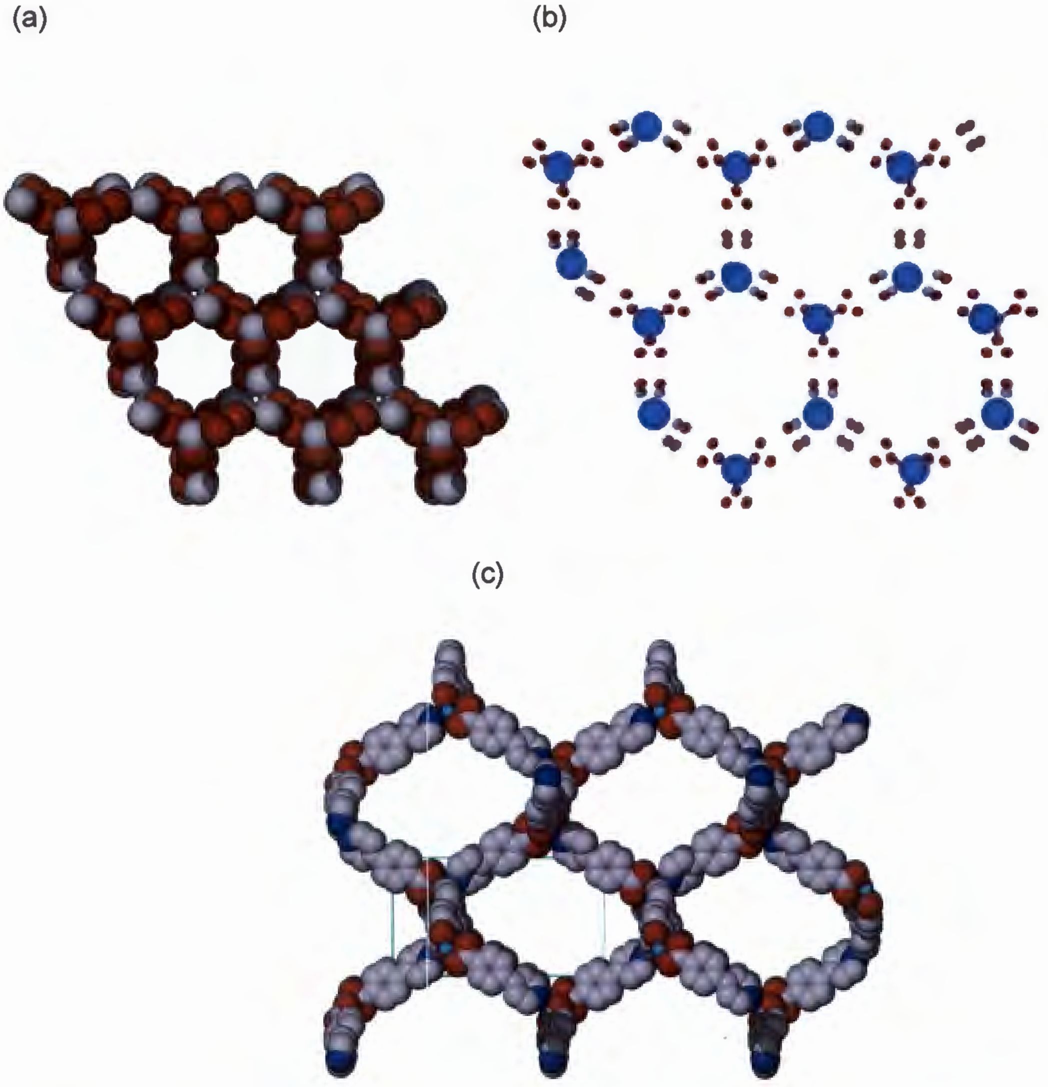

Figure 7.23: (a) Guest connectivity found in compound **10** drawn with van der Waals radii (b) guest connectivity drawn in ball and stick form illustrating node assignment depicted as blue circles, (c) framework connectivity found in compound **6**

Figure 7.23 displays the guest topology in compound **10** and the framework topology in compound **6**. Similar features exist between the topology of the guest in **10** and that of the framework in compound **6**. From the projection shown in figure 7.23.b and c 6-membered rings can be identified in both the guest network of **10** and the framework of **6,** these rings represent the largest circuit of the essential rings that define the topology.

The six membered rings in the guest network may have played a role in templating the six membered rings in the host framework of **6** resulting in its reestablishment. This is further supported by the reaction cavity concept which states that, among many possible solid state products, the one most likely to be formed is the one which fits the cavity that would remain after the molecules are removed from the mother crystal.[7] Hence, as observed by topological analysis the framework of **6** fits well with the channels of **10**.

7.5 Preparation of $\{[Ni(44pba)_2]\cdot0.5CH_3OH\cdot2.5H_2O\cdot0.1I_2\}_n$ (11)

Crystals of compound **11** were obtained by soaking crystals of compound **(7)** $\{[Ni_4(44pba)_8]\cdot4DMF\cdot0.5CH_3CH_2OH\cdot3H_2O\}_n$ for 24 hours in dry methanol. During this period it is expected that all the DMF molecules would be replaced by methanol molecules as previously observed with the cobalt analogue. The methanol solvated crystals were then exposed to vapours of iodine for 24 hours to give compound **11.**

Table 7.10: Crystallographic and refinement parameters of compound **11**

	11
Empirical formula	$\{[Ni(44pba)_2]\cdot 0.5CH_3OH\cdot 2.5H_2O\cdot 0.1I_2\}_n$
Molecular Mass	542.16
Crystal Size $(mm)^3$	0.22 x 0.25 x 0.34
Temp. of collection / K	173(2)
Crystal symmetry	tetragonal
Space group	$P42_12$
a / Å	22.488(4)
c / Å	12.605(3)
Z	8
Volume $Å^3$	6374(4)
Dc / g cm^{-3}	1.123
2θ range	5.123- 33.52
F(000)	2172
No. of reflections collected	20300
Index ranges (h, k, l)	-25:17; -14:26; -14:17
No. Unique reflections	5648
No. Reflections with $I > 2\sigma(I)$	2867
Goodness of fit, S	1.03
R	0.1218
Final wR_2	0.3598
Min, Max e density / e $Å^{-3}$	-1.43, 1.01

The maximum electron density is located close to the metal centre.

7. 5. 1 Structural description of 11

Compound **11** is an analogue of compound **8**; hence its full structural description will not be given. Single crystal x-ray diffraction shows that the compound crystallises in the tetragonal crystal system chiral space group *P42₁2*. The coordination geometry around the Ni(II) ion is very similar to its cobalt analogue compound **8**. However, the Ni – O bond lengths are slightly longer than those found in compound **8**. Conversely, the Ni - N bond distances in **11** are shorter than those found in **8** (Table 7.11). As noted with compound **6**, **7** and **8**, adjacent 3D networks in **11** are also linked by weak hydrogen bonding interactions.

In the asymmetric unit of **11**, several guest molecules were modelled. A total of 0.5 methanol molecules were modelled over two positions each with site occupancy of 0.25. These methanol were located at Wyckoff positions of *a* and *c*. An iodine molecule was modelled with refined site occupancy of 0.1. In addition to this, a total of 2.5 water molecules were located and were disordered over six positions. Figure 7.24 shows the packing diagram of compound **11** with the guest molecules in the 1D channels.

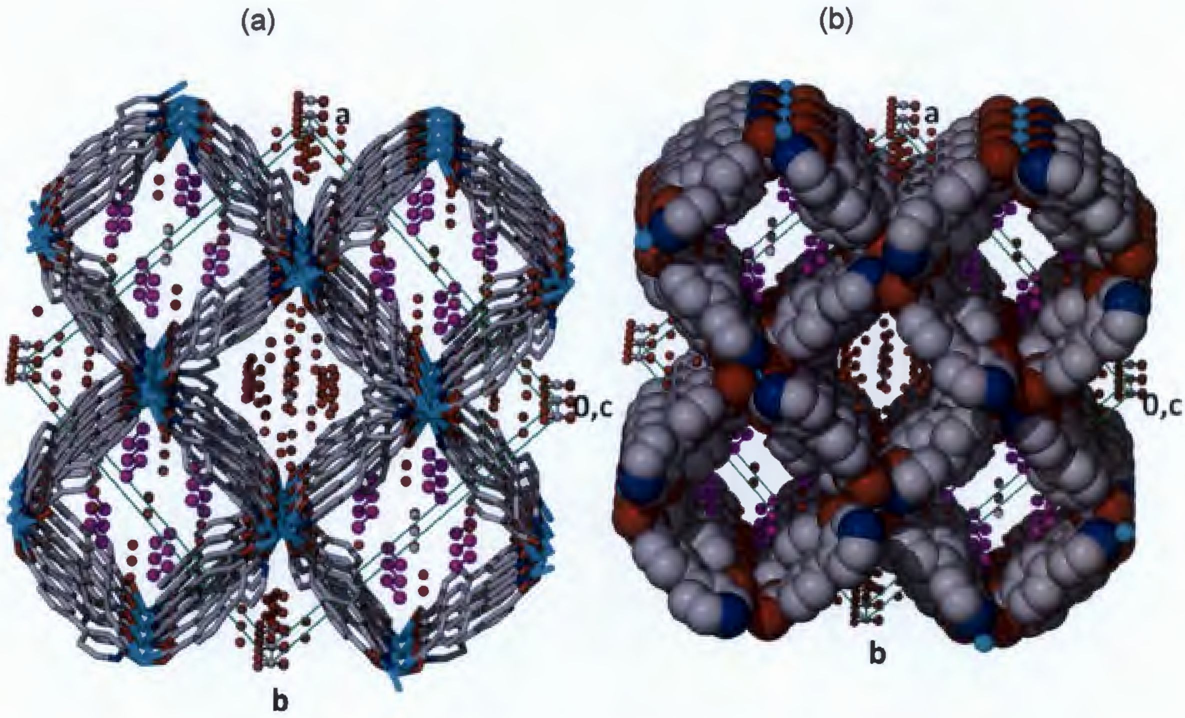

Figure 7.24: a) Iodine- methanol exchanged structure. The structure shows the inclusion of iodine upon exposure of the methanol and water solvated crystals to iodine vapour. Data collection for the structure was performed after 24 hrs of exposure to iodine vapour. Iodine molecules are shown as purple sticks. Water and methanol molecules are also present in the structure. b) Framework drawn with van der Walls radii.

Table 7.11: Bond length around the Ni(II) centre in compound **11**

Bond Type	*Bond length(Å)*	*Bond type*	*Bond type(Å)*
N11 - O14A	2.213(9)	Ni1 - O15B	2.193(9)
Ni1 - O14B	2.035(10)	Ni1 - N1A	2.014(13)
Ni1 - O15A	2.051(10)	Ni1 - N1B	2.029(11)

7.6 Thermal analysis of 11

Thermal analysis by TGA of compound **11** is depicted in Figure 7.25. The TGA trace displays a total mass loss of 18.9% with a temperature range of 30 - 150 °C. This suggests that there could be further solvents present in the structure of **11** that were not modelled due to the quality of the data because this mass loss is more that the calculated guest content (15.9%). Decomposition of the guest free compound occurs above 330 °C

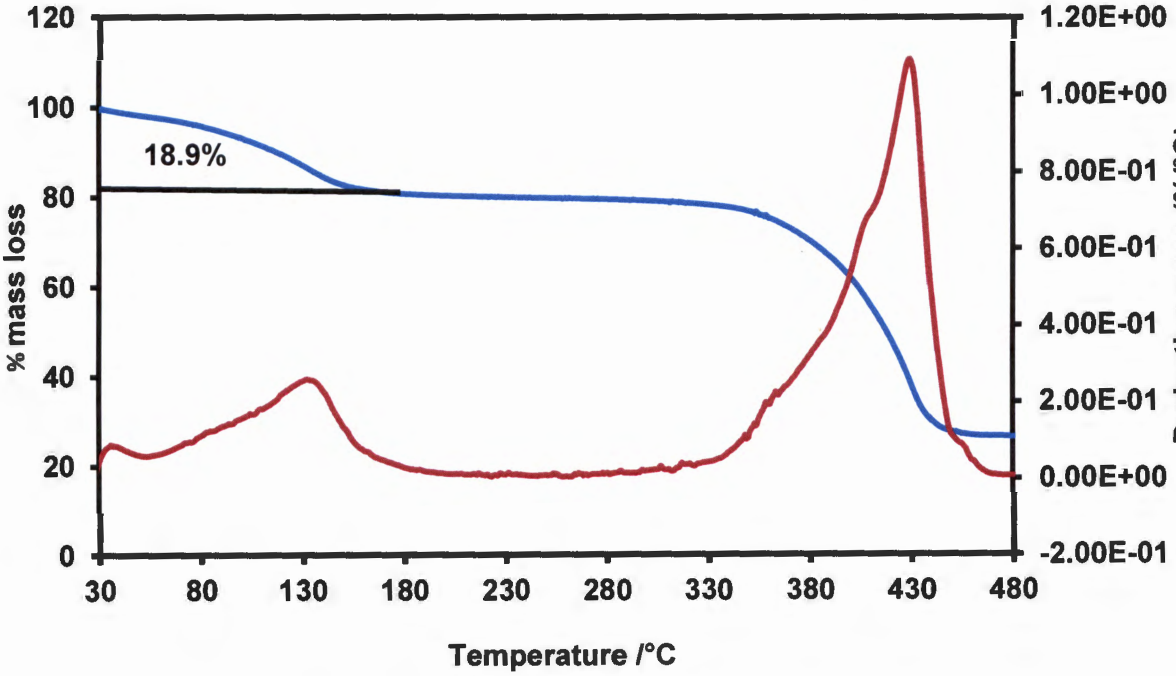

Figure 7.25: TGA (blue) trace and the % mass derivative (red) of compound **11**.

7. 7 Iodine sorption studies

Iodine sorption studies were carried out using $[Ni(44pba)_2]_n$ **(7d)** because it was found to be more stable in air than its cobalt analogue compound $[Co(44pba)_2]_n$ **6d** . The preparation of **7d** was described in Chapter 6 section 6.3. To evaluate the uptake of I_2 molecules by the activated phase **7d**, crystals were exposed to iodine vapour for a period of two weeks. The amount of iodine uptake was monitored by TGA analysis (Figure 7.26.)

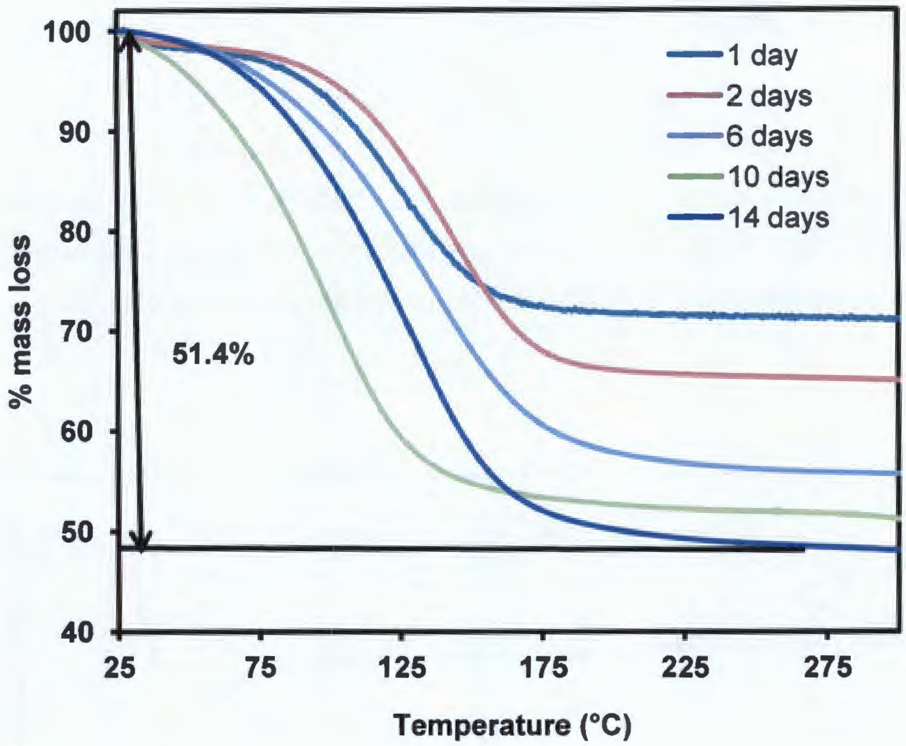

Figure 7.26: TGA analysis for the uptake of iodine by **7d** as a function of time in days.

The amount absorbed as a function of time is given in Table 7.12 and modelled based on the formula $[Ni(44pba)_2]\cdot xI_2$ where x represents the number of iodine molecules per formula unit.

Table 7.12: Parameters for the gravimetric uptake of iodine by $[Ni(44pba)_2]$ (**7d**)·

Time (days)	*%TGA mass loss*	*$[Ni(44pba)_2]\cdot xI_2$*
1	27.51	0.68
2	36.32	1.02
6	46.86	1.58
10	48.86	1.71
14	51.43	1.89

The maximum amount of iodine uptake corresponds to 1.9 I_2 per formula unit as determined by gravimetric analysis. Elemental analysis results suggest an uptake of $2I_2$ per formula unit, calculated % C 29.92, N 2.91, H 1.66 from **7d·2I₂**, % found C 30.30, N 2.18, H 1.82 . This equates to 1.10g/g uptake of iodine on the activated sample. The amount of iodine uptake is slightly higher than the one reported using a MOF with double walls $\{[Zn_3(dl\text{-}lac)_2(pybz)_2]\cdot 3DMF\}n$ (dl-**lac**=lactate, pybz=4-(4-pyridyl)benzoate), (1.01 g/g) which exceeded zeolite 13X (0.32-0.38 g/g), activated carbon (0.84 g/g) and other systems.[8-12] The high affinity of the double walled MOF to iodine molecules was attributed to the structural character from the regular π-electron walls made of 4-(4-pyridyl)benzoate ligands. The same effect may also be assumed for the activated sample under study since it was constructed from the same ligand. The larger iodine uptake achieved in our study may be attributed to the 47 % free channel volume compared to the 43.5 % found in the double walled MOF. PXRD studies in Figure 7.27 show the trace of the activated phase (**7d**), iodine loaded sample (**7d·2I$_2$**) and the trace after releasing iodine in methanol. Upon capture of iodine by **7d** there is a significant decrease in peak intensity for the Bragg peak located at 7.9° which corresponds to the (0 2 0) reflections. The (0 2 0) plane is parallel to the [1 0 0] direction and cuts through the centre of the channels which run along the *c*-axis. This suggests that the I_2 molecules are not highly ordered in the channels. However, upon release of iodine in methanol, the intensity of this peak increases while those at higher 2θ positions decrease. Upon iodine sorption, the appearance of a new peak absent in the activated phase is observed at about 11.2° and is due to the (0 1 2) reflections. This peak is attributable to the inclusion of iodine in the channels, and it decreases significantly upon releasing iodine in methanol. Additionally there is an increase in peak intensity for peaks located at 21.4 and 23.8° 2θ positions upon exposure vapour. The intensity of these peaks also decrease when iodine is released in methanol.

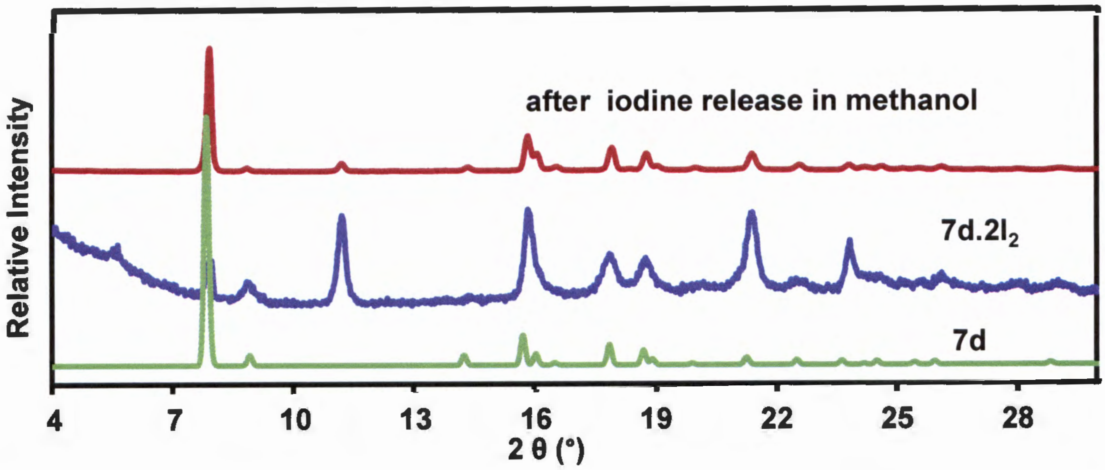

Figure 7.27: A comparison of the PXRD patterns before iodine loading (**7d**), iodine loaded and after iodine release in methanol.

It is observed that the PXRD peaks in the iodine loaded samples are very broad. This may be attributed to the strain/stress that is induced on the framework upon loading the iodine in the channels or the disorder of the I_2 molecules in the channels as evidenced by the decrease in the peak intensity at 7.9° 2θ position.

Efforts to get a crystal structure of the iodine inclusion compound were thwarted by the poor diffraction exhibited by the crystals. The PXRD trace after releasing iodine in methanol is very similar to the activated phase. This confirms that the uptake of iodine is a reversible process.

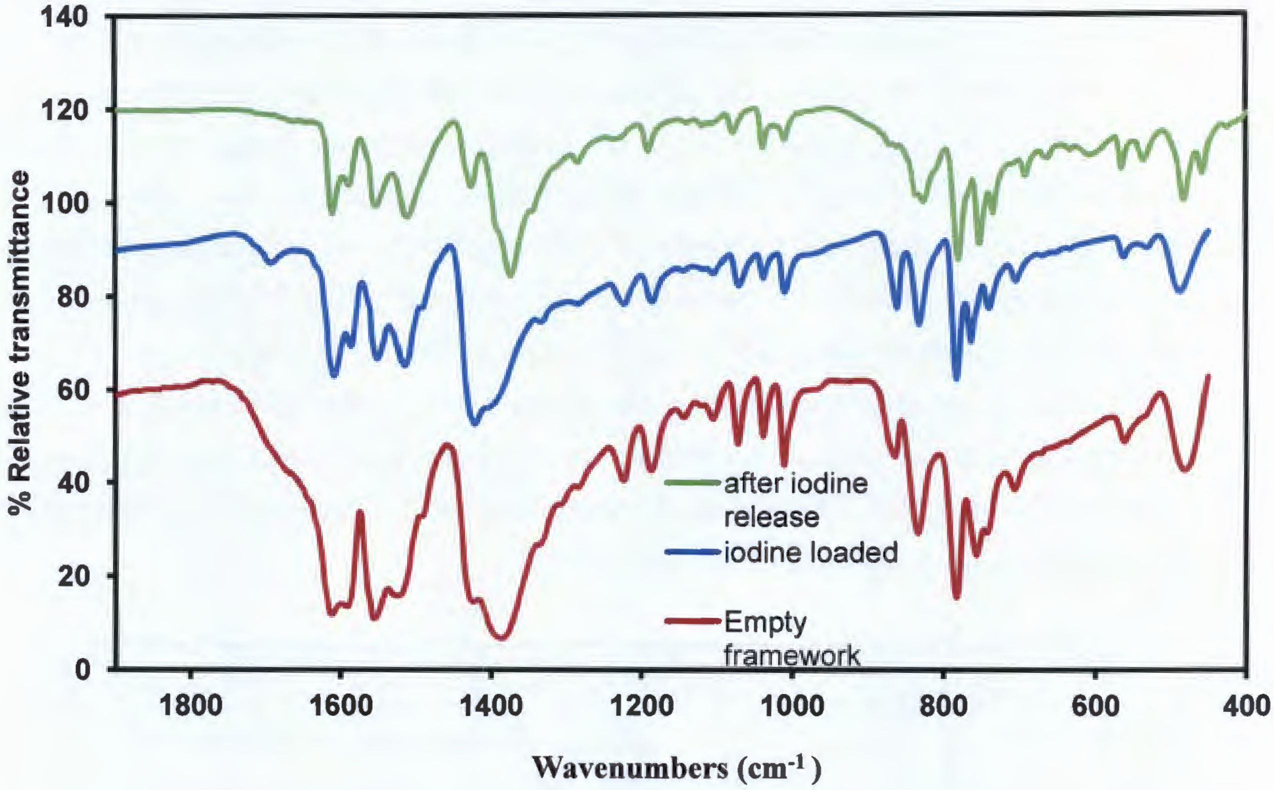

Figure 7.28: IR spectra of the empty network (**7d**), iodine loaded (**7d·2I$_2$**) and after iodine release in dry methanol.

To gain further insight into the sorption of iodine into the channels of **7d**, samples with maximum I_2 loading were analysed by infrared spectroscopy (Figure 7.28). Results obtained were compared to the IR of **7d** and the trace obtained upon iodine release in methanol. The asymmetric carboxylate stretch appears at approximately the same frequency (ca 1587 cm^{-1}) in the empty network, iodine loaded and after iodine release in methanol. The symmetric carboxylate vibrations appear as a shoulder at 1401 cm^{-1} after capturing iodine. The shift from 1388 cm^{-1} frequency observed is attributed to the strong interactions of the iodine molecules with the host framework. IR traces of the iodine loaded crystals show a band at 1695 cm^{-1} which is characteristic of a carbonyl band. However, this band is too weak for it to be assigned to carbonyl stretch. This band disappears after unloading iodine in methanol, and the IR trace found is very similar to that of the activated phase, a result which reinforces the reversibility of the process.

The release of iodine was performed by soaking 25 mg of the iodine loaded crystals in dry methanol. Iodine release was immediately noted by the colour of the solution which changed from clear to dark red as depicted in Figure 7.29.a

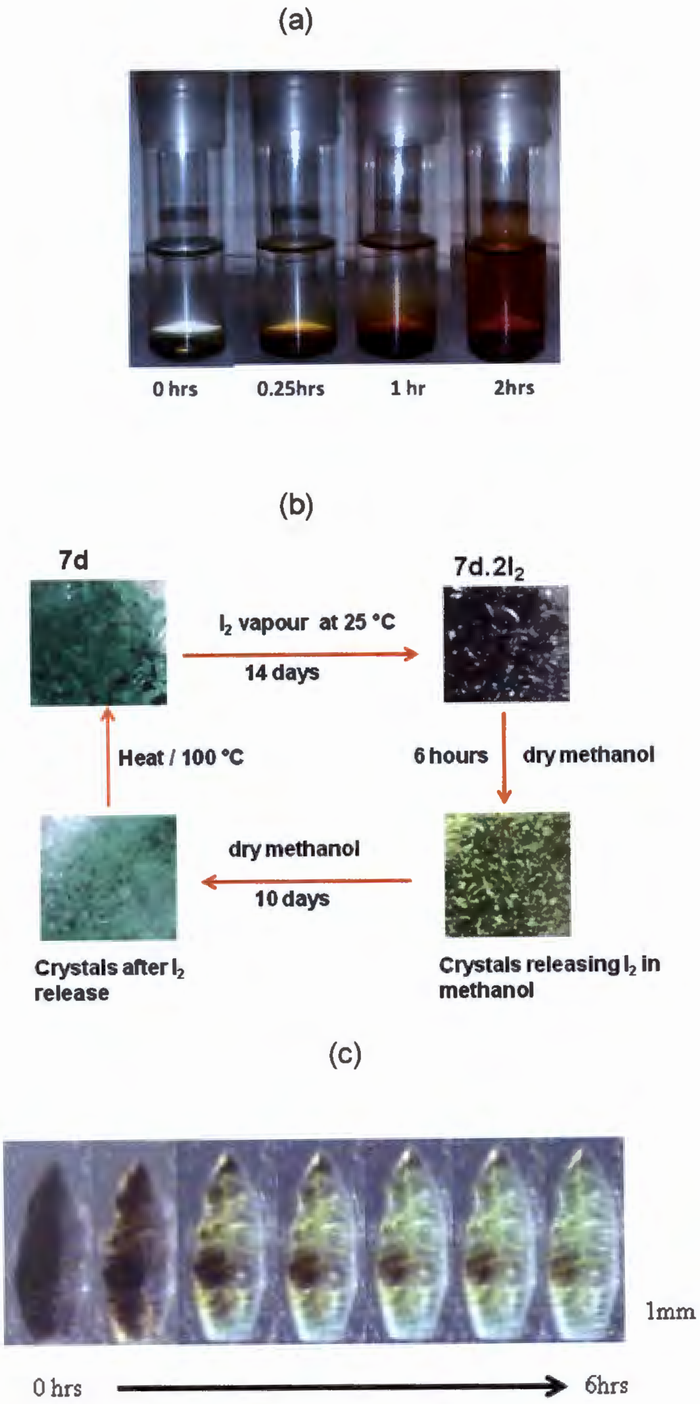

Figure 7.29: (a) Crystals of **$7d{\cdot}2I_2$** releasing iodine in dry methanol (b) Scheme illustrating the iodine loading and in release (c) a selected crystal undergoing the iodine release process in methanol.

Figure 7.29 shows crystals of **7d** exposed to iodine vapour, iodine loaded crystals, and the colour changes that takes place upon unloading iodine in methanol. Complete iodine release was achieved in 10 days as evidenced by the complete colour change from black to green. Although detailed studies of the kinetics of iodine release were not carried out, the kinetics of release of the iodine from the channels is very similar to other reported systems, which show that complete removal is achieved in more than ten days.[8,13]

TG analysis before loading, after loading iodine and upon releasing iodine from the channels is illustrated in Figure 7.30. TGA of **7d** (activated phase) is featureless until decomposition which shows that no solvent was included. The observed 51.14% mass loss for the iodine loaded compound corresponds to about $2I_2$ per $Ni(44pba)_2$. The 14% mass loss observed for the TG of the compound after iodine release in methanol may be attributed to loss of methanol molecules occupying the channels. This mass loss is comparable to the mass loss **7d-methanol** presented in Chapter 6.10 which showed a 13.1% weight loss. Compared to zeolite 13X and activated carbon the release of iodine from our MOF is a very slow process. This is because conventional adsorbents such as zeolites lack interactions between the I_2 and the host framework. It was noted that iodine could also be released in ethanol but the crystals turned to a whitish colour.

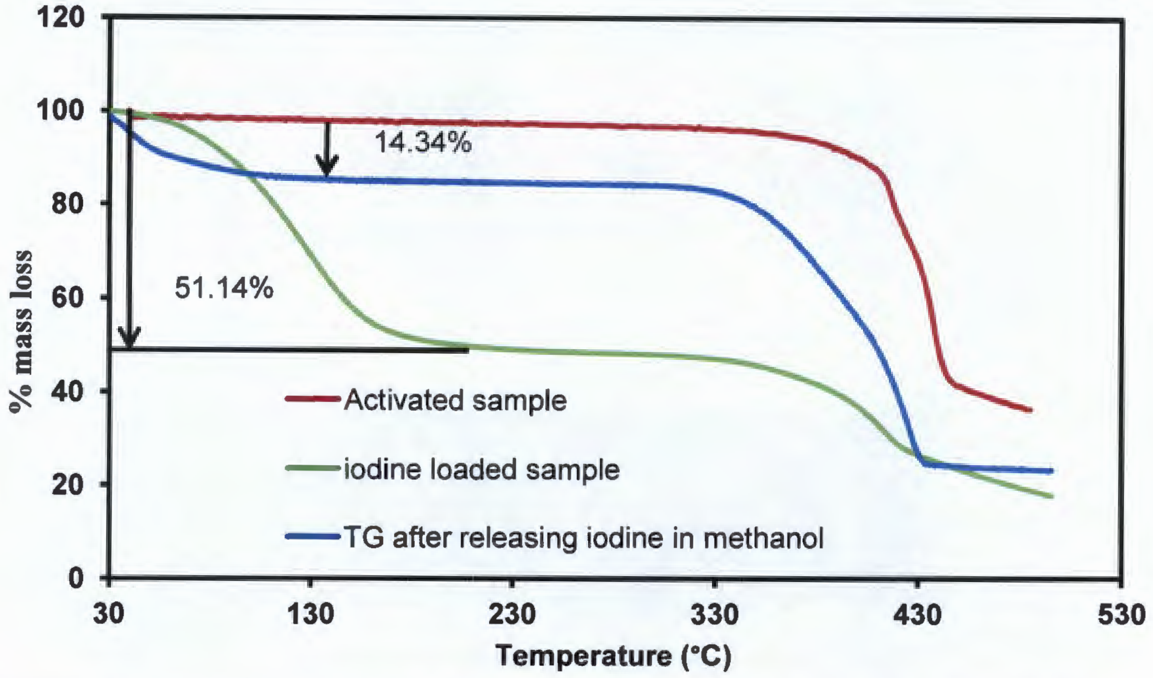

Figure 7.30: Thermogravimetric traces illustrating iodine loading and iodine release in methanol for compound **7d**.

To understand the nature of interactions between the iodine and the framework, compound **11** was prepared as described in section 7.5 of this Chapter. This method allows one to retain single crystallinity. Single crystal diffraction shows that iodine was included in channel **B** with 10% occupancy. High iodine content in the crystals results in poor diffraction of the crystals. This has been noted in other previous studies;[14] hence our strategy was to carry out structure elucidation with partial I_2 occupancy in the host framework. We expected the occupancy of the I_2 molecules to increase with increased time of exposure. The structure obtained gives us some insights on the sites that are occupied by the iodine molecules and the nature of the interactions between the iodine and the framework. A notable difference is the contraction of the unit cell volume upon inclusion of the gaseous iodine when compared with the previously reported analogues of the framework.[15,3] The refined I - I distance of (2.669 Å) is within the expected range. The iodine molecules align themselves parallel with the walls of the channels, and hence interact with the π- electrons of the framework (Figure 7.24), a result which explains the slow release of iodine from the network.

7.8 Summary

A series of structural transformations were triggered by soaking compound **6** in methanol for four weeks to give compounds **8**, **9** and **10.** Single crystal X-ray diffraction showed that the transformations involved breaking and formation of new bonds around the metal centre. This process gave rise to formation of new compounds which could not be obtained by conventional methods. The framework in compound **6** was reconstituted by soaking compound **10** in a DMF/ethanol mixture for 72 hours. This reversible transformation could be attributed to the guest topology in **10** which may template the formation of the framework in **6**.

Iodine sorption studies were carried out using the activated phase of compound **7**. The activated phase absorbs 1.10 g/g of iodine when exposed to iodine vapour for 14 days. The iodine loaded crystals were found to release the iodine in methanol. However, the process of iodine release was found to be a very slow process as it took 10 days for the colour of the crystals to change from black to the original green colour. To understand the nature of interactions between the iodine and the framework, methanol solvated crystals were exposed to iodine vapour for 24 hours. Single crystal X-ray diffraction revealed that the iodine molecules interact with the π electron system of the framework as they are located close to the walls of the channels. These interactions explain why the release of iodine from the framework took several days.

7.9 References

1. A. L. Spek, *Acta Crystallogr. D. Biol. Crystallogr.*, 2009, **65**, 148.
2. S. Ma and L. Meng, *Pure Appl. Chem.*, 2010, **83**, 167.
3. M.-H. Zeng, Y.-X. Tan, Y.-P. He, Z. Yin, Q. Chen, and M. Kurmoo, *Inorg. Chem.*, 2013, **52**, 2353.
4. C.-L. Chen and A. M. Beatty, *J. Am. Chem. Soc.*, 2008, **130**, 17222.
5. K. Biradha, A. Mondal, B. Moulton, and M. J. Zaworotko, *J. Chem. Soc. Dalton. Trans.*, 2000, **2**, 3837.
6. J. Lu, B. Moulton, M. J. Zaworotko, and S. A. Bourne, *Chem. Commun.*, 2001, 861.
7. H. E. Zimmerman and E. E. Nesterov, *Acc. Chem. Res.*, 1973, **6**, 217.
8. M.-H. Zeng, Q.-X. Wang, Y.-X. Tan, S. Hu, H.-X. Zhao, L.-S. Long, and M. Kurmoo, *J. Am. Chem. Soc.*, 2010, **132**, 2561.
9. F. Sun, Z. Yin, Q.-Q. Wang, D. Sun, M.-H. Zeng, and M. Kurmoo, *Angew. Chem. Int. Ed. Engl.*, 2013, **52**, 4538.
10. J. Li, P. Huang, X.-R. Wu, J. Tao, R.-B. Huang, and L.-S. Zheng, *Chem. Sci.*, 2013, **4**, 3232.
11. B. Xin, G. Zeng, L. Gao, Y. Li, S. Xing, J. Hua, G. Li, Z. Shi, and S. Feng, *Dalton Trans.*, 2013, **42**, 7562.
12. A. K. Chaudhari, S. Mukherjee, S. S. Nagarkar, B. Joarder and S. K. Ghosh, *CrystEngComm*, 2013, **15**, 9465.
13. Z. Yin, Q.-X. Wang, and M.-H. Zeng, *J. Am. Chem. Soc.*, 2012, **134**, 4857.
14. C. Falaise, C. Volkringer, J. Facqueur, T. Bousquet, L. Gasnot, and T. Loiseau, *Chem. Commun.*, 2013, **49**, 10320.
15. G. Mehlana, G. Ramon, and S. A Bourne, *CrystEngComm*, 2013, **15**, 9521.

Chapter 8

Conclusion

8.1 Summary

MOFs have received great attention due to their useful properties. These provide a unique platform for achieving materials with controllable physical properties such as framework flexibility which is normally triggered upon guest sorption. The work presented in this thesis focussed on preparation and characterisation of MOFs and evaluating their ability to absorb a wide range of solvent molecules as well as their chromic properties. Pyridyl carboxylate ligands, 3-(4-pyridyl)benzoate and 4-(4-pyridyl)benzoate were used to connect metal ions to give 2D and 3D extended structures which were porous. The advantage of using these ligands is that they give rise to compounds which are dynamic and are capable of responding to their environment. The flexibility of the materials arises from the ability of the ligands to rotate about their connecting points as well as the different binding modes that can be assumed by the carboxylate moiety under different conditions. Such materials are ideally suitable for solvatochromic sensing. The MOFs made were characterised by thermal techniques such as Differential Scanning Calorimetry, Thermogravimetric analysis, Hot Stage Microscopy and variable temperature PXRD. Structural elucidation was performed by single crystal X-ray diffraction and powder X-ray diffraction studies were used to check the phase purity and phase transition of the prepared materials. Rietveld refinement and Pawley fitting were performed on powder X-ray data to validate unit cell parameters in situations where single crystals were not suitable for data collection. Topological analyses of the crystal structures were performed using the TOPOS computer program to gain a better understanding of the underlying net of the structures. This allowed for simplification of complicated structures to more general structures that we are familiar with from general chemistry textbooks.

8.1.1 3-(4-pyridyl)benzoate compounds

Compound **1** and **2** have the same molecular formula $[\{Co(34pba)_2]\cdot DMF]\}_n$ but differ in the molecular building blocks which construct the frameworks. The two compounds were obtained concomitantly under solvothermal conditions from the reaction of 3-(4-pyridyl) benzoic acid and cobalt(II) nitrate hexahydrate at 105 °C. **1** had a **bcu** net while **2** formed a square grid lattice topology. Optimisation of the reaction conditions led to the formation of **1** at 120 °C while **2** was obtained with another **unidentified** product at 75 °C. **1** was referred to as a thermodynamic product while **2** was identified as a kinetic product.

The reaction of zinc(II) nitrate hexahydrate with 3-(4-pyridyl)benzoate at room temperature in a DMF solution afforded two metal organic frameworks based on an **sql** net (**3** and **4**) with the same molecular formula $[\{Zn(34pba)_2]\cdot DMF]\}_n$. These compounds differ in the binding mode of the carboxylate group; in compound **3** the carboxylate moiety exhibits a monodentate binding mode while in **4** it assumes a chelating binding fashion. Compound **3** crystallised in a $P2_1/c$ space group while **4** crystallised in a chiral space group $P4_32_12$. Compound **4** was isolated exclusively in high yields at 80 °C while the conditions that could lead to the isolation of **3** could not be established. Niu *et al* reported a similar structure $\{[Zn(34pba)_2]\cdot 1.5H_2O]\}_n$ to **3** which was synthesised under hydrothermal conditions in the presence of auxiliary acids[1].

8.1.2 4-(4-pyridyl)benzoate compounds

The solvothermal reaction of 4-(4-pyridyl)benzoic acid (compound **5**) with cobalt nitrate hexahydrate or nickel nitrate hexahydrate in a 5:2 DMF/ethanol mixture at 105 °C for 72 hours afforded $\{[Co_4(44pba)_8]\cdot 4DMF\cdot 0.5CH_3CH_2OH\cdot 4H_2O\}_n$ **(6)** or $\{Ni_4(44pba)_8\cdot 4DMF\cdot 0.5 CH_3CH_2OH \cdot 3H_2O\}_n\}$ **(7)**. The two compounds are isostructural and crystallise in a chiral space group *I4*. Large channels were constructed by *dextro* and *levo* helical nets which run along the [001] direction. Compound **6** and **7** exhibited a **dia** topology.

Compounds $\{[Co(44pba)_2]\cdot 2.5CH_3OH\cdot H_2O\}_n$ **(8)**, $\{[Co(44pba)_2(CH_3O)_2]\cdot 2CH_3OH\cdot 0.5H_2O\}_n$ **(9)**, $\{[Co_{0.5}(44pba)(CH_3O)]\cdot 0.5CH_3OH\cdot 0.25H_2O\}_n$ **(10)** are subsequent structures of **6**. Soaking crystals of **6** in methanol for 24 hours resulted in the exchange of DMF for methanol to give **8**. The structure of **8** is very similar to that of **6** in terms of the geometry around the metal centre as well as the network topology. Minor modifications are observed in the dihedral angles between the pyridyl and phenyl ring as well as some bond length changes for the atoms coordinated to the metal centre. Compound **8** transformed into **10** *via* the intermediate phase **9** after four weeks. Networks of **9** and **10** exhibited a **pts** and **qtz** topology respectively.

Compound **11** $\{[Ni(44pba)_2]\cdot 0.5CH_3OH\cdot 2.5H_2O\cdot 0.1I_2\}_n$ was obtained by soaking crystals of **7** in methanol for 24 hours followed by exposing the crystals to iodine vapour for 24 hours. The compound is an analogue of **8**, and only differs in the nature of metal centre and the guest content.

8.2 Thermochromic behaviour

The thermochromic properties of the compounds presented in this thesis were studied by HSM and IR analysis. From these studies it can be concluded that there are a few mechanisms which were associated with the colour changes upon heating the crystals which are;

(i) Loss of solvent molecules: This causes some subtle changes which in turn trigger minor modifications of the framework. This was observed with crystals of compound **4.** These crystals turned from colourless to a golden yellow. Single crystal x-ray diffraction showed significant changes in the dihedral angles between the phenyl and pyridyl ring while the geometry around the metal centre remained the same. The observed thermochromic behaviour may be attributed to the π to π* transition.

(ii) Change in the binding mode of the carboxylate moiety from chelating or bidentate to monodentate, which changes the coordination geometry around the metal centre, thus altering the visible d-d transitions. This is illustrated by **1** and **2** as suggested by IR results.

(iii) Structural rearrangement upon phase change. For compound **6** and **7**, the thermochromic behaviour could have originated from this phenomenon

8.3 Solvatochromic behaviour

Activated phases of compounds **1**, **6** and **7** showed some solvatochromic behaviour upon soaking in a wide range of solvents. The phenomenon was studied by HSM, IR and UV-vis. The mechanism of solvatochromism based on the results presented in this study may stem from changes in the crystal packing induced by strong hydrogen bonding for compound **6**. In compound **1** and **7** this effect could be attributed to both changes in the crystal packing and changes in the binding mode of the carboxylate moiety which cause changes in the geometry around the central metal ion. A change in the spin state induced upon sorption of guest molecules has also been reported to cause a change in the colour of crystals. [2]

8.4 Non-isothermal and isothermal kinetics

The energy associated with the removal of the guest molecules in the network was studied by non-isothermal kinetics. The majority of the compounds presented in this thesis showed that the energy required for removing the guest molecules increased with an increase in the percentage of conversion level. This implies that the energy increases as the reaction proceeds to completion. One might expect the energy to be high at the beginning of the reaction and then decrease as the reaction nears completion, but results such as ours may suggest different mechanisms operating throughout the course of the reaction. As the material is heated it may behave differently at different temperatures, which may explain why the energy increases.

Isothermal kinetics of guest uptake by the activated phase of compound **6** and **7** was performed using an in-house built balance. The mechanism for water uptake was found to be controlled by diffusion based model. The results obtained are consistent with the crystal structures of the compounds with large 1D channels running along the c-axis. The contracting volume (D2) model which fitted well with both **6d** and **7d** phases suggests that the network is flexible. This may be brought about by the movement of the interpenetrated **dia** nets, thus allowing diffusion of water in two dimensions. The low activation energies obtained for the uptake of water by **6d** and **7d** show that there are no obvious directional constraints on the diffusion of guest water molecules.

8.5 Flexing of metal organic frameworks

Flexing is an important aspect in the field of metal organic frameworks with applications in separation and sensing. In most cases describing "breathing mechanisms" the system are 3D.[3-8] However, this interesting phenomenon has not been widely explored for 2D networks. Single crystal X-ray diffraction studies revealed the breathing mechanism of the activated phase of **4** upon absorption of linear chain alcohols. The key mechanisms for the breathing were (a) movement of adjacent 2D sheets along the *c*-axis and (b) dynamic motion of the phenyl and pyridyl rings which gave rise to cleavage of the metal to oxygen. The latter resulted in the lengthening of the twisted ligands thus increasing the distance separation of the metal centres within the same layer.

8.6 Thermal stability

The majority of compounds presented in this thesis showed high thermal stability. 2D interdigited nets based on square lattice topology had relatively low thermal stability in comparison to 3D networks of **6**, **7**, **8**, **9**, **10** and **11** with interpenetrated frameworks. In addition to the interpenetration which provided some high thermal stabilities, the presence of hydrogen bonding interactions between adjacent nets have a significant contribution to the overall stability of the metal organic framework.[9,10] This manifested in compound **6** and **7**. Compound **6** had relatively stronger hydrogen bonding interactions than **7** on adjacent **dia** nets which resulted in a higher temperature of decomposition in comparison to its nickel analogue.

8.7 Future work

The primary objectives of the work presented in this thesis were given in Chapter 1 section 1.8.2. All the objectives of the study were achieved. Novel MOFs based on Zn(II), Ni(II) and Co(II) with solvatochromic and thermochromic properties were prepared using 3-(4-pyridyl) benzoate and 4-(4-pyridyl)benzoate. The chromic properties were investigated and attributed to structural changes induced by external stimuli such as heat and sorption of guest molecules. The use of 3-(4-pyridyl)benzoate ligand in constructing MOFs gave rise to a flexible material as a result of the change in conformation of the ligand under different conditions. This property has been exploited to separate a mixture of *n*-butanol and methanol.

Future work should be directed towards the preparation of metal organic frameworks with Cu(II). Such materials should also exhibit thermochromic and solvatochromic properties owing to the rich coordination geometry of copper. It would be also interesting to investigate the preparation of metal organic frameworks using mixed ligand systems. In this case, compounds such as 4-(4-biphenyl)-dicarboxylic acid, 3, 5 pyridine-dicarboxylic acid and 2,6 pyridine-dicarboxylic acid can be mixed with the pyridyl benzoate ligands (44pba and 34pba). Materials prepared from mixed ligand systems are expected to have superior properties when compared to those prepared from a single ligand. This is because such materials inherit properties of the two ligands and the metal ion used.

8.8 Final Comments

The work presented here is of value in high temperature detection as well as sensing of molecules through colour changes.[11] The crystal structure of the desolvated phase of compound **4** unequivocally prooved that colour changes in crystals may also stem from minor modifications in the network rather than changes in the geometry around the metal centre. Niu's compound $\{[Zn(34pba)_2]\cdot 1.5H_2O]\}_n$ and compound **4** $[\{Zn(34pba)_2]\cdot DMF]\}_n$ presented in this thesis show how the solvent molecules in the crystal structures influence the physical appearance of the crystals. This behaviour towards different solvent molecules is of paramount importance in the design of chemical sensors.

8.9 References

1. C.-Y. Niu, X.-F. Zheng, Y. He, Z.-Q. Feng, and C.-H. Kou, *CrystEngComm*, 2010, **12**, 2847.

2. B. Li, R.-J. Wei, J. Tao, R.-B. Huang, L.-S. Zheng, and Z. Zheng, *J. Am. Chem. Soc.*, 2010, **132**, 1558.

3. I. Imaz, G. Mouchaham, N. Roques, S. Brandès, and J.-P. Sutter, *Inorg. Chem.*, 2013, **52**, 11237.

4. F. Millange, N. Guillou, R. I. Walton, J.-M. Grenèche, I. Margiolaki, and G. Férey, *Chem. Commum.*, 2008, 4732.

5. F. Millange, C. Serre, N. Guillou, G. Férey, and R. I. Walton, *Angew. Chem. Int. Ed. Engl.*, 2008, **47**, 4100.

6. P. G. Yot, Q. Ma, J. Haines, Q. Yang, A. Ghoufi, T. Devic, C. Serre, V. Dmitriev, G. Férey, C. Zhong, and G. Maurin, *Chem. Sci.*, 2012, **3**, 1100.

7. S. Henke, A. Schneemann, A. Wütscher, and R. A Fischer, *J. Am. Chem. Soc.*, 2012, **134**, 9464.

8. S. Horike, R. Matsuda, D. Tanaka, S. Matsubara, M. Mizuno, K. Endo, and S. Kitagawa, *Angew. Chem. Int. Ed. Engl.*, 2006, **45**, 7226.

9. M. Usman, C.-H. Lee, D.-S. Hung, S.-F. Lee, C.-C. Wang, T.-T. Luo, L. Zhao, M.-K. Wu, and K.-L. Lu, *J. Mater. Chem. C*, 2014, **2**, 3762.

10. M.-H. Zeng, Y.-X. Tan, Y.-P. He, Z. Yin, Q. Chen, and M. Kurmoo, *Inorg. Chem.*, 2013, **52**, 2353.

11. G. Mehlana, S. A. Bourne, G. Ramon, and L. Öhrström, *Cryst. Growth Des.*, 2013, **13**, 633.

Appendices

Appendices

Appendices can be found on the enclosed disk.

Appendix A contains the supplementary crystallographic information for each structure. The files have been saved in a subfolder under their structure number.

Appendix B contains the supplementary Rietveld refinement data

Appendix C contains supplementary material such as TGA, DSC, PXRD and solvent sorption data. The files are in subfolders under chapter names

The following files are attached for each crystal structure:

File Extensions	Contents
.hkl	reflection data
.res	SHELX coordinate data
.mercury	crystallographic information file
.fcf	contains tables of observed and calculated structure factors
.lis	PLATON output
.pdf	CheckCIF Report
.txt	Rietveld refinement details